The demographics, obscuration, and accretion properties of X-ray AGN

BRIVAEL MARIE PATRICK LALOUX

The demographics, obscuration, and accretion properties of X-ray AGN

Brivael Laloux

A Thesis presented for the degree of
Doctor of Astrophysics

Department of Physics
Durham University
United Kingdom
April 2024

Abstract

Most massive galaxies host a Supermassive Black Hole (SMBH) at their centre. SMBHs primarily grow by accreting surrounding material, releasing significant amounts of energy as radiation across all wavelengths. SMBHs experiencing such accretion phases are classified as Active Galactic Nuclei (AGN). AGN are believed to play an important role in the formation and evolution of their host galaxies as suggested by well-established correlations between the mass of the SMBH and properties of the host galaxy bulge. Therefore, building a complete census of AGN, which serve as tracers of SMBH growth, is crucial for understanding the mechanisms behind the AGN and galaxies parallel evolution.

However, most AGN are hidden behind clouds of gas and dust that absorb their emission, especially in the UV/optical regime. This obscuration introduces biases in our observations, leading to an underestimation of the intrinsic obscured population. X-ray photons, on the other hand, are less affected by obscuration than UV/optical photons, thus providing a less biased AGN sample. Moreover, the obscuration, characterised by the line-of-sight hydrogen column density $N_{\rm H}$, imprints its signature on X-ray spectra. Analysing these spectra provides constraints on both $N_{\rm H}$ and the intrinsic X-ray luminosity $L_{\rm X}$. With both parameters, it is possible to quantify the detection probability of a source as a function of its properties and, therefore, statistically infer the intrinsic AGN demographics from an observed sample.

In this thesis, I aim to quantify the impact of obscuration on AGN demographics and properties. For that purpose, I develop a new methodology that combines multi-wavelength information with X-ray spectral analysis to break down the degeneracy between obscuration and intrinsic X-ray luminosity measurements and, thereby, improving the constraints on the AGN physical properties. This approach involves fitting the mid-to-far Infrared (IR) Spectral Energy Distribution (SED) of a source to separate the AGN IR emission at $6\,\mu$m from the host galaxy IR contribution. The expected intrinsic X-ray luminosity is then computed using an empirical $L_{\rm X}-L_{6\,\mu{\rm m}}$ relationship. The uncertainties from the SED fitting are convolved with the scatter of the $L_{\rm X}-L_{6\,\mu{\rm m}}$ relationship to build a $L_{\rm X}$ normalisation prior for the X-ray spectral analysis. This approach yields robust measurements of the column density $N_{\rm H}$, especially for the most obscured and

Compton-Thick AGN (CTK, $N_{\rm H} > 10^{24}\,{\rm cm}^{-2}$) with low photon counts X-ray spectra.

I apply this methodology to a sample of 1744 AGN detected in the hard X-ray band (2-7 keV) within the *Chandra* COSMOS-Legacy field. Thanks to the well-defined X-ray selection function in this field, I measure the AGN space density as a function of $L_{\rm X}$, $N_{\rm H}$ and z in a non-parametric way. The uncertainties of the different measurements are consistently combined within a fully Bayesian framework, yielding reliable results in agreement with previous studies. Additionally, this multi-wavelength guided X-ray spectroscopy approach significantly reduces the number of observed CTK AGN in the sample compared to simple X-ray spectroscopy. Similarly to the AGN space density analysis, I carefully account for survey sensitivity to measure the intrinsic fraction of CTK AGN, finding it to be $21.0^{+16.1}_{-9.9}\%$ at $z < 0.5$. At higher redshifts, I established 3-σ upper limits for the AGN CTK fraction of $\lesssim 40\%$. These values are at the low end of previous estimations, suggesting a lower significance of the CTK AGN population than previously thought.

Furthermore, I present the analysis of two additional *Chandra* deep extragalactic X-ray fields, CDFS and AEGIS, for a total of 3882 X-ray-selected AGN. The focus of this work is the comparison of the accretion properties of obscured and unobscured AGN. The Eddington ratio $\lambda_{\rm Edd} \propto L_{\rm bol}/M_{\rm SMBH}$ is a fundamental characteristic of AGN, quantifying how fast an AGN is accreting relative to its maximum rate, beyond which radiation pressure exceeds gravitational pull and expels the accreting material. Outside of the local Universe, the masses of SMBHs $M_{\rm SMBH}$ are determined mainly from the broadening of their optical spectral lines, however, these lines are suppressed in obscured AGN. Therefore, I use the specific accretion rate (SAR) $\lambda \propto L_{\rm X}/M_{\star}$ as a proxy for the Eddington ratio. Indeed, the stellar mass of the host galaxy $M_{\star}$ can be measured by optical-to-IR SED fitting and is proportional to $M_{\rm SMBH}$. By combining $M_{\star}$, $L_{\rm X}$ and $N_{\rm H}$ measurements and their uncertainties in a Bayesian non-parametric approach, I measure the SAR distribution (SARD) for obscured and unobscured AGN for the first time up to $z \sim 3$. The SARD represents the probability of a galaxy with mass $M_{\star}$ at redshift z hosting an AGN with a given SAR λ and obscuration $N_{\rm H}$.

My results show that the SARD shapes of both unobscured and obscured AGN are broadly similar, as expected from the orientation unification model, and shift towards higher accretion rates with increasing redshift, indicating AGN "downsizing". However, the SARDs of unobscured AGN display a systematic offset towards higher accretion rates compared to the obscured population, resulting in a sharp decrease in the obscured AGN fraction at $\log \lambda_{\rm break} \sim -2$ for $z < 0.5$, in agreement with local Universe observations. Nevertheless, as redshift increases, $\lambda_{\rm break}$ shifts to higher values, and the AGN density in the unstable blow-out region of the $\lambda - N_{\rm H}$ plane increases. These results provide evidence for a radiation-regulated obscuration model coupled with increasing obscuration from the Interstellar Medium (ISM) of the host galaxy.

Overall, this thesis highlights the power of inference of X-ray analysis when coupled with multi-wavelength information to study the intrinsic demographics and properties of AGN across redshifts as a function of their obscuration. This work paves the way for future studies to unveil the nature of AGN obscurer and establish the AGN phase in the galaxy-SMBH evolutionary picture.

Résumé

La plupart des galaxies hébergent un trou noir supermassif (*Supermassive Black Hole*, SMBH) en leur centre. Les SMBHs grossissent principalement par l'accrétion de la matière environnante, libérant de grandes quantités d'énergie sous forme de radiation à toutes les longueurs d'onde. Durant une telle phase d'accrétion, les SMBHs sont classifiés en tant que noyaux galactiques actifs (*Active Galactic Nuclei*, AGN). Les AGN doivent jouer un rôle important dans la formation et l'évolution de leur galaxie hôte comme le suggèrent les corrélations entre la masse du SMBH et les propriétés de la galaxie hôte. Par conséquent, construire un recensement complet des AGN qui servent d'indicateur de la croissance des SMBH, est crucial pour comprendre les mécanismes derrière l'évolution parallèle des AGN et galaxies hôtes.

Cependant, la plupart des AGN sont cachés derrière des nuages de gaz et de poussière qui absorbent leur émission, en particulier dans le régime UV/optique. Cette obscuration introduit des biais dans nos observations entraînant une sous-estimation de la population intrinsèque des AGN obscurcis. Les photons rayon-X sont en revanche moins impactés par l'obscuration que les photons UV/optique, ce qui permet d'obtenir un échantillon d'AGN moins biaisé. L'obscuration est caracterisée par la densité de colonne d'hydrogène dans la ligne de mire $N_{\rm H}$ qui laisse son empreinte sur les spectres rayon-X. L'analyse de ces spectres fournit des contraintes sur $N_{\rm H}$ et aussi sur la luminosité intrinsèque en rayon-X $L_{\rm X}$. Avec ces deux paramètres mesurés, il est possible de quantifier la probabilité de détection d'une source en fonction de ses propriétés et donc d'en déduire la démographie intrinsèque des AGN à partir d'un échantillon.

Dans cette thèse, mon objectif est de mesurer l'impact de l'obscuration des AGN sur leur démographie reelle et leur propriétés physiques. Pour cela, je développe une nouvelle méthode qui combine des informations de plusieurs longueurs d'onde avec une analyse spectrale des rayons-X pour rompre la dégénérescence entre les mesures d'obscuration et de luminosité intrisèque en rayon-X, et ainsi améliorer les contraintes sur les propriétés physique des AGN. Cette approche implique l'ajustement de la distribution spectrale d'énergie (*Spectral Energy Distribution*, SED) d'infrarouge (IR) moyen à lointain d'une source pour séparer l'émission infrarouge à 6 μm de l'AGN de la contribution en infrarouge

de la galaxie hôte. En utilisant une relation empirique entre $L_{\rm X}$ et $L_{6\,\mu{\rm m}}$, la luminosité intrinsèque attendue en rayon-X peut être mesurée. Les incertitudes de l'ajustement de SED sont convoluées avec la dispersion de la relation $L_{\rm X}-L_{6\,\mu{\rm m}}$ pour construire une distribution à-priori de la normalisation $L_{\rm X}$ pour l'analyse spectral à rayon-X. Cette méthode produit des mesures fiables de la densité de colonne $N_{\rm H}$, notamment pour les AGN les plus obscurcis et Compton-opaques (*Compton-Thick*, CTK) avec un nombre réduit de photons rayons-X.

J'applique cette méthodologie à un échantillon de 1744 AGN détectés en rayon-X durs (2-7 keV) à l'intérieur du champ COSMOS-Legacy, observé par le télescope *Chandra*. Grâce à la fonction de sélection en rayon-X bien définie dans ce champ, je mesure la densité spatiale d'AGN en fonction de $L_{\rm X}$, $L_{\rm X}$, et z de façon non-paramétrique. Les incertitudes des différentes mesures sont précautionneusement combinées dans un cadre bayésien ce qui fournit des résultats fiables en accord avec des études antérieures. De plus, cette approche de spectroscopie à rayon-X utilisant des données multi-longueurs d'onde réduit de manière significative le nombre d'AGN CTK observés dans l'échantillon par rapport à une simple spectroscopie à rayon-X. D'une manière similaire à l'analyse de la densité spatiale d'AGN, je prends soigneusement en compte la sensibilité des observations pour mesurer la fraction intrinsèque d'AGN CTK que j'ai estimée à $21,0^{+16,1}_{-9,9}\%$ à $z<0,5$. À des décalages vers le rouge (*redshift*) plus élevés, j'ai établi des limites hautes 3-σ à $\lesssim 40\%$ pour la fraction d'AGN CTK. Ces valeurs se situent à la limite inférieure des estimations précédentes, suggérant une importance moindre de la population d'AGN CTK que ce qui était auparavant envisagé.

Ensuite, je présente l'analyse de deux champs extragalactiques profonds à rayon-X supplémentaires de *Chandra*, CDFS et AEGIS, pour un total de 3882 AGN sélectionnés par rayons X. L'objectif de cette étude est la comparaison des propriétés d'accrétion des AGN obscurcis et non-obscurcis. Le ratio d'Eddington $\lambda_{\rm Edd}\propto L_{\rm bol}/M_{\rm SMBH}$ est une caractéristique fondamentale des AGN qui quantifie la rapidité d'accrétion d'un AGN par rapport à son rythme maximale, au-delà duquel la pression de radiation dépasse l'attraction gravitationnelle et expulse la matière à accréter. En dehors de l'Univers local, les masses des SMBH $M_{\rm SMBH}$ sont principalement déterminées à partir de la largeur de leurs lignes spectrales optiques ; cependant, ces lignes ne sont pas visible dans les AGN obscurcis. Par conséquent, j'utilise le rythme d'accrétion spécifique (*Specific Accretion Rate*, SAR) $\lambda\propto L_{\rm X}/M_\star$ comme substitut pour le ratio d'Eddington. En effet, la masse stellaire de la galaxie hôte $M_\star$ peut être mesurée par ajustement de SED de l'optique à l'IR et est proportionnelle à $M_{\rm SMBH}$. En combinant les mesures de $M_\star$, $L_{\rm X}$ et $N_{\rm H}$ ainsi que leurs incertitudes dans une approche bayésienne non-paramétrique, je mesure la distribution du SAR (*Specific Accretion Rate Distribution*, SARD) pour les AGN obscurcis et no-obscurcis pour la première fois jusqu'à $z\sim 3$. La SARD représente la probabilité qu'une galaxie de masse $M_\star$ ayant un *redshift* z héberge un AGN avec un SAR λ et une obscuration $N_{\rm H}$ donnés.

Mes résultats montrent que les formes des SARD des AGN non-obscurcis et obscurcis sont globalement similaires, comme prévu par le modèle d'unification des AGN par orientation, et se déplacent vers des rythme d'accrétion plus élevés avec l'augmentation du *redshift*, indiquant un "rétrécissement" des AGN. Cependant, les SARD des AGN non-obscurcis affichent un décalage systématique vers des rythmes plus élevés par rapport à la population obscurcie, ce qui entraîne une diminution nette de la fraction des AGN

obscurcis à $\log \lambda_{\rm break} \sim -2$ pour $z < 0,5$, en accord avec les observations de l'Univers local. Néanmoins, à mesure que le *redshift* augmente, $\lambda_{\rm break}$ se déplace vers des valeurs plus élevées et la densité des AGN dans la région instable du plan $\lambda - N_{\rm H}$ augmente. Ces résultats fournissent des preuves en faveur d'un modèle d'obscuration régulé par radiation, couplé à une augmentation de l'obscuration par le milieu interstellaire (*Interstellar medium*, ISM) de la galaxie hôte.

Dans l'ensemble, cette thèse met en évidence la puissance de l'inférence de l'analyse des rayons-X lorsqu'elle est couplée à des informations multi-longueurs d'onde pour étudier la démographie intrinsèque et les propriétés des AGN à differents *redshift* en fonction de leur obscuration. Cette recherche ouvre la voie à de futures études visant à dévoiler la nature de la matière obscurcissante des AGN et à placer la phase "AGN" dans le contexte d'évolution syncrhonisée des galaxies et de leur SMBH.

Acknowledgements

I want to express my deepest gratitude to my main supervisor Dr Antonis Georgakakis for accompanying me all along this 4-year-long research journey. Thank you for everything, for your guidance, your enthusiasm, and your patience, I would not have done it without you! You are a great researcher and a great person, a model for me to follow. Thank you as well to my further away supervisor Dr Dave Alexander, for your kindness during my visits to Durham and your precious advice throughout the thesis. J'aimerais aussi remercier Dr Patrick Petitjean pour avoir été le premier à croire en moi.

Je veux évidemment remercier ma famille pour leur soutien continu depuis toujours. À mon père et ma mère pour leur amour, leur éducation et leurs encouragements, à ma grand-mère pour sa joie de vivre, à ma soeur pour m'avoir laissé dormir ailleurs que dans la salle de bain et à Maycol pour supporter ma soeur à ma place.

Then I would like to thank my friends and colleagues at the Observatory of Athens. Notably, Angel, my third supervisor, you helped me so much; to Stephan and the numerous pool evenings and gyros; to Maria and our long deep conversations at work and to all the others: Gonzalo, Maria junior, Ivan, Evangelia, Kostas, Ivan M., Ektoras, Stavroula...

Ensuite vient la seule et unique team EZAK dont les trois autres incroyable membres m'ont carry jusqu'ici: Emilien, mon fraté, nos roadtrips on fait de nous ce qu'on est aujourd'hui; Victor, mon meilleur duo toxique sponso Logitech; et Antho, même si on se voit uniquement au nouvel an, en vrai t'es toujours là. Merci pour toutes ces soirées sur discord, ces fous rires, ces balayettes et ces moments de rage, mais surtout ces moments d'amitié. Il faudra qu'on se refasse un voyage ensemble, en Italie cette fois?

I also want to thank Dr Francesco Shankar and Dr Marcella Brusa for the organisation of the Bid4Best training network, a unique opportunity for me. In this ITN, I want to thank the wild gang for the good moments: Ivan L., Nischal and Carolina; it was 3 amazing months in San Sebastian. Thank you as well to all the other members of the

ITN network, it was a pleasure to work and hang out with you: Blessing, Evgenii, Luca, Hao, Alex, Alba, Ivan M., Giovanna, and Mathilda.

Je veux également remercier mes plus vieux amis, même si on n'habite pas dans le même pays et qu'on se voit pas souvent, vous comptez pour moi: Alexis, Erwann, Léonie, Anaïs et Maxime.

Finally, I want to thank the one who lightened up these two last years, Carolina, thank you for everything! This thesis wouldn't be as it is now without you, we discussed everything, you gave me a lot of advice and you supported me all along. I am glad we lived this chapter of our lives together, I am excited to see the next one.

Declaration

The work in this thesis is based on research carried out at the Department of Physics, Durham University, United Kingdom. No part of this thesis has been submitted elsewhere for any other degree or qualification and it is all my own work unless referenced to the contrary in the text.

Contents

List of Figures

List of Tables

List of Equations

CHAPTER 1

Introduction

Nowadays, the general public knows what black holes are. Despite many approximations, fantasies and misconceptions, the notion of an object from which nothing can escape, not even the light, is now generally accepted. However, in the scientific community, many mysteries regarding them remain to be solved, notably concerning the growth of supermassive black holes (SMBHs), lurking at the centre of galaxies and observed with masses up to 10 billion times that of the Sun. The main objective of this introductory chapter is to present to the reader the context and motivation of this research thesis. §1.1 provides a brief historical background of the field; §1.2 presents the different types of growing SMBH and the standard model to unify them as active galactic nuclei (AGN); §1.3 describes the physical structure and electromagnetic emission of AGN; §1.4 comments on the necessity and the methods to obtain a complete AGN census; §1.5 presents an overview of the proceeding chapters of the thesis.

1.1 Brief History

1.1.1 The Birth of the Black Hole Concept

The term "black hole" was employed for the first time in a scientific conference in January 1964 (Ewing, 1964). However, the idea of celestial objects rendered invisible to our sight by their gravitational potential was independently conceptualised in the late eighteenth century by Reverend John Michell in 1784 and Pierre-Simon Laplace in 1796 (Michell, 1784; Laplace, 1796; Montgomery et al., 2009). Despite Laplace's mathematical proof a few years later (Laplace, 1799), the black hole concept did not convince the contemporary scientific world and remained dormant for over a century.

In 1915, Albert Einstein published his groundbreaking general relativity theory (Einstein, 1915), describing gravitation as a curvature of space-time. A solution to Einstein's equations was provided the following year by Karl Schwarzschild (Schwarzschild, 1916), predicting the existence of a gravitational field from which photons cannot escape beyond a certain radius from a massive object:

$$R_{\mathrm{S}} = 2\,\frac{G \cdot M}{c^2} \tag{1.1}$$

where G is the gravitational constant ($G = 6.674 \times 10^{-11}\,\mathrm{m^3\,kg^{-1}\,s^{-2}}$), M is the mass of the object in kg and c is the speed of light in vacuum ($c = 2.9979 \times 10^{8}\,\mathrm{m\,s^{-1}}$). R_{S} is the Schwarzschild radius in meters defining the event horizon of an electrically neutral and spinless object[1]. The mathematical concept of a black hole was born.

In the following decades, the scientific community rigorously tested the general relativity theory (Dyson et al., 1920). In parallel, stellar evolution and the collapse of dying stars was progressively investigated (Chandrasekhar, 1931; Oppenheimer & Volkoff, 1939). It was finally in 1939 that Robert Oppenheimer and Hartland Snyder predicted that heavy stars, when depleted of thermonuclear fusion fuel, would continuously collapse, eventually becoming smaller than the Schwarzschild radius, therefore forming a stellar black hole (Oppenheimer & Snyder, 1939). Nevertheless, it was not until more than 25 years later that the first stellar black hole, Cygnus X-1, was observed (Bowyer et al., 1965) and

[1] see Section 1.3.1 for a more detailed physical description.

later confirmed (Webster & Murdin, 1972; Bolton, 1972).

1.1.2 The Development of Extragalactic Astronomy

From theory and much later observations, we know that massive stars can produce black holes, but let's return to the visionary predictions of John Michell (Michell, 1784), according to which a "star" with the density of the Sun but 500 times its radius ($R_\odot$) would trap its emitted light. Such an object would have a mass of 500^3 solar masses ($M_\odot$), which using Equation 1.1, corresponds to a Schwartzschild radius of $R_\mathrm{S} = 3.69 \cdot 10^{11}\,\mathrm{m}^2 \sim 500 \cdot R_\odot$. Since its radius is equivalent to the Schwartzschild radius, this object theorised in the eighteenth century would indeed correspond to a black hole but with a mass of approximately $10^8\,M_\odot$. While no star matches these parameters, could astrophysical objects of such dimensions exist and be hidden from our sight? We know now that they do, and their progressive observational discovery goes hand-in-hand with the development of extragalactic observational astronomy.

Indeed, before the twentieth century, our astronomical knowledge extended only to one vast coherent ensemble of stars: our galaxy, the Milky Way. However, since the 1750s, the observation of nebulae by Thomas Wright (Wright, 1750) and Immanuel Kant (Kant, 1755) gave rise to the hypothesis of "island Universes" similar to our Milky Way but situated at great distances. As for the black hole concept, this idea, ahead of its time, was mostly ignored, notably with Charles Messier dismissing them as "nuisance" in his comet-searching catalogue of 110 nebulae (Messier, 1781). The interests began to emerge when the King's astronomer William Herschel compiled a large catalogue containing thousands of nebulae (Herschel, 1786, 1789, 1802), fueling the controversy of their potential location outside the Milky Way. Observational progress during the following century allowed Lord Rosse in 1850 to distinguish a spiral structure in some nebulae (Rosse, 1850), such as Messier 51, nowadays known as the Whirlpool Galaxy (see Figure 1.1). The spiral structure and the point-like objects within it, potentially stars, suggested that nebulae were not mere gas clouds as previously thought. It was later supported by James E. Keeler, who compiled 120,000 nebulae, the majority of them displaying spiral structures

[2] Appproximately twice the distance Sun-Earth.

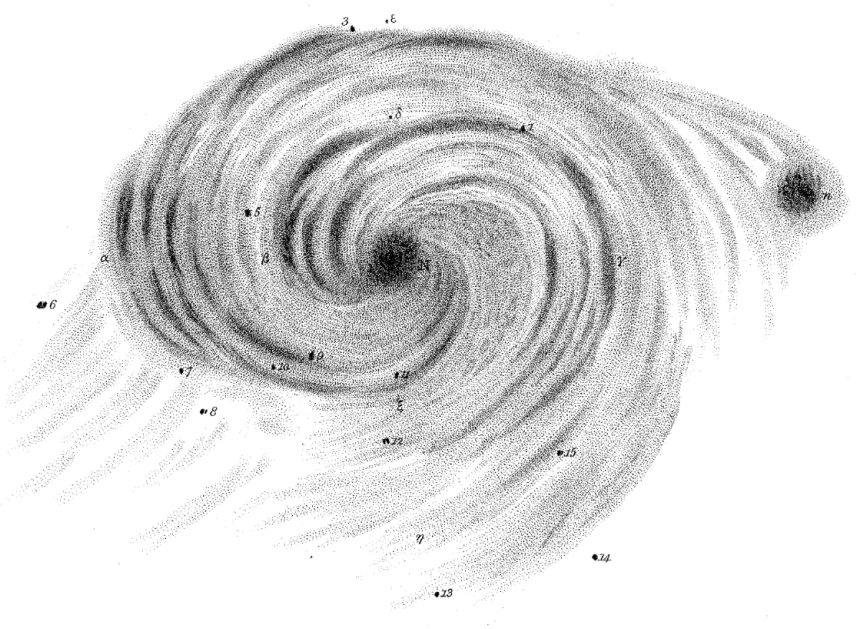

Figure 1.1: The Whirlpool Galaxy, or Messier 51, drawn by Lord Rosse in 1850 (Rosse, 1850).

(Keeler, 1908).

At the start of the twentieth century, the debate on the extra-galactic origin of nebulae was shaken by the technological improvement of optical spectroscopy. This technique consists of decomposing the received light as a function of the wavelength of the photons. By doing so, emission and absorption lines appear and indicate the chemical composition of an object. Edward A. Fath used this methodology to investigate nebulae, discovering that they did not exhibit continuous spectra like stars. He deduced from his observations that nebulae consist of a multitude of stars located at great distances, or else, they would be optically resolved (Fath, 1909). In the 1920s, various independent methods measured the distance of the Andromeda nebula (M31), revealing it to be of the order of hundreds of thousands of parsecs (pc, $3 \cdot 10^{16}$ m). For instance, Harlow Shapley compared the brightness of a supernova within M31 with those of the Milky Way (Shapley, 1917) while Ernst Öpik used the rotational velocity to determine the mass of the galaxy (Campbell & Moore, 1916) and, by applying the Milky Way mass-to-light ratio, estimated the M31 luminosity (Opik, 1922). Finally, Edwin Hubble discovered that some stars in nebulae behaved like Cepheids stars. By using the period-luminosity relation of these variable stars found by Henrietta Leavitt (Leavitt, 1908), E. Hubble estimated their intrinsic luminosity

and compared it with their apparent magnitude. Doing so, he measured the distance of several "extragalactic nebulae" (Hubble, 1925, 1926a,b) as their large distance confirmed their presence outside of the Milky Way.

A few years later, with the same methodology, E. Hubble showed the crucial relation between the distance of galaxies and the shift of their emission lines. In a similar way that the Doppler effect affects sound waves, the radial velocity of an object would shift the frequency of a given emission or absorption line. If the object is coming towards the observer, the line would be shifted to lower frequencies, i.e. towards the blue side of the spectrum, and respectively, if moving away, to higher frequencies, i.e. towards the red part of the spectrum. By noticing that the further a galaxy is, the redder its spectrum is, i.e. the faster it moves away, Hubble discovered the expansion of the Universe (Hubble, 1929). Conversely, the redshift, a measurement of the spectrum reddening, can be used as a distance measurement. The redshift, denoted z, is calculated as:

$$z = \frac{\lambda_{\text{obs}} - \lambda_{\text{emit}}}{\lambda_{\text{emit}}}, \tag{1.2}$$

with λ_{emit} and λ_{obs}, respectively, the emitted and observed wavelength of a specific emission or absorption line.

1.1.3 The Discovery of Active Galactic Nuclei

Two decades before the confirmation of the extra-galactic nature of nebulae, in 1909, E. Fath noticed strong high-excitation lines (H, O, Ne) in the spectrum of the centre of NGC 1068 (Fath, 1909). Unknowingly, he had observed for the first time a new class of extragalactic objects. In 1917, Vesto Slipher measured the broadening of emission lines in the same galaxy, corresponding to velocities of $\sim$1000 $\mathrm{km\,s^{-1}}$. Nevertheless, it was not until 1943 that the study of this new class of objects finally took off with the description of 6 galaxies similar to NGC 1068 by Carl K. Seyfert (Seyfert, 1943). These galaxies shared a bright point-like centre called a "nucleus" and strong and broad emission lines in the spectrum. This type of source later became known as Seyfert galaxies, and further categorized into type I, showing broader permitted emission lines compared to forbidden

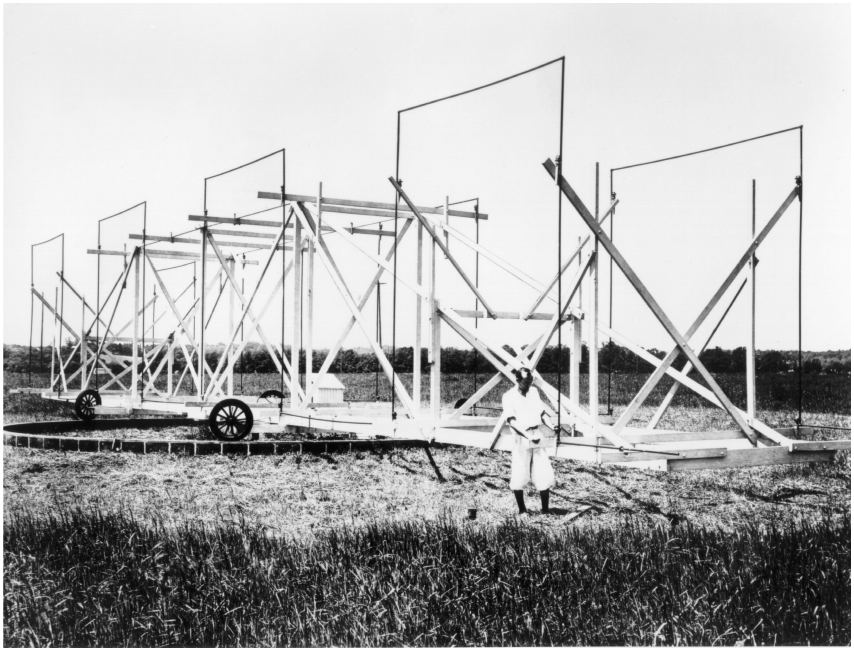

Figure 1.2: Karl Jansky next to his rotating radio antenna in 1931. With this antenna, K. Jansky was able to identify the first extra-terrestrial radio source, giving birth to radio astronomy. Image credits: NRAO/AUI Archives.

ones[3], and type II, with similar-width permitted and forbidden lines (Weedman, 1970, 1977).

In parallel with progress in optical extragalactic astronomy, Karl Guthe Jansky opened a completely new field of research: radio astronomy. As a radio engineer, he built a rotating radio antenna as shown in Figure 1.2, allowing him to pinpoint the origin of a faint static signal. Initially attributing it to the Sun, Jansky later realized it originated from the centre of the Milky Way (Jansky, 1933, 1984). However, the physical process producing these radio waves remained uncertain. Inspired by K. Jansky's work, Grote Reber mapped the Cygnus constellation at 160 MHz (Reber, 1944), paving the way for systematic radio mapping. After the Second World War and the technological improvement of radio technologies, different institutes around the world conducted radio catalogues, exploring different frequencies (Edge et al., 1959; Ekers, 1969; Ehman et al., 1970). The extended non-thermal emissions observed in Baade & Minkowski (1954) suggested the presence of jets powered by synchrotron emission. One of the primary challenges of the time was to

[3] Forbidden lines can only be produced in environments with very low density providing stability to specific excitation levels. Such low density cannot be reached on Earth, hence their name. Permitted lines are emitted in denser environments.

identify an optical counterpart for compact radio sources; they were believed to be radio stars, bright in the radio but invisible in optical (Ryle et al., 1950). However, in 1960, Rudolph Minkowski found the optical counterpart of 3C 295 and measured its redshift at $z = 0.46$. In subsequent years, the optical counterpart of several other radio sources were identified and their spectra indicated high redshifts, up to $z = 2.012$ for 3C 9, measured by Marteen Schmidt (Schmidt, 1963, 1965). These high redshifts combined with the redshift-distance relation (Hubble, 1929), proved the extragalactic nature of this "quasi-stellar radio objects" eventually abbreviated to "quasar" by Hong-Yee Chiu (Chiu, 1964). In 1965, following the identification of sources with quasar-type optical spectra but no radio emission, Allan Sandage proposed that quasars no longer be defined solely by their radio emission (Sandage, 1965).

The different optical and radio observations of Seyfert galaxies and quasars indicated that, in opposition to regular galaxies, most of their radiative emission was produced within a nucleus, a small and dense area at their centre. Lodewijk Woltjer, for instance, suggested that reproducing Seyfert galaxy properties required a mass of a few times 10^8 solar masses within a 100 pc region (Woltjer, 1959). Similarly, the observed optical luminosity variability on the time scale of a year for some quasars (Smith & Hoffleit, 1963; Sandage, 1964; Fitch et al., 1967) constrained their size to less than 1 pc. The radiation power of these small central regions led to the classification of these objects as Active Galactic Nuclei (AGN). Independently, in 1964, Edwin Salpeter (Salpeter, 1964) and Yakov Zel'dovich and Igor Novikov (Zel'dovich & Novikov, 1964) proposed that AGN were powered by the progressive accumulation of matter due to gravitational attraction onto a massive and compact body. This process, called accretion, forms a disc in which the gravitational potential energy is converted into thermal radiation, requiring the accretion of only 1 solar mass per year with a 10% energy-to-light efficiency to produce the equivalent of the whole galaxy stellar light (Lynden-Bell, 1969). Based on the mass and size of the AGN central regions, the concept of supermassive black holes (SMBH) with masses ranging from 10^6 to 10^{10} solar masses emerged. Soon, SMBHs powering AGN at the heart of galaxies via mass accretion was widely accepted (Lynden-Bell & Rees, 1971; Lynden-Bell, 1978; Rees, 1984), however, the existence of these SMBH remained theoretical or indirectly observed for several decades. The conclusive evidence was brought in 2019

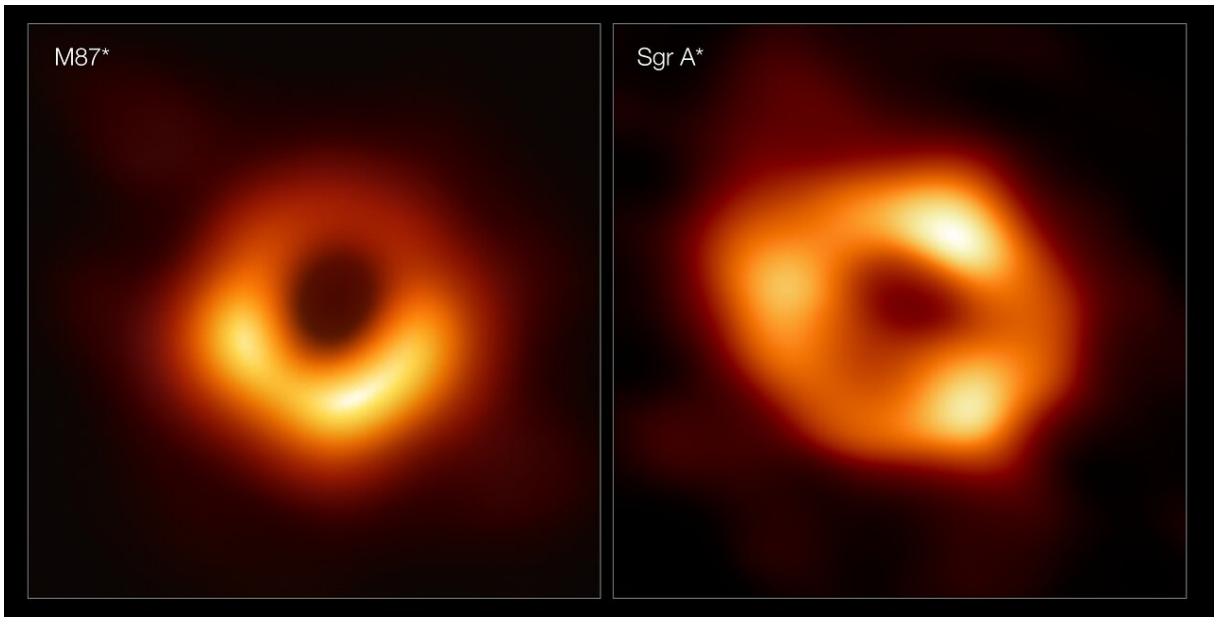

Figure 1.3: The first two images ever taken of SMBHs by the Event Horizon Telescope collaboration: on the *left*, M87⋆ in the galaxy Messier 87 and, on the *right*, Sagittarius A⋆ in the centre of the Milky Way. Both SMBHs have an angular size of a few μas. Image credits: EHT Collaboration.

by the Event Horizon Telescope (EHT) collaboration. This network of radio telescopes around the world reaches a sufficient angular resolution to observe the radio emission of the event horizon delimiting a SMBH. This collaboration led to the publication of the first direct observation of a SMBH, M87⋆ in the centre of the galaxy Messier 87 (Event Horizon Telescope Collaboration et al., 2019a). As shown in the left panel of Figure 1.3, the SMBH can be inferred by the absence of radio emission, allowing a measurement of the radius and mass of the SMBH. For instance, the gravitational radius of M87⋆ has an angular size of $\theta_g = 3.8 \pm 0.4\,\mu$as[4], resulting in a mass estimation of $M_{\mathrm{M87}^\star} = 6.5 \pm 0.7 \times 10^9\,M_\odot$ (Event Horizon Telescope Collaboration et al., 2019b). Three years later, the SMBH hidden in the centre of the Milky Way, Sagittarius A⋆, was observed by EHT (right panel in Figure 1.3). With a similar angular size ($\theta_g = 4.8^{+1.4}_{-0.7}\,\mu$as) to M87⋆, Sagittarius A⋆ is nonetheless significantly less massive ($4.0^{+1.1}_{-0.6} \times 10^6\,M_\odot$) (Event Horizon Telescope Collaboration et al., 2022).

Between the theoretical prediction of SMBH and their recent direct observation, a

[4] One arcsec, labeled as or ", is defined as $1/(60\times60)$ degree. Then, for M87⋆, θ_g is approximately one billionth of a degree.

new field emerged: X-ray astronomy. A natural limitation of this waveband is the Earth's atmosphere absorbing most X-ray radiation, leaving the Sun as the only known X-ray source in the first half of the twentieth century. Advancements in rocket technologies, notably the Aerobee developed by James Van Allen (van Allen et al., 1948), enabled the deployment of X-ray detectors into the upper atmosphere, to an altitude of a few kilometres, overcoming this atmospheric limitation. Early X-ray missions primarily focused on solar studies, but in 1962, while attempting to study the Moon's X-ray emission, Riccardo Giacconi observed the first X-ray source outside of the Solar System, the X-ray binary Scorpius X-1 (Giacconi et al., 1962). Moreover, Giacconi's observations also detected for the first time the Cosmic X-ray Background (CXB), a diffuse isotropic emission, that we know now to be the sum of the emission of all resolved and unresolved X-ray sources. Subsequent observations via Aerobee rockets in the following years detected the first X-ray extragalactic emissions from nearby radio-galaxies such as M87 (Friedman & Byram, 1967; Bowyer et al., 1970). Throughout the following decades, progress in extragalactic X-ray astronomy accelerated thanks to the advent of X-ray space telescopes that have larger collecting areas, higher spectral resolution and, in opposition to rockets, stay in orbit for much longer exposure times. Notable missions include Uhuru (1970), Ariel-V (1974), HEAO 1 (1976), HEAO 2 (1978), HEAO 3 (1979), EXOSAT (1983) (e.g. Tucker & Giacconi, 1985). A decade of X-ray observations revealed that X-ray emission is a ubiquitous characteristic among AGN (Elvis et al., 1978; Tananbaum et al., 1979) which are significantly contributing to the CXB (Comastri et al., 1995). Moreover, the luminosity variability in this band, up to hour-scale, reduces even more the size of these objects, further supporting the SMBH concept (Türler et al., 1999). By the late 1990s, the launch of new X-ray telescopes, notably *Chandra* observatory (1999) and *XMM-Newton* (1999), firmly established the X-ray band as a crucial tool for studying SMBH growth through AGN observations.

Since their discovery in the 1960s, the list of new types of AGN has continuously expanded, driven by the presence or absence of specific features across various wavelengths (Padovani et al., 2017). For instance, blazars were found exhibiting significant non-thermal continuum emission (Schmitt, 1968; Strittmatter et al., 1972), attributed to a highly-collimated jet. The diversity of AGN types and their unification models are

presented in Section 1.2 while Section 1.3 depicts the different components of AGN and their multi-wavelength emission processes. Moreover, far from being rare, SMBHs reside at the centre of most massive galaxies (Kormendy & Ho, 2013), with millions of quasars, the brightest AGN subset, identified across all redshifts, up to $z = 8.50$ (Kokorev et al., 2023) and potentially even higher $z > 10$ (Goulding et al., 2023; Maiolino et al., 2023). Section 1.4 presents a brief overview of our current understanding of the growth of SMBH: §1.4.1 How to identify AGN at all redshift in the different wavebands? §1.4.2 How many AGN are hidden by their local environment? §1.4.3 What are the mutual interactions between AGN and their host galaxies?

1.2 The AGN Zoo and the Unification Model

As mentioned in the historical introduction (Section 1.1), the AGN group contains several types of objects, totalling 50 according to Padovani et al. (2017), each exhibiting distinct morphologies or observational properties. These different AGN types form the AGN "zoo", with the main subtypes presented in §1.2.1. The standard unification model, or how the different AGN subclasses offer different perspectives on one unique object type, is described in §1.2.2.

1.2.1 The Main AGN Types

The AGN classification in subgroups depends on three main observational factors: the radio emission, the presence or absence of broad lines and the bolometric luminosity. Radio-Quiet (RQ) AGN represent 80-90% of the AGN population (Ivezić et al., 2002; Kellermann et al., 2016) and are characterised by low radio-loudness $\mathcal{R} \lesssim 10$. This parameter is defined as $\mathcal{R} = \frac{f_{6\,\mathrm{cm}}}{f_{4400\,\text{Å}}}$ (Kellermann et al., 1989), ratio of the radio flux at 6 cm (or 5 GHz) to the accretion luminosity flux at 4400 Å. RQ AGN are subdivided into type I and type II AGN based on the width of their permitted emission lines in their optical spectra: the Full Width at Half Maximum (FMWH) is larger than $1\,000\,\mathrm{km\,s^{-1}}$ for type I AGN and lower for type IIs (Weedman, 1977). For instance, the top right panels C and D in Figure 1.4 display the spectra of NGC 4151 and NGC 4941, respectively, type I and II radio-quiet AGN, and one can notice the apparent broadening of the Balmer emission lines

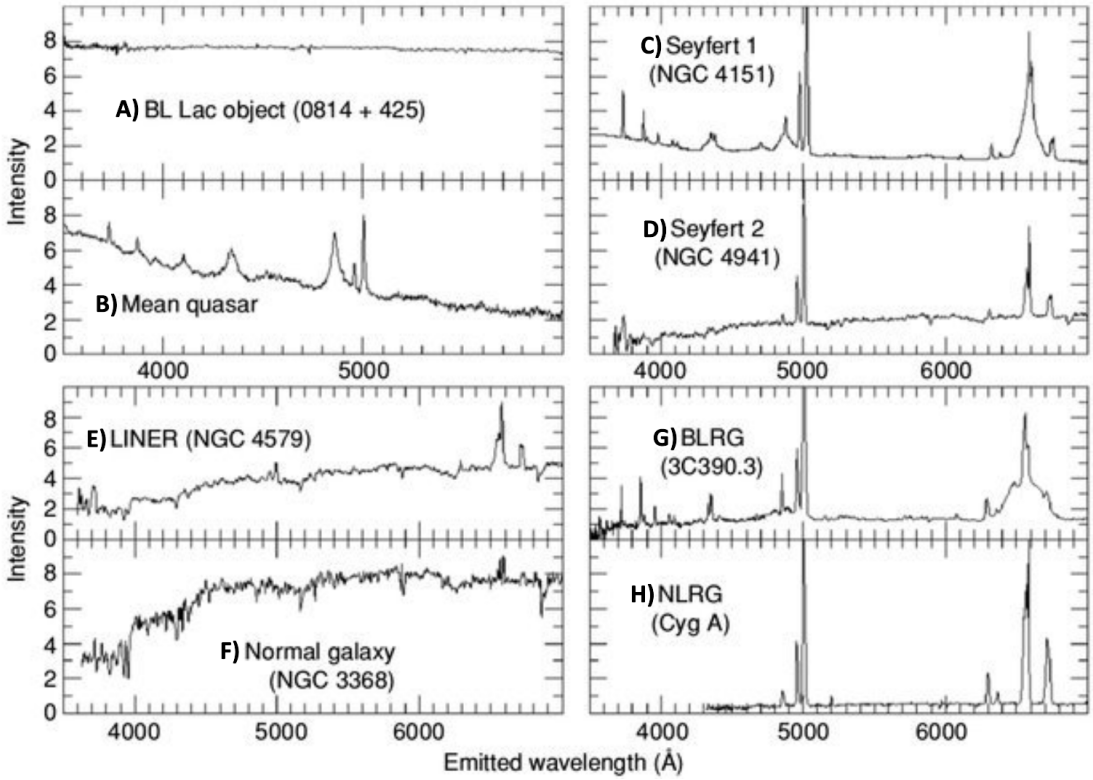

Figure 1.4: Example of spectra for the different AGN types indicated in each panel. Figure from Andika (2016).

Hα λ6563, Hβ λ4861 and Hγ λ4340. Intermediate subgroups such as type 1.5, 1.8 or 1.9 exist, referring to the relative intensity of broad and narrow lines (Osterbrock, 1977, 1981). Seyfert galaxies (type I and II) are RQ galaxies with luminous point-like nuclei, while RQ quasars (panel B in Figure 1.4) are bright enough to outshine their host galaxies. The separation between the two classes was conventionally set at absolute magnitude $M_{\rm B} < -23\,{\rm mag}$[5] or bolometric luminosity[6] $L_{\rm bol} \gtrsim 10^{45}\,{\rm erg\,s^{-1}}$ for quasars (Padovani et al., 2017). A last subclass of RQ AGN is the Low-Ionization Nuclear Emission-line Regions (LINERs) (Heckman, 1980) that are similar to Seyfert galaxies, except they exhibit weak or absent high-ionisation lines like [OIII]λ5007 (Heckman & Best, 2014). The bottom left panels E and F in Figure 1.4 compare a LINER (NGC 4579) with a typical galaxy

[5] The absolute magnitude refers to the brightness of an object after correcting for the distance. The magnitude system was defined by Hipparchus in the second century BC: the brighter an object is, the lower its magnitude is. The Sun and the second brightest star of the sky, Sirius, have an apparent magnitude of -26.8 and -1.5, respectively, while their absolute magnitudes are +4.74 and +1.43, respectively.

[6] The bolometric luminosity is the total radiation emitted across all wavelengths. The bolometric luminosity of the Sun is $L_\odot = 3{\times}10^{35}\,{\rm erg\,s^{-1}}$. An erg is an energy unit equal to $10^{-7}\,{\rm J} = 1\,{\rm g\,cm^2\,s^{-2}}$.

(NGC 3368), respectively. Unlike other AGN, the ionisation in LINER is believed to be produced by shocks from the interaction of AGN winds and host-galaxy material (Ho et al., 1993; Veilleux et al., 1995). However, it has been established that not all LINERs are AGN (Yan & Blanton, 2012), and LINER-like emission may also arise from photoionisation driven by star formation processes.

In the Radio-Loud (RL) AGN group ($\mathcal{R} > 10$), there is a similar type I-type II distinction between the Broad Line Radio Galaxies (BLRG) and Narrow Line Radio Galaxies (NLRG) as shown in the bottom right panels G and H in Figure 1.4, respectively. Similarly to the RQ classification, RL quasars represent the brightest subset of radio AGN with $M_{\mathrm{B}} < -23\,\mathrm{mag}$. Radio sources are further categorised according to the morphologies of their radio jets (Fanaroff & Riley, 1974). Edge-darkened sources or Faranoff-Riley I (FR I) have jets that gradually fade away from the source, while edge-brightened or FR II sources have higher brightness at the end of the collimated jets. Furthermore, the RL AGN displaying non-thermal radiation across the entire magnetic spectrum are known as blazars, subdivided into two subclasses, the Flat Spectrum Radio Quasars (FSRQs) and the BL Lacs. The former ones display strong emission features compared to the latter ones that can even be featureless (Stickel et al., 1991; Giommi et al., 2012) as shown on the top left panel A in Figure 1.4. The last of the main AGN classifications are the Weak-Line Radio Galaxies (WLRG), similar to the LINERs but in the RL regime.

1.2.2 The Standard Unification Model

The discovery and classification of the AGN types mentioned in the previous subsection were progressively made throughout the second half of the twentieth century, and several pioneer attempts were made to unify these objects. For instance, Rowan-Robinson (1977) observed that the nature of the AGN is independent of the host galaxy morphology (e.g. elliptical or spiral), and suggested that strong dust obscuration could be the difference between type I and type II Seyfert galaxies. A few years later, the presence of dust in type II Seyfert was confirmed via spectropolarimetry (Antonucci, 1984; Antonucci & Miller, 1985; Miller et al., 1991), notably in the nearby narrow-line Seyfert NGC 1068. As the light emitted by the AGN is originally unpolarised, the detection of broad emission lines in NGC 1068's polarised spectrum shows evidence for the presence of dust reflecting photons

onto the line-of-sight. Moreover, it suggests that type II AGN can also emit broad lines which are absorbed by surrounding dust.

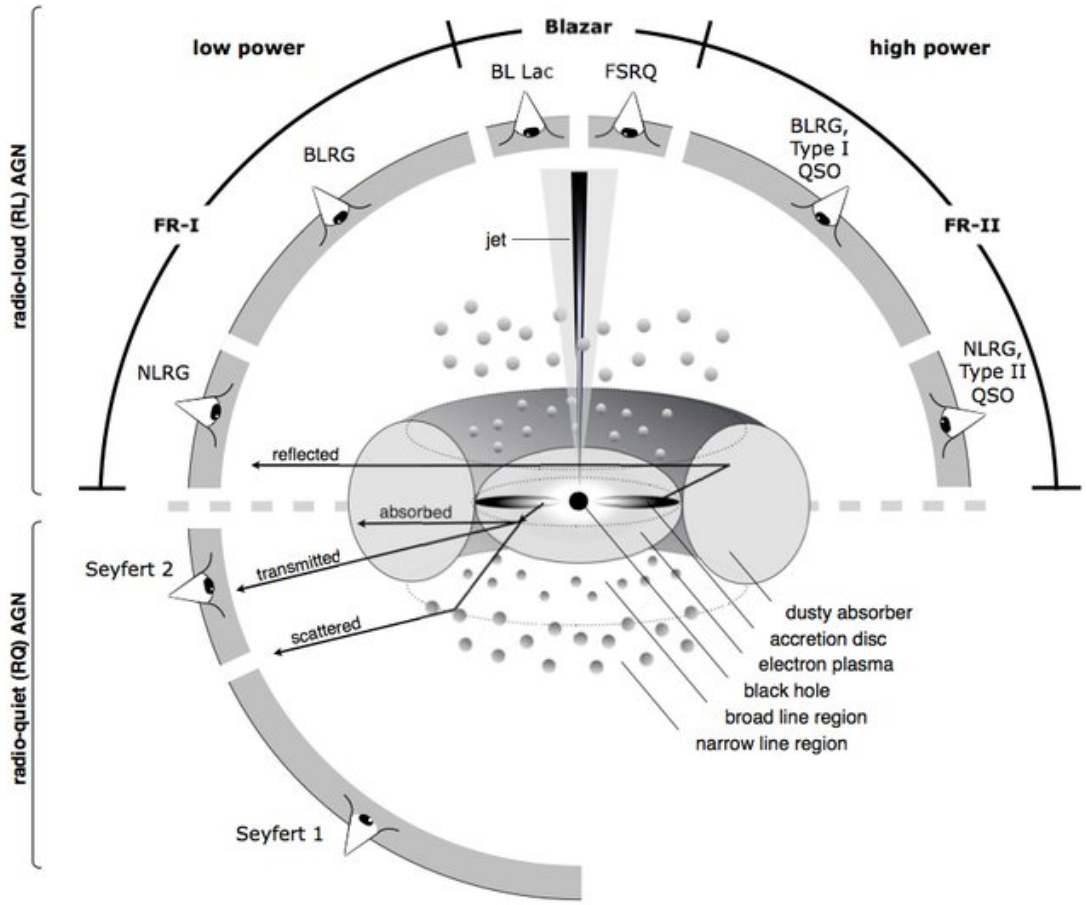

Figure 1.5: Illustrative diagram of the structure of an AGN according to the unification model. The AGN is composed of: a SMBH at its centre (§1.3.1) with an accretion disc around it (§1.3.2), an electron plasma (called hot corona in the rest of the text, §1.3.3), a dusty torus-shaped absorber in the equatorial plane (§1.3.4), the broad and narrow line regions along the polar axis (§1.3.5) and eventually a jet (§1.3.6). The AGN types are divided by two main criteria: radio-loud on *top* and radio-quiet at the *bottom*; on the *left*, low-power AGN and high-power AGN on the *right*. Radio quiet quasars exist but are not represented in the *bottom right* for clarity. Broad line or type I sources have a direct view of the centre of the AGN, while narrow line or type II sources have the dusty absorber in the line-of-sight. The blazer subgroup is radio-loud AGN when the collimated jet is toward the observer. Figure from Beckmann & Shrader (2012).

Building upon these findings, the unification model, popularised by the reviews of Antonucci (1993) and Urry & Padovani (1995), claims that all AGN have the same components and the same structure, and that the different AGN classifications result only from the viewing angle of the observer, as depicted in Figure 1.5.

- In the case of a high inclination angle with the equatorial plane (face-on), all the AGN emission components are visible to the observer, including the accretion disc (UV/optical continuum, §1.3.2), the hot corona (X-ray continuum, §1.3.3), the broad line region (BLR, §1.3.5), the narrow line region (NLR, §1.3.5), the dusty torus (IR continuum, §1.3.4) and the potential jets (radio continuum, §1.3.6). Consequently, such AGN are classified as type I or unobscured AGN whose typical Spectral Energy Distribution (SED) is illustrated in the left panel of Figure 1.6.

- At low inclination (edge-on), the dusty torus blocks the view of the central region, significantly impacting the AGN SED as shown in the right panel of Figure 1.6. Indeed, the X-ray corona being hidden results in an obscured X-ray spectrum where soft X-ray emission ($< 10\,\mathrm{keV}$[7]) is strongly absorbed, while hard X-ray emission ($> 10\,\mathrm{keV}$[7]) is less suppressed due to the higher penetrability through dust of higher energy photons. Additionally, as the accretion disc and BLR are also hidden, the UV/optical continuum and broad lines are suppressed, while the narrow lines remain detectable since the NLR is located further away than the torus. Similarly, due to the extent of the jet, the radio emission can be seen at all inclinations. Finally, the orientation does not affect the IR emission originating from the torus. Such AGN are classified as type II or obscured AGN.

- The last scenario in the unification model is when the collimated radio jet (§1.3.6) of a RL AGN is directly oriented towards the observer as depicted at the top of Figure 1.5. In that case, the entire SED is dominated by the powerful non-thermal synchrotron emission from the jet (panel A in Figure 1.4), leading to the classification of the AGN as a blazar.

However, the orientation model alone fails to account for the dichotomy between radio-quiet and radio-loud AGN, leaving the origin or absence of radio jets unresolved yet. While the spin of the SMBH has been proposed as a factor in jet production (Begelman et al., 1984; Narayan & McClintock, 2012; Blandford et al., 2019, see §1.3.6), the presence of large-spin radio-quiet AGN suggests the existence of other independent factors influencing jet formation, possibly linked to the accretion state of the SMBH (Blandford et al., 2019).

[7] An X-ray photon of 10 keV has a frequency $\sim 2.4 \times 10^{18}\,\mathrm{Hz}$

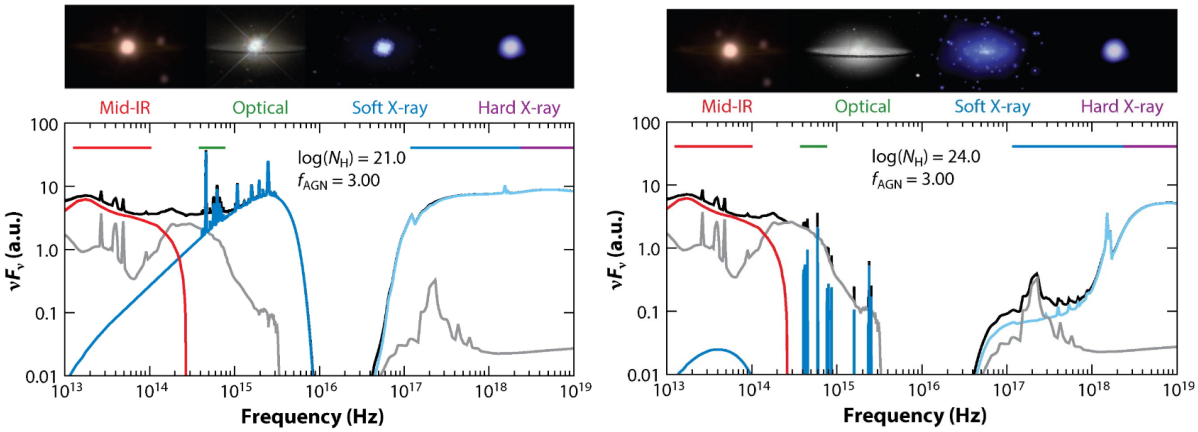

Figure 1.6: Infrared (IR) to hard X-ray Spectral Energy Distribution (SED) for unobscured (*left*) and obscured (*right*) AGN. The torus IR emission, the accretion disc UV/optical emission and the X-ray corona emission are displayed by *red*, *blue* and *cyan solid lines*, respectively. The *grey solid line* represents the host galaxy SED with notably a peak in the X-ray caused by X-ray binaries. In obscured AGN, the UV/optical continuum is suppressed, only the narrow lines remain. Additionally, the soft X-rays ($< 10\,\mathrm{keV}$) are strongly absorbed compared to the hard X-rays ($> 10\,\mathrm{keV}$). Respectively, the IR emission is mostly unaffected. Figure adapted from Hickox & Alexander (2018).

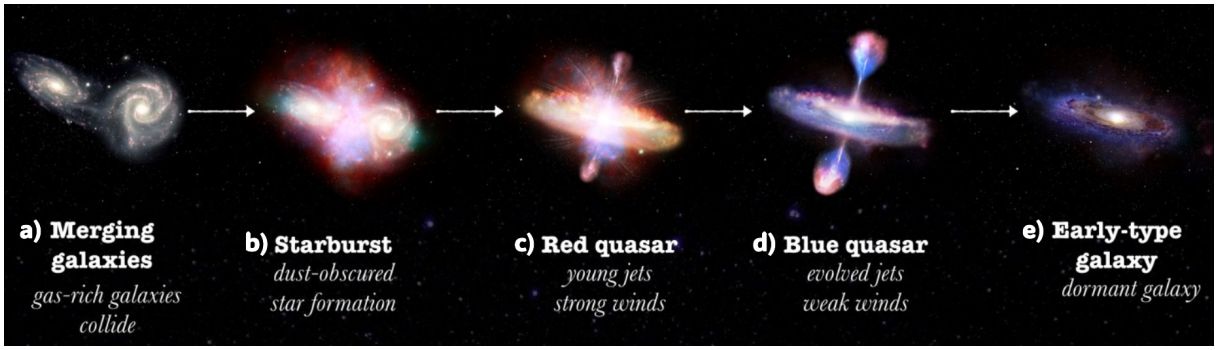

Figure 1.7: Evolutionary sequence showing the transition between red (mildly obscured) and blue (unobscured) quasars. With the courtesy of L. Klindt & S. Munro (Klindt, 2022).

Often put in opposition with the unification model despite not being antinomic, the evolutionary models suggest that AGN subclasses are not solely determined by the line-of-sight orientation but also by the stage of the AGN-galaxy co-evolution (Di Matteo et al., 2005; Hopkins et al., 2006, 2008; Klindt et al., 2019). These models are supported by evidence of parallel evolution between the AGN and its host galaxy; for instance, their masses are correlated (Gebhardt et al., 2000; Marconi & Hunt, 2003; Kormendy & Ho, 2013) despite being several orders of magnitude different in size. As illustrated in Figure 1.7, this common growth history is possibly triggered by a merger event rapidly funnelling large quantities of material into the central SMBH (phase a). The galaxy experiences a starburst phase (phase b) while the rapidly accreting SMBH enters the AGN phase as a powerful quasar. However, the dusty gas enshrouding the central region reddens the quasar's emission (phase c). Due to the radiation feedback of the AGN, the dust cocoon is progressively expelled, and the quasar appears unobscured (phase d). The AGN keeps accreting until all the material is either blown away or absorbed, becoming then quiescent (phase e). In this evolutionary framework, the obscuration is then not only due to the orientation of the dusty torus but also to large-scale obscuration from the host galaxy. Furthermore, red (mildly obscured) and blue (unobscured) quasars, representing preferentially different stages of the AGN life cycle, may display distinct physical properties while the orientation-only unification model predicts identical ones. Recent studies, in agreement with this basic picture, found that red quasars show enhanced radio emission (Klindt et al., 2019; Fawcett et al., 2023) and star formation (Andonie et al., 2022a) compared to their blue counterparts. Nevertheless, the connection between galaxy merger and AGN activity is still debated as some results indicate no significant correlation (Villforth et al., 2017; Sharma et al., 2024) while others support a connection (Koss et al., 2010; Treister et al., 2012; Gao et al., 2020).

1.3 Structure and Spectral Energy Distribution of AGN

Nowadays, we know that AGN are powered by a central SMBH and we have a global idea of the anatomy of an AGN (see §1.2.2), however, determining the precise structure and

physical processes ongoing in each AGN components are active research topics. Figure 1.8 represents a modern sketch of the structure of an AGN along the equatorial and polar directions with size scales of the different components. The combination of these various components emissions results in the AGN characteristic Spectral Energy Distribution (SED) presented in Figure 1.9. These components and their respective emission SEDs are described in the following subsections.

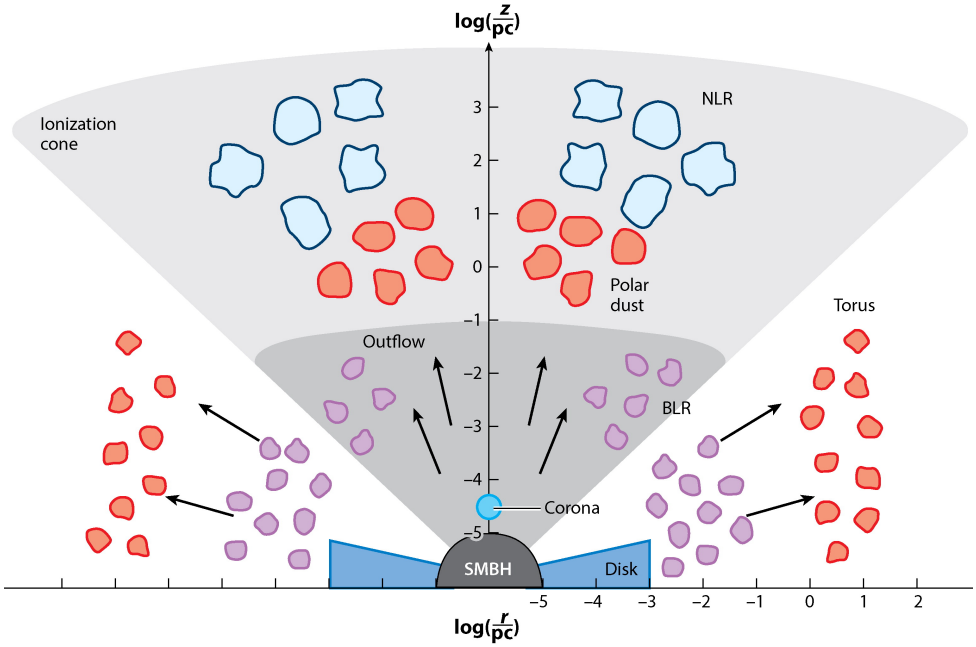

Figure 1.8: Schematic representation of the structure of an AGN. From the centre to host-galaxy scales: SMBH, accretion disc and X-ray corona, broad line region, torus and narrow line region. The colours of the different structures are matched with their respective SED contribution in Figure 1.9. Figure from Hickox & Alexander (2018), adapted from Ramos Almeida & Ricci (2017a).

1.3.1 The Supermassive Black Hole

As previously described in the historical introduction (§1.1), black holes (BHs) are a direct consequence of Einstein's relativity equations (Einstein, 1915). BHs are characterised by two primary quantities: the mass and the spin. A third quantity would be the electric charge of the BH, but a significant electric charge relative to the gravitational pressure is unlikely. The Scharzschild radius given by Equation 1.1 (Schwarzschild, 1916) corresponds to the event horizon of a neutral spinless BH, i.e. the radius at which the escape velocity is higher than the speed of light. As no photon can escape the gravitational potential

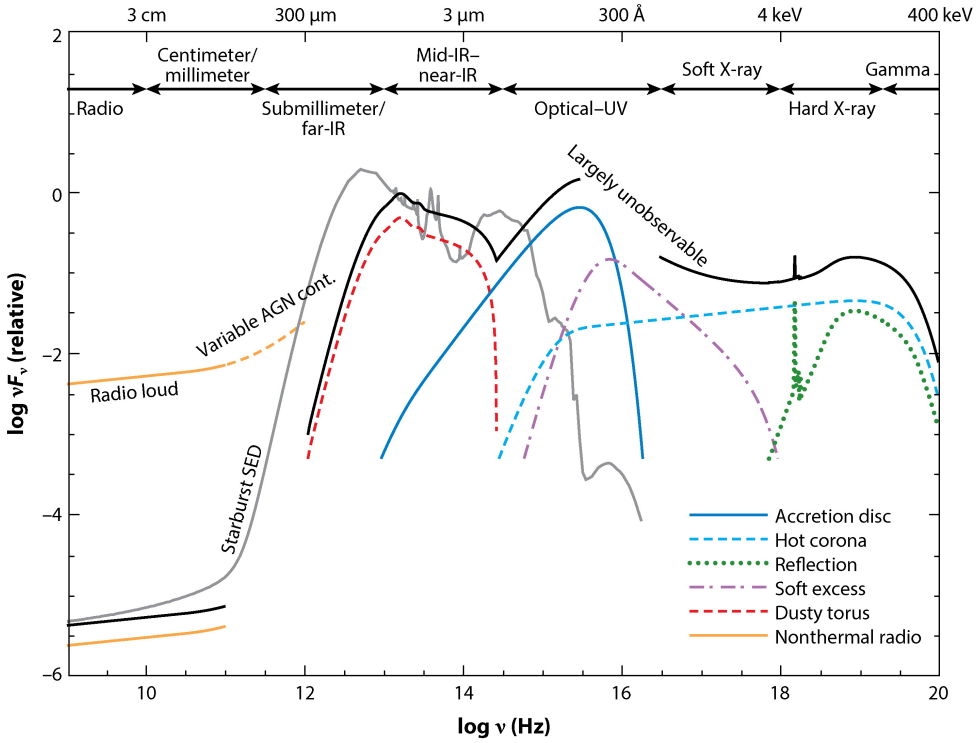

Figure 1.9: Spectral Energy Distribution (SED) of an unobscured AGN (*black solid line*). The host galaxy emission is represented by a *grey solid line*, while the different AGN emission features are displayed according to the legend. Figure adapted from Harrison (2014).

of a BH, it appears black to an observer. A neutral rotational BH with an angular momentum J would have an event horizon radius in meters given by:

$$r_+ = \frac{G \cdot M}{c^2} + \left[\left(\frac{G \cdot M}{c^2} \right)^2 - \left(\frac{J}{M \cdot c} \right)^2 \right]^{1/2} \tag{1.3}$$

where G is the gravitational constant ($G = 6.674 \times 10^{-11}\,\mathrm{m^3\,kg^{-1}\,s^{-2}}$), M is the mass of the object and c is the speed of light in vacuum ($c = 2.9979 \times 10^8\,\mathrm{m\,s^{-1}}$) (Kerr, 1963). The dimensionless BH spin parameter, defined as $a \equiv \frac{Jc}{G \cdot M^2}$, varies in the range $-1 < a < 1$. As a consequence, the event horizon radius r_+ varies between $2\,\frac{G \cdot M}{c^2}$ for a non-rotating BH and $\frac{G \cdot M}{c^2}$ for a maximally rotating BH (Reynolds, 2021).

Stellar BHs are formed by the collapse of massive dying stars (Oppenheimer & Snyder, 1939) and are, therefore, of the same order of the mass $< 150\,M_\odot$ (Figer, 2005). Supermassive black holes (SMBHs) are alike stellar BHs but orders of magnitude more massive with masses in the range of $10^6\,M_\odot$ (Greenhill et al., 2003; Seth et al., 2010;

Gültekin et al., 2019) and $10^{10}\,M_\odot$ (Dietrich et al., 2009; Wang et al., 2014; King, 2016; Inayoshi & Haiman, 2016). As a consequence, their event horizon radius ranges between $10^{-7}\,\mathrm{pc} \lesssim r_+ \lesssim 10^{-3}\,\mathrm{pc}$ (Equations 1.1 and 1.3). They are found in the centre of massive galaxies (Kormendy & Ho, 2013); for instance, the SMBH in our galaxy, Sagittarius A*, has a mass of $M_{\mathrm{BH}} \approx 4.0 \times 10^6 M_\odot$ (Eckart & Genzel, 1997; Ghez et al., 2008; Genzel et al., 2010; Do et al., 2019; GRAVITY Collaboration et al., 2019; Event Horizon Telescope Collaboration et al., 2022). Before the advent of the EHT and the direct measurement of its event horizon radius, directly correlated with its mass (Event Horizon Telescope Collaboration et al., 2022), the mass of Sagittarius A* was reliably calculated by measuring the velocities and trajectories of stars orbiting the SMBH and applying the following equation:

$$M_{\mathrm{BH}} = \frac{V_{\mathrm{vir}}^2\, R}{G} \tag{1.4}$$

with V_{vir} the virial velocity of the stars and R the distance to the SMBH.

For other galaxies for which EHT cannot measure the event horizon radius and in which individual stars cannot be resolved, different methodologies were developed to exploit stellar or gas dynamics with different models and assumptions to estimate V_{vir} and then the central BH mass (e.g. Vestergaard & Gültekin, 2023, for a review). For bright AGN outshining their host galaxies, the width of the broad emission lines (mostly the Balmer lines Hα and Hβ) can constrain the virial velocity V_{vir} in Equation 1.4 (Greene & Ho, 2005; Trakhtenbrot & Netzer, 2012; Koss et al., 2017). Additionally, reverberation mapping can be used to estimate the distance R by measuring the time delay τ between the luminosity variation of the continuum with the one of the emission lines (Blandford & McKee, 1982; Uttley et al., 2014). This lag represents the travel time of photons between the central source and the broad line region (see Section 1.3.5), and, therefore, we obtain $R = \tau \cdot c$. However, reverberation mapping is not always possible as it necessitates the monitoring of the target sources. Nevertheless, an empirical relation between the AGN luminosity and the size of the BLR has been established (Bentz et al., 2013; Du & Wang, 2019). Therefore, using the luminosity as a proxy of R and the broad line width as a proxy of V_{vir} in Equation 1.4, single-epoch M_{BH} estimations can be made in return of larger uncertainties.

These methodologies allow the estimate of SMBH masses up to high redshifts $z > 5$

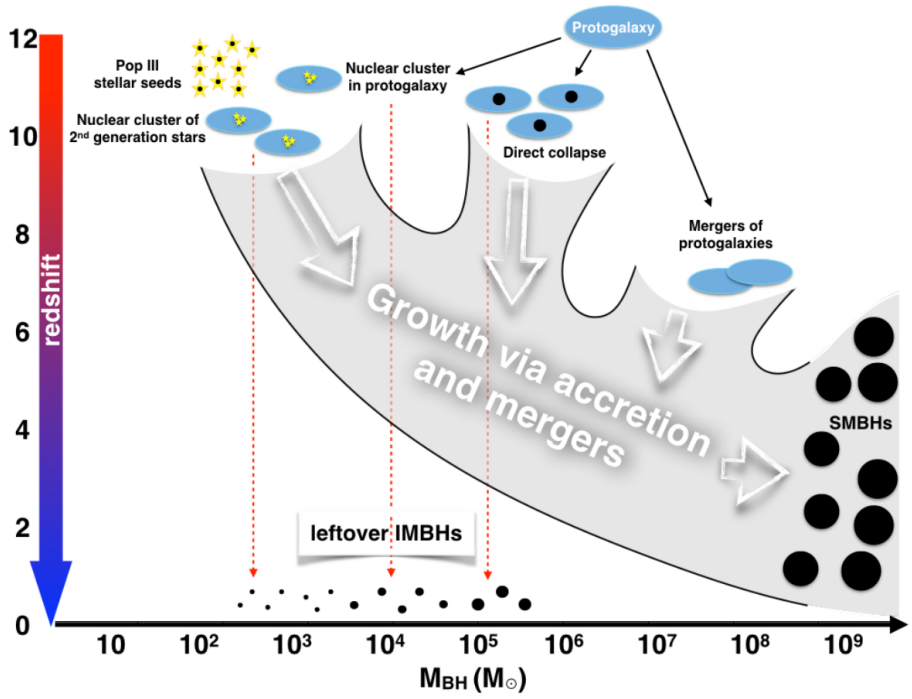

Figure 1.10: Schematic representation of the scenarios explaining the growth of SMBH at high redshift. *i*- Remnants of population III stars with exponential growth; *ii*- Merger by collision of stars in dense clusters; *iii*- Direct collapse of protogalaxies; *iv*- Merger of massive protogalaxies. Figure from Mezcua (2017).

(Wu et al., 2015; Bañados et al., 2016; Yang et al., 2024), when the Universe was less than one billion years old, and make us ponder on the question of how SMBH grew so massive in such a short period of time. While several theories have been proposed for the rapid initial growth of the first SMBHs, no global consensus has been found yet (Latif et al., 2013; Pacucci et al., 2015; Mezcua, 2017; Yang et al., 2021). These theories differ from the origin and initial mass of the BH seeds that will grow to become SMBH (see Figure 1.10 and Mezcua (2017) and references therein). There are two distinct mechanisms of growth, either by merger with other BH (Volonteri et al., 2003; O'Neill et al., 2022), or by accreting surrounding material (Soltan, 1982; Alexander & Hickox, 2012). The merger of SMBHs is an important producer of low-frequency gravitational waves (GW) that should be observed by interpreting the lags in pulsar timing (Antoniadis et al., 2023) or with the future Laser Interferometry Space Antenna (LISA) observatory (Wyithe & Loeb, 2003; Arun et al., 2022). The second mechanism is the dominant channel for SMBH growth (Soltan, 1982) and is the main focus of this thesis. This mechanism forms an accretion disc around the SMBH (§1.3.2), which releases a large luminous energy across

the electromagnetic spectrum and, by doing so, activates the AGN phase of the SMBH.

Moreover, the spin a of a SMBH can theoretically provide information regarding its growth history. Indeed, growth through material accretion should increase the SMBH's spin while mergers with SMBHs with random spin directions, notably counter-rotating, should, on average, decrease the spin of the resulting SMBH King et al. (2008); Sala et al. (2023). However, as the BH spin only affects the region where the gravitational field is the most intense, i.e. close to the BH, the observational determination of the spin is complex (see Reynolds, 2021, for a review). Several methods nonetheless exist to estimate this parameter. The most rapid developments in this field concern GWs of merging binary BHs as the combination of both BH spins imprints signatures on the GW waveform (Vitale et al., 2014; Pürrer et al., 2016; Abbott et al., 2023). However, as only the GW of stellar BH binaries are currently detectable, this approach cannot be used to measure the spin of SMBH. On the other hand, X-ray reflection spectroscopy (further described in §1.3.3) can provide constraints of a SMBH's spin. As X-ray emission lines, mostly the iron Fe Kα line, get distorted due to Doppler effects close to the BH, the resulting emission line is skewed with a low-energy truncation linked to the SMBH spin. Therefore, the fit of high-resolution X-ray spectra with detailed relativistic models can constrain the spin of SMBHs (Brenneman & Reynolds, 2006; Risaliti et al., 2013). Another method involves fitting the thermal continuum to estimate the spin. The higher the spin is, the smaller the horizon event radius is (Equation 1.3), as well as the innermost stable circular orbit, corresponding to the inner edge of the accretion disc (§1.3.2). Consequently, the temperature distribution of the accretion disc varies, affecting the shape of the continuum and allowing a determination of the SMBH spin (Done et al., 2013; Capellupo et al., 2016). These methods suggest that SMBHs with masses below $M_{\rm BH} \lesssim 3 \times 10^7\,M_\odot$ are spinning rapidly with $a > 0.9$, while higher mass SMBHs exhibit lower spin on average (Reynolds, 2014, 2021), in agreement with the numerical predictions of multiple mergers history.

1.3.2 The Accretion Disc and the UV/Optical Continuum

AGN are amongst the most luminous sources in the Universe due to the accretion of gas onto a SMBH via the conversion of gravitational potential energy into thermal radiation. As accretion physics is a vast and active field of research, this section will only give an

overview of the main aspects (see Davis & Tchekhovskoy, 2020, for a recent review).

The first attempt to model the accretion of matter onto a BH was by Bondi (1952) in which the gas accretion was assumed to be spherical. However, this approach was unable to reproduce the observed high luminosities of AGN. Shakura & Sunyaev (1973) proposed a model in which the infalling matter forms an optically-thick geometrically-thin accretion disc. The relativistic generalisation of this model was provided by Novikov & Thorne (1973), and 50 years later, it remains the basis of accretion physics for X-ray binaries and AGN.

Due to the scale difference between the SMBH ($\sim 10^{-5}$ pc) and the gas reservoir from the host galaxy ($\sim 1-10$ kpc), the infalling gas inevitably has an angular momentum and starts orbiting around the SMBH, forming a rotationally-supported disc (see Figure 1.8). The loss of angular momentum of the orbiting matter depends on anomalous viscosity or stress within the disc. Among other possible mechanisms, magnetorotational instability appears the dominant internal source of turbulence (Balbus & Hawley, 1991, 1998) while magnetised outflows can provide additional external stress (Blandford & McKee, 1982; Frank et al., 1992). Therefore, the orbiting material progressively spirals down to the SMBH. This energy loss is converted into heat and radiated as a black-body. As the temperature decreases with the distance to the centre following a powerlaw distribution, the total accretion disc emission is a composite of black-body emitters that peaks in the UV (innermost hotter rings) and extends to the mid-IR (outermost colder rings). This characteristic emission can be referred to as the "big blue bump" and is displayed with a *blue solid line* in Figure 1.9.

The total luminosity, or bolometric luminosity $L_{\rm bol}$, emitted by an accretion disc can be expressed as:

$$L_{\rm bol} = \eta \dot{M} c^2 \tag{1.5}$$

with $\dot{M}$ the accretion rate of matter into the SMBH and η the radiative efficiency, i.e. the fraction of the accreted rest mass energy that is converted into radiation. The remaining fraction $(1-\eta)$ feeds the growing SMBH. Analytically, for a NT-type[8] disc, the efficiency factor η varies as a function of the spin between $\eta \approx 0.057$ for a non-spinning SMBH

[8]Novikov & Thorne (1973)

and $\eta \approx 0.42$ for a maximally-spinning SMBH. Davis & Laor (2011) observed a radiative efficiency dependence on the SMBH mass with $\eta \approx 0.03$ for $M_{\rm BH} = 10^7 M_\odot$ and $\eta \approx 0.4$ for $M_{\rm BH} = 10^9 M_\odot$ for a sample of 80 quasars. As a comparison, the efficiency of hydrogen fusion powering stars is approximately $\eta_{\rm fusion} = 0.007$.

A statistical approach can be used to constrain the mean radiative efficiency $\langle\eta\rangle$ of the entire AGN population over cosmic time. Indeed, by assuming that mergers are negligible, the mass of a SMBH is the integrated accretion of matter across cosmic time, and as the accretion rate is proportional to the bolometric luminosity divided by the radiative efficiency (Equation 1.5), then a comparison between the AGN luminosity function (i.e. number of AGN per Gpc^3 as a function of the bolometric luminosity) and the SMBH mass function (i.e. number of AGN per Gpc^3 as a function of the SMBH mass) can yield constraints on $\langle\eta\rangle$. While Elvis et al. (2002) and Yu & Tremaine (2002) found high radiative efficiency $\langle\eta\rangle > 15\%$, other works suggest lower efficiency with $0.04 < \langle\eta\rangle < 0.16$ for Marconi et al. (2004) and $0.065 < \langle\eta\rangle < 0.09$ for Shankar et al. (2009).

The quantity of matter accreted into a black hole is limited by the radiation pressure when the bolometric luminosity is such that the accreting material is in hydro-static equilibrium, i.e. the outward radiation pressure is equal to the gravitational pull. This maximum luminosity, or Eddington luminosity $L_{\rm Edd}$, can be computed assuming a non-rotating fully ionised gas with a spherical isotropic emission. In that scenario, the gravitational force onto a hydrogen atom at the distance r is:

$$F_G = \frac{G\, M_{\rm BH}\, m_{\rm H}}{r^2} \tag{1.6}$$

with the mass of a hydrogen atom $m_{\rm H}$. Conversely, the radiation pressure is given by:

$$F_{\rm rad} = \frac{L}{4\pi r^2}\frac{\sigma_{\rm T}}{c} \tag{1.7}$$

with the Thomson cross-section $\sigma_{\rm T} = 6.65 \times 10^{-25}\,{\rm cm}^2$. Therefore, at equilibrium $F_G(M_{\rm BH}) = F_{\rm rad}(L_{\rm Edd})$, we obtain by combining Equation 1.6 and 1.7:

$$L_{\rm Edd} = G\, M_{\rm BH} m_{\rm H} \frac{4\pi c}{\sigma_{\rm T}} = 1.26 \times 10^{46} \left(\frac{M_{\rm BH}}{10^8\, M_\odot}\right) {\rm erg\,s^{-1}} \tag{1.8}$$

In this spherical fully-ionised model, $L_{\rm Edd}$ depends only on the mass of the SMBH. Using Equation 1.5, the maximum accretion rate of a SMBH can be derived as a function of the SMBH mass and the radiative efficiency:

$$\dot{M}_{\rm Edd} = \frac{L_{\rm Edd}}{\eta c^2} = 2.22 \left(\frac{\eta}{0.1}\right)^{-1} \left(\frac{M_{\rm BH}}{10^8\, M_\odot}\right) M_\odot\, {\rm yr}^{-1} \tag{1.9}$$

From these equations, the Eddington rate, defined as $\lambda_{\rm Edd} = L_{\rm Bol}/L_{\rm Edd}$, quantifies how fast an AGN is accreting with respect to its Eddington limit. An AGN accreting at $\lambda_{\rm Edd} < 1$ is in the sub-Eddington regime while at $\lambda_{\rm Edd} > 1$, in the super-Eddington regime. This Eddington limit self-regulates the growth of AGN through time at all redshifts. The Salpeter time t_S characterises the time needed for a black hole accreting at the Eddington rate to double its mass. It is defined as follows:

$$t_S = \ln(2)\, \frac{\eta}{1-\eta}\, \frac{\sigma_{\rm T}\, c}{4\pi\, G\, m_{\rm H}} \sim 0.3\, \frac{\eta}{1-\eta}\, {\rm Gyr} \tag{1.10}$$

Assuming a radiative efficiency $\eta = 10\%$, the Salpeter time is approximately $t_S \sim 35\,{\rm Myr}$.

Nevertheless, AGN can live through episodes of super-Eddington accretion (Zubovas & King, 2013), and super- or even hyper-Eddington rates ($\dot{M} > 10^2\, \dot{M}_{\rm Edd}$) are proposed to explain the observed SMBH masses at very high redshift (Lapi et al., 2014; Inayoshi et al., 2016; Ryu et al., 2016) (see §1.3.1). The possibility to accrete above the Eddington limit is due to the fact that several assumptions were made, and it should only be regarded as a useful approximation. For instance, $\lambda_{\rm Edd}$ has been established with a spherical emission, while due to the thin disc geometry of the accretion, the emission is, in reality, anisotropic: maximal along the polar axis and decreasing with the inclination angle (Netzer, 1987; Namekata & Umemura, 2016; Ishibashi et al., 2018). Similarly, the value of the Eddington luminosity is for a fully ionised gas, while for a dusty medium, the Eddington limit can be significantly lower (Murray et al., 2005; Fabian et al., 2008, 2009). This particular effect will be discussed further in Section 1.3.4.

The optically-thick geometrically-thin disc (Shakura & Sunyaev, 1973) is not the only model for the accretion flows into SMBH: the hot accretion flow model (SLE, Shapiro et al., 1976) or the advection-dominated accretion flows (ADAF, Ichimaru, 1977) are the two other main type of solutions with several variations each (see Yuan & Narayan, 2014,

for a review).

1.3.3 The Hot Corona and X-ray Emission

The X-ray Continuum

X-ray emission appears to be a ubiquitous characteristic of AGN (Elvis et al., 1978; Brandt & Alexander, 2015). However, the inner sections of the accretion disc cannot reach a temperature high enough to produce such X-ray emission. The solution proposed to emit this high energy radiation is that a fraction of the photons emitted by the accretion disc, the "seed photons", are up-scattered by hot non-relativistic electrons (Thorne & Price, 1975; Katz, 1976; Sunyaev & Truemper, 1979) via inverse Compton scattering (Rybicki & Lightman, 1979). Such mechanisms would produce the power law-shaped spectrum (Haardt & Maraschi, 1991, 1993) found by observations (Mushotzky, 1984; Turner & Pounds, 1989). More specifically, as illustrated by the *cyan dashed line* in Figure 1.9, the shape of the X-ray continuum follows a cutoff power law:

$$F(E) = C \cdot E^{-\Gamma} \exp(-E/E_{\text{cut}}) \tag{1.11}$$

where E is the energy, Γ the powerlaw index and E_{cut} the cut-off energy. E_{cut} depends on the electron temperature T_e of the corona because photons with similar energy will not be up-scattered. The power law index, or photon index, on the other hand, can be approximated (Rybicki & Lightman, 1979) by:

$$\Gamma = -1.2 + \sqrt{\frac{9}{4} + \frac{4}{y}} \tag{1.12}$$

where y is the Compton parameter:

$$y = \max(\tau, \tau^2) \, \frac{4kT_e}{m_e c^2} \tag{1.13}$$

with τ being the corona's optical depth, i.e. the average number of scatters per photon passing through the corona. The higher the optical depth is, the more energetic the escaping photon is. Using hard X-ray spectra ($> 10\,\text{keV}$), the main physical parameters of the corona can be estimated: $T_e \sim 40 - 100\,\text{keV}$ and $\tau \sim 1 - 2$ (Lubiński et al., 2016).

However, the heating mechanisms of the electrons are still uncertain, although they are possibly due to magnetic flares similar to those that produce the solar corona, hence the name of this component (Liang & Price, 1977). Moreover, the precise photon index depends on the actual geometry of the corona, which is still highly debated (Fabian et al., 2015). Several models have been proposed; earlier ones suggested hot parallel planes on both sides of the accretion discs (Haardt & Maraschi, 1991, 1993) or a sphere surrounding the SMBH, as represented in Figure 1.5 (Zdziarski et al., 1999). One can also cite the "lamp-post" model with a compact source located on the rotational axis illuminating the accretion disc, as illustrated in Figure 1.8 (Martocchia & Matt, 1996; Miniutti & Fabian, 2004; Fabian et al., 2017). More recent models suggest aborted jets (Ghisellini et al., 2004), a clumpy corona (Lusso & Risaliti, 2017) or a 2-temperature accretion disc with a spherical hot corona (Kubota & Done, 2018). As the different models would not polarise the X-ray photons in the same way, one of the main objectives of the recently-launched *Imaging X-ray Polarimetry Explorer* (*IXPE*, Weisskopf et al., 2022) is to reveal the geometry of the corona (Ursini et al., 2022). While the initial analyses do not give a consensus yet with the lamp-post model rejected for NGC 4151 (Gianolli et al., 2023) but the lamp-post and conical models consistent with MCG-05-23-16 (Marinucci et al., 2022), X-ray polarimetry is a promising approach to understand the physics of the AGN most central region.

The X-ray Absorption

X-ray photons emitted by the hot corona can interact with gas along the line of sight. The incident photon can be photoelectrically absorbed, leading to the ejection of an electron from the atom. The optical depth of the material is given by $\tau(E) = \sigma(E)\, N_{\mathrm{H}}$ where $\sigma(E)$ is the energy-dependent cross-section and N_{H} represents the hydrogen column density, i.e., the number of atoms of hydrogen along the line of sight within an area of 1 cm^2. As the photoelectric absorption cross-section of neutral hydrogen decreases proportionally to E^{-3}, lower energy X-ray photons are more strongly absorbed than their higher energy counterparts. Therefore, as the column density increases, higher energy X-ray emission is progressively suppressed, causing the spectral shape to change, as illustrated in Figure 1.11.

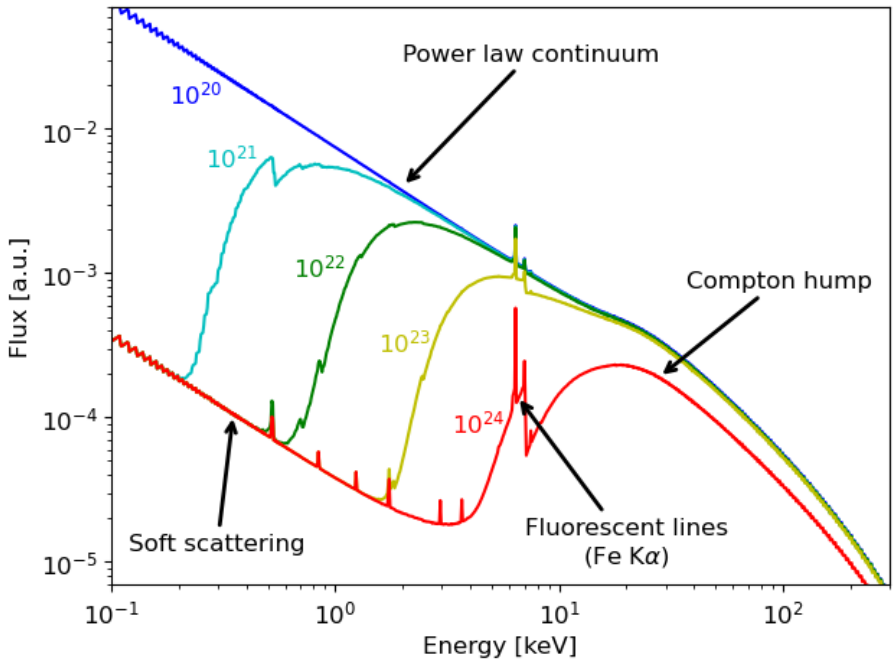

Figure 1.11: X-ray spectra for different column densities $N_{\rm H}$ in $\rm cm^{-2}$ as indicated for each curve. The spectra were produced by the physically motivated UXCLUMPY model (Buchner et al., 2019) with a photon index $\Gamma = 2$, a high energy cutoff at $E_{\rm cut} = 200\,\rm keV$. The power law continuum, the Compton hump, the fluorescent lines and the soft scattering are also indicated.

Despite being significantly less abundant than hydrogen, other heavier elements, notably helium, carbon, nitrogen and oxygen, slightly increase the total cross-section, impacting X-ray photons at higher energies compared to hydrogen alone. Moreover, photoelectric absorption produces ions, and for elements heavier than helium, this reduces the total cross-section and, consequently, decreases the photo-electric absorption at low energies. Since ions can recombine with free electrons before interacting with an X-ray photon, the importance of ionised photo-electric absorption depends on the ratio of photon density to free electron density.

The impact of absorption on the X-ray emission can be reversed in such a way that the shape of the observed X-ray spectrum of an AGN returns the column density $N_{\rm H}$ and reveals the quantity of matter along the line-of-sight. A column density of $N_{\rm H} = 10^{22}\,\rm cm^{-2}$, assuming typical gas-to-light ratios, corresponds to an optical extinction $A_V \sim 5\,\rm mag$ where most optical/UV emission is absorbed. Above and below this $N_{\rm H}$-threshold, AGN are typically considered obscured and unobscured, respectively. The presence of obscuration is often associated with the presence of the dusty torus (§1.3.4) along the

line-of-sight in a similar way that the presence of the torus distinguishes between type I and type II AGN. Obscuration levels below $N_{\rm H} < 10^{22}\,{\rm cm}^{-2}$ may be due to BLR material (§1.3.5), thinner regions of the torus or the interstellar medium (ISM) of the host galaxy.

The Reflection Components

In competition with the photo-electric absorption effect, X-ray photons have a probability of being scattered or reflected when interacting with free electrons. Unlike the absorption cross-section, the Thomson cross-section $\sigma_{\rm T}$, or the electron scattering cross-section for neutral material, is relatively energy-independent. Thus, while reflection is dominated by absorption at low energies, the reflection probability exceeds absorption at energies $\gtrsim 10\,{\rm keV}$. The scattering optical depth of an AGN is equal to unity for $N_{\rm H} = \sigma_T^{-1} = 1.5 \times 10^{24}\,{\rm cm}^{-2}$. AGN with column densities larger than this $N_{\rm H}$-threshold are labelled Compton-Thick (CTK), meaning they are optically thick to X-ray photons with soft X-rays being absorbed and hard X-rays reflected. Below this $N_{\rm H}$-threshold, the material is considered Compton-Thin (CTN).

Nevertheless, reflected photons can be scattered into the observer's line-of-sight, producing additional components in the AGN X-ray spectra, as illustrated in Figure 1.11: the Compton hump (Guilbert & Rees, 1988; Lightman & White, 1988; Matt et al., 1991), the soft scattering (Krolik & Kriss, 1995) and the fluorescent lines (Nandra et al., 1991; Mushotzky et al., 1993).

At high energies, the interaction of the photons with the free electrons is inelastic, photons lose energy while electrons gain kinetic energy. This Compton scattering effect does not absorb the photons but only reduces their energy, resulting in a break of the X-ray power law at high energies and a characteristic peak around 20-50 keV called Compton hump (George & Fabian, 1991; Matt et al., 1991). This hump is mostly produced when the X-ray photons interact with the accretion disc (Ross & Fabian, 1993), but its shape is also believed to be dependent on the BLR and the dusty torus.

In the soft X-ray regime, an additional soft X-ray component is seen in obscured AGN spectra. It is believed to be a fraction of the primary unobscured emission that either passed through the obscurer unabsorbed or has been reflected by Thomson scattering (elastic interaction) in warm photo-ionized gas clouds located above the torus into the

line-of-sight (Krolik & Kriss, 1995; Bianchi et al., 2006; Guainazzi & Bianchi, 2007).

The fluorescence lines are produced mostly after an atom absorbs an X-ray photon and ejects an inner-shell electron. This electron vacancy can be filled by a higher-level electron and the energy difference is released either by the ejection of a valence electron (Auger effect) or by the emission of a photon (fluorescence). Fluorescence photons can be scattered into the observer's line of sight resulting in an emission line. The most prominent fluorescent line is the iron Fe Kα at 6.4 keV produced by the transition of an L-shell electron to the K-shell. Its prominence is due to the fluorescence probability increasing with atomic number and that iron is the heaviest astrophysically abundant element. The iron Kβ line at 7.06 keV (M-shell to K-shell) is also relatively strong. The "Kα line", when observed at high spectral resolution, reveals a complex of emission lines with broad and narrow components that can provide valuable information on the geometry and dynamics of material in the central part of an AGN (Andonie et al., 2022b; Gandhi et al., 2022). For instance, the narrow component ($\sim 1\,000\,\mathrm{km\,s^{-1}}$) might originate from the torus or the BLR, while the broader component ($\sim 20\,000\,\mathrm{km\,s^{-1}}$) show relativistic features and probably originates from the inner part of the accretion disc, providing constraints on the spin of the SMBH.

These three reflection components appear stronger in the overall X-ray spectrum as the column density increases, progressively suppressing the dominating X-ray continuum. In the case of CTK sources, the reflection components become the primary X-ray emission source. Figure 1.9 displays the sum of the fluorescent lines and the Compton hump with a *green dotted line*.

The Soft Excess

Unobscured AGN often show a soft X-ray excess, i.e. the observed X-ray emission at low energies < 1 keV is higher than expected from the continuum emission measured between 2-10 keV (Arnaud et al., 1985; Boller et al., 1996; Gierliński & Done, 2004). This excess is illustrated by the *purple dash-dotted line* in the total AGN SED in Figure 1.9. The soft excess differs from the soft scattering mentioned earlier by the origin of this emission. Several models have been suggested: the presence of a secondary warm corona producing UV and soft X-rays (Magdziarz et al., 1998; Petrucci et al., 2013; Boissay et al., 2016),

blurred ionised reflection (Crummy et al., 2006) or photo-ionised reflection of the accretion disc (Ross & Fabian, 1993), but the nature of this excess is still debated (Done et al., 2012; Petrucci et al., 2018). In this work, the soft X-ray excess is mostly located outside of the observed energy band, and therefore, ignored.

1.3.4 The Obscuring Material and the Reprocessed Emission

As mentioned in Section 1.2.2, the presence of a toroidal dusty obscurer surrounding the SMBH, referred to as "torus", is a fundamental component of the unification model established 30 years ago (Antonucci, 1993; Urry & Padovani, 1995). This model explains various observational characteristics based on the AGN orientation with respect to the observer. Specifically, when positioned along the line-of-sight, the torus obscures the accretion disc and the BLR, suppressing respectively the UV/optical continuum and the broad emission lines while the narrow lines emitted further away remain observable (§1.3.5). Moreover, the torus shapes the X-ray spectrum as a function of the column density $N_{\rm H}$ on the line-of-sight (§1.3.3). It is also responsible for some X-ray reflection components, such as the Compton hump at $\sim 30\,\rm keV$. Importantly, by reprocessing the UV/optical emission from the accretion disc, the torus re-emits thermally in the infrared regime (IR; 1-1000 μm, Rees et al., 1969), allowing AGN to be identified from their bright IR emission. As illustrated by the *red dashed line* in Figure 1.9, the torus IR emission peaks in the mid-IR (5-30 μm) and drops rapidly in the far-IR (30-500 μm) (Elvis et al., 1994; Alonso-Herrero et al., 2003; Richards et al., 2006; Mullaney et al., 2011). As the far-IR regime is dominated by the host galaxy emission, most particularly by the star formation emission (*grey solid line*), the mid-IR luminosity, especially at 6 μm and 12 μm, is considered the best proxy of the intrinsic torus emission (Horst et al., 2008; Gandhi et al., 2009). Notably, as the X-ray emission also results from the reprocessing (Compton up-scatter) of the primary UV/optical emission, a strong correlation exists between X-ray and mid-IR (Gandhi et al., 2009; Asmus et al., 2015; Mateos et al., 2015; Stern, 2015; Toba et al., 2019).

Despite several indirect evidence for its existence, due to its small predicted angular size and challenges in high-spatial resolution imaging at infrared wavelengths, the torus was only recently confirmed by high-resolution imaging (García-Burillo et al., 2016; Combes et al., 2019; GRAVITY Collaboration et al., 2020; Gámez Rosas et al., 2022).

Nevertheless, its exact geometry and dynamics remain debated. The torus is believed to be axis-symmetric and is located further than the accretion disc, the hot corona and the BLR from the SMBH, extending from $< 1\,\mathrm{pc}$ to $10-100\,\mathrm{pc}$ (Alexander & Hickox, 2012; Hickox & Alexander, 2018). These inner and outer radius sizes have been established using mid-IR imaging (Packham et al., 2005), reverberation lags (Suganuma et al., 2006; Vazquez et al., 2015), interferometry (Kishimoto et al., 2009; Burtscher et al., 2013) and sub-millimeter observations (Imanishi et al., 2016; García-Burillo et al., 2016; Combes et al., 2019; Gámez Rosas et al., 2022). The inner radius corresponds to the sublimation radius of graphite dust (Barvainis, 1987), which varies as a function of the AGN luminosity $\propto L^{1/2}$ Kishimoto et al. (2011). Conversely, the outer radius corresponds to the gravitational sphere of influence of the SMBH given by:

$$r < \frac{G\,M_{\mathrm{BH}}}{\sigma^2} \tag{1.14}$$

with M_{BH} the mass of the SMBH and σ the velocity dispersion (Alexander & Hickox, 2012). For a $10^8\,M_\odot$ SMBH, this radius is approximately 10 pc.

Due to complexity and computational limitations, the first torus models were developed assuming a smooth geometry, i.e., a homogeneous distribution of dust within the torus. However, nowadays, it is widely accepted that the torus is clumpy (Ramos Almeida & Ricci, 2017a), composed of clouds of gas and dust, some of them CTK, as pictured in Figure 1.8. Several arguments favour the clumpiness of the torus, starting with theoretical claims that an extended torus can only be maintained if clumpy (Krolik & Begelman, 1988; Pier & Krolik, 1992). Additionally, if the torus was smooth, the IR emission of the inner part of the torus should be partially obscured by the torus itself, while clumpy models predict less orientation-dependent mid-IR emission (Nenkova et al., 2008), as observed comparing obscured and unobscured AGN (see both panels in Figure 1.6). Moreover, smooth torus models predict deep silicate absorption lines for type II AGN while observations reveal shallow silicate lines, in better agreement with clumpy models (Hönig et al., 2006; Roche et al., 2006; Ramos Almeida et al., 2009; Alonso-Herrero et al., 2016), even if it could be also explained by larger dust grains (Maiolino et al., 2001). Furthermore, the eclipsing event of some X-ray AGN, i.e. variation of the column density N_{H} over

periods of time, indicate the passage of a cloud of dust on the line-of-sight, favouring the clumpiness of the torus (Turner & Pounds, 1989; Risaliti et al., 2002; Markowitz et al., 2014).

The covering factor of the torus, parametrised by its opening angle, represents the fraction of the SMBH sky that is obscured by the torus. For individual sources, the covering factor can be obtained by computing the ratio of the torus IR emission to the bolometric AGN luminosity (Maiolino et al., 2007; Toba et al., 2014; Ricci et al., 2023), as most of the AGN IR emission results from dust reprocessing. Additionally, in the X-rays, detailed spectroscopy with recent torus models can also provide constraints on the covering factor of the surrounding dust (Murphy & Yaqoob, 2009; Brightman & Nandra, 2011; Baloković et al., 2018; Buchner et al., 2019; Tanimoto et al., 2019; Ricci & Paltani, 2023). Similarly, fitting the mid-IR SED with physical models can also provide insights on the physical parameters of the torus (Mor et al., 2009; Stalevski et al., 2017; García-Bernete et al., 2019).

The torus covering factor can also be statistically constrained using a large sample of sources. As each AGN is observed with a random inclination angle, the fraction of obscured AGN with respect to the total population yields the mean covering angle of the torus (Lawrence, 1991). However, observational biases must be carefully taken into account as, at a given intrinsic luminosity, obscured AGN would appear fainter than their unobscured counterparts, reducing their probability of detection, especially in the CTK regime. As it has been found that the majority ($\geq 70\%$) of AGN are obscured (Buchner et al., 2015; Ricci et al., 2015, 2017b), and approximately $20 - 30\%$ are CTK (Burlon et al., 2011; Buchner et al., 2015; Ricci et al., 2015), this statistical approach suggest that the torus covering factor align with these values. Furthermore, this method allows us to study the dependences of the torus covering factor; for instance, it appears to increase with redshift (La Franca et al., 2005; Tozzi et al., 2006; Ueda et al., 2014; Buchner et al., 2015) and decrease with increasing bolometric luminosity (Lawrence, 1991; Akylas et al., 2006; Sazonov et al., 2007; Hasinger, 2008; Oh et al., 2015). This last result favours a receding torus model, in which, as the luminosity increases, the dust sublimation radius expands, along with the torus inner radius, leading to a decrease of the covering factor at fixed torus height. Conversely, the obscured AGN fraction also appears to decrease with

decreasing luminosity below $L_{\rm bol} \leq 10^{42}\,{\rm erg\,s^{-1}}$ (Burlon et al., 2011; González-Martín et al., 2015), suggesting that low luminosity AGN cannot maintain the torus. However, other studies point toward a weaker luminosity-dependence of the obscured AGN fraction (Dwelly & Page, 2006; Sazonov et al., 2015; Stalevski et al., 2016).

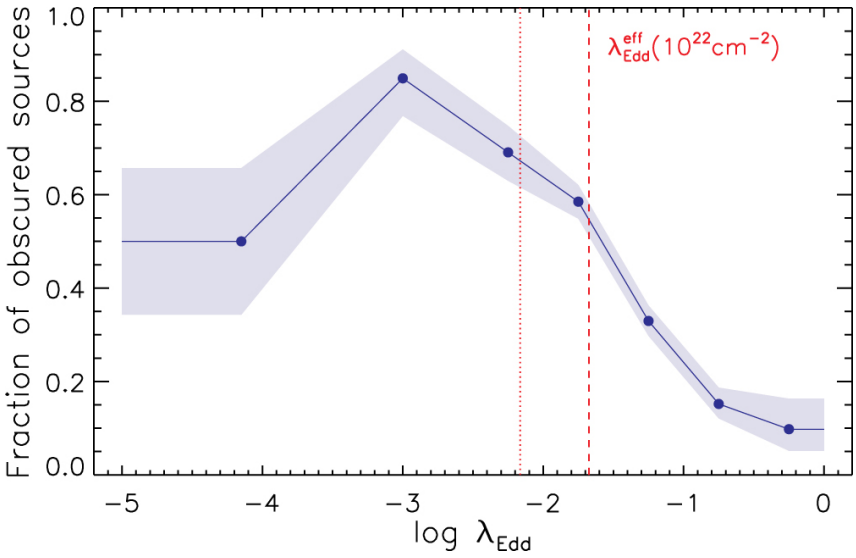

Figure 1.12: Fraction of obscured Compton-thin sources ($22 < \log(N_{\rm H}/{\rm cm^{-2}}) < 24$) as a function of the Eddington ratio $\lambda_{\rm Edd}$. The *red vertical* lines indicate the effective Eddington limit at $\log(N_{\rm H}/{\rm cm^{-2}}) = 22$ according to Ishibashi et al. (2018) and Fabian et al. (2008) (*dotted* and *dashed* lines, respectively). Figure from Ricci et al. (2022).

More recent works have shown that, rather than the luminosity, the Eddington ratio might be the key parameter driving the evolution of the covering factor (Buchner et al., 2015; Ricci et al., 2017b, 2022; Ananna et al., 2022a; Ricci et al., 2023). For example, Ricci et al. (2017b) found that the obscured AGN ($22 < \log(N_{\rm H}/{\rm cm^{-2}}) < 24$) fraction decreases significantly above a $\lambda_{\rm Edd} \geq 1\%$ threshold (see Figure 1.12). This strong decline is attributed to dusty radiation pressure blowing away the Compton-thin obscuring material of the torus (Fabian et al., 2006, 2008; Venanzi et al., 2020). The Eddington limit, given by equation 1.8, was computed using the Thomson cross-section $\sigma_{\rm T}$ of hydrogen while dusty gas has a larger cross-section, implying a lower effective Eddington limit varying with $N_{\rm H}$. Therefore, despite having $\lambda_{\rm Edd} < 1$, the dusty radiation pressure can exceed the gravitational pull and push away the obscuring material, decreasing the torus covering factor. These findings motivate the radiation-regulated model illustrated in Figure 1.13. After an accretion event (phase 1), e.g. merger or disc instability, the accretion rate of the SMBH increases, along with $N_{\rm H}$ and the covering factor, until becoming an obscured AGN

(phase 2). When the AGN enters the blow-out region (phase 3) delimited by the effective Eddington limit for a dusty gas, the radiation pressure blows away the obscuring material, decreasing $N_{\rm H}$ and the covering factor, and the AGN transitions to an unobscured AGN (phase 4). When all the gas is either consumed or blown away, the accretion stops and the SMBH returns to quiescence. The key phase in this scenario is the blow-out region, also called the *forbidden* region, in which the AGN transit from obscured to unobscured on short time scales compared to the AGN lifetime (Jun et al., 2021a; Ananna et al., 2022a), therefore, the incidence of AGN in this region should be low, as observed in the local Universe (Ricci et al., 2017b; Toba et al., 2022).

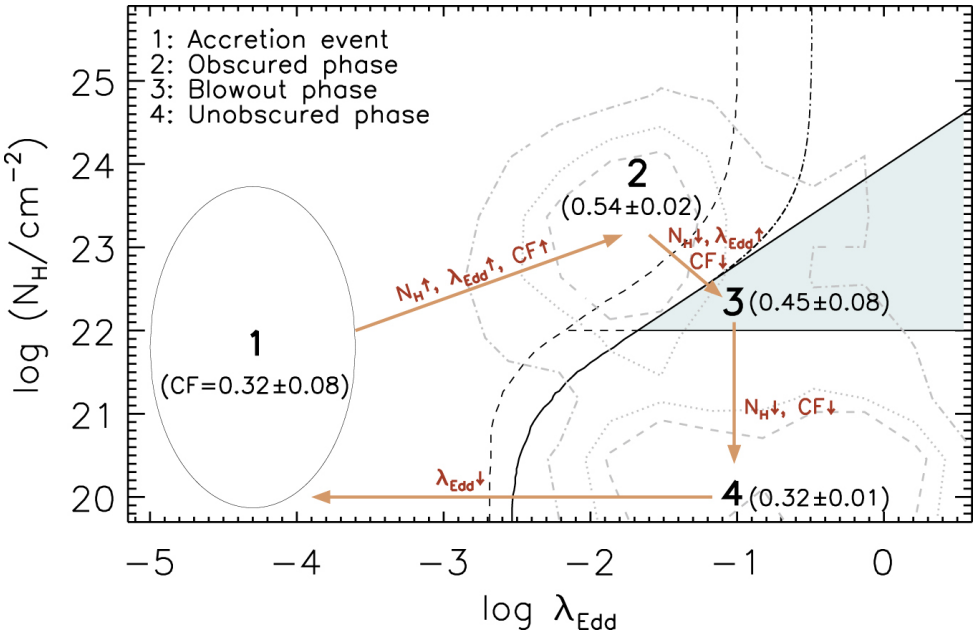

Figure 1.13: Schematic representation of the radiation-regulated model in the $\lambda_{\rm Edd} - N_{\rm H}$ plane, representing the AGN phase of a SMBH following the orange arrows. At each stage of the AGN life cycle, the median IR covering factor is indicated. The solid, dashed and dashed-dotted lines represent the effective Eddington limit from Fabian et al. (2008), Ishibashi et al. (2018) and Lansbury et al. (2020), respectively. The grey contours represent the 50%, 68% and 90% density distribution of the sources. The *grey* area is the blow-out region. Figure from Ricci et al. (2023).

It is worth mentioning that other models of the obscuring region exist. For instance, there is evidence for dust emission along the polar axis of the AGN (Hönig et al., 2013; López-Gonzaga et al., 2014; Tristram et al., 2014), potentially due to dusty AGN-driven outflows (Hönig, 2019). This polar dust can extend to hundreds of parsecs (Asmus et al., 2016) and strongly impact the X-ray spectrum. Furthermore, as most toroidal models are

static with time, hydrodynamical models propose a more realistic picture of the torus. By accounting for gas inflows and AGN and supernova feedback, these models can produce an axis-symmetric structure similar to the torus that evolves through time (Wada, 2012, 2015; Hönig & Kishimoto, 2017). However, despite being more realistic, these models are more difficult to compare with observation than simpler geometrical models often due to limited constraints.

1.3.5 The Broad and Narrow Emission Lines Regions

The broad line region (BLR) and narrow line region (NLR) are, as the names suggest, the regions of the AGN responsible for the emission of the broad and narrow spectral lines, respectively. Both regions are composed of gas clouds, ionized by the UV continuum of the accretion disc (Davidson & Netzer, 1979), but their geometry and dynamics are distinct.

Broad Line Region:

The aforementioned broad lines consist of the hydrogen Balmer (H$\alpha\,\lambda$6563, H$\beta\,\lambda$4861, H$\gamma\,\lambda$4340) and Lyman (Ly$\alpha\,\lambda$1216, Ly$\beta\,\lambda$1026) series lines along with some ion lines, mainly C IV λ1549, C III λ1909 and Mg II λ2798 (Peterson, 1997). Their width corresponds to velocities in the $10^3{-}10^4\,\mathrm{km\,s^{-1}}$ range. As such velocities cannot be explained by thermal motion with $T \sim 10^4\,\mathrm{K}$ (Kallman & Mushotzky, 1985), this broadening is then the result of Keplerian velocities of the BLR clouds, therefore, the width of the lines can be used to constrain the black hole mass (see Section 1.3.1). Moreover, the relative strength of these lines indicates a dense environment with an electron density $n_{e,\,\mathrm{BLR}} \sim 10^{10}\,\mathrm{cm^{-3}}$.

As indicated by reverberation mapping, the BLR is located near the SMBH, with a radius scaling with the AGN luminosity $R_{\mathrm{BLR}} \propto L^{0.7}$ (Kaspi et al., 2000; Peterson et al., 2004), ranging from 0.01 pc for low luminosity AGN to 1 pc for bright quasars (Bentz et al., 2009; Beckmann & Shrader, 2012). Despite these constraints, the formation and geometry of the BLR remain highly debated. Located between the torus and accretion disc, the BLR is believed to be the transitional region for the inflowing material of the torus and the radiation pressure-driven outflowing material (Gaskell, 2009; Czerny et al., 2015), as represented by the *purple clouds* in Figure 1.8.

Narrow Line Region:

The narrow emission lines have a velocity broadening between 200-1000 $\mathrm{km\,s^{-1}}$ (Osterbrock, 1989; Greene et al., 2011). In addition to the permitted and semi-forbidden lines, such as Lyα λ1216, C IV λ1549, C III] λ1909, the BLR also emits strong forbidden lines, mainly [OIII]$\lambda\lambda$4959,5007, [NII]$\lambda\lambda$6548,6583, [OII]$\lambda\lambda$6300,6364, and [SII]$\lambda\lambda$6716,6731. The presence of such forbidden lines indicates a less dense region than the BLR, with an electron density $n_{e,\,\mathrm{NLR}} \sim 10^4\,\mathrm{cm^{-3}}$. From line diagnostics, the temperature is estimated to be similar to the BLR, $T \sim 10^4\,\mathrm{K}$.

In opposition to the BLR, the NLR can be optically resolved due to its large extension (Malkan et al., 1998). Resulting from the collimation of the AGN radiation due to the presence of the torus (§1.3.4), the NLR has a biconical shape, also referred to as ionisation cones, that can extend between 10^2-10^4 pc, as a function of the AGN luminosity (Capetti et al., 1996; Bennert et al., 2002). The NLR is represented by *cyan clouds* in Figure 1.8. As briefly mentioned in Section 1.3.3, the ionized cones are potentially the origin of the soft-scattering reflection component in the X-ray for obscured AGN.

1.3.6 The Jets and Radio Emission

About 10% of the AGN population are radio-loud (RL), i.e. bright in the radio band compared to the accretion disc emission, characterised by a radio-loudness parameter $\mathcal{R} > 10$. In comparison, radio-quiet (RQ) AGN are typically 10^3 times fainter in the radio band for similar accretion luminosities. The primary radio emission mechanism is non-thermal synchrotron radiation, when relativistic charged particles are accelerated perpendicularly to their velocity, often when travelling through magnetic fields. The flux density of synchrotron radiation follows a power law:

$$S_\nu \propto \nu^{-\alpha} \tag{1.15}$$

with the frequency ν and the spectral index α, varying between $-0.5 < \alpha < 1.5$ depending on the frequency and AGN type (Kellermann & Owen, 1988; Planck Collaboration et al., 2011). The flattening of the power law is likely to be a consequence of synchrotron self-absorption (Kellermann & Owen, 1988) or free-free absorption by surrounding ionised gas (Stawarz et al., 2008).

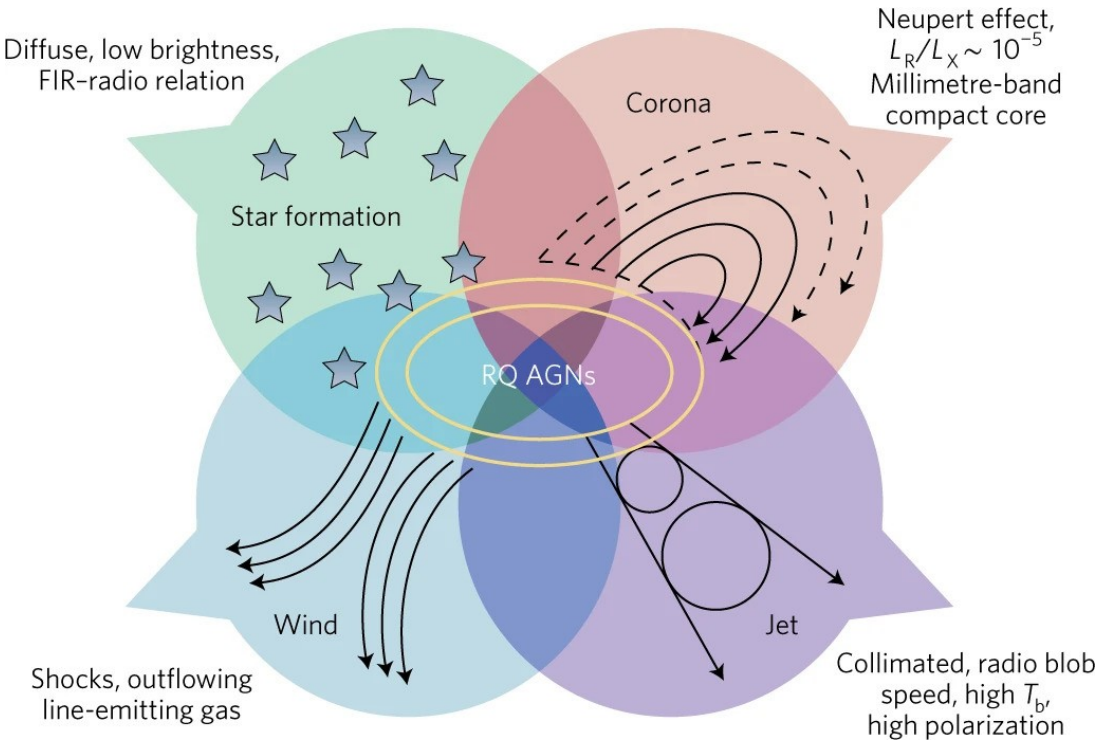

Figure 1.14: Sketch summarising the 4 main mechanisms producing radio emission in RQ AGN: star formation, coronal activity, AGN wind shock and weak jets. For each mechanism, the potential observables are indicated. Figure from Panessa et al. (2019)

In RL AGN, the radio emission by synchrotron radiation is produced by powerful relativistic jets (see Blandford et al., 2019, for a review). These highly collimated jets are perpendicular to the accretion disc and can extend from pc to Mpc scales. The lobes of the jets result from the interaction of the jets with the interstellar medium (ISM) (Kaiser & Alexander, 1997). These powerful jets can even be responsible for a fraction of the X-ray and γ-ray emission (Grandi et al., 2006). The formation of such jets remains highly debated and may be related to magnetohydrodynamics, where the rotating material of the accretion disc produces a strong magnetic field, accelerating particles to relativistic velocities and forming two opposite jets (Blandford, 1976; Lovelace, 1976; Hardcastle & Croston, 2020). Additionally, the magnetic field could also extract rotational energy from the black-hole spin (Blandford & Znajek, 1977) as a correlation is observed with the jet power in X-ray binaries (Penna et al., 2013). However, many AGN with large spin are found to be RQ (Reynolds, 2014), and according to Soltan (1982); Elvis et al. (2002); Yu & Tremaine (2002), most AGN must be rapidly spinning despite being RL.

Despite being much weaker than their RL counterparts, RQ quasars can nonetheless

emit in the radio band. Panessa et al. (2019) list 4 different mechanisms explaining this weak radio emission (see Figure 1.14):

- Host-galaxy star formation: supernovae and stellar winds can produce synchrotron radiation by shocks (Sopp & Alexander, 1991; Condon et al., 2013; Padovani et al., 2015). Such radio emission should, therefore, be diffused and correlated to the far-IR dust-obscured star formation emission.

- Coronal activity: the magnetically heated corona can produce radio emission (Laor & Behar, 2008; Behar et al., 2018), mostly self-absorbed except in the high-frequency regime. In this scenario, the radio luminosity correlates with the X-ray luminosity, following a $L_{\mathrm{R}}/L_{\mathrm{X}} = 10^{-5}$ relation, found for coronally active stars (Guedel & Benz, 1993).

- AGN wind: radio emission can originate from synchrotron radiation caused by the shock front of outflows that interact with the ISM and accelerate particles (Zakamska & Greene, 2014; Nims et al., 2015). This mechanism is supported by the [O III] outflow velocity correlated to the radio luminosity (Molyneux et al., 2019).

- Jets: Similarly to the extended radio emission in RL AGN, RQ radio emission can be produced by jets, but more compact and with lower radio power (Falcke & Biermann, 1995; Kukula et al., 1998), or "frustrated" by a dense circumnuclear environment (O'Dea et al., 1991; Patil et al., 2020). The difference between RQ and RL is potentially related to the efficiency to accelerate particles, the jets being less relativistic for RQ AGN (Falcke & Biermann, 1995).

The radio emission in RQ AGN is likely a combination of these four mechanisms with different intensities. In RL AGN, the bright emission from the powerful jets dominates the radio band, masking the other mechanisms.

1.4 The Growth of SMBH

It is now clear that SMBHs grow primarily through accretion (Soltan, 1982), therefore, studying the accretion luminosity of AGN at different redshifts is key for understanding

the SMBH growth history. As AGN radiate across the entire electromagnetic spectrum (Section 1.3), they can be detected and identified across various wavebands, including UV/optical, IR, radio and X-ray wavebands (Hickox & Alexander, 2018). §1.4.1 presents for each waveband the different AGN identification methods, assessing their completeness and reliability levels and justifying the multi-wavelength approach adopted in this thesis. Notably, one limitation of most methods is the AGN obscuration, biasing our understanding of the overall population. §1.4.2 emphasizes the importance of the obscured AGN by presenting the current knowledge on their demographics and properties. Moreover, given that the growth of SMBH is governed by AGN feeding and feedback cycles, §1.4.3 presents how AGN population studies can investigate these mechanisms by analysing the AGN accretion rates as a function of their host galaxy properties.

1.4.1 AGN Selection Methods

UV/Optical/Near-IR selection

Given that the accretion disc is bright in the UV-optical band (§1.3.2), AGN can be efficiently detected in this waveband (Padovani et al., 2017). Moreover, as the accretion disc can reach higher temperatures than stars, with the exception of young white dwarfs, AGN show bluer colours than stellar emission. Based on this, Richards et al. (2002) established a photometric colour cut below which sources are either white dwarfs or AGN at $z < 2.2$. This $u^* - g^* < 0.6$ cut is represented by the *yellow vertical line* in the left panel of Figure 1.15. The authors also propose other colour-colour criteria to identify AGN at different redshift intervals. However, the main limitation of UV/optical photometric AGN identification is the host galaxy "dilution", i.e., the host galaxy stellar emission is dominant compared to the AGN in this waveband. Host galaxy dilution occurs when an AGN is intrinsically faint with respect to its host galaxy or when the AGN UV/optical emission is strongly suppressed by obscuration due to the dust's high optical depth in this waveband (Calzetti et al., 1994; Draine, 2003). Therefore, AGN optical photometric identification is inefficient for obscured AGN. Moreover, due to the increasing ISM obscuration with redshift (Buchner & Bauer, 2017; Gilli et al., 2022), the efficiency of this approach decreases with redshift. In summary, while UV/optical photometry is effective

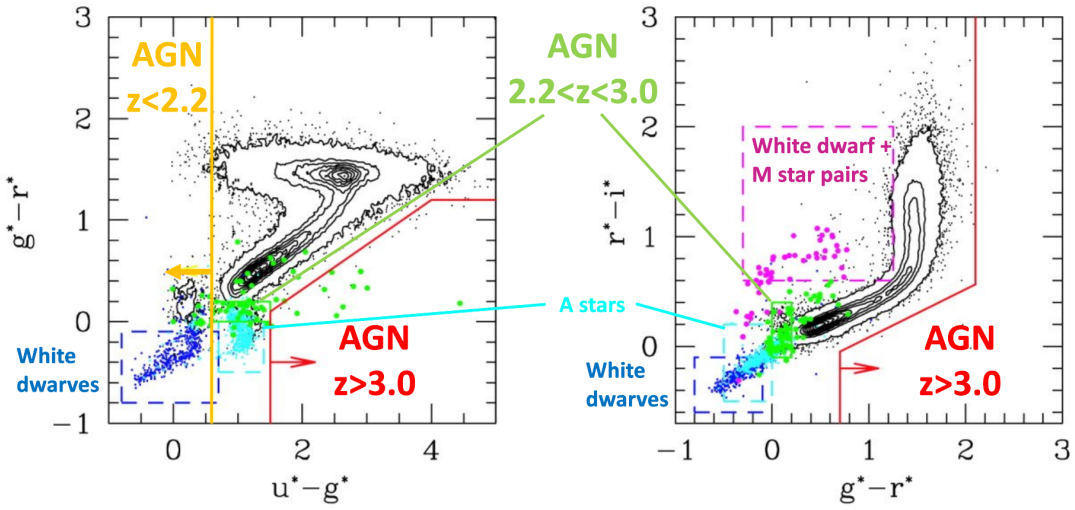

Figure 1.15: SDSS g^*-r^*/u^*-g^* (*left* panel) and r^*-i^*/g^*-r^* (*right* panel) colour-colour diagrams. The black contours and dots represent the stellar population. The blue, cyan and magenta dashed boxes are the exclusion boxes of the white dwarfs, A star and white dwarf+M star pairs populations, respectively. The orange vertical solid line represents the colour cut for AGN at $z < 2.2$. The red line corresponds to the colour cut for $z > 3.0$ AGN while the small green box selects AGN within the $2.2 < z < 3.0$ redshift range. Figure adapted from Richards et al. (2002).

in selecting large samples of bright unobscured quasars, its reliability and completeness regarding the overall AGN population are limited.

Due to the ionisation of the BLR and NLR by the accretion disc radiation (§1.3.5), AGN optical spectra display strong emission lines that can be used for their identification (Seyfert, 1943) and classification as type I and type II (Weedman, 1977). The identification of unobscured AGN is straightforward as only AGN can broaden the lines to such velocities ($>10^3\,\mathrm{km\,s^{-1}}$). As narrow lines are not affected by the torus obscuration, they can be used for the identification of obscured AGN. However, as star formation processes also emit narrow emission lines, additional criteria are needed to separate both populations. The pioneering work of Baldwin et al. (1981) proposed an emission-line diagnostic relying on the fact that AGN have a higher ionisation power than star-forming galaxies, therefore, large flux ratios of highly-ionised emission lines (e.g. [O III], [N II], [S II]) to low-ionised lines (e.g. Hα, Hβ) can indicate the presence of an AGN (Veilleux & Osterbrock, 1987; Ho et al., 1997; Kauffmann et al., 2003; Kewley et al., 2006; Zhang et al., 2020). Figure 1.16

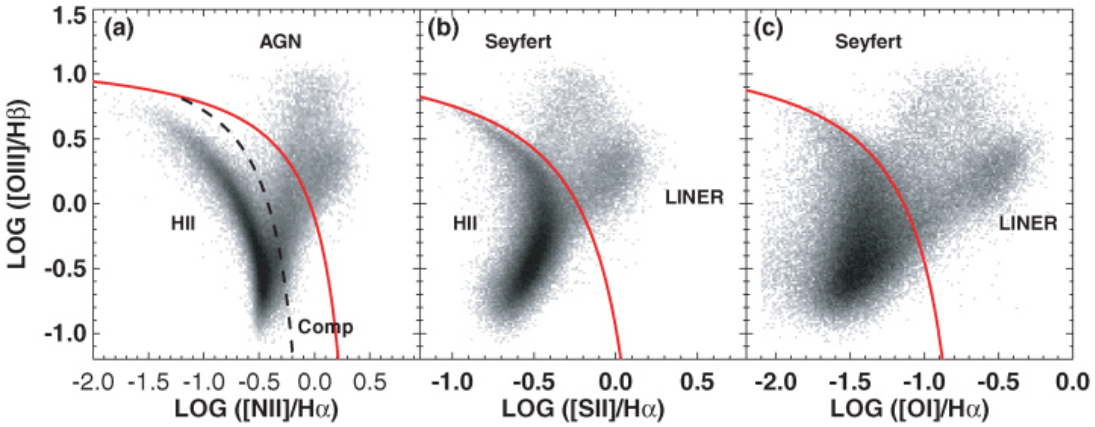

Figure 1.16: Example of BPT diagram separating AGN from star-forming galaxies ("HII") and LINERs. The *red solid line* corresponds to the limit of extreme starburst galaxies (Kewley et al., 2001), while the *black dashed line* is the AGN/star-forming galaxy demarcation by (Kauffmann et al., 2003). Sources located in between the two lines ("comp") are composites, i.e. AGN within a star-forming host. Figure from Kewley et al. (2006).

presents three BPT[9] diagnostic diagrams separating the AGN, LINERs and "H II" star-forming galaxies.

The lines chosen to compute the flux ratio should have similar wavelengths to minimize the impact of host galaxy ISM obscuration that can redden the spectra and dilute or suppress emission lines. Conversely, as the flux ratio between Balmer lines is fixed for given physical conditions (Brocklehurst, 1971; Gaskell & Ferland, 1984), then deviations from the expected ratio can provide constraints on the dust reddening up to moderate obscuration (Gaskell, 2017), although a steep Balmer decrement may also arise from a low Eddington rate (Wu et al., 2023). However, at higher redshift, the lines required for the BPT diagnostic will fall outside of the optical waveband. To address this challenge, different approaches were developed, using different line ratios (Kewley et al., 2013) or combining them with other observables such as stellar masses (Juneau et al., 2011), photometric colours (Yan et al., 2011) or Dn4000 index (Marocco et al., 2011) (i.e. amplitude of the 4000Å discontinuity, Bruzual A., 1983). Additionally, the unique presence of highly ionised lines such as [NeV]λ3426 can be sufficient to reveal the AGN activity (Gilli et al., 2010; Feuillet et al., 2024). Overall, optical spectroscopy is an efficient and reliable method for identifying AGN, except for the faintest sources, but it is observationally expensive,

[9]Baldwin-Phillips-Terlevich, the authors of Baldwin et al. (1981)

requiring long exposure time. Moreover, optical spectroscopy is mainly used for follow-up observations, targeting sources previously detected and/or identified by other approaches rather than being the primary AGN-identification method. Optical spectroscopy, therefore, strongly relies on these other approaches, adopting the same biases and limitations to build a complete census of AGN.

Infrared selection

By reprocessing the accretion disc UV/optical emission, the AGN dusty torus is bright in the mid-IR (§1.3.4). Consequently, the mid-IR waveband can be a robust tool for constructing complete samples of AGN. Moreover, as shown in Figure 1.6, the AGN mid-IR emission is less impacted by obscuration than other wavelengths, ensuring a high AGN completeness in mid-IR surveys regardless of the obscuration. However, dusty star formation also emits in this band, impacting the reliability of mid-IR AGN selection, especially for low-luminosity systems. In a similar way to the UV/optical, colour-colour techniques are developed to improve the reliability of AGN selection (Padovani et al., 2017). Each mid-IR space telescope has its own wedges to distinguish AGN from star-forming galaxies. For instance, colour-colour wedges defined by Lacy et al. (2004, 2007); Stern et al. (2005); Donley et al. (2012) were based on *Spitzer* colours, while those by Mateos et al. (2012); Stern et al. (2012); Assef et al. (2013) used *WISE* colours (see Figure 1.17). However, this approach necessitates that the AGN dominate the mid-IR SED with respect to its host galaxy, potentially missing low-luminosity AGN. Moreover, the mid-IR colours of star-forming galaxies at higher redshift $z > 2-3$ are similar to that of AGN (Donley et al., 2012), making the use of colour-colour diagrams less reliable, or requiring a luminosity cut to separate AGN from star-forming galaxies. The complete UV-to-IR SED fitting is an efficient approach to separate the AGN mid-IR luminosity from the host galaxy emission, especially if far-IR photometry is available to put solid constraints on the star formation properties. Nevertheless, this method is model-dependent and holds some parameter degeneracies.

Mid-IR spectroscopy can provide additional insights into the AGN identification, notably by the presence of high-ionisation lines such as [Ne VI] 7.6 μm or [Ne V] 14.3 μm (Spinoglio & Malkan, 1992; Mordini et al., 2021). Moreover, mid-IR spectra can reveal

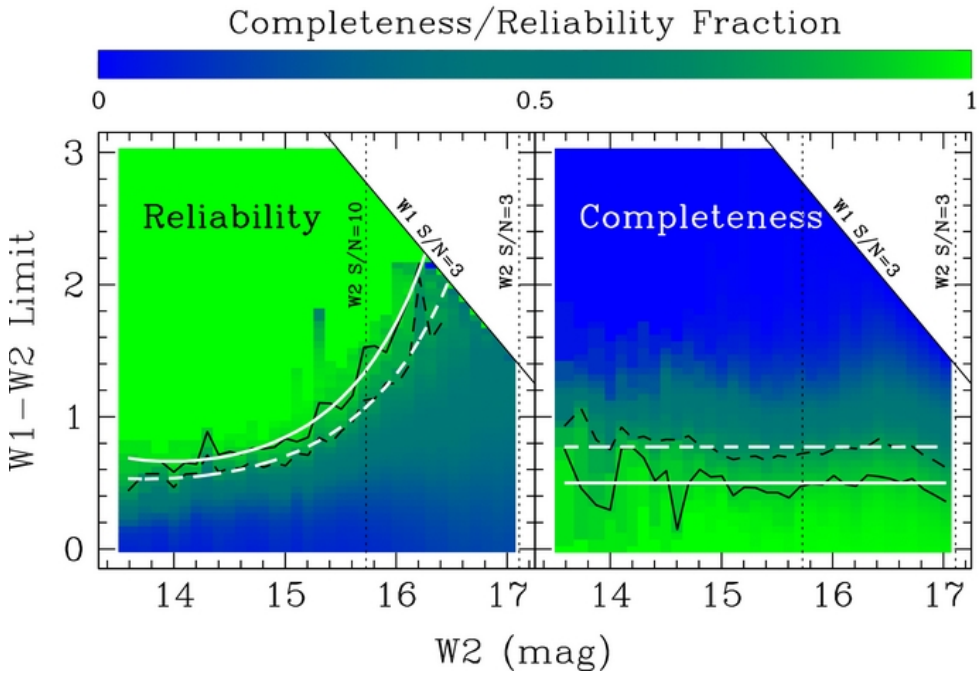

Figure 1.17: AGN selection criteria in the W1-W2/W2 plane (Assef et al., 2013). *Left panel*: reliability criteria for 90% and 75% represented with the white solid and dashed lines, respectively. Above these lines, 90% and 75% of the sources are actual AGN, respectively. *Right panel*: completeness criteria for 90% and 75% represented with the white solid and dashed lines, respectively. Above these lines, 90% and 75% of the entire AGN population are selected. The top-right corner of the panel is missing due to the W1 signal-to-noise requirement. Figure from Assef et al. (2013)

Polycyclic Aromatic Hydrocarbons (PAHs) features, produced by IR fluorescence of large molecules induced by far-UV photons (Allamandola et al., 1989; Smith et al., 2007), themselves tracing star formation. Therefore, the PAHs features can constrain the host-galaxy mid-IR contribution and isolate the AGN torus reprocessed emission (Tielens, 2008; Pope et al., 2008). Additionally, the silicate absorption features at 9.7 μm and 18 μm can provide an estimation of the obscuration (Draine & Lee, 1984) as it has been found correlated to the column density measured in the X-ray (Hönig & Kishimoto, 2010). Nevertheless, not all obscured AGN exhibit Si absorption features, suggesting a potential connection to the host galaxy rather than the torus (Goulding et al., 2012).

As the successor of *Spitzer*/IRS (Houck et al., 2004; Werner et al., 2004), the Mid-Infrared Instrument (MIRI) onboard of the James Webb Space Telescope (*JWST*, Gardner et al., 2006) is currently revolutionising the mid-IR spectroscopy field (Lyu et al., 2023). By discovering previously undetected AGN, *JWST*/MIRI is building the most

complete AGN sample. Moreover, as optical lines used for AGN identification are shifted to the near-IR band at high redshift, the *JWST* Near-Infrared Spectrograph (NIRSpec) allows the discovery of AGN at unprecedented redshift. For instance, Kokorev et al. (2023) reliably estimate the redshift of an AGN at $z = 8.50$, while several AGN candidates are potentially located at even higher redshifts ($z \gtrsim 10$, Goulding et al., 2023; Maiolino et al., 2023). Notably, observations of AGN above $z > 5.5$ probe the SMBH population within the first billion years of the Universe, providing crucial insights into SMBH formation scenarios (see §1.3.1). Moreover, JWST has identified a large population of obscured and faint AGN, missed by any other AGN selection method, improving our understanding of galaxy and SMBH co-evolution through cosmic times (Kocevski et al., 2023; Yang et al., 2023). To summarise, the mid-IR band AGN selection is the most complete approach, but its reliability is compromised by the contamination from the host galaxy star formation. Nevertheless, with the advent of JWST, the near-IR and mid-IR wavebands promise new discoveries in the coming years.

Radio selection

As mentioned in the brief history of AGN study (Section 1.1), radio astronomy has been a pioneering method to identify AGN (Baade & Minkowski, 1954; Schmidt, 1963) and presents the advantage of being little impacted by obscuration, except by the Hydrogen 21 cm absorption feature of the intergalactic medium (Madau et al., 1997). However, the AGN radio luminosity spans 4-5 orders of magnitude between radio-loud and radio-quiet AGN and the physical reasons behind this dichotomy are not yet understood (Blandford et al., 2019). Moreover, the size of the AGN radio emission can range from pc to Mpc scales. Alongside this broad luminosity and resolution range, radio identification of AGN suffers from contamination from star-forming galaxies (Condon et al., 2013). For these reasons, the radio selection function is not well-constrained, preventing the extrapolation of the intrinsic AGN population from an observed sample.

Nevertheless, two modes of AGN feedback have been identified, the radiative and the kinetic mode (Fabian, 2012). AGN in the radiative mode are accreting efficiently, and their radiation pressure can produce winds affecting their host galaxy, while AGN in kinetic mode, also known as radio mode, convert most of the accretion power into powerful

radio jets, and tend to have low-Eddington rates. Consequently, radio observations can efficiently probe this AGN population under-represented in other wavebands. Additionally, the correlation between far-IR and radio luminosity from star formation (Helou et al., 1985; Appleton et al., 2004) allows for the detection of AGN via excess radio emission (Donley et al., 2005; Delhaize et al., 2017). Additionally, a low radio spectral index in radio sources suggests self-absorption, characteristic of a compact source like AGN. Overall, while radio selection is efficient in the radio loud regime to identify AGN, radio-quiet AGN are mostly missed. However, recent facilities like LOFAR or MeerKAT and future ones such as SKA are progressively exploring fainter radio luminosities towards a better understanding of the radio-loud/radio-quiet dichotomy.

X-ray selection

The identification of AGN in the X-ray band is one of the most reliable and complete approaches (Brandt & Alexander, 2015; Hickox & Alexander, 2018). Its completeness is ensured by the ubiquity of X-ray emission among AGN (Kormendy & Ho, 2013). However, two factors limit the completeness of X-ray AGN identification: low accretion rates AGN, i.e. with low radiative efficiency, and AGN obscuration. Nevertheless, obscuration has a significantly lesser impact on AGN X-ray emission compared to UV/optical emission, as the optical depth of the obscuring material decreases with increasing energy (Wilms et al., 2000). The first consequence of this energy dependence is that above rest-frame $> 10\,\mathrm{keV}$, the X-ray emission is not significantly suppressed by obscuration up to the Compton-thick regime (CTK, $N_{\mathrm{H}} \gtrsim 10^{24}\,\mathrm{cm}^{-2}$). Therefore, hard X-ray observatories such as *INTEGRAL* (International Gamma-Ray Astrophysics Laboratory, 3-35 keV, Winkler et al., 2003), *Swift*-BAT (Burst Alert Telescope, 15-150 keV, Gehrels et al., 2004; Barthelmy et al., 2005) and *NuSTAR* (Nuclear Spectroscopic Telescopic Array, 3-79 keV, Harrison et al., 2013) provide a reliable and obscuration-unbiased sample of Compton-thin AGN in the local Universe. Moreover, in the CTK regime, the AGN X-ray emission is primarily dominated by reflection components (§1.3.3), especially the Fe Kα line at 6.4 keV and the Compton hump above $> 10\,\mathrm{keV}$ (Levenson et al., 2006a), rendering AGN detectable. It is worth mentioning that, with increasing redshift, softer X-ray observatories (0.5-10 keV) such as *X-ray Multi-Mirror Mission* (*XMM*)*-Newton* (Jansen et al., 2001) and

Chandra (Weisskopf et al., 2000) are probing higher rest-frame energies, thereby becoming less sensitive to obscuration. The second consequence of the energy dependence of the absorption effects is that obscuration imprints its signature on the X-ray spectrum (see Figure 1.11). This allows the determination of the line-of-sight column density $N_{\rm H}$ via X-ray spectroscopy, thus enabling the recovery of the intrinsic X-ray luminosity, and correcting for obscuration bias.

Conversely, the high reliability of the X-ray AGN identification relies on the minimal contamination by other X-ray sources. Besides AGN, only hot gas in clusters ($T > 10^6\,\mathrm{K}$) and star-forming regions with X-ray binaries emit in the X-ray band, but both contaminants can be efficiently identified. Indeed, hot gas in clusters emits a diffuse X-ray radiation distinct from point-like AGN emission. Moreover, they exhibit a thermal spectral shape different from the AGN power-law, often peaking at low energies ($\leq 2\,\mathrm{keV}$) (Kravtsov & Borgani, 2012). On the other hand, X-ray binaries have significantly lower luminosities than AGN (Alexander et al., 2005; Aird et al., 2017), and while the threshold $L_{\mathrm{X,\,2-10\,keV}} = 10^{42}\,\mathrm{erg\,s^{-1}}$ is often used to conveniently separate both populations, this thesis meticulously models the X-ray binary contamination allowing for lower-luminosity AGN to be identified. Combining the low contamination by other X-ray sources with the ability to model the obscuration bias allows a precise determination of the X-ray selection function. This function quantifies the probability of detecting an AGN as a function of its physical parameters, mainly redshift, column density and intrinsic X-ray luminosity (Georgakakis et al., 2008). With this selection function, X-ray-selected AGN studies can extrapolate and investigate the intrinsic AGN population from observed samples, yielding strong insights into the AGN demographics (Buchner et al., 2015; Georgakakis et al., 2017b). For these reasons, the research presented in this thesis is based on X-ray-selected AGN samples but also benefits from the physical parameters constraints obtained using other wavebands, notably mid-IR.

1.4.2 Obscured AGN Demographics

As discussed in the previous subsection §1.4.1, AGN X-ray identification is the most effective waveband to obtain a complete and reliable census of AGN, selecting even heavily obscured AGN with minimal contamination from galaxies. There are two primary ap-

proaches for studying intrinsic demographics of obscured AGN using X-ray data: population synthesis to model the Cosmic X-ray Background (CXB) or extrapolation from observed populations.

Since its first detection in 1962 (Giacconi et al., 1962), the CXB has been progressively refined with successive observations. For instance, the isotropy of the CXB was confirmed by the Uhuru satellite (Giacconi et al., 1974). Two main explanations were initially proposed concerning its origin: either diffuse, such as hot intergalactic medium (Marshall et al., 1980), or discrete, such as AGN (Boldt & Leiter, 1987). The latter scenario would require a much larger number of sources than estimated from observations (Hamilton & Helfand, 1987). Moreover, most X-ray-detected sources are AGN and the bright ones are well fitted with a power law using a $\Gamma \sim 1.7$ photon index (Mushotzky, 1982, 1984) while the CXB exhibits a photon index $\Gamma \sim 1.4$ below $< 10\,\mathrm{keV}$ (Gendreau et al., 1995), steepening at higher energies. This so-called "spectral paradox" (Boldt, 1987) could be reconciled within the framework of the emerging AGN unification model if a significant fraction of the overall AGN population is obscured. Indeed, as the impact of obscuration is energy-dependent, low-energy photons are more efficiently absorbed than high-energy ones, leading to a lower observed photon index, better fitting the CXB (Setti & Woltjer, 1989; Awaki et al., 1991). Later observations by *ROSAT*, *Chandra* and *XMM* confirmed progressively the discrete origin of the CXB and the importance of obscured AGN (Comastri et al., 1995; Brandt & Hasinger, 2005). Despite several CXB population synthesis models requiring a significant fraction of heavily obscured CTK AGN (Treister & Urry, 2005; Gilli et al., 2007; Ananna et al., 2019), this fraction is one of the major sources of uncertainties in CXB studies. Indeed, it is either arbitrarily fixed to the fraction of obscured CTN AGN (Gilli et al., 2007; Ueda et al., 2014), or dependent on the assumptions on the AGN spectral shape (Treister et al., 2009). For instance, Akylas et al. (2012) estimate that the CTK fraction ranges between 5% and 50% for different spectral shape assumptions. Nevertheless, more recent results from Ananna et al. (2019) suggest a CTK fraction of $50 \pm 9\%$ at $z = 0.1$ and $56 \pm 7\%$ at $z = 1$. The CXB best-fit population synthesis model is displayed in Figure 1.18, showing the prevalence of obscured AGN (*purple dashed line*) at energies $\gtrsim 2\,\mathrm{keV}$ and the importance of CTK AGN (*purple dashed-dotted line*) at higher energies $\gtrsim 10\,\mathrm{keV}$.

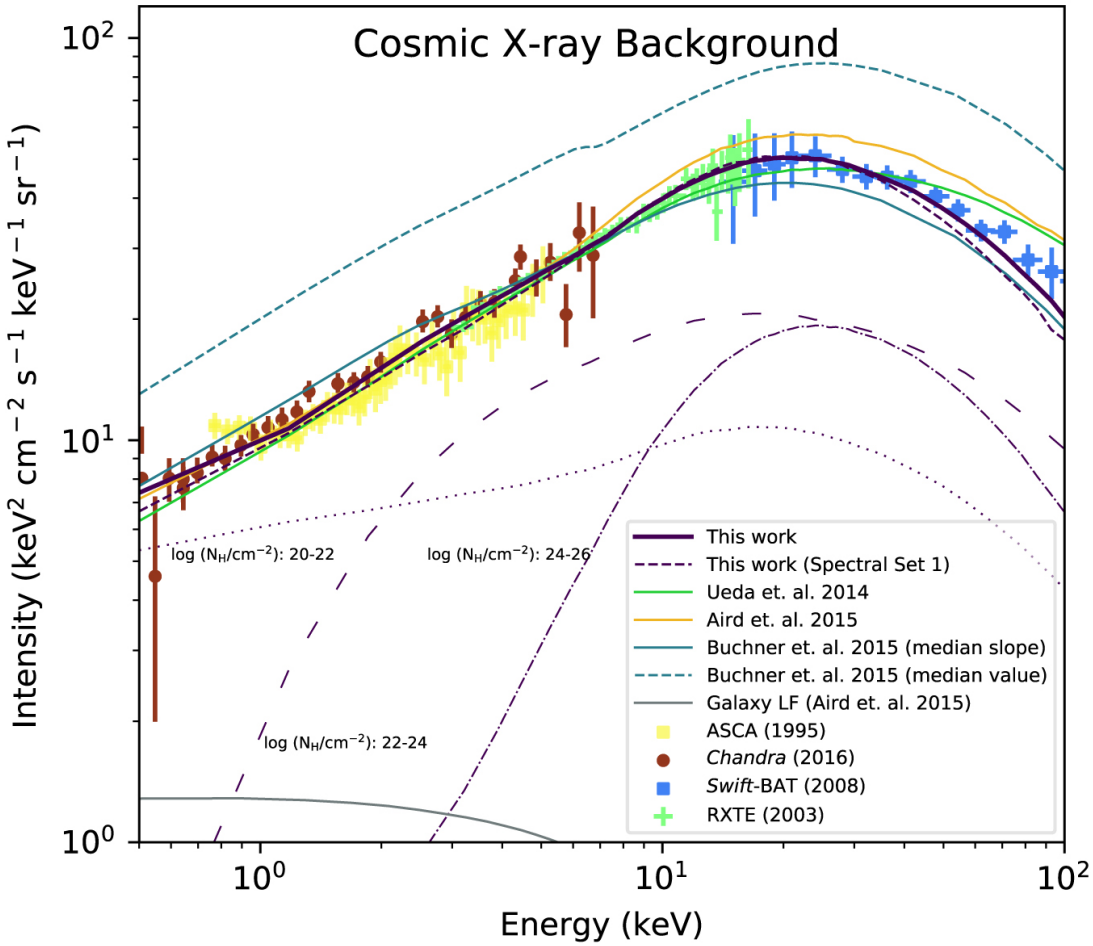

Figure 1.18: Cosmic X-ray Background (CXB) from *ASCA* (*green crosses*), *Chandra* (*red dots*), *Swift-BAT* (*blue squares*) and *RXTE* (*yellow squares*). The *black solid line* is the best-fit model of Ananna et al. (2019), the sum of the contributions of the unobscured AGN (*purple dotted line*), CTN obscured AGN (*purple dashed line*), CTK obscured AGN (*purple dashed-dotted line*) and galaxies (*grey line*). The results of other works are also overplotted (Ueda et al., 2014; Aird et al., 2015; Buchner et al., 2015). Figure from Ananna et al. (2019).

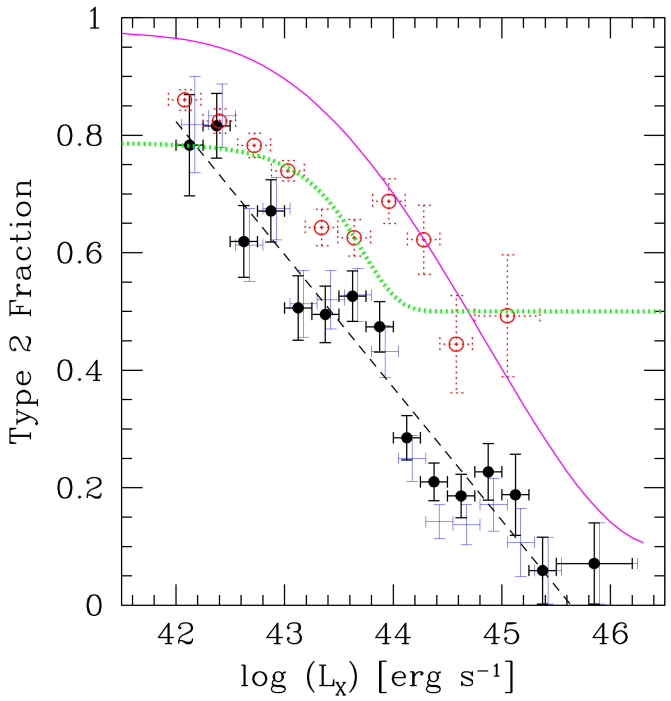

Figure 1.19: Fraction of type 2 AGN as a function of the X-ray luminosity. The *blue* and *black dots* are the results of Hasinger (2008) while the *red dots* are from Simpson (2005). The *green dotted line* and the *solid magenta line* are from Gilli et al. (2007) and Maiolino et al. (2007), respectively. Figure from Hasinger (2008).

Another approach to investigate AGN demographics is to extrapolate from observed samples. Maccacaro et al. (1991) is the first attempt to measure the X-ray Luminosity Function (XLF) of AGN, representing the number of AGN per unit volume as a function of the X-ray luminosity. The authors employ the $1/V_{\rm max}$ method (Schmidt, 1968; Avni & Bahcall, 1980), which consists of computing the maximum redshift at which each source can be detected and converting it into volume. The XLF is then derived by summing the inverse of the volume of each source within a redshift interval. With this approach, Maccacaro et al. (1991) find that the XLF follows a broken power law shape with a steep decline above $L_{\rm X} > 5 \times 10^{42}\,{\rm erg\,s^{-1}}$ and a flatter trend at lower luminosities. Moreover, they observe a shift of the XLF towards higher luminosities at higher redshift, indicating a cosmological evolution. However, this study relies on soft X-ray (0.3-3.5 keV) observations, thus, sensitive to obscuration. The advent of *Chandra* and *XMM* with sensitivity extending up to 10 keV allows the simultaneous determination of the XLF for obscured and unobscured AGN (e.g. La Franca et al., 2005; Hasinger, 2008). As shown in Figure 1.19,

these works indicate that the fraction of obscured AGN decreases with increasing luminosity, suggesting a receding torus model (see §1.4.1). Moreover, these studies reveal a luminosity-dependent density evolution (LDDE) of the XLF, where the peak of the AGN space density shifts towards lower luminosities with decreasing redshift. This observed so-called "cosmological downsizing" might provide crucial information on AGN fueling mechanisms. More recent works use the well-defined X-ray selection function and improved statistical approaches, which account for measurement uncertainties in a Bayesian framework, to confirm and refine these earlier results (Aird et al., 2010, 2015; Buchner et al., 2015; Georgakakis et al., 2015), notably finding that the fraction of CTN obscured AGN decreases at high luminosity and increases with redshift.

Nevertheless, the fraction of heavily obscured CTK AGN remains a significant source of uncertainty. For instance, Buchner et al. (2015) estimate the CTK AGN fraction to $38^{+8}_{-7}\%$, showing no significant redshift evolution or luminosity dependence, while Aird et al. (2015) find an increase with redshift up to $f_{\rm CTK} \sim 17\%$ at $z \sim 0.5$ before stagnating or slowly decreasing at higher redshifts as illustrated in Figure 1.20. Indeed, as explained previously (§1.4.1), the CTK AGN X-ray emission in the 2-10 keV band is mainly dominated by reflection features. Therefore, the intrinsic AGN population inferred from this approach is model-dependent. At higher energies where the absorption is less impactful, observations provide a more complete and reliable census of CTK AGN. The *Swift-BAT* all-sky survey (Ajello et al., 2008; Tueller et al., 2008), observing in the 15-150 keV band, has significantly increased the number of CTK AGN detected in the local Universe. Despite being less biased than in the 2-10 keV band, these hard X-ray observations are nonetheless biased against the most obscured AGN as the fraction of observed flux significantly decreases from $\sim 70\%$ at $N_{\rm H} = 10^{24}{\rm cm}^{-2}$ to $\sim 20\%$ at $N_{\rm H} = 10^{25}{\rm cm}^{-2}$ (Ricci et al., 2015). Based on the three-year *Swift-BAT* survey data, Burlon et al. (2011) measure a CTK fraction of $20^{+9}_{-6}\%$ (*green cross* in Figure 1.20) while, using the 70-months *Swift-BAT* catalogue, Ricci et al. (2015) estimate this fraction to be $27 \pm 4\%$. These values are significantly different from the ones derived from CXB studies, which suggest fractions up to 56% (Ananna et al., 2019).

In parallel to X-ray AGN population studies, recent works use samples of IR-selected quasars as they have the potential to be more complete than X-ray samples since they

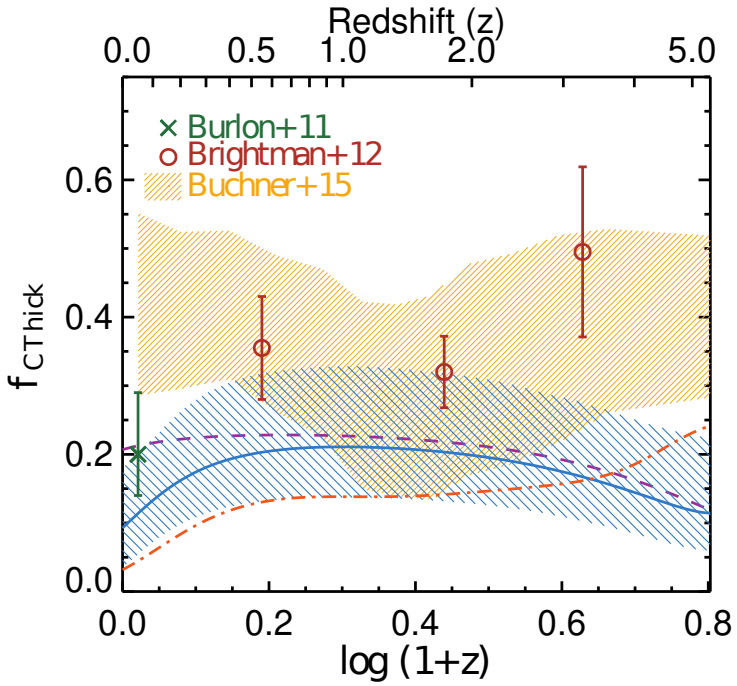

Figure 1.20: Fraction of CTK AGN as a function of the redshift. The *blue curve* and *shaded region* are the median values and uncertainties for $L_{\rm X} = 43.5$ from Aird et al. (2015), respectively. The *purple* and *orange dashed curves* are the median values for $L_{\rm X} = 42.5$ and $L_{\rm X} = 44.5$, respectively (Aird et al., 2015). These results are compared with the values of Burlon et al. (2011), Brightman & Ueda (2012), and Buchner et al. (2015) (*green cross*, *red circles* and *orange shaded region*, respectively) Figure from Aird et al. (2015).

can identify AGN so heavily obscured that even hard X-ray emission is suppressed. For X-ray-detected quasars, these studies find a fraction of obscured AGN $f_{\rm obs} \sim 60-70\%$, while X-ray-undetected IR-selected quasars are considered likely to be CTK, resulting in a relatively high CTK fraction $24 - 48\%$ (Del Moro et al., 2016). Despite being based on relatively small AGN samples and being limited to luminous quasars due to IR-AGN selection incompleteness and unreliability at lower luminosities (§1.4.1), these IR studies provide a new perspective on the demographics of obscured AGN. In Chapter 3, we take advantage of the well-defined X-ray selection function combined with multi-wavelength information to investigate the CTK fraction discrepancy.

1.4.3 AGN Feeding and Feedback Cycle

Despite uncertainties on the most obscured AGN, the overall SMBH growth history is believed to be well-constrained. As shown in Figure 1.21, the total SMBH accretion den-

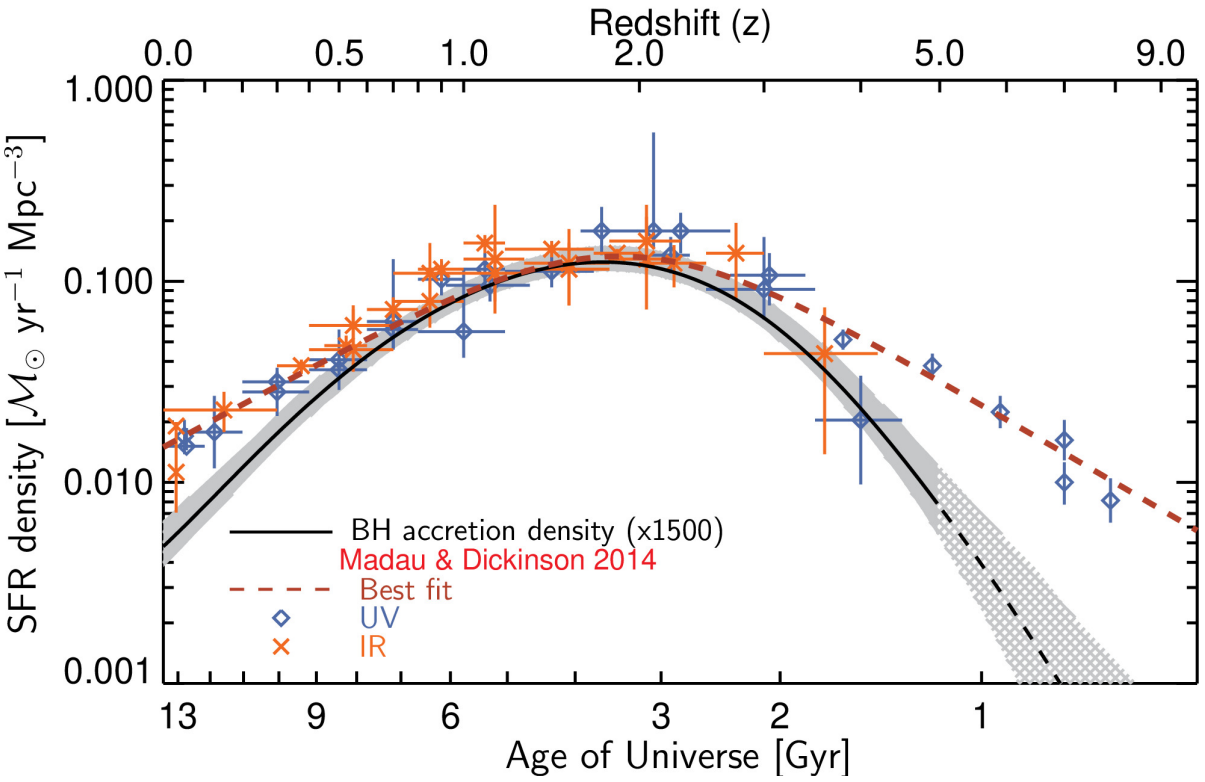

Figure 1.21: Comparison of the total SMBH accretion density with the total star formation rate (SFR) density. The *red dashed* line corresponds to the best fit of SFR density evolution from Madau & Dickinson (2014), derived by UV and IR observations represented by *blue diamonds* and *orange crosses*, respectively. The *black solid line* and the *grey-shaded region* correspond to the SMBH accretion density and its 99 per cent confidence interval estimated by (Aird et al., 2015) scaled up by a factor of 1500. Figure from Aird et al. (2015).

sity (*solid black line*) shows a rapid increase with redshift up to $z \sim 2$, followed by a decline towards earlier cosmic times (Ueda et al., 2003; Hasinger et al., 2005; Ueda et al., 2014; Aird et al., 2015). Interestingly, the total Star Formation Rate (SFR) follows a similar trend, peaking at a comparable redshift (*dashed red line* in Figure 1.21, Madau et al., 1998; Zheng et al., 2009; Behroozi et al., 2013; Madau & Dickinson, 2014). Furthermore, the mass of central SMBHs is found to correlate with the properties of their host galaxy bulge, such as velocity dispersion or stellar mass (Magorrian et al., 1998; Gebhardt et al., 2000; Ferrarese & Merritt, 2000; Kormendy & Ho, 2013; Reines & Volonteri, 2015). Combined, these observations suggest a common growth history in which AGN and host galaxy interact through feeding and feedback cycles (e.g. Hopkins et al., 2006).

AGN feedback, i.e. the AGN impact on its environment, encompasses different mechanisms realising energy into the host galaxy, including radiative pressure, disc winds or

jets, which are often referred to as "AGN outflows". Several studies investigating the impact of AGN outflows on the SFR find both positive and negative feedback, respectively activating and suppressing the SFR of the host galaxy. Positive feedback can be explained by the compression of the gas at the edge of AGN outflow, triggering local star formation, as supported by theoretical (Silk, 2013; Zubovas & Bourne, 2017) and observational (Cresci et al., 2015; Bessiere & Ramos Almeida, 2022) studies. Conversely, some galaxy formation models require AGN to provide negative feedback to suppress star formation in massive systems, and several observational works indicate such effects powered by strong winds in luminous AGN (Cano-Díaz et al., 2012; Alatalo et al., 2015; Wylezalek & Zakamska, 2016). Additionally, some studies indicate both positive and negative feedback can occur in individual sources (Cresci et al., 2015; Bessiere & Ramos Almeida, 2022; Mercedes-Feliz et al., 2023). Determining the impact of AGN outflows on SFR is challenging, as highlighted by the recent review of Harrison & Ramos Almeida (2024), particularly due to the different time scales involved. Given that an AGN represents a phase in the lifetime of a SMBH and not a persisting object in opposition to a galaxy, a single accretion event might not be significant on a galaxy scale, while the accumulation of several accretion phases has much greater potential to significantly influence the galaxy properties on longer timescales.

A statistical approach can, therefore, offer a new perspective on the impact of AGN feeding and feedback by constructing a complete census of AGN across different galaxy populations as a function of redshift and linking accretion properties to host galaxy characteristics. By carefully accounting for selection effects, this approach can determine the environments where AGN live. For that exercise, a fundamental observable is the Eddington ratio $\lambda_{\rm Edd} \propto L_{\rm bol}/M_{\rm BH}$ (§1.3.2). It reflects how fast the AGN is accreting with respect to the Eddington limit at which the radiation pressure exceeds the gravitational pull, thereby self-regulating SMBH growth (e.g. Di Matteo et al., 2005). While the Eddington ratio can be measured for large samples of local AGN (Kauffmann & Heckman, 2009; Schawinski et al., 2010; Ananna et al., 2022a), the direct estimation of the SMBH mass is challenging for obscured AGN outside the local Universe. However, given that the stellar mass $M_\star$ of the host galaxy can be measured via SED fitting and, that $M_\star$ and $M_{\rm BH}$ are correlated (Marconi & Hunt, 2003; Duras et al., 2020), the Specific Accre-

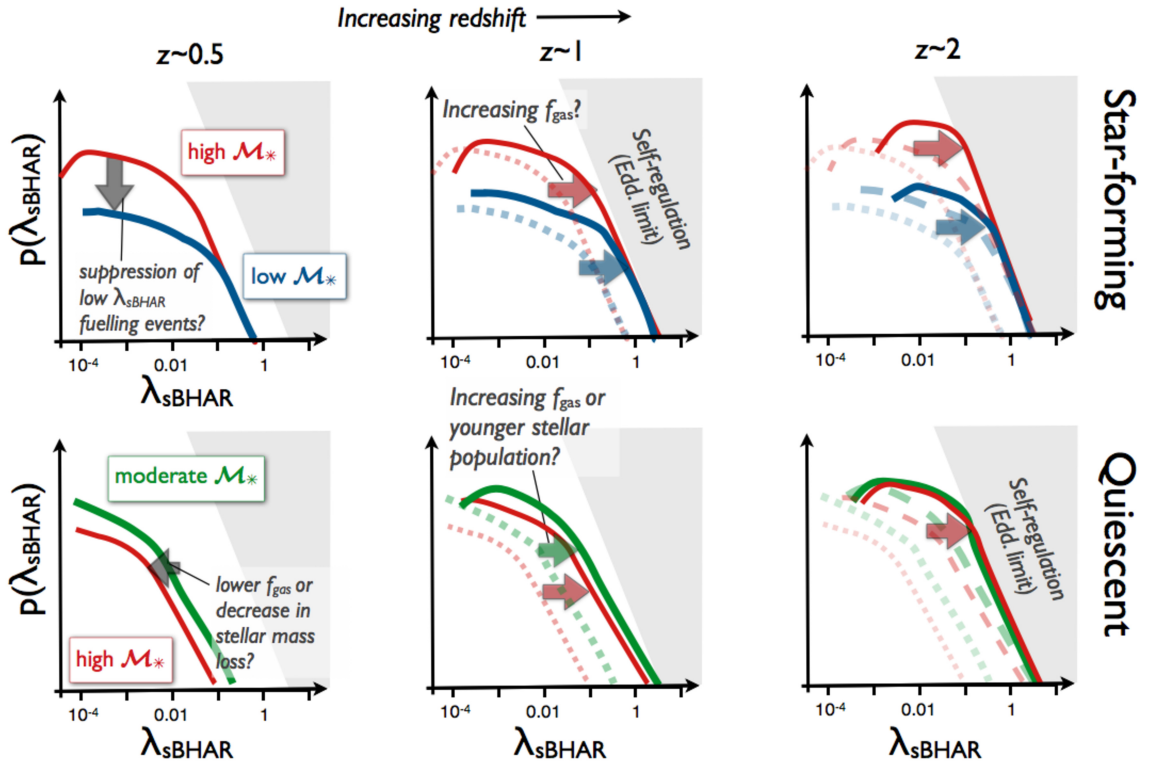

Figure 1.22: Sketch representing the evolution of the Specific Accretion Rate Distribution (SARD or sBHAR distribution) as a function of the redshift and the stellar mass for star-forming and quiescent galaxies. Figure from Aird et al. (2018).

tion Rate (SAR) $\lambda_{\rm SAR} \propto L_{\rm bol}/M_\star$[10] can be used as a proxy of the Eddington ratio for understanding the evolution of AGN incidence in galaxies. Consequently, several studies have investigated the SAR Distribution (SARD), representing the probability of a galaxy hosting an AGN with a given SAR $\lambda_{\rm SAR}$[10], as a function of the redshift (Bongiorno et al., 2012; Georgakakis et al., 2014; Bongiorno et al., 2016; Aird et al., 2018). Figure 1.22 summarises the main dependencies of the SARD:

- At high stellar masses ($M_\star > 10^{10}\,M_\odot$, *red curves*), the SARD of quiescent galaxies is shifted towards lower $\lambda_{\rm SAR}$ compared to star-forming galaxies. Massive quiescent galaxies tend to host weaker AGN and to have a lower duty cycle, i.e. the probability of hosting an AGN with $\lambda_{\rm SAR} > 0.01$.

- The SARD of both quiescent and star-forming galaxies shifts rapidly to higher $\lambda_{\rm SAR}$

[10]The $\lambda_{\rm SAR}$ is labelled $\lambda_{\rm sBHAR}$ in Figure 1.22.

with redshift, indicating an increased duty cycle. This redshift evolution is stronger for the most massive galaxies. However, the SARD appear to not exceed a certain threshold approximately corresponding to the Eddington limit, suggesting a self-regulating process.

- The impact of host galaxy stellar mass on the SARD differs for star-forming and quiescent galaxies. While more massive star-forming galaxies have a higher duty cycle than their lower mass counterparts (*blue curve* in top panels), more massive quiescent galaxies exhibit a slightly lower duty cycle than their moderate mass counterparts (*green curve* in bottom panels).

Additionally, AGN feeding and feedback cycles are potentially associated with the AGN obscuration, manifesting as infalling gas fueling the AGN and outflowing material (Sanders et al., 1988; Hopkins et al., 2008; Wada, 2012). Notably, using local Universe AGN samples, recent studies have explored the relationship between the Eddington ratio and the obscuration (Ricci et al., 2017b, 2022; Ananna et al., 2022a,b), finding that the fraction of obscured AGN drops rapidly above $\log \lambda_{\rm Edd} \gtrsim -2$. These observations are consistent with the scenario of radiation-driven outflows expelling the dusty obscuring material (Fabian et al., 2008), potentially self-regulating the accretion onto the SMBH (see §1.3.4). In Chapter 4, we investigate the redshift evolution of the covariance between SAR and obscuration.

1.5 Thesis outline

This thesis aims to understand and quantify the impact of the local environment on AGN. How does obscuration bias our census of AGN across cosmic time, and how do we compensate for it? Is there a relationship between the obscuration and the accretion rate of matter into the SMBHs? To answer these questions, this work analyses a large sample of X-ray-selected AGN from *Chandra* deep extragalactic fields. X-ray spectroscopy and SED fitting methodologies are combined to constrain the physical parameters of each source. These observational constraints are then processed in a Bayesian approach to examine the properties of the intrinsic population and investigate the role of obscuration.

The thesis is structured as follows:

- **Chapter 2: Data and methodology**

  In this Chapter, we describe the characteristics of the *Chandra* observatory and its deep extragalactic surveys. We also present the methodologies for source detection, counterpart identification and redshift estimation. Finally, we detail the different data analysis methods we employ to constrain the AGN physical parameters.

- **Chapter 3: The demographics of obscured AGN from X-ray spectroscopy guided by multi-wavelength information**

  In this Chapter, we analyse a sample of ~ 2000 hard-band-selected ($2-10\,\mathrm{keV}$) AGN to investigate the AGN space density as a function of intrinsic X-ray luminosity, column density and redshift. The novelty of the analysis resides in the combination, in a Bayesian framework, of SED fitting results to guide X-ray spectroscopy, yielding improved constraints on the column density N_{H}. With these new physical constraints and by accounting for the survey sensitivity, we investigate the intrinsic demographics of obscured AGN. The findings of this chapter were published in Laloux et al. (2023).

- **Chapter 4: Accretion properties of X-ray AGN: Evidence for radiation-regulated obscuration with redshift-dependent host galaxy contribution**

  In this Chapter, we compare the accretion properties of unobscured and obscured AGN. For ~ 4000 sources from three *Chandra* deep surveys, we measure the specific accretion rate $\lambda \propto L_{\mathrm{X}}/M_{\star}$, a proxy of the Eddington rate. By combining these observables and the survey sensitivity in a Bayesian non-parametric approach, we infer for the first time up to $z \sim 3$ the specific accretion rate distribution (SARD), i.e. the probability of a galaxy with mass $M_{\star}$ at redshift z hosting an AGN with column density N_{H} and specific accretion rate λ. We discuss how the dependence of the SARD on λ and its redshift evolution provide valuable information on the nature of the obscuring material. This work has been published in Laloux et al. (2024).

- **Chapter 5: Conclusion and future work**

  This final chapter summarises the main results of this thesis and the future potential research applications. For instance, the reliability of the multi-wavelength

analysis proposed in Chapter 3 would benefit from a revised $L_{\rm IR}-L_{\rm X}$ relationship, notably exploring its dependence on obscuration or black hole mass. This improved $L_{6\,\mu{\rm m}}$-based prior X-ray spectroscopy approach could then be used to analyse large and deep extragalactic fields to constrain the SARD of the CTK AGN population. Additionally, multi-wavelength follow-up studies could investigate the AGN and host-galaxy interactions by targeting sources in the blow-out region (§1.3.4) and inspecting their SFR, radio-detection or outflow properties.

CHAPTER 2

Data and Methodology

In this Chapter, I provide an overview of the data and the data analysis methodologies used throughout this thesis. As emphasized in the introductory Chapter 1, the study of the demographics and accretion properties of obscured AGN requires a large sample of X-ray-selected AGN. The sources studied in this thesis belong to three different deep extragalactic survey fields observed by the *Chandra* X-ray Observatory. The characteristics of this telescope and its onboard instruments are summarised in Section 2.1. The multi-wavelength observations for each deep field are detailed in Section 2.2. Chapter 3 focuses on the analysis of AGN detected within the COSMOS-Legacy field (§2.2.1), while the work presented in Chapter 4 also include the AEGIS-XD (§2.2.2) and CDFS (§2.2.3) fields. Section 2.3 presents the preliminary data analysis processes used to produce the data catalogues used in this thesis, including X-ray source detection (§2.3.1), multi-wavelength counterpart identification (§2.3.2) and redshift estimation (§2.3.3). Finally, Section 2.4 describes the advanced data analysis methodologies employed throughout this thesis, such as X-ray spectral extraction (§2.4.1), X-ray spectral fitting (§2.4.2) and UV-to-far-IR SED fitting (§2.4.3).

2.1 *Chandra* Space Observatory

The *Chandra* X-ray space observatory (hereafter *Chandra*) was launched on July 23rd, 1999. *Chandra* was placed on a highly elliptical orbit with a 63.5-hour period, maximising the observation time, operating more than 70% of each orbit. A week later, on August 12th, 1999, *Chandra* collected its first light, and since then, it has revolutionised X-ray astronomy with its unprecedented combination of angular resolution, spectral resolution and sensitivity in the 0.1-10 keV range. Although it was designed for 5-years operations and its fuel capacity was foreseen for 10 years, *Chandra* is still providing high-quality observations, 25 years after launch. In the following, I provide an overview of the characteristics of the telescope and its instruments, which are illustrated in Figure 2.1.

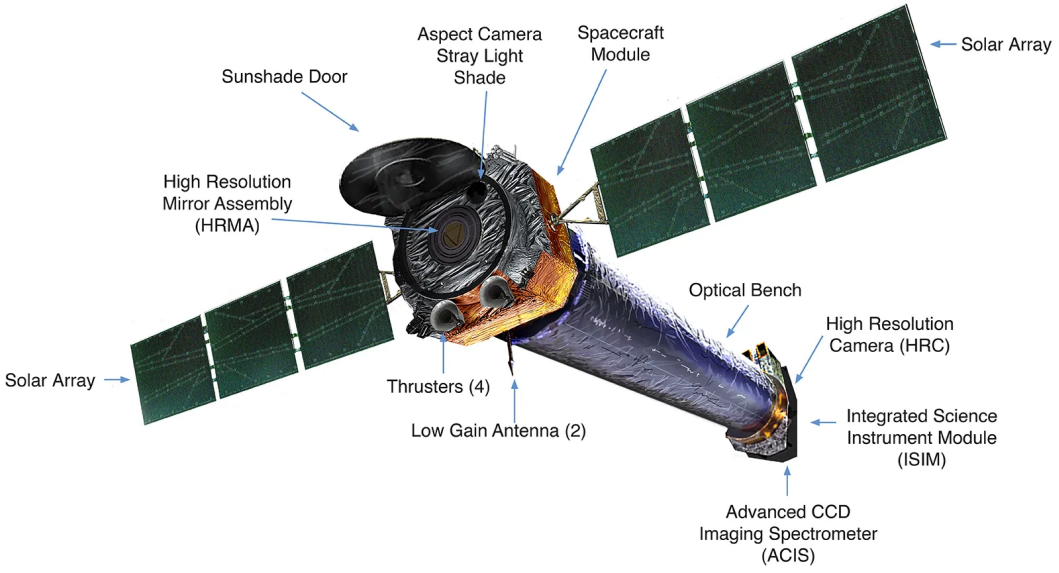

Figure 2.1: *Chandra* X-ray Space Observatory and its different components. In the front, the HRMA collects the X-ray photons, which are focused along the 10-m long optical bench. Behind it, the ISIM contains the transmission grating and the 2 focal-plane instruments HRC and ACIS.

Chandra is a Wolter type-I telescope best suited for X-ray high-energy photons with an effective area of 400 cm^2 at 5 keV. These photons are collected by the High-Resolution Mirror Assembly (HRMA, van Speybroeck, 1997), a 4-mirror-pair grazing-incidence optic system with a 10-m focal length. The HRMA is located at the centre of Figure 2.1. Notably, the HRMA's design allows *Chandra* to achieve exceptional imaging angular resolution, with an on-axis Point Spread Function (PSF) characterised by an on-axis Full

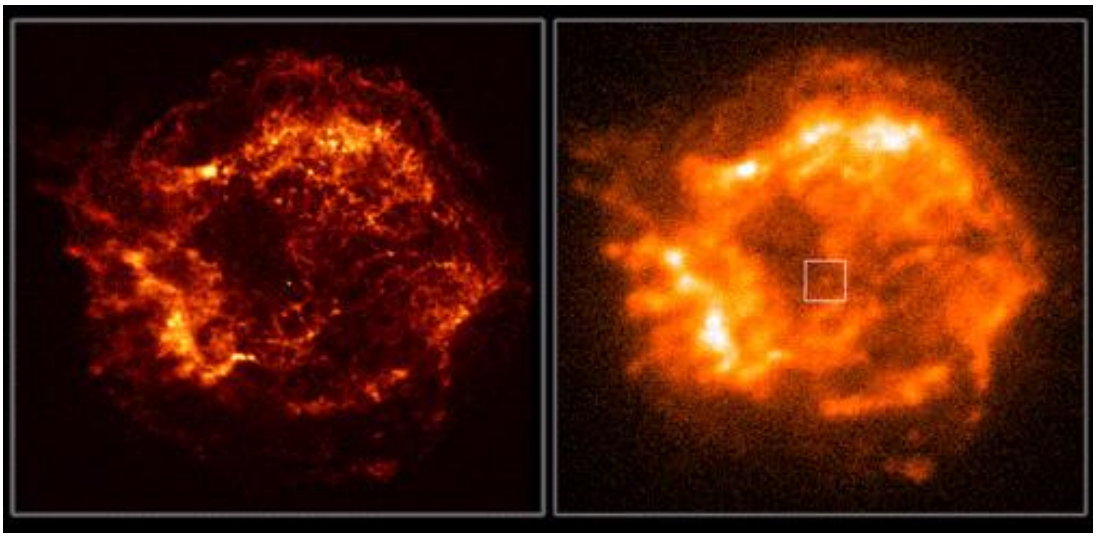

Figure 2.2: Supernova remnant Cassiopeia-A seen by *Chandra* (2.7 ks, *left* panel) and *ROSAT* (200 ks, *right* panel). This comparison shows *Chandra*'s superior angular resolution, notably with the previously undetected point-like source at the centre. Figure from Weisskopf et al. (2000).

Width at Half Maximum (FWHM) of less than 0.5 arcsec (Weisskopf et al., 2000). As an example, Figure 2.2 compares the image of a supernova remnant taken by *Chandra* with a 2.7 ks exposure time (*left* panel) with the image taken with a 200 ks exposure by *ROSAT* (*right* panel), the first X-ray imaging telescope, launched in 1990. The improvement in spatial resolution and sensitivity is significant and even allows the observation of a previously undetected point-like source at the centre of the image.

The Integrated Science Instrument System (ISIM), located behind the mirrors and the optical bench, on the right side of Figure 2.1, contains two sets of transmission gratings used for high-resolution spectroscopy: the Low-Energy Transmission Grating (LETG, Brinkman et al., 2000) and the High-Energy Transmission Grating (HETG, Canizares et al., 2005). LETG is composed of 180 grating modules, each with 3 diffraction grating facets, resulting in a high spectral resolution $\Delta\lambda \simeq 0.06$ Å in the soft X-ray energy range from 0.07 to 2.5 keV. HETG is an array of 336 grating facets giving a resolving power varying from $E/\Delta E \sim 800$ at 1.5 keV to $E/\Delta E \sim 200$ at 6 keV in the 0.4-10 keV energy band. The transmission gratings can be switched or removed for imaging, depending on the science objective of the observations.

Additionally, the ISIM contains two focal-lane instruments: the High-Resolution Camera (HRC, Murray et al., 1997, 2000) and the Advanced CCD Imaging Spectrometer

(ACIS, Bautz et al., 1998). The HRC is a microchannel plate with two detectors, the HRC-I for a wide field of view (FOV, 30'×30') imaging with sub-arcsecond resolution, while the HRC-S is used in combination with LETG to provide low-energy high-resolution spectra with a 6'×99' FOV. On the other hand, ACIS has two sets of Charged Coupled Devices (CCDs), which record the position, the energy and the time of arrival of each individual X-ray photon. Therefore, each CCD can provide high-resolution imaging and moderate-resolution spectroscopy within an 8.3'×8.3' FOV. ACIS-S is a 1×6 CCD array that includes 4 front-illuminated and 2 back-illuminated CCDs. Back-illuminated CCDs have better quantum efficiency at low energies than the front-illuminated ones and worse efficiency at high energies. ACIS-S is used for the transmission gratings readout, mainly from HETG, for high-resolution spectroscopy. ACIS-I is a 2×2 array of front-illuminated CCDs for wide-field imaging and moderate-resolution spectroscopy for a 16.9'×16.9' FOV. Due to the combination of sensitivity loss at the low and high energy end, *Chandra* effective energy range for X-ray surveys is 0.5-8 keV. The standard read-out mode of the CCDs is by integrating events over a defined amount of time, by default 3 seconds. Alternative exposure times and continuous clocking are two other read-out modes but are not used in deep extragalactic fields. Additionally, *Chandra* offers three telemetered data formats: faint, very faint, or graded. In faint mode, the position, arrival time and amplitude of an event are transmitted along with the signal amplitude of each pixel in the 3×3-pixels island determining the event grade. The very faint mode uses a 5×5-pixel event island which provides a reduced background rate. The graded mode is used for bright sources to avoid telemetry saturation by transmitting only the event grading instead of the signal amplitude of each surrounding pixel. The various instrument configurations provide flexibility in *Chandra* science goals: supernova remnants, X-ray binaries, pulsars, hot gas in clusters and, the focus of this thesis, AGN.

2.2 *Chandra* Deep Extragalactic Field Surveys

In this Section, I present the three *Chandra* deep extragalactic fields analysed in this thesis. For each field, I extensively describe the various multi-wavelength observations available from X-ray to radio, used or not in the analysis. The chosen photometric catalogue of each

field is later presented in the multi-wavelength counterpart identification Section §2.3.2.

2.2.1 COSMOS

The Cosmic Evolution Survey (COSMOS, Scoville et al., 2007) was the largest survey ($\sim 2\,\mathrm{deg}^2$) undertaken by the Hubble Space Telescope (HST) at the time in 2004 and has been extensively observed in various wavebands, from radio to X-ray, employing ground-based and space telescopes. The COSMOS field is a $1.4^\circ \times 1.4^\circ$ square, centred on RA=10:00:28.6, DEC= +02:12:21.0 (J2000). The position of the field was chosen because it is relatively devoid of bright sources, e.g. galactic stars or nearby galaxies, making it ideal for deep imaging to detect faint and/or distant extragalactic sources. Additionally, the galactic extinction is low and uniform across the COSMOS field and its position in the sky offers the possibility to be observed from both the northern and southern hemispheres. Benefiting from its comprehensive multi-wavelength coverage, the COSMOS science objectives are diverse, encompassing the relationship between large-scale structure and dark matter, galaxy assembly and evolution, and AGN evolution across cosmic time.

X-ray: The first uniform X-ray survey of the entire COSMOS field was conducted by the *XMM-Newton* telescope (Hasinger et al., 2007; Cappelluti et al., 2009). Observed by the EPIC CCD cameras for a $\sim 1.5\,\mathrm{Ms}$ total exposure time, the survey consists of 55 pointings with an average depth of 40 ks, reaching a $9.3 \times 10^{-15}\,\mathrm{erg\,s^{-1}}$ flux limit in the 2-10 keV band. The *XXM*-COSMOS region is delineated by the *black dashed line* in Figure 2.3. The central region of the COSMOS field was later on targeted by *Chandra*/ACIS-I as part of the C-COSMOS survey (Elvis et al., 2009). This survey adopts a half-a-field shift tiling strategy, with each pointing covering 50% of the previous one, ensuring that each point in the central region was covered by four observations, while the edges received coverage from two pointings. C-COSMOS is constituted of 36 pointings of 50 ks exposure time. The inner region, C-COSMOS deep, has an area of $0.5\,\mathrm{deg}^2$ with an effective exposure of $\sim 160\,\mathrm{ks}$, while the outer region covers $0.4\,\mathrm{deg}^2$ with a depth of $\sim 80\,\mathrm{ks}$. These regions are represented in Figure 2.3 by the *green dashed* and *solid lines*, respectively. This overlapping observing strategy results in a remarkably uniform exposure map, flat to $\pm 12\%$. Lastly, the COSMOS-Legacy survey (Civano et al., 2016) is an extension of C-COSMOS,

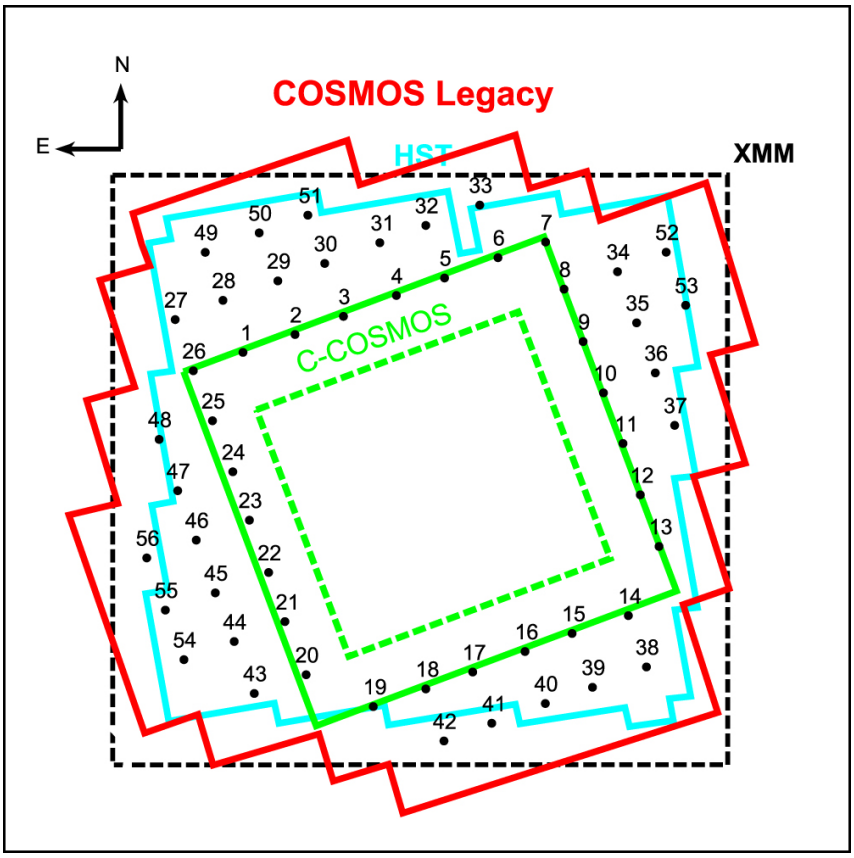

Figure 2.3: X-ray coverage of the COSMOS field by the *XMM*-COSMOS (*dashed black line*), C-COSMOS (*solid green line*), C-COSMOS deep (*dashed green* line) and COSMOS-Legacy (*solid red line*) compared to the *HST* survey (*solid cyan line*). Each dot and corresponding number represents a *Chandra* pointing, completing C-COSMOS to produce COSMOS-Legacy. Figure from Civano et al. (2016).

broadening *Chandra* coverage area to 2.2 deg^2 (*red solid line* in Figure 2.3), including a deep exposure area of 1.5 deg^2. The observing strategy is identical to C-COSMOS with 56 overlapping tiling as depicted by the *black dots* in Figure 2.3, providing uniform coverage with a flux limit of 1.5×10^{-15} erg s^{-1} in the 2-10 keV band. As COSMOS-Legacy is deeper than *XMM*-COSMOS and has a lower background level, this thesis focuses on the analysis of *Chandra* observations, using a custom source detection process described in §2.3.1.

The COSMOS field has also been observed in the hard X-ray by *NuSTAR* (Harrison et al., 2013) in the 3-79 keV band (Civano et al., 2015). Adopting the same half-overlapping pointing strategy as C-COSMOS and COSMOS-Legacy, the *NuSTAR* survey consists of a 11×11 grid of 12'×12' pointings. With a total exposure time of 3.12 Ms, the *NuSTAR* coverage of the COSMOS field offers a homogeneous depth of 50-60 ks effective exposure in the inner area (1.2 deg^2) and half of that for the outer region (0.5 deg^2).

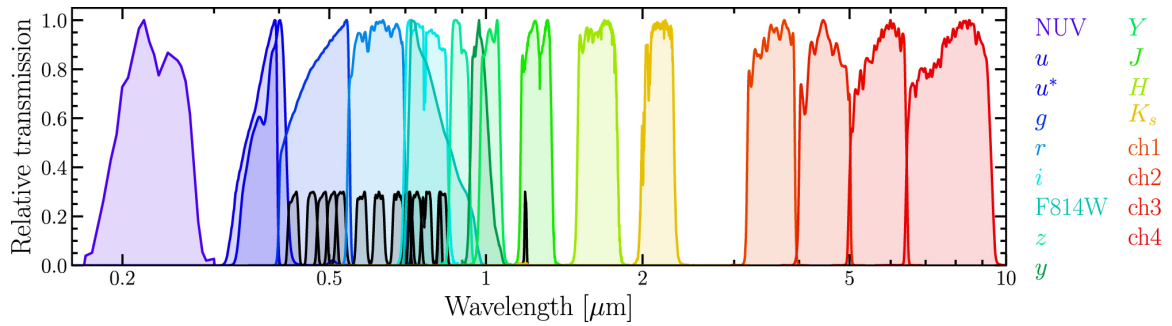

Figure 2.4: Transmission curves of the various photometry bands, including all observational effects, in COSMOS-Legacy. The black curves correspond to the medium and narrow bands, normalised to 0.3, while the coloured ones are the broad bands, normalised to 1. Figure from Weaver et al. (2022).

Despite the significant exposure time, the relatively low sensitivity of *NuSTAR* results in a 20% completeness at a flux of $5.9 \times 10^{-14}\,\mathrm{erg\,cm^{-2}\,s^{-1}}$ in the 3-24 keV band. It is also worth mentioning that *NuSTAR*'s resolution is significantly lower than *Chandra* and *XMM* due to a PSF with a FWHM of 18 arcsec and a 50% EEF radius of 58 arcsec. As a result of its low sensitivity and resolution, *NuSTAR* detected only 91 sources in COSMOS compared to the 1887 and 4016 sources detected by *XMM* (Cappelluti et al., 2009) and *Chandra* (Civano et al., 2016), respectively. Nevertheless, due to its unique hard X-ray coverage, *NuSTAR* is a powerful instrument for studying in detail the entire X-ray spectrum, including the Compton hump of AGN (§1.3.3), notably of the most obscured systems.

UV to mid-IR: The photometry available in the UV-to-mid-IR has been compiled and presented in Laigle et al. (2016) (COSMOS2015) and more recently in Weaver et al. (2022) (COSMOS2020). As illustrated in Figure 2.4, the multi-wavelength coverage is almost continuous from $\sim 0.2\,\mu$m to $\sim 10\,\mu$m, with the exception of a gap at $\sim 3\,\mu$m. The spatial distribution of the surveys carried out in different wavebands is depicted in Figure 2.5.

The Galaxy Evolution Explorer (*GALEX*, Martin et al., 2005) provides the UV photometry (Zamojski et al., 2007) of the COSMOS field in two bands: far-UV (FUV) and near-UV (NUV), with the median of the transmission curves at 1526 Å and 2307 Å, respectively. With four pointings with an exposure time of ∼50 ks, the limiting magnitude in both bands is ~ 26.0 mag (AB).

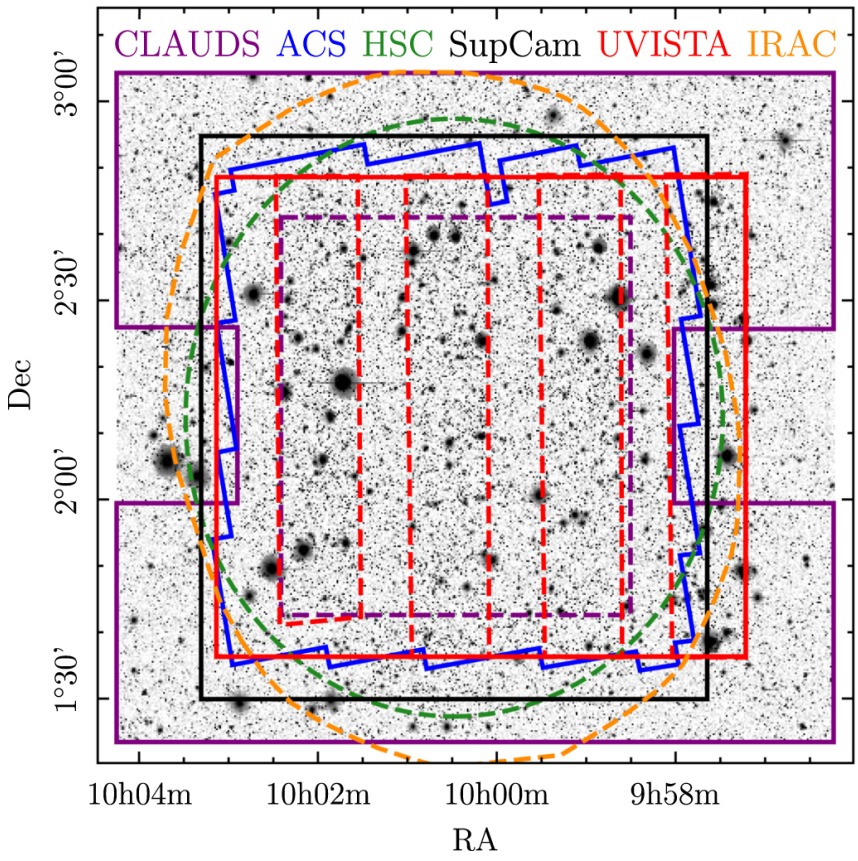

Figure 2.5: Schematic representation of the different photometric field surveys: CLAUDS U and U^* bands (*purple solid and dashed lines*), ACS F814W band (*blue solid line*), HSC g, r, i, z, y bands *green dashed line*, Suprime-Cam g, r, i, z and narrow bands *black solid line*, UVISTA Y, J, H, K bands (*red solid line*) and IRAC ch1, ch2, ch2, ch3 bands (*orange dashed line*). The *red dashed lines* delimit the ultra-deep stripes observed by UVISTA. Figure from Weaver et al. (2022).

The U band photometry was collected by the Canada-France-Hawaii Telescope (CFHT), using the MegaCam instrument. The U band data is a combination of archival data using the U^* filter (*dashed purple line* in Figure 2.5) and the data from CFHT Large Area U band Deep Survey (CLAUDS) (*dashed purple line* in Figure 2.5) using an updated U filter (Sawicki et al., 2019). The limiting magnitude in the U^* and U bands is 27.1 and 27.2 mag (AB), respectively.

Optical broad-band photometry (g, r, i, z, y) for the COSMOS field was obtained using the Hyper Suprime-Cam (HSC, Miyazaki et al., 2018, *green dashed line* in Figure 2.5), mounted on the Subaru Telescope, as part of the HSC Subaru Strategic Program (HSC-SSP, Aihara et al., 2019), with a limiting magnitude of 27.5, 27.2, 27.0, 26.6 and 25.9 mag (AB), respectively. The previous optical photometry used in COSMOS2015 was collected

by Subaru's Suprime-Cam (Taniguchi et al., 2007, 2015, *black solid line* in Figure 2.5). This dataset includes 7 broad-band, 2 narrow-band, and 12 intermediate-band filters. The broad-bands B, g^+, V, r^+, i^+, z^+, z^{++} have a limiting magnitude of 27.1, 25.6, 26.2, 26.5, 26.1, 25.1, 25.7 mag (AB), respectively. Additionally, COSMOS2015 and COSMOS2020 incorporate the original high-resolution photometry in the *F814W* band obtained by the Advanced Camera for Surveys (ACS) on board of the *HST* (Leauthaud et al., 2007) with a limiting magnitude of 27.8 mag (AB).

The Y, J, H, K_S near-IR broad-band photometry was collected by the VIRCAM instrument on the VISTA telescope. The fourth data release of the UltraVISTA survey (UVISTA, McCracken et al., 2012), includes a large region (*red solid lines* in Figure 2.5) with respectively 24.8, 24.7, 24.4, 24.8 mag (AB) limiting magnitudes, along with four ultra-deep stripes (*red dashed lines* in Figure 2.5) with 26.1, 25.9, 25.5, 25.2 mag (AB), respectively. Older photometry in the K_S band was collected by CHFT with a depth of 23.7 mag (AB) while the J band was observed by the United Kindom InfraRed Telescope (UKIRT, Salvato et al., 2009) up to 23.7 mag (AB).

The mid-IR data was obtained from channels 1, 2, 3, and 4 of the InfraRed Array Camera (IRAC, *orange dashed line* in Figure 2.5) on board the *Spitzer* space telescope. The limiting magnitudes are respectively 25.7, 25.6, 22.6 and 22.5 mag (AB). Euclid Collaboration et al. (2022a) compiled the mid-IR data from different observational programmes, notably the Spitzer Extended Deep Survey (SEDS, Ashby et al., 2013).

Far-IR to radio: The Jin et al. (2018) photometric catalogue of the COSMOS field spans from far-IR to (sub)millimetre wavelengths and employs a "super-deblending" technique (Liu et al., 2018) to reduce the source confusion due to the large beam size of the detectors. This method uses K_S+radio source positions to iteratively deblend the different far-IR/(sub)mm images and detect fainter sources.

This deblended catalogue integrates data from multiple surveys. Specifically, the 24 μm photometry was collected by the Multiband Imaging Photometer for *Spitzer* (MIPS) as part of the COSMOS-*Spitzer* programme (Le Floc'h et al., 2009). The 100 μm and 160 μm photometry was obtained by the Photodetector Array Camera and Spectrometer (PACS) on board the *Herschel* space telescope, from the PACS Evolutionary Probe survey (PEP, Lutz et al., 2011) and the Cosmic Assembly Near-infrared Deep Extragalactic

Legacy Survey (CANDELS, Grogin et al., 2011; Koekemoer et al., 2011). Additionally, the photometric data at 250 μm, 350 μm and 500 μm comes from the *Herschel* Multi-tiered Extragalactic Survey (HerMES, Oliver et al., 2012) using the Spectral and Photometric Imaging REceiver (SPIRE) aboard *Herschel*.

Observations at 850 μm were conducted using SCUBA2 (Geach et al., 2017), while data at 1.1 mm and 1.2 mm wavelengths were obtained by AzTEC (Aretxaga et al., 2011) and MAMBO (Bertoldi et al., 2007), respectively. Furthermore, the deep radio data at 3 GHz (Smolčić et al., 2017) and at 1.4 GHz (Schinnerer et al., 2010) were collected by the Very Large Array (VLA).

Spectroscopic data: The COSMOS field has been, is currently and will continue to be the target of several large spectroscopic programmes. While the analysis of emission and absorption lines can provide valuable constraints on the physical properties of sources, the primary objective for the majority of the spectroscopic programmes is precise redshift determination (§2.3.3).

zCOSMOS is the first large spectroscopic survey in the COSMOS field (Lilly et al., 2007, 2009), observing ∼10K sources using the VIsible Multi-Object Spectrograph (VIMOS, Le Fèvre et al., 2003) mounted on the Very Large Telescope (VLT) during 600 hours of observing time. In parallel, the Inamori-Magellan Areal Camera and Spectrograph (IMACS) instrument on the Magellan (Baade) telescope examined more than 1K sources (Trump et al., 2007). Moreover, the VIMOS Ultra Deep Survey (VUDS, Le Fèvre et al., 2015) observed $\sim$ 4K new sources. Complementing these surveys, the Fiber Multi-Object Spectrograph (FMOS) instrument of the Subaru telescope obtained the spectroscopic redshift of $\sim$ 2K sources as part of the FMOS-COSMOS survey (Kashino et al., 2019). Furthermore, the Deep Imaging Multi-Object Spectrograph (DEIMOS, Faber et al., 2003) on the Keck II telescope obtained the spectra for $\sim$ 10K objects within the COSMOS field (Hasinger et al., 2018).

Given its deep multi-wavelength coverage, the COSMOS field is an ideal target for ongoing and future missions. For instance, the COSMOS-Web survey (Casey et al., 2023) used 255 hours of observation time with the James Webb Space Telescope (JWST) to observe the COSMOS field, while Euclid will use this field for calibration (Euclid Collaboration et al., 2022b). In the future, the COSMOS field will be one of the initial

targets of the next generation of telescopes with diameters exceeding 20 meters, such as the Extremely Large Telescope, the Thirty Meter Telescope or the Giant Magellan Telescope.

2.2.2 AEGIS

The All-wavelength Extended Groth Strip International Survey (AEGIS, Davis et al., 2007) is a project combining different space- and ground-based telescopes to provide extensive deep multi-wavelength coverage from radio to X-ray in the Extended Groth Strip (EGS) region. The EGS region is an extension of the 28 Wide-Field Planetary Camera 2 (WFPC2) pointings by *HST* (Groth et al., 1994; Rhodes et al., 2000). Centred at $\alpha = 14\text{h}17\text{m}$, $\delta = +52°30'$, EGS covers an area of $0.25' \times 2'$ and benefits from low galactic extinction. Figure 2.6 displays the X-ray image of the EGS field (Laird et al., 2009) along with various multi-wavelength coverage regions. However, due to the numerous surveys in the EGS, for clarity, not all the multi-wavelength coverage regions are indicated (e.g. Barro et al., 2011).

X-ray: As illustrated in Figure 2.6, the EGS field has been targeted by two distinct X-ray *Chandra* programmes: AEGIS-X Wide (AEGIS-XW, Nandra et al., 2005; Laird et al., 2009) and AEGIS-X Deep (AEGIS-XD, Nandra et al., 2015), both of them using the *Chandra*/ACIS-I instrument. The AEGIS-XW survey covers a strip area of $0.67\,\text{deg}^2$ and consists of eight pointings with a nominal exposure time of $\sim 200\,\text{ks}$. Conversely, the AEGIS-XD survey (Nandra et al., 2015) increases the depth of the X-ray observations in the central region of the AEGIS-WD field, with an area of approximately $0.29\,\text{deg}^2$ (*black dashed region* in Figure 2.6). This survey consists of three pointings, each with a $\sim 600\,\text{ks}$ exposure time. When combined with AEGIS-WD, each pointing reaches a depth of $\sim 800\,\text{ks}$, for a limiting flux of $2.5 \times 10^{-16}\,\text{erg}\,\text{cm}^{-2}\,\text{s}^{-1}$ in the 2-10 keV band. As we aim to study the redshift evolution and detect faint sources, this thesis focuses only on the AEGIS-XD field.

UV/Optical: The EGS field was observed by *GALEX* in two bands, far-UV and near-UV, accumulating a total exposure time of 58 ks and 12 ks, respectively. The limiting magnitude in both channels is approximately ~ 25.1 mag.

The *HST*/ACS targeted a 10.5'×70.5' strip in the central region of the EGS field

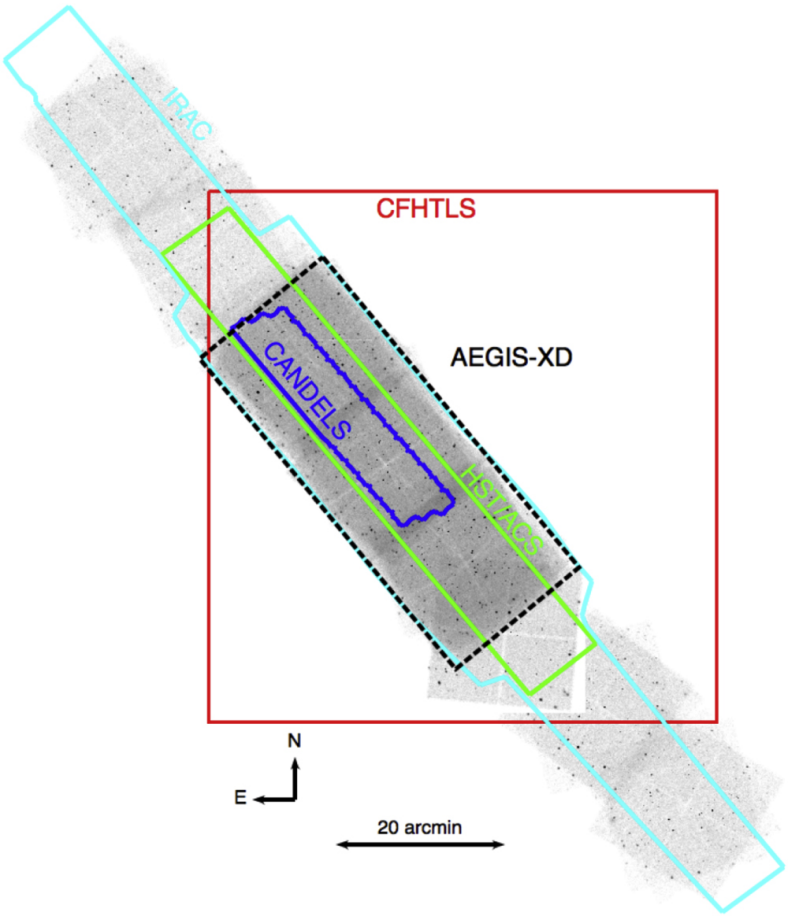

Figure 2.6: Multi-wavelength coverage of the AEGIS field. The background greyscale image is the AEGIS-XW (X-ray,Laird et al. (2009)). The *cyan region* has been covered by IRAC (mid-IR, Barmby et al. (2008)), the *red region* by CFHT Legacy Survey (CFHTLS, optical, Gwyn (2012)), the *green region* by the ACS instrument of *HST* (optical, Lotz et al. (2008)) and the *blue region* by CANDELS (near-IR, Grogin et al. (2011); Koekemoer et al. (2011)). The *black dashed region* corresponds to the AEGIS-XD field (X-ray, Nandra et al. (2015)). Figure from Nandra et al. (2015).

(Lotz et al., 2008, *yellow region* in Figure 2.6). This survey obtained the photometry in the *F606W* and *F814W* bands with approximately 2200 s of exposure time per pixel and a limiting magnitude of $\sim$ 28 mag. Additionally, the CFHT Legacy Survey (CFHTLS, Gwyn, 2012) covered a $1^\circ \times 1^\circ$ area (*red region* in Figure 2.6) with the MEGACAM instrument, obtaining the photometry in the u^*, g', r', i', z' bands over the 350 nm$< \lambda <$940 range. The above observations are complemented by shallower photometry in the B, R and I bands taken by the wide field 12K mosaic camera mounted on CFHT for the DEEP2 spectroscopic survey (Coil et al., 2004). Furthermore, the Megacam on the MMT telescope observed the EGS field in the u', g, i, z bands with a limiting magnitude $>$ 26 mag,

while the Suprime-Cam on the Subaru telescope obtained the R band photometry with a limiting magnitude of 26 mag.

Near-IR: Simultaneously with the ACS optical observations, the Near-Infrared Camera and Multi-Object Spectrometer (NICMOS) on board *HST*, obtained the photometry in the $F110W$ and $F160W$ bands, with a limiting magnitude of 23.5 and 24.2, respectively. Moreover, the WIRC camera on the Palomar 5m telescope covered 0.6 $\deg^2$ of EGS in the J and K bands with a limiting magnitude of 21.9 mag and 22.9 mag, respectively (Bundy et al., 2006). The Centro Astronómico Hispano en Andalucía (CAHA) also obtained the photometry in the J band, up to 22.9 mag (Villar et al., 2008). Additionally, as part of the CANDELS survey (Grogin et al., 2011; Koekemoer et al., 2011), *HST* covered the EGS field using the WFC3/IR instrument on 3×15 tiles ($6.7' \times 30.6'$ each), collecting photometry in the *F105W*, *F125W* and *F160W* bands. Finally, the NOAO Extremely Wide-Field Infrared Imager (NEWFIRM) mounted on the Mayall 4-m telescope covered the EGS field in the $J1$, $J2$, $J3$, $H1$, $H2$ and K bands with a limiting magnitude of 25.2, 25.3, 24.5, 24.1, 24.4, 24.2 mag, respectively (Whitaker et al., 2011).

Mid-to-far-IR: *Spitzer* observed the EGS field in the mid-IR band using the IRAC instrument (Barmby et al., 2008) which includes 4 photometric bands peaking at 3.6, 4.5, 5.8, and 8.0 μm, respectively. This data was collected as part of the SEDS (Ashby et al., 2013) with 52 pointings, providing a uniform depth over a $2^\circ \times 10'$ strip (*cyan region* in Figure 2.6), with a width varying between 10' and 17'. The respective depths are 23.9, 23.9, 22.3, 22.3 mag.

The Far-Infrared Deep Extragalactic Legacy survey (FIDEL, Dickinson & FIDEL Team, 2007) obtained the photometry of the EGS field at 24 μm and 70 μm, using the *Spitzer*/MIPS instrument. The MIPS coverage overlaps with IRAC observations. At 24 μm and 70 μm, the mean exposure time per pixel is 7200 s and 3800 s respectively, leading to a flux limit of 60 μJy and 3.5 μJy, respectively.

Radio: The EGS field has been covered in the radio band by the VLA at 1.4 GHz (Ivison et al., 2007). This survey results in a catalogue of 1123 radio-emitting sources above the threshold $> 50\,\mu$Jy.

Spectroscopic data: The AEGIS-XD field has been targetted by several spectroscopic surveys such as DEEP2 (Coil et al., 2004; Newman et al., 2013) and DEEP3 (Cooper

et al., 2011) using the DEIMOS instrument on Keck II. Another significant spectroscopic survey, with the MMT/Hectospec instrument, specifically targeted sources missed by DEEP2 (Coil et al., 2009). Additionally, the Canada-France Redshift Survey (CFRS, Lilly et al., 1995), the Sloan Digital Sky Survey (SDSS, Alam et al., 2015), and the Lyman Break Galaxy survey (LBG[1], Steidel et al., 2003) obtained spectra for a handful of sources each.

2.2.3 CDFS

The *Chandra* Deep Field South (CDFS) is the deepest X-ray survey to date and has been extensively covered in a variety of wavebands (Guo et al., 2013). Centred at $\alpha_{\rm J2000} = 03^{\rm h}32^{\rm m}28^{\rm s}.27$, $\delta_{\rm J2000} = -27°48'21''.8$, CDFS covers an area of 484 arcmin^2. It benefits from a very low galactic absorption ($N_{\rm H} \approx 8 \times 10^{19}\,{\rm cm}^{-2}$), the absence of bright stars ($m_v = 14$) and the possibility to be observed by southern observatories such as VLT or Gemini.

X-ray: The X-ray data of CDFS consists of 102 overlapping *Chandra* observations accumulating a total of 6.727 Ms of exposure time. These observations were taken during 4 separate epochs: between 1999 and 2000 for the 1 Ms CDFS (Giacconi et al., 2002), in 2007 for the 2 Ms CDFS (Luo et al., 2008), in 2010 for the 4 Ms CDFS (Xue et al., 2011), and between 2014 and 2016 for the 7 Ms CDFS (Luo et al., 2017). The 102 observations were taken by the ACIS-I instrument in very faint mode, with the exception of 10 early observations in faint mode. Different roll angles around the central point were employed to homogenise the sensitivity across the field and reduce CCD gap effects. Figure 2.7 illustrates the effective-exposure map of CDFS, with a nearly uniform circular central region. Overall, the 7 Ms CDFS observations achieved an average flux limit in the soft (0.5-2 keV) and hard (2-7 keV) bands of $6.4\times10^{-18}\,{\rm erg\,cm^{-2}\,s^{-1}}$ and $2.7\times10^{-17}\,{\rm erg\,cm^{-2}\,s^{-1}}$, respectively.

The *XMM-Newton* telescope has also surveyed CDFS, for a nominal exposure time

[1]Photons below the Lyman continuum at 912Å are absorbed by hydrogen gas, forming a so-called Lyman break in the source spectrum. At $z \sim 3$, this break falls between the U and B optical filters, leading to a characteristic photometric difference between these filters used by the LBG survey to target galaxies in that redshift range.

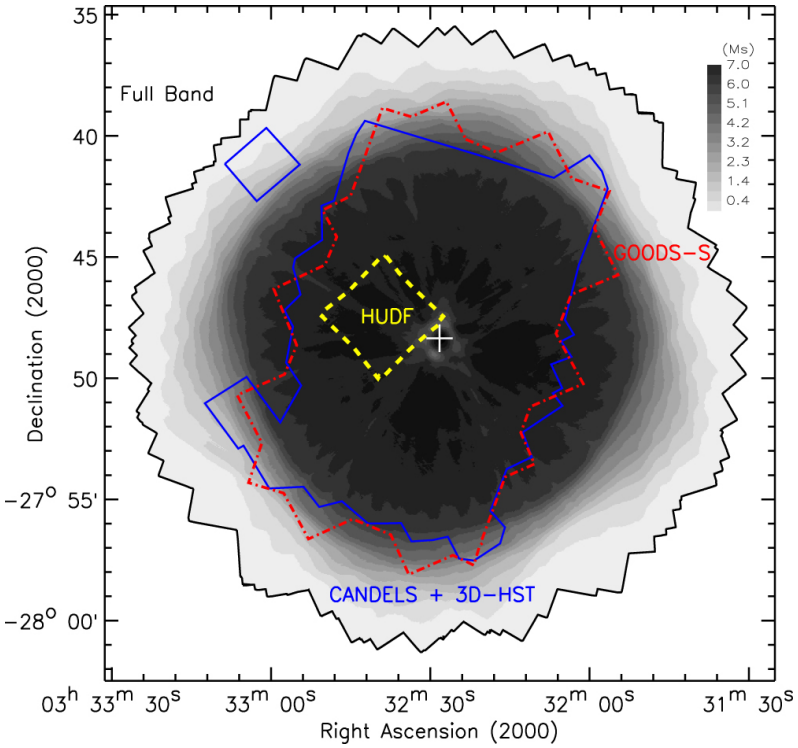

Figure 2.7: CDFS full-band effective-exposure map indicated by the linear grey scale bar in Ms. The deep optical coverage regions are also indicated: in *solid blue*, the CANDELS+3D-*HST* survey (Skelton et al., 2014), in *red dash-dotted*, the GOODS-S (Grogin et al., 2011) and in *yellow dashed*, the HUDF (Beckwith et al., 2006). Figure from Luo et al. (2017).

of 3.45 Ms (Ranalli et al., 2013). The primary aim of this survey is the discovery of obscured AGN, notably CTK systems, as the effective area above $\gtrsim 5$ keV drops less sharply compared to *Chandra*'s. However, *XMM* suffers from a larger PSF that leads to source confusion, and a higher instrumental background that makes it less suitable for faint fluxes sources. With approximately ∼3 Ms exposure time, the average flux limit of *XMM*-CDFS in the 2-10 keV band is 1.8×10^{-15} erg cm^{-2} s^{-1}. For these reasons, in Chapter 4 of this thesis, we exclusively analyse *Chandra*'s X-ray data. More specifically, as the multi-wavelength counterpart identification was based on the 4 Ms CDFS observations (Xue et al., 2011), the X-ray source detection was conducted on this data (§2.3.1), while the X-ray spectral extraction (§2.4.1) and analysis (§2.4.2) benefits from the deeper 7 Ms CDFS observations (Luo et al., 2017).

UV/Optical: *GALEX* (Martin et al., 2005) provided the UV photometry in the far-UV (1350-1750 Å) and near-UV (1750-2800 Å) bands in the CDFS field. For the *U* band,

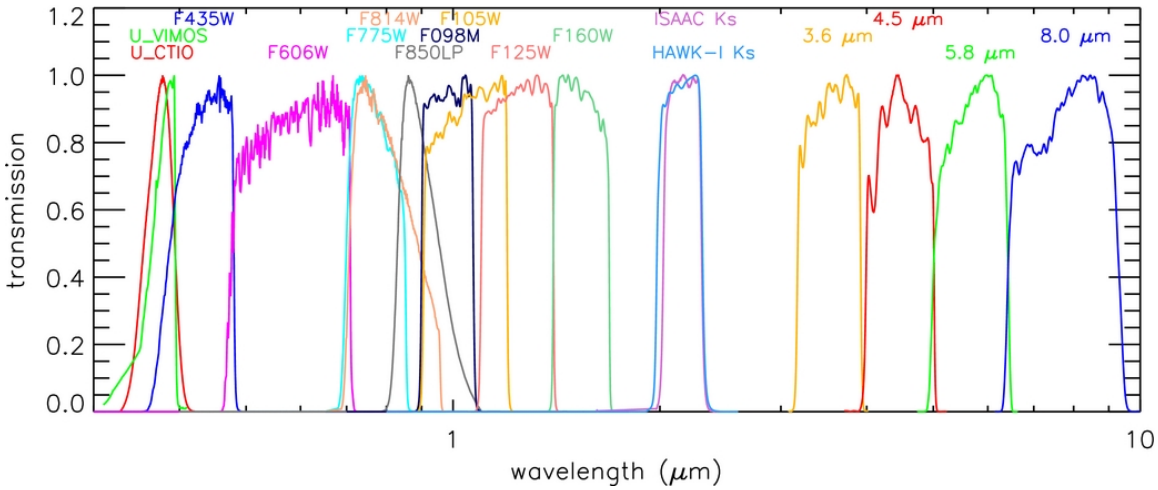

Figure 2.8: Transmission curves of the various photometry bands in CDFS, normalised to 1. Figure from Guo et al. (2013).

as shown in Figure 2.8, the photometric data originated from both the CTIO instrument on the Blanco telescope and VIMOS on VLT. In the optical, the photometry was collected by the *HST*/ACS in the $F435W$, $F606W$, $F775W$, $F814W$ bands and by *HST*/WFC3 in the $F105W$, $F125W$, $F160W$ bands as part of the GOOD-S surveys (Grogin et al., 2011; Koekemoer et al., 2011) and CANDELS+3D-*HST* (Skelton et al., 2014) (respectively, *red dashed* and *blue solid* regions in Figure 2.7). Additionally, the Hubble Ultra Deep Field survey (HUDF, Beckwith et al., 2006), using *HST*/WFC3, covers a small area of CDFS (*yellow dashed* region in Figure 2.7). However, as shown in Figure 2.7, these optical surveys do not cover the entire CDFS field and sources located outside of these regions benefit from the photometry in the V, R, I, and Z bands obtained by the Wild Field Imager (WFI, Arnouts et al., 2001) on the ESO-MPG 2.2m telescope.

Near-to-far-IR: The K_S band was collected by the Infrared Spectrometer and Array Camera (ISAAC) and the High Acuity Wide field K-band Imager (HAWK-I) on the VLT (Guo et al., 2013). Moreover, the Taiwan ECDFS Near-Infrared Survey (TENIS, Hsieh et al., 2012) obtained deep photometry in the J and K_S bands using the WIRCam instrument on CFHT. Additionally, the SEDS survey (Ashby et al., 2013) provides the photometry in the four *Spitzer*/IRAC channels: 3.6, 4.5, 5.8, and 8.0 μm. Finally, the central region of CDFS benefits from far-IR photometry, compiled in Elbaz et al. (2011) and obtained using *Herschel*/PACS bands at 100 μm and 160 μm as part of the PEP survey (Lutz et al., 2011), along with *Herschel*/SPIRE at 250 μm, 350 μm and 500 μm

within the HerMES mission (Oliver et al., 2012).

Radio: The radio observations of CDFS were carried out by the VLA at 1.4 GHz (Miller et al., 2013). It covers a third of a square degree and reaches a sensitivity of 6.4 μJy per beam. Additionally, the Australia Telescope Large Area Survey (ATLAS, Mao et al., 2012) observed CDFS at 1.4 GHz for 173 hours, reaching a uniform sensitivity of 10 μJy per beam.

Spectroscopic data: Due to the great X-ray depth of the CDFS and the large multi-wavelength coverage, several follow-up spectroscopic surveys targeted CDFS sources, providing spectroscopic redshift estimations for numerous sources. For instance, in 7 Ms CDFS, Luo et al. (2017) reported the spectroscopic redshifts for 653 out of 986 sources ($\sim$ 66%). More details on the redshift estimation are provided in §2.3.3. Optical and near-IR spectra were notably collected by FORS1/FORS2 instruments on VLT (Szokoly et al., 2004; Mignoli et al., 2005; Vanzella et al., 2008; Kurk et al., 2013), DEIMOS on KECK (Doherty et al., 2005; Silverman et al., 2010), VIMOS on VLT (Ravikumar et al., 2007; Balestra et al., 2010; Silverman et al., 2010; Le Fèvre et al., 2013; Tasca et al., 2017), Gemini Near-InfraRed Spectrograph (GNIRS, Kriek et al., 2008), IMACS on the Magellan telescope (Treister et al., 2009; Cooper et al., 2012), LDSS3 on the Magellan telescope (Xia et al., 2011), ISAAC on VLT (Casey et al., 2011), AAOmega on the Anglo-Australian Telescope (AAT, Mao et al., 2012) and WFC3/G141 grism on *HST* (Morris et al., 2015).

2.3 Preliminary Data Processing Methodology

In this Section, I present the methodologies employed to combine consistently the various multi-wavelength catalogues presented in Section 2.2 to produce for each survey a unique catalogue of X-ray detected sources with their multi-wavelength photometry. The first step is the X-ray source detection (§2.3.1), followed by the optical counterpart identification of these sources (§2.3.2), complemented by spectroscopic or photometric redshift information (§2.3.3).

2.3.1 X-ray Source Detection

In this thesis, for the three deep extragalactic fields (COSMOS-Legacy, (Civano et al., 2016), AEGIS-XD (Nandra et al., 2015), 4 Ms CDFS (Xue et al., 2011)), we use custom X-ray source catalogues constructed following the aperture-based source detection methodology described in Laird et al. (2009) and Nandra et al. (2015), itself an improvement of Nandra et al. (2005); Laird et al. (2006). This approach was notably designed for the AEGIS field, but later applied to the other two fields (Aird et al., 2017; Georgakakis et al., 2017b). The data reduction and source detection processes are performed using the *Chandra* Interactive Analysis of Observations software (CIAO, Fruscione et al., 2006).

For each observation, the raw event files are corrected to produce cleaned level-2 event files which are then used for source detection and spectral extraction. This cleaning consists first of removing the hot pixels and cosmic rays afterglow with the `run_hotpix_task` task. Then, the event files are corrected for Charge Transfer Inefficiency (CTI), i.e. the loss of charge in a CCD as it is shifted from one pixel to the next during readout. Additionally, the time-dependent gain of the ACIS CCDs is accounted for. Moreover, the ACIS pixel randomisation is removed and replaced by the PHA randomisation to correct for an aliasing problem affecting the spectra of sources with a large number of counts. Besides, if the data was collected in very faint mode, the ACIS particle background cleaning algorithm is applied to remove bad events most likely associated with cosmic rays. Finally, the periods of high background are removed using the background light curves following the approach of Nandra et al. (2007). These background flares are due to the observation of areas with high densities of charged particles depositing their energy on the detectors and being registered as real events, impacting the efficiency of the source detection. Using the cleaned event files, images are created in the 4 energy bands referred to as full (0.5-7 keV), soft (0.5-2 keV), hard (2-7 keV) and ultrahard (4-7 keV) bands. The corresponding exposure maps are produced using the `merge_all` task, accounting for telescope and instrument efficiencies as well as chip gaps and dithering. Lastly, the multiple overlapping observations are co-added along with their respective exposure maps to produce the stacked X-ray image of each field.

For accurate source detection, a good knowledge of the Point Spread Function (PSF) is needed. Laird et al. (2009) advocates for the use of the MARX ray-tracer simulator

(Davis et al., 2012) to generate PSF lookup tables by simulating the PSF for different Encircled Energy Fractions (EEF) values in a 10-pixel-spaced grid covering the ACIS-I detectors. At each position, an image PSF is created using 200 000 input rays with a 1 keV energy for the soft band. As elliptical apertures are best suited to describe PSFs, the semi-minor axis value and orientation are determined for increasing semi-major axis values at each position. The counts extracted from the elliptical aperture are then divided by the total counts over the entire detector to compute the EEF. The ellipse parameters are then interpolated at specific EEF values (50, 60, 70, 80, 90 and 95%) and stored in look-up tables. This process is repeated for the other energy bands using different monochromatic energies: 2.5 kev, 4 kev, 5.5 kev to represent the full, hard and ultrahard bands, respectively.

The initial source candidate list is constructed using the CIAO wavelet-detection algorithm `wavdetect` with different wavelet scales. This algorithm is applied to the entire survey area with at least 10% of the maximum field exposure time. The low significance threshold, set to 10^{-4}, is likely to select a large fraction of spurious sources but not to miss real sources. Given the multiple observations, each source candidate has multiple positions on the detector. Therefore, the PSF look-up tables are used to generate an exposure time-weighted PSF for each candidate. Following Nandra et al. (2005), an aperture with a radius corresponding to the 70% EEF of the weighted PSF is used to extract the source counts and effective exposure of the candidate. The background counts are then extracted within an annulus with an inner radius 1.5 times larger than the 95% EEF radius and a 100-pixel width. The background counts are then scaled by the ratios of the source and background areas and average exposure times. For each source and energy band, the extracted counts from the source and the background are used to determine the Poisson false probability. It corresponds to the probability that the observed source counts are generated by random background fluctuations and is defined as:

$$\mathcal{P}(\geq S|B) = 1 - \sum_{n=0}^{S-1} \frac{B^n\, e^{-B}}{n!} \tag{2.1}$$

with S the photon counts in the aperture and B the scaled background counts. Sources with false detection probability below a $\mathcal{P}(\geq S|B) < 4 \times 10^{-6}$ threshold are considered

Table 2.1: Number of sources per energy band for each deep field (COSMOS-Legacy, AEGIS, CDFS).

Field	Full 0.5-7 keV	Soft 0.5-2 keV	Hard 2-7 keV	Ultra-Hard 4-7 keV	Any Band
COSMOS	3372	2772	2140	971	3627
AEGIS	859	732	574	298	937
CDFS	490	472	326	195	569
Total	4721	3976	3040	1464	5133

real. However, statistically non-significant sources should be part of the background estimation, therefore, the source detection process is reiterated by only considering as candidates the statistically significant sources of the first iteration. Sources below the 4×10^{-6} Poisson false-detection threshold at the second iteration are considered genuine.

For each field, the source catalogues of the four energy bands (Full, Soft, Hard, Ultra-hard) are then merged by position to produce a single source catalogue containing all sources detected in at least one of the energy bands. Across the three different fields, there are 5133 detected sources: 3627 in COSMOS-Legacy, 937 in AEGIS and 569 in 4 Ms CDFS. The number of sources detected in each band and survey is indicated in Table 2.1.

Additionally, thanks to this aperture-based source detection methodology, the minimum counts required for detecting a source can be accurately measured across the three fields. By normalising the minimum counts by the exposure time, sensitivity maps can be generated, indicating the minimum count rate (defined as the number of counts per second) for a source to be detected as a function of its position (Georgakakis et al., 2008). By integrating the sensitivity maps for each field, the area that is sensitive to a given X-ray photon count rate can be determined as illustrated in Figure 2.9 for the full band (0.5-7 keV). The total sensitivity curve (*black dashed line*) is the sum of the sensitivity curves from the individual surveys. While COSMOS-Legacy has a significantly larger sensitivity area at higher count rates, CDFS is sensitive to lower count-rate sources. In Chapters 3 and 4, these sensitivity maps are crucial to extrapolate the intrinsic AGN population from the observed sample.

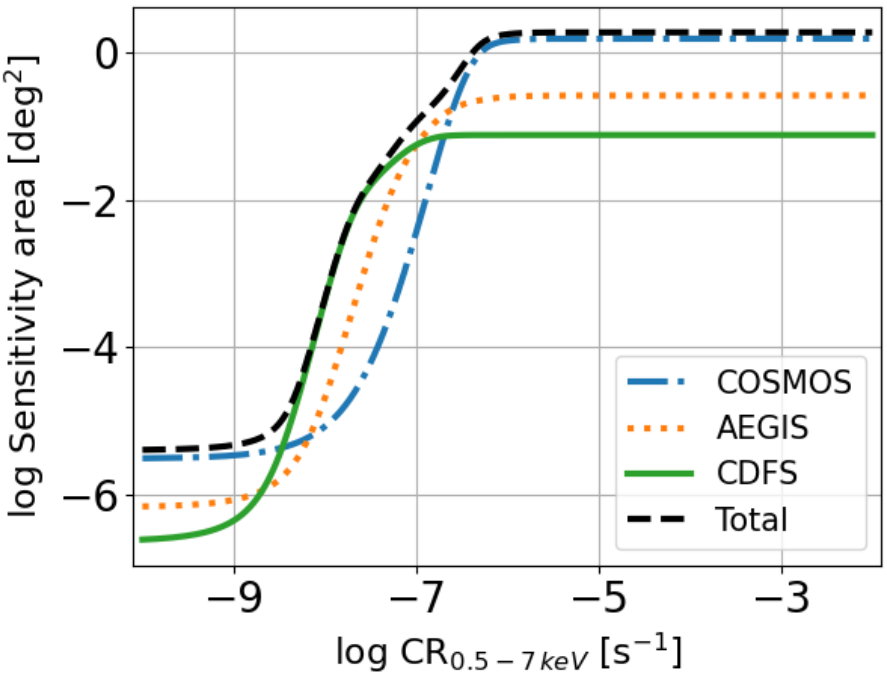

Figure 2.9: Sensitivity curve as a function of count rate in the full band (0.5–7 keV) for the COSMOS-Legacy (*dash-dotted blue*), AEGIS-XD (*dotted orange*) and CDFS (*solid green*) surveys. The total sensitivity area for the three fields is shown with the *dashed black curve*.

2.3.2 Optical Counterpart Identification

The multi-wavelength counterpart identification for the X-ray-detected sources in the COSMOS-Legacy, AEGIS and CDFS fields is presented in Aird et al. (2017), using the Likelihood Ratio method (*LR*, Sutherland & Saunders, 1992; Ciliegi et al., 2003; Brusa et al., 2005, 2007; Luo et al., 2010). Due to X-ray positional errors and the high density of faint sources in optical-to-near-IR catalogues, traditional methods that rely solely on spatial proximity to associate X-ray sources with multi-wavelength counterparts result in a high fraction of false identifications, especially in the faint regime. To address this, the *LR* approach considers both the angular separation between the X-ray source and its potential counterpart and the magnitude of this counterpart relative to the background magnitude distribution. The *LR* is defined as the ratio of the probability of a candidate being a true counterpart to the probability of it being a spurious association. It is defined as:

$$LR = \frac{q(m)\, f(r)}{n(m)} \tag{2.2}$$

where $q(m)$ is the expected probability distribution of the real counterparts as a function of the magnitude m, $f(r)$ is the probability distribution function of the angular separation r, and $n(m)$ is the surface density of background sources as a function of the magnitude m.

Assuming that the positional errors of both the optical-IR and the X-ray observations follow a Gaussian distribution with standard deviations $\sigma_{\rm o}$ and $\sigma_{\rm X}$, respectively, then, following Ciliegi et al. (2003), the probability distribution of the angular separation is computed as:

$$f(r) = \frac{1}{2\pi\sigma^2}\exp\left(\frac{-\mathrm{r}^2}{2\sigma^2}\right) \tag{2.3}$$

with $\sigma = \sqrt{\sigma_{\rm o}^2 + \sigma_{\rm X}^2}$. $\sigma_{\rm X}$ is provided by the X-ray catalogue and notably increases with decreasing X-ray photon counts of the source, while $\sigma_{\rm o}$ can either be provided by the multi-wavelength catalogue or computed by matching within a specific waveband.

The background source surface density $n(m)$ corresponds to the distribution of sources within the optical-IR catalogue located between $5''$ and $30''$ from any X-ray source, normalised by the surface area, as a function of the magnitude.

The magnitude distribution of the real counterparts $q(m)$ is iteratively determined using the following steps:

1. **Initial magnitude distribution:** The magnitude distribution of all the counterpart candidates within $1''$ of any X-ray source is denoted total(m). The number of candidate sources in this sample is N_1. The *solid line histogram* in Figure 2.10 illustrates total(m), derived in the CDFS field (Luo et al., 2010) but using a different photometric catalogue, the GEMS z-band catalogue (Caldwell et al., 2008).

2. **Real counterpart distribution:** The magnitude distribution of real candidates is calculated by subtracting the expected background sources from the initial counterpart distribution:

$$\mathrm{real}(m) = \mathrm{total}(m) - \pi r_0^2 N_{\rm X} n(m) \tag{2.4}$$

where $N_{\rm X}$ is the total number of X-ray sources and r_0 is the matching radius fixed to $1''$. Figure 2.10 illustrates total(m) with a *solid line* and $\pi r_0^2 N_{\rm X} n(m)$ with a *dashed*

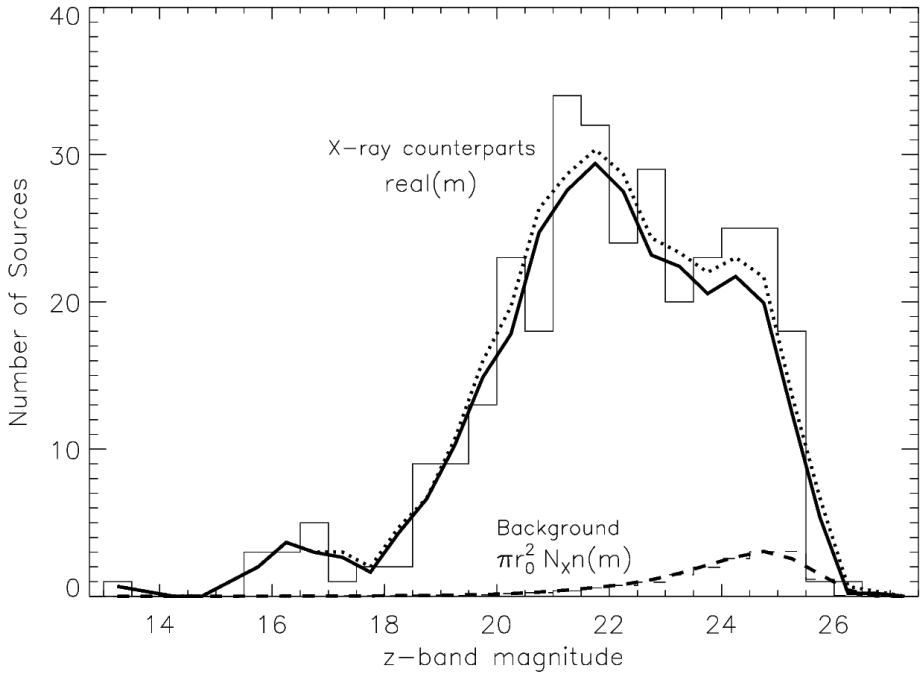

Figure 2.10: Example of magnitude distribution in the z-band for the GEMS catalogue (Caldwell et al., 2008) used in Luo et al. (2010) to compute the likelihood ratio for the CDFS X-ray sources. The *solid line histogram* represents total(m) in the first iteration, i.e. all sources within 1″ radius from any X-ray source, while the *dashed line histogram* corresponds to the surface density of the background sources $n(m)$ scaled by the area $\pi r_0^2 N_{\rm X}$. The *thick solid* and *dotted lines* correspond to the smoothed distribution of real(m) and $\pi r_0^2 N_{\rm X} n(m)$ respectively. The *thick dotted line* represents the final magnitude distribution of the counterparts after three iterations. Figure from Luo et al. (2010).

line for the GEMS catalogue in CDFS.

3. **Normalisation:** The expected magnitude distribution of real counterparts $q(m)$ is then normalised and multiplied by the expected fraction of X-ray sources with detected optical counterpart $\mathcal{Q}$:

$$q(m) = \frac{\text{real}(m)}{\sum_m \text{real}(m)} \cdot \mathcal{Q} \tag{2.5}$$

with $\mathcal{Q}$ initially defined as $\mathcal{Q} = N_1/N_{\rm X}$.

4. **Computing *LR*:** With $q(m)$, $f(r)$ and $n(m)$, LR is computed for each candidate counterpart within 5″ radius of any X-ray source.

5. **Selecting the real counterparts**: A LR threshold value $L_{\rm th}$ is established. A

candidate counterpart is considered real if its likelihood exceeds $LR > L_{\rm th}$. In the case of an X-ray source with multiple counterparts above this threshold, the one with the highest LR is considered as the only real counterpart.

6. **Calculating the reliability:** For each real counterpart, the reliability parameter R_c is computed as:

$$R_c = \frac{LR}{(1 - \mathcal{Q}) + \sum LR} \tag{2.6}$$

This parameter represents the probability that a given counterpart is correctly identified.

7. **Optimising reliability and completeness:** The threshold $L_{\rm th}$ is adjusted to maximise the sum of the completeness parameter C and the average reliability parameter R, which are respectively defined as $C = \sum R_c/N_{\rm X}$ and $R = <R_c>$.

This iterative process is repeated but with real(m) defined as the magnitude distribution of the real candidates defined in the previous iteration and with $\mathcal{Q}$ set to the completeness parameter value C of the previous iteration. The final real counterpart sample is defined by convergence after a few iterations. In Figure 2.10, using the GEMS catalogue, the final counterpart magnitude distribution of the X-ray sources in CDFS is displayed by the *dotted line* Luo et al. (2010).

For the X-ray detected sources within CDFS, the multi-wavelength photometry used for the LR-based counterpart identification and SED fitting analysis in Chapter 4 is presented by Hsu et al. (2014)[2], while for the AEGIS field, the multi-wavelength photometric catalogue is described by Barro et al. (2011) and publicly available through the *Rainbow* Cosmological Surveys Database[3](Pérez-González et al., 2005, 2008; Barro et al., 2011). For the COSMOS field, multi-wavelength counterparts are identified by applying the LR methodology in the COSMOS Intermediate and Broad Band Photometry Catalogue 2008[4] (Capak et al., 2007) and the S-COSMOS 3.6 μm-based catalogue[5] (Sanders et al., 2007). However, in Chapter 3, when we aim to constrain the torus IR luminosity, the

[2]https://www.mpe.mpg.de/XraySurveys/CDFS/
[3]https://arcoirix.cab.inta-csic.es/Rainbow_Database/Home.html
[4]http://irsa.ipac.caltech.edu/data/COSMOS/datasets.html
[5]https://irsa.ipac.caltech.edu/data/SPITZER/S-COSMOS/

Table 2.2: Number and fraction of sources with reliable spectroscopic measurement, photometric estimates or no redshift estimations for each of the three *Chandra* deep fields.

Survey	COSMOS	AEGIS-XD	CDFS	All
z-spec	1917 (52.9%)	364 (38.7%)	361 (63.4%)	2642 (51.4 %)
z-phot	1593 (43.9%)	573 (61.8%)	200 (35.1%)	2366 (46.1 %)
no z estimate	117 (3.2%)	0 (0%)	8 (1.4%)	125 (2.4 %)
Total	3627	937	569	5133

far-IR photometry from the super-deblended catalogue (Jin et al., 2018) is necessary. As optical and IR positional errors are very small, instead of using the LR approach, the counterparts in the Jin et al. (2018) catalogue are identified by simply cross-matching the position of the optical counterparts of our X-ray sources with the positions of the sources in this catalogue. Since the Jin et al. (2018) catalogue was constructed from the COSMOS2015 catalogue (Laigle et al., 2016), we also use COSMOS2015 photometry at shorter wavelengths in Chapter 3. In contrast, in Chapter 4, our objective is to constrain the stellar mass of the host galaxies for which far-IR photometry is not required. Thus, we employ the same photometric catalogue used for the LR-based counterpart identification and photometric redshift estimation (Capak et al., 2007; Sanders et al., 2007).

2.3.3 Redshift Estimation

As discussed in Section 2.2, the *Chandra* COSMOS-Legacy, AEGIS-XD and CDFS deep extragalactic fields benefit from extensive multi-wavelength data, allowing photometric redshift estimations, complemented by various spectroscopic surveys providing secure spectroscopic redshift measurements. The compilation of redshifts for the X-ray-detected sources in the three deep fields is presented in Georgakakis et al. (2017b). As indicated in Table 2.2, 51.4% of these sources have reliable spectroscopic redshifts, 46.1% have photometric redshifts, and only 2.4% do not have redshift estimations, mostly due to the lack of reliable optical counterparts.

The number and fraction of sources with spectroscopic redshift for each of the three fields are shown on the first row of Table 2.2. Of the 3627 X-ray-detected sources in COSMOS-Legacy, 1994 have spectroscopic redshifts, with 1917 being reliable according to the zCOSMOS redshift classification with a confidence ≥ 3 (Lilly et al., 2007). Most of the spectroscopic redshift measurements were provided by the COSMOS-Legacy field

Table 2.3: Spectroscopic compilations in the COSMOS-Legacy field with the corresponding number of available spectra and reliable spectroscopic redshift measurements.

Survey	Reference	Number spectra	Number reliable z-spec
COSMOS-Legacy	Marchesi et al. (2016a)	1875	1805
XMM-COSMOS	Brusa et al. (2007)	42	42
C-COSMOS	Civano et al. (2012)	20	20
zCOSMOS	Lilly et al. (2007)	24	17
PRIMUS	Coil et al. (2011)	12	12
SDSS	Alam et al. (2015)	7	7
MOSDEF	Kriek et al. (2015)	5	5
3DHST (Grism)	Momcheva et al. (2016)	7	7
3DHST	Skelton et al. (2014)	1	1
VUDS	Le Fèvre et al. (2015)	1	1
Total	-	1994	1917

counterpart catalogue by Marchesi et al. (2016a), while the remaining spectroscopic redshifts originate from various compilations listed in Table 2.3. In AEGIS, the spectroscopic redshifts presented by Nandra et al. (2015), are mainly obtained from DEEP2 and DEEP3 (Davis et al., 2003; Cooper et al., 2011, 2012; Newman et al., 2013) with the Keck telescope, complemented notably by a campaign using the MMT/Hectospec instrument (Coil et al., 2009). As presented in Table 2.4, a few spectroscopic redshifts originate from SDSS (Alam et al., 2015) and LBG (Steidel et al., 2003). Out of 937 X-ray sources in AEGIS, 472 have spectra, with 364 yielding reliable redshift estimates. In CDFS, the spectroscopic redshifts are compiled by Hsu et al. (2014), collected from various surveys (Le Fèvre et al., 2004; Szokoly et al., 2004; Zheng et al., 2004; Mignoli et al., 2005; Ravikumar et al., 2007; Vanzella et al., 2008; Popesso et al., 2009; Treister et al., 2009; Balestra et al., 2010; Silverman et al., 2010). This extensive number of spectroscopic surveys gives CDFS the highest spectroscopic redshift completeness among the three fields, with 63.4% of the sources having a reliable spectroscopic redshift measurement.

The photometric redshift estimations in the three fields are carried out using the methodology specifically developed for X-ray AGN by Salvato et al. (2009, 2011). This approach, originally designed for the *XMM*-COSMOS survey, takes into account several physical properties of the sources, including optical variability and morphology, as well as X-ray flux. Figure 2.11 shows the flow chart illustrating this procedure (Salvato et al., 2011). The first step is to measure the optical variability of the sources using

Table 2.4: Spectroscopic compilations in the AEGIS-XD field with the corresponding number of available spectra and reliable spectroscopic redshift measurements.

Survey	Reference	Number spectra	Number reliable z-spec
DEEP2 / DEEP3	Newman et al. (2013) / Cooper et al. (2011)	349	257
MMT	Coil et al. (2009)	111	95
SDSS	Alam et al. (2015)	6	6
LBG	Steidel et al. (2003)	6	6
Total	-	465	364

the multiple optical surveys covering the COSMOS field at different epochs over several years. The average variability of the individual sources is then estimated and subtracted to obtain variability-corrected photometry. Variability correction is essential when the photometry from different bands is collected at different times over a period of years. The second step is to determine the optical morphology of the sources using *HST*/ACS observations, identifying whether they are point-like or extended. All point-like and/or variable sources are considered AGN-dominated, forming the *QSOV* subgroup. Extended non-variable sources belong to the *EXTNV* subgroup, which is then divided into two subclasses based on their X-ray flux in the 0.5-10 keV band: galaxy-dominated sources below $F_{0.5-2\,\mathrm{keV}} < 8{\times}10^{-15}\,\mathrm{erg\,s^{-1}}$ and AGN-dominated above this flux threshold. To minimise redshift-luminosity degeneracies, Salvato et al. (2009) applies absolute magnitude priors to the different subgroups: $-30 < M_B < -20$ for *QSOV* sources and $-24 < M_B < -8$ for *EXTNV* sources. To estimate the redshift probability distribution for each source, the variability-corrected photometry and morphology-based magnitude priors are fed into the LePhare χ^2 template-fitting code (Arnouts et al., 1999; Ilbert et al., 2006). The accuracy of the photometric redshift estimates is assessed by comparing them to spectroscopic redshifts, computing the Normalized Median Absolute Deviation ($\sigma_{\mathrm{NMAD}} = 1.48{\times}\mathrm{median}(|z_{\mathrm{phot}} - z_{\mathrm{spec}}|/(1 + z_{\mathrm{spec}}))$, Hoaglin et al., 1983) and determining the fraction of outliers, i.e. sources with $|z_{\mathrm{phot}} - z_{\mathrm{spec}}|/(1 + z_{\mathrm{spec}}) > 0.15$. Using this approach on a training sample, Salvato et al. (2009) fine-tune the magnitude prior boundaries and define a library of SED templates for AGN-dominated sources. This template library is designed to reproduce a comprehensive range of SEDs, while minimising degeneracies and catastrophic failures. The library notably includes AGN-galaxy hybrids

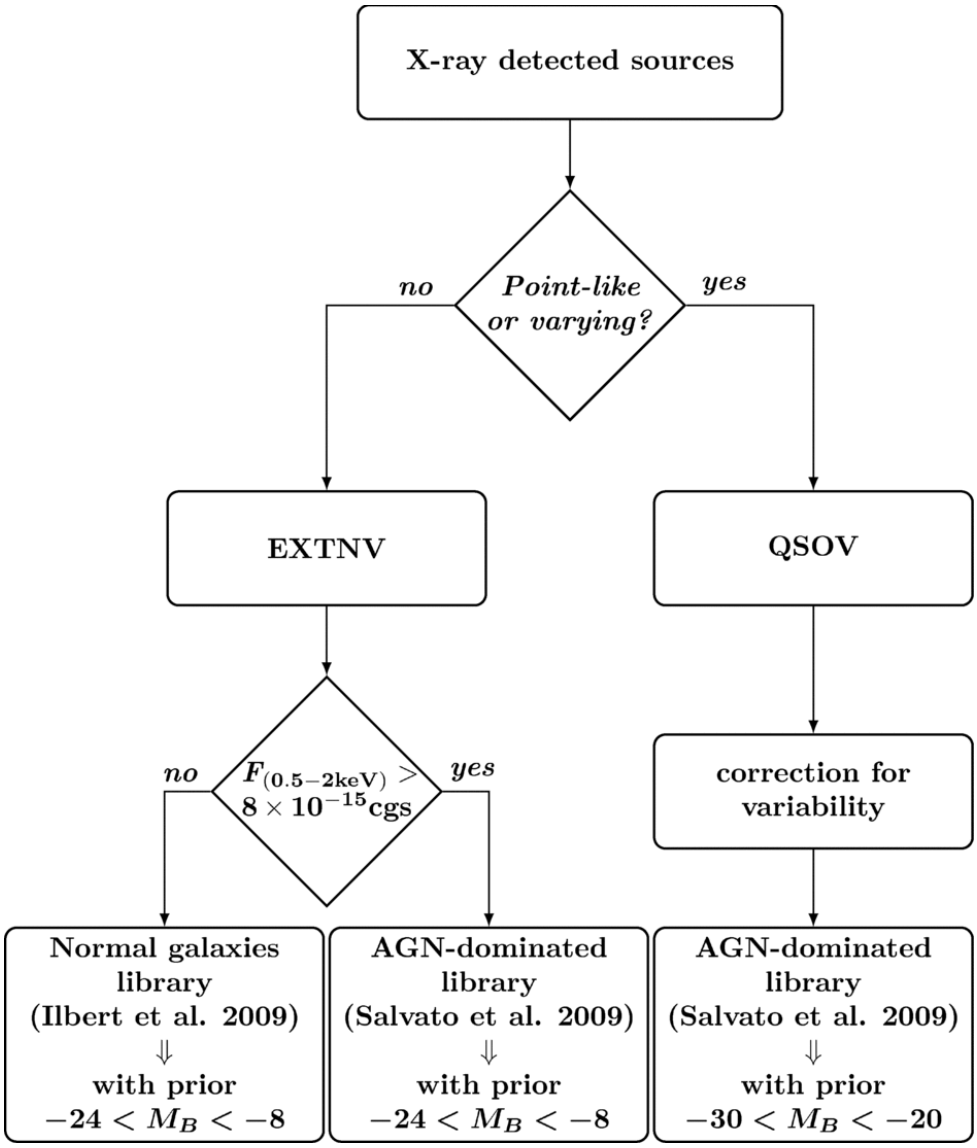

Figure 2.11: Flow chart of the procedure to determine the photometric redshift of AGN. Figure from Salvato et al. (2011).

by associating AGN and galaxy templates with varying relative normalisations. On the other hand, for galaxy-dominated sources, the photometric redshift estimation process employs the normal galaxy template library presented by Ilbert et al. (2009).

Using this methodology, the photometric redshift of sources in CDFS, AEGIS and COSMOS-Legacy are estimated and presented in Hsu et al. (2014), Nandra et al. (2015) and Marchesi et al. (2016a), respectively. Among these fields, only the COSMOS field provides enough multi-epoch optical photometry to allow for variability correction. As demonstrated in Salvato et al. (2009), this correction does not significantly affect σ_{NMAD}, but does lead to a twofold decrease in the fraction of outliers within the *XMM*-COSMOS

Table 2.5: Photometric redshift accuracy showing the normalised median absolute deviation, the fraction of outliers for each survey. The redshift catalogue reference for each survey is also provided.

Survey	$\sigma_{\rm NMAD}$	$f_{\rm outliers}$	Reference
COSMOS-Legacy	0.03	$< 8\%$	Marchesi et al. (2016a)
C-COSMOS	0.045	14.2%	Aird et al. (2015)
AEGIS *QSOV*	0.063	8.0%	Nandra et al. (2015)
AEGIS *EXTNV*	0.033	3.6%	-
CDFS $z < 1.5$	0.014	4.34%	Hsu et al. (2014)
CDFS $z > 1.5$	0.012	9.65%	-

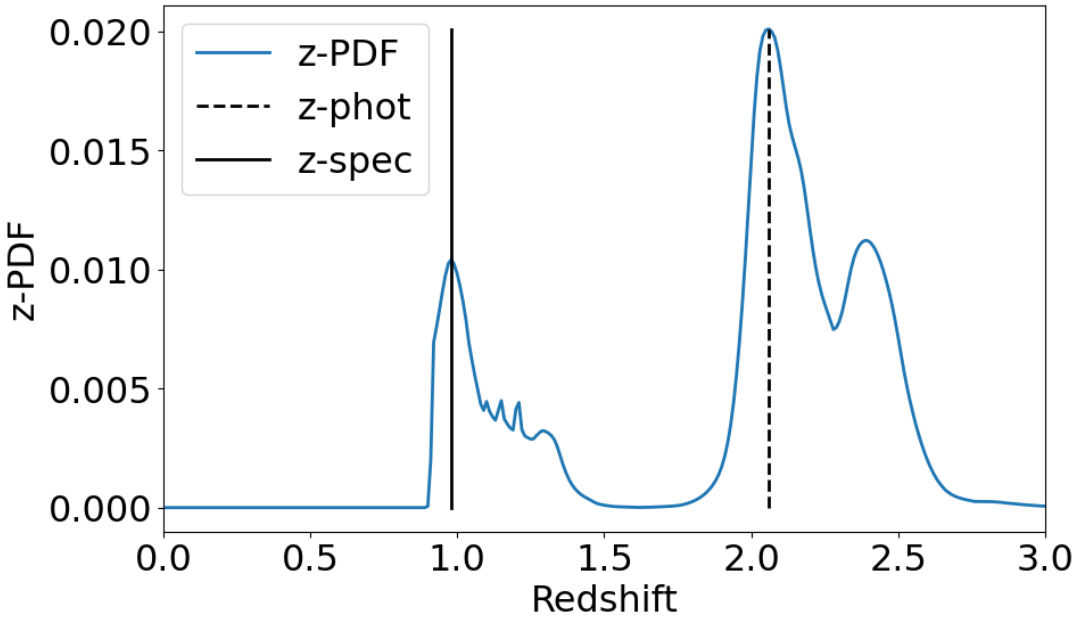

Figure 2.12: Example of photometric redshift PDF (*blue solid line*) showing two distinct peaks. While the best-fit photometric redshift (*black dashed line*) indicates $z_{\rm phot} = 2.058$, the spectroscopic redshift $z_{\rm spec} = 0.978$ is in better agreement with the secondary peak.

catalogue. Additionally, Hsu et al. (2014) construct new hybrid templates better reproducing the SED of faint X-ray sources, which are more numerous in the deeper CDFS. These templates are reused in Nandra et al. (2015) for the AEGIS field. Table 2.5 shows the photometric redshift accuracy and the fraction of outliers for each survey. Moreover, Nandra et al. (2015) find that most of the outliers have non-unique redshift solutions, with the correct redshift often appearing as a secondary peak in the redshift Probability Distribution Function (PDF) as shown as an example in Figure 2.12. This observation highlights the importance of using the full redshift PDF as it is done in this thesis (see §2.4.2 and §2.4.3).

In the COSMOS-Legacy field, for the X-ray sources that do not appear in the redshift catalogue of Marchesi et al. (2016a) due to a different source detection method, photometric redshifts are estimated using the methodology presented by Aird et al. (2015). The SED of these sources is fitted with the EaZY photo-z code (Brammer et al., 2008), which uses simultaneously galaxy and AGN templates. A key feature of the EaZY code is the inclusion of a template error function which accounts for the typical uncertainty of the templates as a function of the rest-frame wavelength and also reduces the impact of AGN-flux variability. The accuracy of this approach is also presented in Table 2.5, labelled as C-COSMOS. However, as the photometric redshift PDF is not available for these sources, a Cauchy distribution centred on the best-fit photometric redshift (Aird et al., 2015) is attributed. The absolute deviation of the Cauchy distribution is set according to the scatter of the difference between the spectroscopic and photometric redshifts in Marchesi et al. (2016a).

2.4 Advanced Data Analysis Methodology

In this Section, I describe the data analysis processes to constrain the physical parameters of the X-ray-detected sources within the catalogues built in Section 2.3 for each deep field (COSMOS, AEGIS-XD and CDFS). For each source, I extract (§2.4.1) and fit (§2.4.2) its X-ray spectrum, notably to measure the intrinsic X-ray luminosity and column density $N_{\rm H}$. Additionally, I use two different algorithms to fit the multi-wavelength SED to constrain the AGN IR luminosity or the stellar mass of the host galaxy (§2.4.3).

2.4.1 X-ray Spectra Extraction

The first step of the X-ray analysis is the extraction of the spectra of each of the sources detected in the three *Chandra* X-ray deep fields (§2.3.1). For that purpose, using CIAO 4.13 (Fruscione et al., 2006) routines, we develop an automated spectral extraction pipeline similar to the one described in Marchesi et al. (2016b) but modified to derive the optimal aperture maximising the Signal-to-Noise Ratio (SNR) of individual sources. The maximal SNR is particularly important to obtain robust constraints on the physical parameters for low photon count sources. Moreover, the extraction pipeline is designed to account for

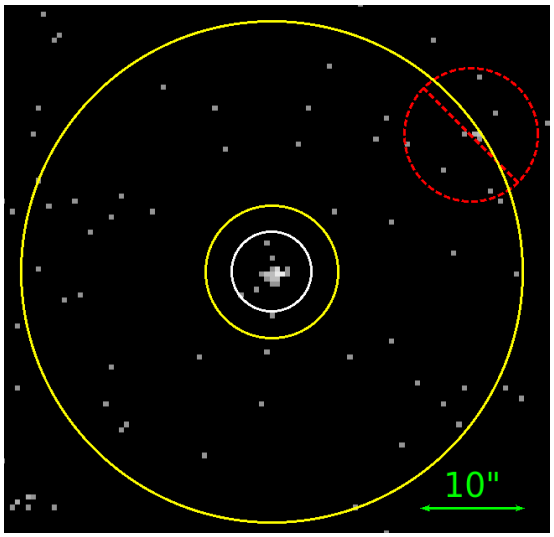

Figure 2.13: Example of a source and background X-ray spectral extraction regions for a radius set to EEF=70%. The source photon extraction region is represented by the *white circle* with a radius of 3.80 arcsec. The background photon extraction region is defined by the *yellow annulus* with an inner and outer radius of 6.30 and 23.80 arcsec, respectively. A nearby X-ray source partially overlaps with the background region in this example. The region around this source, indicated by the *barred red dashed circle* with a 6.34 arcsec radius, is masked out before extracting the background counts.

the multiple overlapping observations of each field.

This extraction pipeline consists of using different aperture radii to extract the source and background photon counts in the full band (0.5-10 keV) and test which aperture maximises the SNR. As described in the source identification Section 2.3.1, the 50, 60, 70, 80, 90, 95% EEF radius parametrising the aperture is provided for each source. For each EEF value, the source and background photons, C_S and C_B, respectively, are extracted from the stacked image as illustrated in Figure 2.13. The source photons are extracted from a circular region centred on the source position with the given EEF radius (*white circle* in Figure 2.13). The extraction region of the background photons is an annulus, also centred on the source position, with inner and outer radii that are respectively 2.5″ and 20″ larger than the extraction radius of the source's X-ray spectrum (*yellow annulus* in Figure 2.13). Any X-ray sources within the background region are masked out by excluding photons that lie within the selected EEF radius plus 2.5 arcsec (*barred red dashed circle* in Figure 2.13). Additionally, the outer radius may be progressively expanded until the background region contains at least 100 photon counts.

Once the source and background photon counts are computed for each EEF value, we

calculate the SNR as follows

$$\mathrm{SNR} = \frac{C_S - C_B \cdot R}{\sqrt{C_S + C_B \cdot R^2}}\,, \tag{2.7}$$

where R is the ratio between the areas of the source and background extraction regions. The number of counts is obtained using the `dmextract` and `get_counts` tasks of CIAO. The aperture radius that maximises the SNR in the full band is used to define the source and background extraction regions.

The extraction regions of a given source are fed into the `specextract` task to extract the source and background spectra from each *Chandra*/ACIS-I observation that overlaps with the position of interest. The same task also generates the corresponding Auxiliary Response Files (ARF) and Redistribution Matrix Files (RMF). The ARF represents the efficiency of a detector as a function of the energy averaged over time. It is the product of the effective area and quantum efficiency. The effective area measures the detector's spatial size which is sensitive to photons of a given energy. The quantum efficiency measures the fraction of the incident photons that are registered by the detector as a function of the energy. The RMF describes how the energy of an incident photon is redistributed to the energy channels of the detector because of the imperfect charge collection. The ARF and RMF calibration files are necessary for the X-ray spectral analysis. To obtain the final spectrum of a source, we combine the spectra extracted from the different observations by using the CIAO `combine_spectra` task. The source and background ARF and RMF calibration files are also combined by weighting by exposure time.

2.4.2 X-ray Spectroscopy

The fitting algorithm: BXA

In our X-ray spectroscopic analysis of the three *Chandra* deep fields, we fit the extracted X-ray spectra using the Bayesian X-ray Analysis (BXA) package presented by Buchner et al. (2014). We assume an observed X-ray spectrum, D, and a spectral model, M, described by a set of parameters, Θ. Within the Bayesian framework, the probability

$\mathcal{P}(\Theta|D, M)$ of the parameter set given the observation and the model is

$$\mathcal{P}(\Theta|D, M) = \frac{\Pi(\Theta|M)}{\mathcal{Z}(D|M)} \mathcal{L}(D|\Theta)\,, \tag{2.8}$$

where $\Pi(\Theta|M)$ is the prior knowledge of the parameter set for the chosen model, while the model evidence, $\mathcal{Z}(D|M)$ is the probability of obtaining the observed data given the model. As the model evidence is independent of the specific parameter set of the model, it is the suited value to compare different models. This is an important feature of the Bayesian analysis that allows the selection of the model that best represents the observations. The likelihood, $\mathcal{L}(D|\Theta)$, expresses the probability of obtaining the observed data for the set of model parameters. Fitting an X-ray spectrum usually involves the optimization of the likelihood to yield constraints on the spectral model parameters. However, nested sampling algorithms such as MLFriends (Buchner, 2014, 2019) adopt a different approach by exploring the entirety of the parameter space at once. These algorithms first draw parameter samples from the prior distribution and then iteratively replace the lowest likelihood points with new ones drawn from the prior with a higher likelihood. The posterior distribution is then constructed from the removed points weighted by their likelihood and the parameter space volume they represent. This type of algorithm is capable of exploring large parameter spaces without getting trapped in local minima, and the returned posterior distribution fully encapsulates the uncertainties of the parameter estimation. The BXA package is using the MLFriends algorithm powered by the UltraNest package (Buchner, 2021).

UltraNest accommodates any likelihood function. Nevertheless, given the typically low number of photon counts of the X-ray spectra, this work adopts a Poisson log-likelihood function often referred to as the CSTAT statistic (Cash, 1979):

$$\mathcal{L}_{\mathrm{CSTAT}} = 2 * \sum_i M'(i) - C(i)\left[\ln C(i) - \ln M'(i)\right]\,, \tag{2.9}$$

where $C(i)$ is the observed number of counts in the energy bin i and $M'(i)$ is the expected photon counts from the given model convolved with the RMF and multiplied by the ARF. The summation extends over all energy bins of the X-ray spectrum.

Given that the extracted X-ray spectra include contributions from both source and

background photons, employing a Poisson likelihood for X-ray spectral analysis necessitates modelling both components, i.e. including a model for both the source and background spectra. Therefore in Equations 2.8 and 2.9, the spectral model, M, is the sum of the source, $M_{\rm source}$, and background, $M_{\rm bkg}$, models. The parameter set Θ also includes the background model parameters.

The spectral model: UXCLUMPY

We choose to fit our *Chandra* observations using a physically-motivated X-ray spectral model that is built upon the current knowledge of the distribution of matter in the vicinity of a black hole (§1.3.4), and which describes the interaction of X-ray photons with the surrounding medium in a self-consistent way. Commonly used AGN-oriented physical X-ray spectral models include BNTORUS (Brightman & Nandra, 2011) and MYTORUS (Murphy & Yaqoob, 2009), both assuming a cylindrically-symmetric uniformly-distributed obscuring medium and describing the transmission of X-ray photons through it. However, as discussed in §1.3.4, several observational evidence from both X-ray (Risaliti et al., 2002; Esparza-Arredondo et al., 2021) and mid-infrared (Ramos Almeida et al., 2009, 2011) studies support the clumpiness of the torus. Hence, in this thesis, we opt for the UXCLUMPY torus model presented in Buchner et al. (2019).

As illustrated in Figure 2.14, the model features a central emitting source, i.e. the hot X-ray corona (§1.3.3), surrounded by a clumpy torus made of two types of obscuring clouds, small clouds distributed in a toroidal geometry and large clouds forming a ring on the equatorial plane. The small clouds are axisymmetrically dispersed, and their number decreases exponentially with the inclination towards the poles. This exponential distribution is characterised by the TORsigma parameter ranging from 0°, an infinitesimally thin torus, to 84°, almost a sphere, as depicted in the different columns of Figure 2.14. The radial distribution of the small clouds remains uniform over two orders of magnitude, with their radii distributed to reproduce the observed rate of the eclipsing events (Markowitz et al., 2014). The column density of each small cloud is drawn from a log-normal distribution with mean $10^{23}\,\mathrm{cm}^{-2}$ and a standard deviation of 1 dex. On the other hand, the large clouds are CTK and in contact with each other, forming a thick doughnut-shaped structure around the central engine. This ring of CTK absorbers is characterised by its

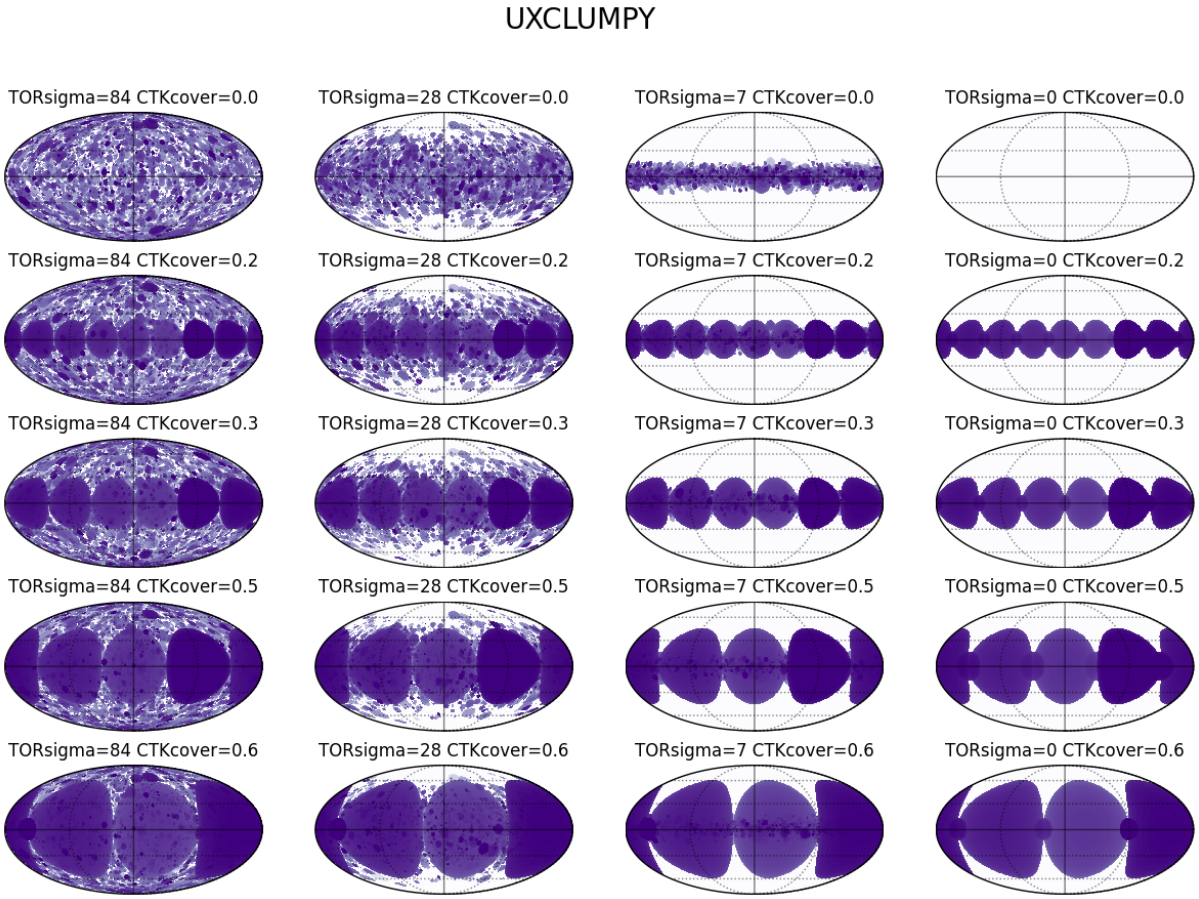

Figure 2.14: Projections of the column densities as seen from the central X-ray corona in the UXCLUMPY model. The column densities vary from $10^{20}\,\mathrm{cm}^{-2}$ to $10^{26}\,\mathrm{cm}^{-2}$, and higher column densities are represented in darker shades of blue. The different panels correspond to different TORSigma and CTKcover values as indicated. Figure from UXCLUMPY GitHub page.

covering factor, the CTKcover parameter. As illustrated in the different rows of Figure 2.14, CTKcover varies from 0, an infinitesimally thin equatorial disk, to 0.6, where the large equatorial CTK clouds cover 60% of the lines of sight.

Depending on both the source's physical properties and the obscurer's geometrical parameters, the UXCLUMPY X-ray spectra are generated using the radiative transfer code XARS (Buchner et al., 2019), which computes the transmission of the photons emitted by the source and interacting with its surrounding material. The escaping photons are then collected in different inclination bins representing the LOS towards the observer. The UXCLUMPY output spectra reproduce the different features of AGN X-ray emission described in Section §1.3.3 and depicted in Figure 1.11. A central source, the hot corona,

emits the X-ray photons with a power-law distribution with a high-energy cut-off: the unabsorbed X-ray continuum (Equation 1.11). Depending on their energy and the column density, emitted photons have a probability of escaping without interacting with the clumpy torus, constituting the transmitted component. The reflected component corresponds to the photons that have been scattered at least once by the obscuring material. The CTK ring is notably responsible for the Compton hump around 20-30 keV by reflecting the intrinsic AGN emission toward the observer without being absorbed by the rest of the clumpy torus. Additionally, XARS self-consistently simulates line fluorescence as photons interact with obscurers, primarily producing the strong FeKα complex emission line at ~ 6.4 keV.

In summary, our spectral modelling based on the UXCLUMPY implementation includes three main components: (i) the transmitted X-ray component, (ii) the reflected component, and (iii) the fluorescence emission lines. These components are combined into a single table model. Additionally, in UXCLUMPY, a soft scattering component can be added to reproduce an excess of soft X-ray photons often observed in the spectra of obscured Seyfert galaxies (Bianchi et al., 2006). For that purpose, an optional table model can be added, mirroring a fraction of the unabsorbed spectrum. The parameters of this additional table model are linked to the parameters of the main table, except for the normalisation, which remains free to vary.

Lastly, Galactic absorption is further applied to the components above. Given the low galactic absorption in the direction of CDFS, AEGIS and COSMOS, we fix galactic absorption to the average $N_{\rm H}$ value in the direction of the COSMOS field, $1.72 \times 10^{20}\,{\rm cm}^{-2}$ (Kalberla et al., 2005).

In our X-ray spectroscopic analysis, several UXCLUMPY parameters are fixed as indicated in Table 2.6. As mentioned above, the CTKcover and TORsigma parameters characterise the geometrical coverage of the obscuring material (see Figure 2.14), but due to degeneracies with the rest of the model parameters, constraining them can be challenging even for high photon count sources. Therefore, in our analysis, we set CTKcover and TORsigma to their default values, 0.4 and 28°, respectively, derived from X-ray spectra fits of local AGN (Buchner et al., 2019). Moreover, the E_cutoff parameter, i.e. the cut-off energy of central engine power-law, is fixed at 200 keV as it does not significantly

Table 2.6: Table summarizing the input parameters of the UXCLUMPY model and their prior used in our analysis.

parameter	prior
CTKcover	fixed = 0.4
TORsigma	fixed = 28°
Inclination	fixed = 18.2° / 45° / 70°
E_cutoff	fixed = 200 keV
photon index	Gaussian(1.95, 0.15)
$\log(N_{\rm H}/{\rm cm}^{-2})$	uniform(20, 26)
log(norm_torus)	uniform(-8, 3)
log(norm_scattering)	uniform(-7, -1.5)
redshift spectroscopic	fixed at source redshift
redshift photometric	photometric PDF
no redshift estimation	uniform(1, 6)
log(norm_background)	uniform(best-fit_val ±2)

impact the 0.5-10 keV observed-frame spectrum. Additionally, the inclination parameter of UXCLUMPY controls the angle of the observer relative to the vertical (symmetry) axis of the adopted torus geometry. The UXCLUMPY table model allows three broad bins of inclination angles 0-30° (face-on), 30-60° (intermediate) and 60-90° (edge-on), each of which includes a wide range of LOS column densities. We consider three inclination setups: 18.2°, 45° and 70° corresponding to these bins. Including or excluding the soft-scattering table model leads to six distinct model setups that are compared and evaluated in Section 3.3.3.

The remaining UXCLUMPY parameters are allowed to vary within predefined prior distributions (see Table 2.6). The photon index, Γ, follows a Gaussian prior distribution centred on 1.95 with a standard deviation of 0.15 (Nandra et al., 1997). The LOS column density, $N_{\rm H}$, the power-law continuum normalisation, and the soft-scattering component normalisation follow a log-uniform prior over the intervals 20 to 26, -8 to 3 and -7 to -1.5, respectively. The soft-scattering normalisation refers to the fractional contribution of the soft-scattering component relative to the intrinsic power-law component. Computationally, this is achieved by setting the normalisation of the soft-scattering model to log(norm_torus) + log(norm_scattering). Additionally, if a source has a good spectroscopic redshift measurement, the UXCLUMPY redshift parameter is fixed to that value. If a photometric redshift PDF is available, it is used as a prior in the modelling process. In cases where no redshift information is available, we assign a uniform prior in the range

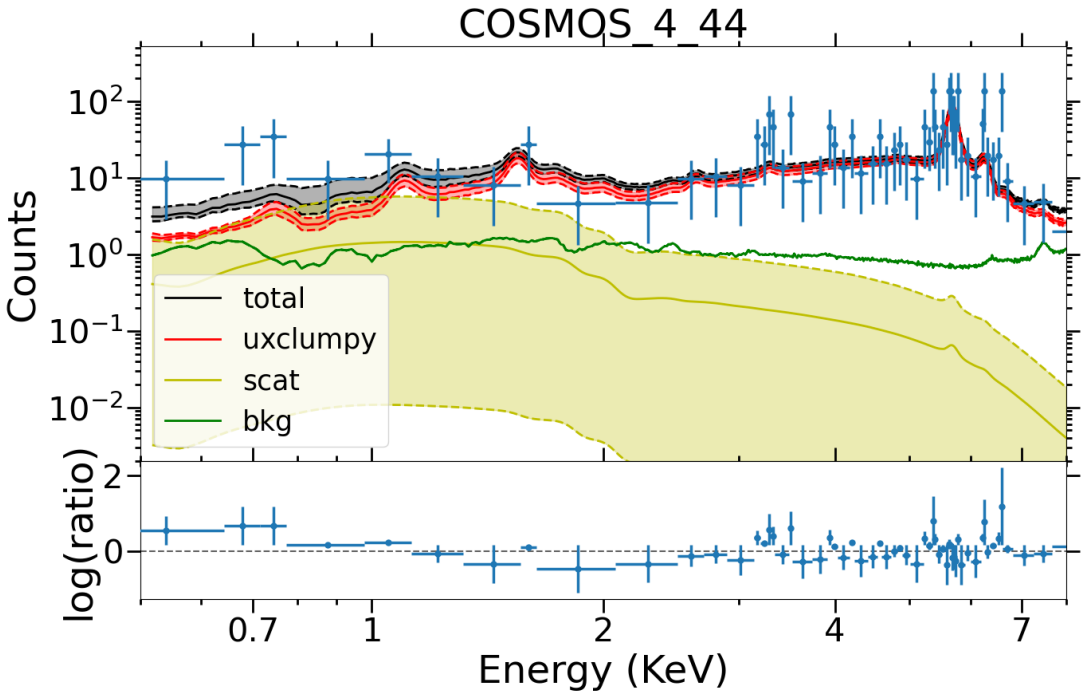

Figure 2.15: Example of X-ray spectral analysis result using BXA with the UXCLUMPY model. The inclination angle is fixed at 45°, and the soft-scattering component is included. The *blue crosses* are the extracted X-ray spectrum grouped to yield an SNR above 1 per bin. The *red line* corresponds to the UXCLUMPY model, the *yellow line* represents the soft scattering, the *green line* is the background model. The sum of all three components above is shown with the *black line*. The *shaded regions* correspond to the 1σ confidence interval of the corresponding component. The lower panel plots the logarithmic ratio between the X-ray spectrum and the best-fit model as a function of the energy. The parameter posterior distributions from this fit are displayed in Figure 2.16.

$1 < z < 6$ to the UXCLUMPY redshift parameter, assuming that sources without redshift estimation are likely above $z > 1$ (Georgakakis et al., 2017c).

Lastly, as the spectrum is a combination of the source and background photons, the latter must also be modelled. In this study, we use the `automatic_background()` command from BXA to model it (Simmonds et al., 2018). This machine-learning-based approach trained on large X-ray surveys, derives the principal components describing the background and its variations. When called, this function fits the background spectrum with the principal component models and progressively increases their complexity. It verifies the background fitting improvement by using the Akaike information criterion (Akaike, 1974). The best-fit background model has all its parameters frozen except for the normalization, which follows a log-uniform prior between the best-fit normalisation ± 2.

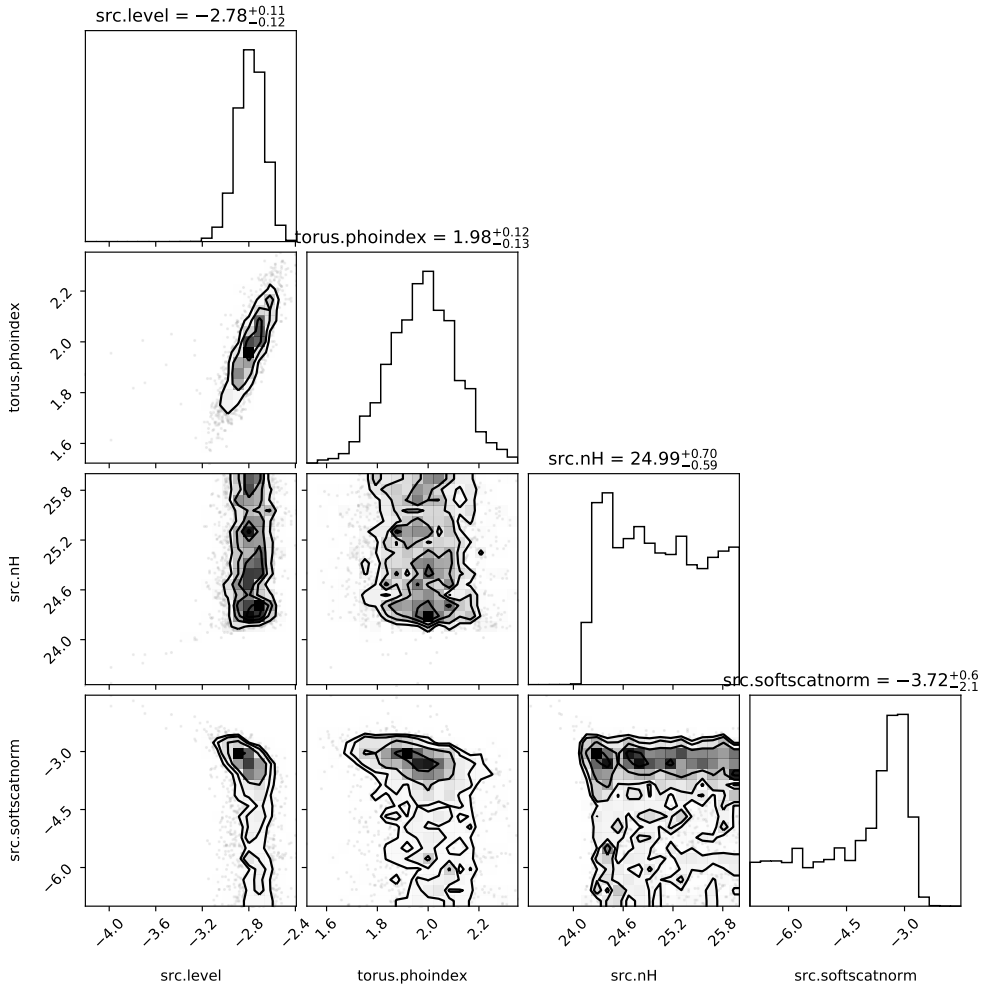

Figure 2.16: Example of parameter posterior distribution from the X-ray spectral analysis using BXA with the UXCLUMPY model. This corner plot shows the posterior distribution of the model normalisation "src.level", photon index "torus.phoindex", column density "src.nH" and relative normalisation of the soft-scattering model "src.softscatnorm". The best-fit model corresponding to this posterior distribution is shown in Figure 2.15. The $N_{\rm H}$ posterior distribution shows that this source is CTK with $\log(N_{\rm H}/{\rm cm}^{-2})/ > 24$.

By fitting the extracted spectra between 0.5 and 8 keV using BXA with UXCLUMPY as the spectral model, we constrain the free parameters in a Bayesian framework. The choice of energy limits does not significantly impact the results. Figure 2.15 presents the X-ray spectrum of a COSMOS-Legacy source along with its best-fit model, and its different components. The error margins are computed from the parameter posterior distribution, representing their 1σ variation. The parameter posterior distributions of this X-ray spectroscopic analysis are displayed in Figure 2.16. The selection of this particular source is justified primarily by its Compton-thickness and relatively high photon counts (116 counts in the 0.5-7 keV band).

2.4.3 Spectral Energy Distribution Fitting

Fitting theoretical and/or empirical model templates to the observed multi-wavelength Spectral Energy Distribution (SED) of extragalactic sources yields valuable information on the physical properties of AGN and their host galaxies (Conroy, 2013). Indeed, multi-wavelength SED fitting is an efficient tool to separate the relative contribution of the AGN and host galaxy SED (see Figure 1.9 in Section 1.3), allowing the recovery of the AGN accretion luminosity, while it can also constrain the host galaxy's Star Formation Rate (SFR) or total stellar mass $M_{\star}$.

In this section, I present the two SED fitting algorithms used in this thesis: FortesFit (Rosario, 2019) in Chapter 3 and CIGALE (Boquien et al., 2019; Yang et al., 2022) in Chapter 4.

FortesFit

In Chapter 3, the objective of the SED fitting process is to constrain the 6 μm luminosity of the torus of the AGN. For that purpose, we fit the 2-500 μm SED of the matched sources within the COSMOS-legacy field using the multi-component Bayesian SED fitting package FortesFit [6] (Rosario, 2019). Before fitting the SED of the sources, FortesFit generates the template SED model of the components to be used for a set of parameter pivot points. During the SED fitting process, the algorithm explores the multi-dimensional parameter space and uses the pre-generated SEDs to interpolate between the parameter pivot points. The normalisation of each component SED is left free to vary.

FortesFit is powered by MultiNest (Feroz et al., 2009), a robust nested Bayesian inference algorithm to explore the parameter space, similar to UltraNest powering BXA (§2.4.2). The decomposition of the AGN and star formation contributions in the IR part of the SED is not trivial and depends on the choice of templates to use and degeneracies between model parameters. However, the fully Bayesian inference methodology (Equation 2.8) of FortesFit tackles these issues and captures accurately the uncertainties of the inferred parameters. These uncertainties are then consistently propagated to the Bayesian X-ray spectral analysis, justifying our choice of SED fitting algorithm.

[6] https://github.com/vikalibrate/FortesFit

In this work, we measure the IR luminosity at 6 μm, where the contrast between the host galaxy star formation and the AGN torus IR emissions is typically large (e.g. Nardini et al., 2008, 2009), thereby facilitating the decomposition. We also choose to use state-of-the-art observationally-motivated model templates that are able to capture the observed diversity of AGN and star formation emission in the infrared. Our SED modelling includes three main components: the unabsorbed stellar emission from Bruzual & Charlot (2003), the IR emission from the dust-obscured star formation (SF) (Dale et al., 2014) and the IR emission coming from the torus based on the empirical DECOMPIR AGN model (Mullaney et al., 2011). The different component parameters and range values are summarised in Table 2.7. The free parameters of the stellar emission template are the mass and age of the stellar population, ranging between 10^7 and 10^{13} solar masses, and 10^6 and 10^{10} years, respectively, while the Initial Mass function (IMF) is fixed to Chabrier (2003) values with solar metallicities (Z=0.02). For the SF emission of the host galaxy, the free parameters during the fit are the 8-1000 μm luminosity $L_{\rm SF}$, and the shape parameter $\alpha_{\rm SF}$ describing a wide range of spectral shapes for normal star-forming galaxies. Their respective ranges are $[10^{42}-10^{48}]$ erg s^{-1} and $[0.06-4]$. Finally, the DECOMPIR template combines a broken power-law and a black body and the IR AGN luminosity $L_{\rm AGN,\,IR}$ in the interval 8-1000 μm and the short-wavelength slope $\Gamma_{\rm S}$ are the free parameters in the range $[10^{38}-10^{48}]$ erg s^{-1} and $[-0.3-1.1]$, respectively, to model the dusty torus. The other parameters, such as the long-wavelength slope $\Gamma_{\rm L}$ and the hot dust temperature $T_{\rm BB}$, are set to 0.2 and 1500 K, respectively, following Mullaney et al. (2011).

Moreover, as our aim is not to constrain the stellar population emission but only to consider its possible excess at rest-frame IR wavelengths that could affect the fit of the AGN emission, we do not include optical/UV photometry in our SED fits. Including optical/UV photometry does not significantly impact the AGN emission constraints and the final results within the error margins (Andonie et al., 2022b).

Figure 2.17 shows an example of SED template best-fit model (*black solid line*). The emission contributions of the stellar population, AGN torus and star formation and their 1σ uncertainties estimated by FortesFit are over-plotted in *orange*, *red* and *blue*, respectively. In our catalogue, the source's ID is COSMOS_1_420 and is 10178753 in the photometric catalogue (Jin et al., 2018). This source was selected due to its double-peaked

Table 2.7: The SED components and their parameter value or range used by FortesFit to fit the SED of our COSMOS-Legacy sources (Section 3.4.1).

Component **Parameter**	**Value/[Range]**
Stellar population emission	
Bruzual & Charlot (2003)	
Stellar mass	$[10^7 - 10^{13}]\ M_\odot$
Age stellar population	$[10^6 - 10^{10}]$ yr
Initial Mass Function	Chabrier (2003)
Metallicity (Z)	0.02
Dust-obscured star formation (SF)	
Dale et al. (2014)	
8-1000 μm $L_{\rm SF}$	$[10^{42} - 10^{48}]$ erg s^{-1}
$\alpha_{\rm SF}$	$[0.06 - 4]$
AGN torus: DECOMPIR	
Mullaney et al. (2011)	
8-1000 μm $L_{\rm AGN,\,IR}$	$[10^{38} - 10^{48}]$ erg s^{-1}
Short-wavelength slope $\Gamma_{\rm S}$	$[-0.3 - 1.1]$
Long-wavelength slope $\Gamma_{\rm L}$	0.2
Hot dust temperature $T_{\rm BB}$	1500 K

$N_{\rm H}$ and $L_{\rm X}$ parameter posterior distributions from X-ray spectroscopy (see §3.3.4 and Figure 3.4).

CIGALE

In Chapter 4, the primary goal of the SED fitting process is to recover the stellar masses of AGN host galaxies by modelling their multi-wavelength (UV to mid-IR) broad-band photometry. The templates we adopt include both stellar population and AGN emission modules, enabling the separation of galaxy light from that associated with the nuclear compact object and thus allowing the estimation of critical galaxy properties, such as stellar mass. For this application, we choose to use the Code Investigating GALaxy Emission (CIGALE hereafter, Boquien et al., 2019; Yang et al., 2022) because it is computationally efficient and extensively tested. This fitting algorithm is the updated Python version of the `FORTRAN` CIGALE code (Noll et al., 2009), both relying on the energy balance principle: the photons absorbed by stellar dust in the UV-optical are re-emitted thermally in the mid- and far-IR.

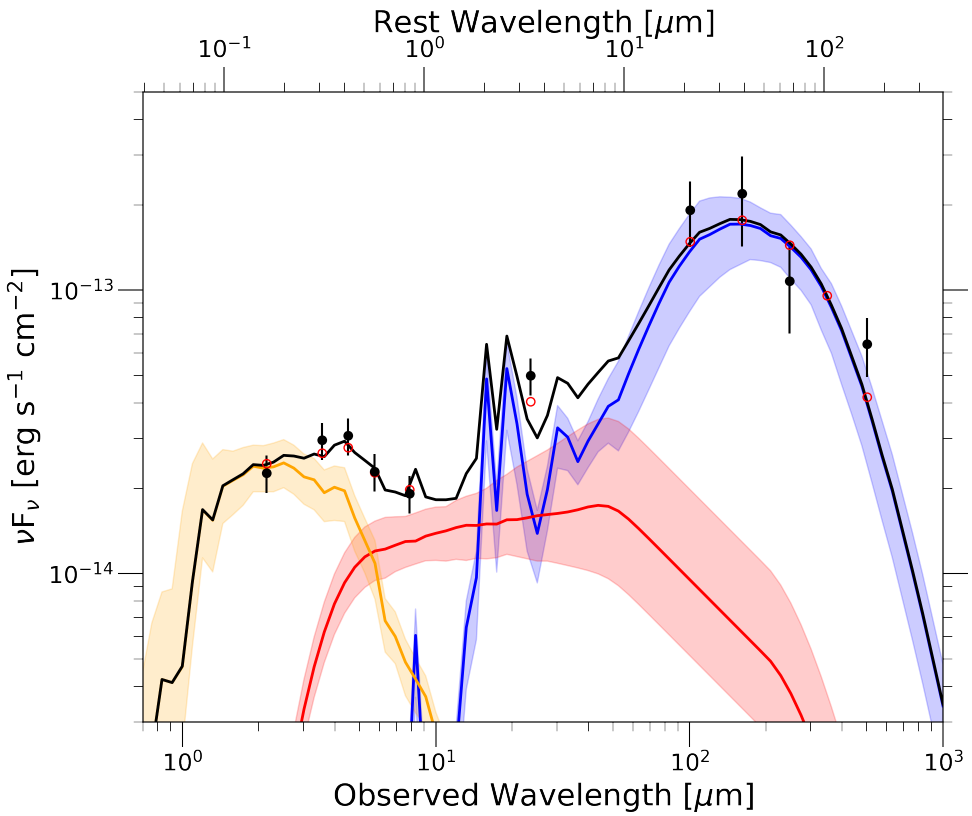

Figure 2.17: Example of a template fit to the IR SED of the X-ray source COSMOS_1_420 (object with ID 10178753 in the Jin et al. (2018) catalogue) using the FortesFit code. The *black dots* and *vertical lines* represent the photometry of the source and its uncertainties. The curves represent the stellar population emission (*orange*), the IR AGN emission (*red*), and the IR emission from star formation (*blue*). The *shaded regions* represent the approximate 1σ-scatter of each SED component as constrained by FortesFit. The *black solid line* corresponds to the sum of the above three components.

CIGALE provides different SED template-generating modules, each corresponding to different emission mechanisms and/or components. These modules are governed by a set of parameters that can vary within a user-defined grid. The combination of the different modules results in a multi-dimensional parameter grid where each node represents a specific combination of parameter values for which CIGALE generates a template SED. The comparison of these models with the observed photometry using the χ^2 statistic yields the best-fit set of module parameters, their associated uncertainties and their PDFs. In comparison with FortesFit (§2.4.3), CIGALE is not fully Bayesian as it does not interpolate between parameter grid points, therefore, not returning the parameter posterior distributions. To ensure the selection of appropriate modules and parameter sets, we follow the prescriptions of previous studies (Mountrichas et al., 2021; López et al., 2023).

The chosen modules and their corresponding parameters are presented in Table 2.8 and briefly described below.

For the host galaxy stellar component, we employed a delayed star formation history that parameterises the SFR as $\mathrm{SFR}(t) \propto t \times \exp(-t/\tau)$. The SFR peaks at the time τ and then declines exponentially, with an optional star formation burst with an e-folding time of 50 Myr to account for recent intense star formation activity. The stellar population is modelled from the stellar templates of (Bruzual & Charlot, 2003) with the initial mass function of Chabrier (2003) and solar metallicity (Z=0.02). We also incorporate the nebular module (Inoue, 2011), which includes the typical nebular emission lines observed in star-forming galaxies with a line width of 200 km s^{-1}. The dust attenuation follows a modified Calzetti et al. (2000) law, and the dust emission from the host galaxy with no AGN contribution is modelled by the Dale et al. (2014) templates. For the AGN emission, we employ the SKIRTOR model (Stalevski et al., 2016), which uses a 3D radiation-transfer code to simulate the interaction of photons emitted by a central source with a two-phase medium torus, consisting of a smooth and low-density medium containing high-density clumps. The scaling factor of the module, the AGN fraction, represents the ratio of the IR emission from the AGN to the total emission (AGN + host galaxy) within the $8-1000\,\mu$m rest-frame range. In this work, we consider both type I and type II AGN, corresponding to viewing angles of 30° and 70° in the SKIRTOR model, respectively.

One limitation of CIGALE is the requirement of a fixed redshift, preventing the utilization of photometric redshift PDFs. Given that a sizeable fraction of the X-ray selected AGN sample used in Chapter 4 has photometric redshift estimations, we need to address this limitation and account for the redshift uncertainties in the derivation of the physical parameters from the SED fitting process. Our approach consists of marginalizing over the redshift uncertainty by importance sampling. We sample the z-PDF in regular redshift intervals, and for each, we perform the SED fitting with the redshift fixed to the mean value of the interval. This approach yields, for a given source, multiple estimates of physical parameters, e.g. stellar mass or SFR, each corresponding to a different redshift bin. These estimates are then weighted and combined to generate posteriors for the parameter of interest.

Figure 2.18 illustrates our approach. We segment the redshift range into bins of 0.1

Table 2.8: The modules and their parameters along their grid values used by CIGALE for the SED fitting of our sources (Section 4.3.2).

Parameter	Value
Module	
Star formation history	
Delayed SFH with recent burst	
Age of the main population	500, 1000, 3000, 5000, 7000, 9000 Myr
e-folding time main population	500, 1500, 3000, 5000, 7000 Myr
Age of the burst	20, 200 Myr
e-folding time of the burst	50 Myr
Burst stellar mass fraction	0.0, 0.1
Simple Stellar population	
Bruzual & Charlot (2003)	
Initial Mass Function	Chabrier (2003)
Metallicity (Z)	0.02
Galactic dust extinction	
Calzetti et al. (2000)	
$E(B\text{-}V)_{young}$	0.0, 0.1, 0.25, 0.5, 0.75, 0.9
UV^{λ}_{bump}	217.5 nm
Galactic dust emission	
Dale et al. (2014)	
α slope in $dM_{dust} \propto U^{-\alpha} dU$	1.0, 1.5, 2.0, 2.5, 3
Nebular	
Inoue (2011)	
log U	-2.0
width lines	200 km.s^{-1}
AGN module: SKIRTOR	
Stalevski et al. (2016)	
Torus optical depth at 9.7 microns	3.0, 7.0
Torus density radial parameter	1.0
Torus density angular parameter	1.0
Torus opening angle	40°
Ratio max-to-min radii of the torus	20
Viewing angle	30°, 70°
Disk spectrum	Schartmann et al. (2005)
Power-law index of the disk	-0.36
AGN fraction	0.01, 0.1, 0.2, 0.3, 0.4, 0.5, 0.6, 0.7, 0.8, 0.9, 0.99
Extinction law of polar dust	SMC
E(B - V) of polar dust	0.0, 0.02, 0.1, 0.5, 1.0
Temperature of polar dust	100 K
Emissivity of polar dust	1.6
Total number of models	792 000

width and calculate their weight based on the fraction of the redshift PDF within each bin. For each source and each redshift bin with a weight exceeding a 10^{-3} threshold, we create duplicates of the photometric data, fixing the redshift to the bin's mean value, and perform SED fitting on each duplicate. Finally, for a given source, the posterior PDF of a parameter of interest, such as the stellar mass, is constructed as a Gaussian mixture. A Gaussian is generated for each redshift bin, centred on the parameter best-fit value from CIGALE. The standard deviation and the amplitude of the Gaussian are given by the uncertainty of the best-fit value and the weight of the redshift bin, respectively. The full posterior parameter distribution is the sum of these Gaussians, allowing easy extraction of the parameter's median and lower/upper limits. The stellar mass distribution of the sources of the three different surveys as a function of the redshift is illustrated in the top panel of Figure 4.3 in Section 4.3.2.

2.5 Summary

In the previous sections, I presented the X-ray data obtained in the three deep extragalactic fields COSMOS-Legacy (§2.2.1), AEGIS-XD (§2.2.2) and CDFS (§2.2.3), detailing the rigorous methodology applied to detect sources in these fields (§2.3.1). As these fields benefit from extended multi-wavelength coverage, a meticulous methodology was applied to identify the counterparts of the X-ray sources (§2.3.2) and estimate their photometric redshift (§2.3.3) to build accurate catalogues of X-ray-selected sources. In the following Chapters 3 and 4, I use these source catalogues to extract (§2.4.1) and fit (§2.4.2) the X-ray spectra of these AGN candidates, measuring their intrinsic luminosity $L_{\rm X}$ and obscuration level $N_{\rm H}$. Combined with detailed UV-to-far-IR SED fitting to measure either the AGN torus IR emission or the stellar mass of the host galaxy, I will study the demographics and accretion properties of obscured AGN.

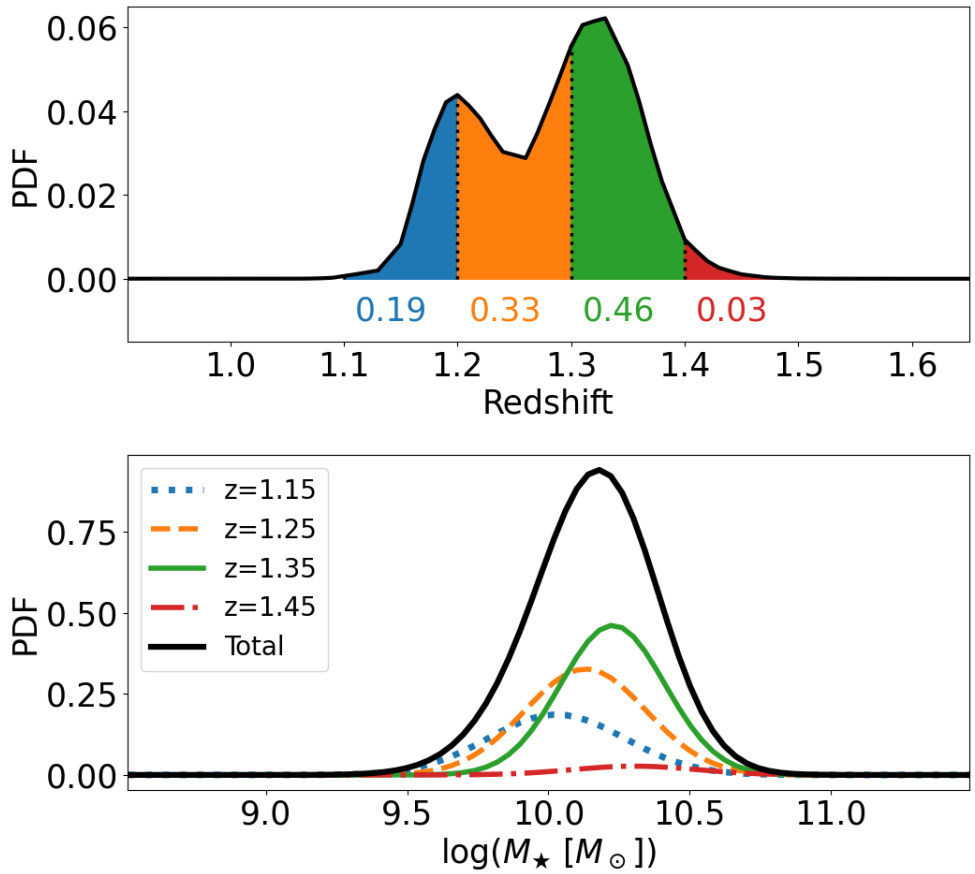

Figure 2.18: Demonstration of how we use CIGALE to account for photometric redshift PDFs of individual sources. *Top panel*: The redshift PDF of an example X-ray source in the sample is split into four intervals with width $\Delta z = 0.1$. For clarity, the part of the PDF within each redshift interval is shaded with a different colour. The fraction of the photometric redshift PDF in each interval is indicated by coloured numbers at the bottom of the panel. *Bottom panel*: Demonstration of the Gaussian mixture model adopted to recover the stellar mass PDF for the same source. For each redshift interval of the top panel, CIGALE returns a best-fit value for the stellar mass, $M_\star$, and the corresponding uncertainty. These are used to generate Gaussians with means equal to the best fit stellar masses and standard deviations equal to the stellar mass uncertainties. These Gaussians are shown with the coloured curves. The colour coding corresponds to the redshift intervals of the top panel. The normalisation of these curves is set by the fraction of the photometric redshift PDF within each redshift interval (i.e. the coloured numbers in the top panel). The sum of the Gaussians (*black solid line*) is the total $\log(M_\star)$ PDF.

CHAPTER 3

The demographics of obscured AGN from X-ray spectroscopy guided by multi-wavelength information

Abstract

A complete census of Active Galactic Nuclei (AGN) is a prerequisite for understanding the growth of supermassive black holes across cosmic time. A significant challenge toward this goal is the whereabouts of heavily obscured AGN that remain uncertain. This Chapter sets new constraints on the demographics of this population by developing a methodology that combines X-ray spectral information with priors derived from multi-wavelength observations. We select X-ray AGN in the *Chandra* COSMOS-Legacy survey and fit their $2.2 - 500\mu$m spectral energy distributions with galaxy and AGN templates to determine the mid-infrared ($6\,\mu$m) luminosity of the AGN component. Empirical correlations between X-ray and $6\,\mu$m luminosities are then adopted to infer the intrinsic accretion luminosity at X-rays for individual AGN. This is used as prior information in our Bayesian X-ray spectral analysis to estimate physical properties, such as line-of-sight obscuration. Our approach breaks the degeneracies between accretion luminosity and obscuration that affect X-ray spectral analysis, particularly for the most heavily obscured (Compton-Thick) AGN with low photon counts X-ray spectra. The X-ray spectral results are then combined with the selection function of the *Chandra* COSMOS-Legacy survey

to derive the AGN space density and a Compton-Thick fraction of $21.0^{+16.1}_{-9.9}\%$ at redshifts $z < 0.5$. At higher redshifts, our analysis suggests upper limits to the Compton-Thick AGN fraction of $\leq 40\%$. These estimates are at the low end of the range of values determined in the literature and underline the importance of multi-wavelength approaches for tackling the challenge of heavily obscured AGN demographics.

3.1 Introduction

SuperMassive Black Holes (SMBHs) are found to be ubiquitous in the nuclear regions of local galaxies (Kormendy & Ho, 2013). As explained in Section 1.3.1, SMBHs grow through intense accretion phases Soltan (1982), during which large amounts of energy are produced and observed as electromagnetic radiation at different parts of the spectrum. The class of astrophysical sources that correspond to such events are broadly dubbed Active Galactic Nuclei (AGN, Antonucci, 1993; Urry & Padovani, 1995; Padovani et al., 2017). Consequently, observational measurements of the space density of AGN in the Universe as a function of cosmic time provide essential constraints on the growth history of SMBHs we observe in the local Universe (Marconi et al., 2004). Although simple in principle, counting AGN in a cosmological volume is challenging because of both observational limitations and the phenomenological complexity of active black holes. Therefore, accounting for lower luminosity events in flux-limited samples is not straightforward and requires a good understanding of observational biases and selection effects. Moreover, as described in Section 1.4.2, a substantial fraction of SMBHs in the Universe is believed to grow their masses behind clouds of dust and gas (Maiolino et al., 1998; Risaliti et al., 1999) that attenuate the emitted radiation and render the identification of such systems difficult. This introduces biases in AGN counting experiments and can lead to a significant underestimation of the true size of the underlying population and therefore, requires a handle on the obscuration distribution of AGN to account for this effect.

As presented in Section 1.4.1, among the different wavebands available for studying AGN obscuration, the X-ray regime offers several advantages briefly summarised below. Particularly at harder rest-frame energies ($\gtrsim 2\,\mathrm{keV}$), X-ray photons are less absorbed by obscuration than their UV/optical counterparts. Moreover, any obscuring material along

the line-of-sight (LOS) imprints characteristic signatures on the X-ray spectra of AGN (see Figure 1.11), which can be used in turn to determine the LOS hydrogen column density $N_{\rm H}$. Finally, the contamination of X-ray observations by X-ray binaries or supernova remnants is low. These advantages allow a precise determination of the selection function of X-ray surveys, i.e. the probability of detecting AGN of a given intrinsic luminosity, redshift and obscuration. This key feature enables the crucial step from an observational census of AGN (i.e. a sample) to the demographics of the underlying population. As a result, the most detailed description of the whereabouts of obscured AGN to date has been painted by high-energy survey programs (e.g. Ueda et al., 2003; Barger et al., 2003; Della Ceca et al., 2008; Ueda et al., 2014; Burlon et al., 2011; Alexander et al., 2013; Buchner et al., 2015; Aird et al., 2015).

X-ray surveys have also identified a deeply buried AGN population, the Compton-Thick (CTK) AGN, for which the surrounding obscuring material is optically thick even to X-ray photons (e.g., Ricci et al., 2015). These sources are characterised by a LOS column density $N_{\rm H} > 1.5 \times 10^{24}\,{\rm cm}^{-2}$. AGN below this threshold are referred to as Compton-Thin (CTN). As mentioned in Section 1.3.3, the spectra of CTK AGN are dominated by reflection components such as the Fe Kα fluorescence line at 6.4 keV (e.g. Levenson et al., 2006b; Nandra et al., 2007) and the Compton hump at high energy (> 10 keV, Piro et al., 1990). However, because of the high level of obscuration, CTK AGN appear X-ray faint and are typically detected at the flux limits of current extragalactic X-ray surveys. As a result, their spectra typically suffer from low count statistics, which translates into significant uncertainties in the determination of their intrinsic properties, such as accretion luminosity and column density (Buchner et al., 2015; Saha et al., 2022). Additional information on these CTK sources is provided by studies of the Cosmic diffuse X-ray Background (CXB) spectrum, which is dominated by the integrated emission of all AGN throughout the Universe. However, as mentioned in Section 1.4.2, the fit of the CXB by AGN population synthesis indicates a significant fraction of CTK AGN, larger than the observed one (Gilli et al., 2007; Akylas et al., 2012; Ananna et al., 2019).

As discussed in Section 1.4.1, the InfraRed (IR) waveband is valuable to study heavily obscured AGN. The AGN mid-IR radiation originates from the absorption of UV/optical photons and the thermal re-emission by the obscuring material itself (§1.3.4), and there-

fore, heavily obscured AGN missed by X-ray surveys should be detected in the IR band. However, star formation also emits in the IR band contaminating IR surveys. As a result, the calculation of the space density of the underlying population from mid-IR selected samples is not straightforward (but see Delvecchio et al., 2014; Assef et al., 2015). Nevertheless, a key feature of the mid-IR observations is that they are thought to provide a good proxy of the intrinsic accretion luminosity even in the case of deeply buried AGN (e.g. Risaliti et al., 1999; Gandhi et al., 2009). As a consequence, sources that appear X-ray faint for their mid-IR luminosity are obscured AGN candidates (Georgantopoulos et al., 2011).

This Chapter presents a methodology that combines X-ray and mid-IR information within a Bayesian framework to constrain the space density of heavily obscured AGN. At the core of the method are X-ray observations that provide estimates of the column density $N_{\rm H}$ of individual sources and a well-understood sample selection function. IR photometry is coupled with template fits to yield estimates of the reprocessed accretion luminosity and help improve X-ray spectral constraints. Section 3.2 describes the multi-wavelength observations used in the analysis. Section 3.3 describes the extraction and fitting of the X-ray spectra and compares the inferred X-ray spectral parameters with previous studies. Section 3.4 presents the new methodology to improve the X-ray fitting by combining it with AGN mid-IR prior information. In Section 3.5, the X-ray spectral analysis results are used to infer the obscured AGN demographics and constrain the AGN space density and intrinsic CTK fraction as a function of z, $L_{\rm X}$ and $N_{\rm H}$. We discuss our results in Section 3.6, and summarize our conclusions in Section 3.7. This Chapter adopts a cosmology with a Hubble constant of $H_0 = 70$km s^{-1}Mpc^{-1}, mass density parameter, $\Omega_M = 0.3$. and effective mass density of the dark matter $\Omega_\Lambda = 0.7$.

3.2 Data

This Chapter uses data from the Cosmic Evolution Survey (COSMOS) field (Scoville et al., 2007), covering an area of nearly 2 deg^2. The multi-wavelength coverage of this field is extensively presented in Section 2.2.1. Specifically, we analyse the AGN detected within the *Chandra* COSMOS-Legacy X-ray survey (Civano et al., 2016). The source detection,

multi-wavelength counterpart identification and redshift estimation in this field are presented in Sections 2.3.1, 2.3.2 and 2.3.3, respectively. Table 3.1 presents the number of sources detected in each X-ray band as a function of the redshift type (e.g. spectroscopic, photometric or no redshift).

Table 3.1: Number of sources in the *Chandra* COSMOS-Legacy detected in different energy bands, full (0.5-7 keV), soft (0.5-2 keV), hard (2-7 keV), ultra-hard (4-7 keV) and any of these bands. The number of sources with spectroscopic, photometric or no redshift measurement is also shown for each subsample. The parenthesis below indicates the number of sources for each band and redshift category after applying the spatial overlap mask.

Bands	Full 0.5-7 keV	Soft 0.5-2 keV	Hard 2-7 keV	Ultra-hard 4-7 keV	Any Band
z spectro	1825 (1469)	1562 (1250)	1318 (1071)	726 (573)	1917 (1551)
z photo	1405 (1146)	1061 (864)	773 (629)	227 (184)	1527 (1259)
No z	142 (119)	149 (122)	49 (44)	18 (17)	183 (155)
Total	3372 (2734)	2772 (2236)	2140 (1744)	971 (774)	3627 (2965)

In this Chapter, the multi-wavelength photometry originates from the far-IR "super-deblended" far-IR to (sub)millimetre photometric catalogue of the COSMOS field presented by Jin et al. (2018) as explained in Section 2.3.2. In Section 3.4.1, the IR Spectral Energy Distributions (SEDs) of our X-ray sources are constructed with this photometric catalogue and then fitted by AGN and galaxy templates to measure their accretion luminosity. This information is used in Section 3.4.2 to guide the X-ray spectral analysis of obscured AGN.

However, the spatial overlap of the Jin et al. (2018) catalogue and the *Chandra* survey of the COSMOS-Legacy field is not perfect. We use the HEALPix (Hierarchical Equal Area isoLatitude Pixelisation, Górski et al., 2005) tessellation of the sky to determine the Multi-Order-Coverage (MOC, Fernique et al., 2019) maps that define the irregular areas covered by two samples and assess their overlap. The maximum HEALPix order parameter for determining the MOCs is set to 14. This value corresponds to a maximum spatial resolution of about 13 arcsec for the resulting MOCs. It is then straightforward to define the overlap region of the two MOCs and determine which X-ray sources have

sky coordinates within the common area of the two samples. This reduces our sample to a total of 2965 X-ray sources, of which 2753, 2282, 1816 and 831 are detected in the full, soft, hard and ultra-hard bands, respectively, as indicated between parentheses in Table 3.1.

3.3 X-ray Spectral Analysis

In this section, we describe our X-ray fitting pipeline. We start by extracting the X-ray spectra while optimising for the signal-to-noise ratio (Section 2.4.1 and 3.3.1). Then, we present the fitting algorithm and the adopted X-ray AGN model (Section 2.4.2 and 3.3.2). Lastly, we justify our choice of baseline model between different setups (Section 3.3.3) and compare our results with previous studies (Section 3.3.4).

3.3.1 Spectral Extraction

The X-ray spectral extraction process for each COSMOS-Legacy source is detailed in the methodology Section §2.4.1.

The distribution of the selected EEF is shown on the left panel of Figure 3.1. The right panel of Figure 3.1 plots the distribution of the photon counts of the combined extracted X-ray spectra at the positions of *Chandra* COSMOS-Legacy sources. The plot also shows the distribution of the photon counts of the corresponding extracted background spectra. As the 100 background counts threshold is applied on the stacked image, the background count can be lower after extraction because pointings with no photon counts in the source region are not extracted, even if the background region contains photon counts.

Previous X-ray spectral studies using the *Chandra* COSMOS-Legacy observations have adopted a limit of 30 net counts in the X-ray spectrum for spectral analysis (Marchesi et al., 2016b; Lanzuisi et al., 2018, hereafter L18). In our work, no such threshold is applied. Instead, we extract and analyse the X-ray spectra of all detected *Chandra* COSMOS-Legacy sources. Among our 2965 X-ray sources (see Section 3.2), 1821 (61%) have at least 30 counts, and 1141 (39%) have less than 30 counts in the $0.5-7\,\mathrm{keV}$ band.

Table 3.2 is an extract of the table compiling the spectral extraction information on the 2965 sources of our sample. A full version of this table is available in electronic format

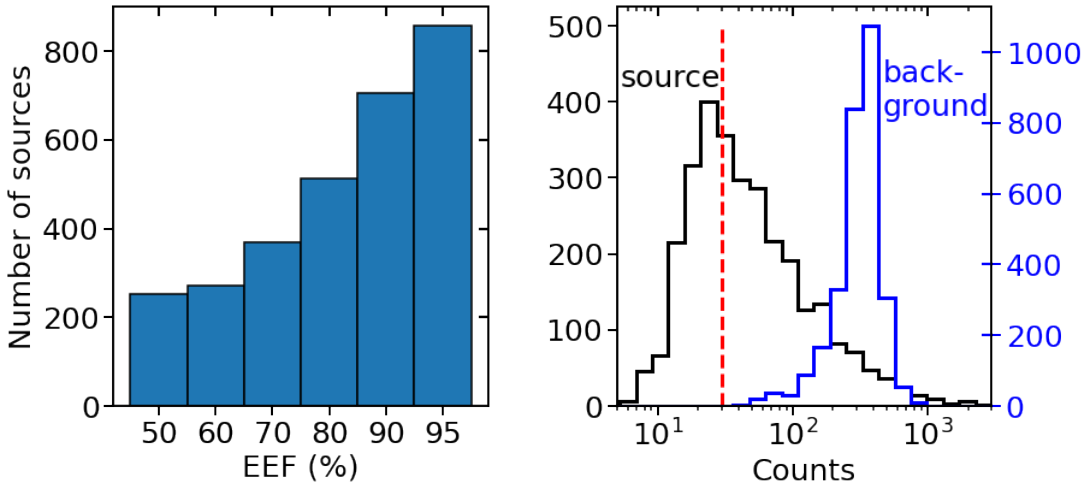

Figure 3.1: *Left panel*: Distribution of the X-ray spectral extraction radius in EEF units for the *Chandra* COSMOS-Legacy sources. *Right panel*: The *black histogram* shows the distribution of the photon counts in the full band of the extracted X-ray spectra of our sources. The *red vertical dashed line* represents the 30-count limit adopted by previous studies as the threshold above which the X-ray spectra are analysed (Marchesi et al. (2016b), L18). The *blue histogram* shows the distribution of the photon counts in the full band of the extracted background spectra of our sources.

at `https://doi.org/10.5281/zenodo.7014625`.

3.3.2 X-ray Spectroscopy

As presented in the methodology Section §2.4.2, we use the BXA package (Buchner et al., 2014) to fit the X-ray spectra of our sources with the UXCLUMPY spectral model (Buchner et al., 2019). In our study, several UXCLUMPY parameters are fixed, while the others are allowed to vary within predefined prior distributions, as indicated in Table 3.3.

3.3.3 Comparison between Different Setups

We employ BXA to fit the spectra of all our sources with six different setups of the UXCLUMPY X-ray spectral model: with an inclination angle fixed at 18.2°, 45° or 70°, and including or not the soft-scattering component. The aim of the comparison is to assess the impact of model setup and determine the one to be used as the baseline model further in our analysis.

As discussed in Section 2.4.2, the model evidence $\mathcal{Z}$ is the best tool to compare two models with the same data set. The larger it is, the more favoured the corresponding

Table 3.2: X-ray spectral extraction properties of the sources. (1) source ID; (2-3) X-ray position; (4-5) optical counterpart position; (6) EEF used for extraction in percent units; (7) source radius in arcsecond; (8) $0.5-7\,\mathrm{keV}$ net photon counts of the source; (9) the net photon counts of the background in all energy band; (10) flag indicating if the source is detected in the hard band (2-7 keV); (11) source ID in L18 if cross-matched. Full table electronically available.

ID (1)	RA (2)	Dec (3)	RA_optical (4)	DEC_optical (5)	EEF (6)	radius_src (7)	cts_057 (8)	cts_bkg (9)	hard_flag (10)	ID L18 (11)
COSMOS_0_10	149.802	1.636	149.802	1.636	70	3.13	25	252	False	–
COSMOS_0_100	149.728	1.719	149.728	1.719	90	6.06	83	362	True	lid_1186
COSMOS_0_102	149.611	1.746	149.611	1.746	80	3.54	28	305	False	–
COSMOS_0_103	149.722	1.753	149.722	1.753	60	3.16	37	356	False	lid_2444
COSMOS_0_104	149.506	1.809	149.506	1.809	95	5.89	88	162	True	lid_970
⋮	⋮	⋮	⋮	⋮	⋮	⋮	⋮	⋮	⋮	⋮
COSMOS_8_95	150.398	2.797	150.398	2.797	90	4.19	54	312	True	lid_427
COSMOS_8_96	150.479	2.798	150.479	2.798	95	5.67	67	286	True	lid_401
COSMOS_8_97	150.454	2.806	150.454	2.806	95	5.3	295	314	True	lid_395
COSMOS_8_98	150.515	2.81	150.514	2.81	95	4.42	64	195	True	lid_410
COSMOS_8_99	150.672	2.811	150.672	2.811	50	2.32	28	116	False	lid_487

Table 3.3: Table summarizing the input parameters of the UXCLUMPY model and their prior used in our analysis.

Parameters	Priors
CTKcover	fixed = 0.4
TORsigma	fixed = 28°
Inclination	fixed = 18.2° / 45° / 70°
E_cutoff	fixed = 200 keV
photon index	Gaussian(1.95, 0.15)
$\log(N_{\rm H}/{\rm cm}^{-2})$	uniform(20, 26)
log(norm_torus)	uniform(-8, 3)
log(norm_scattering)	uniform(-7, -1.5)
redshift spectroscopic	fixed at source redshift
redshift photometric	photometric PDF
no redshift estimation	uniform(1, 6)
log(norm_background)	uniform(best-fit_val ±2)

model. We adopt a logarithmic evidence difference $\Delta \log \mathcal{Z} > 4.6$ as the threshold to select strongly favoured models (Jeffreys, 1961). Additionally, we consider that a difference below this threshold still favours the highest evidence model, but we cannot rule out the alternative model.

Table 3.4 presents the comparison of the different UXCLUMPY X-ray spectral model setups. For individual sources, we estimate the logarithmic evidence difference, $\Delta \log \mathcal{Z}$, between each model setup and the one with soft-scattering and an inclination angle of 45° (baseline model). For a given model setup, we sum up the logarithmic evidence differences of all the sources (following Buchner et al., 2014) and compute its uncertainty using a bootstrap resampling method. It consists of taking N sources with replacement, with N being the number of sources in our sample, and calculating the sum of the logarithmic evidence differences relative to the baseline model. This process is repeated 100 times for each model setup. The standard deviation of $\Delta \log \mathcal{Z}$ estimated from these 100 trials represents the uncertainty of the logarithmic evidence difference of a given model setup. The table also shows the total number of individual X-ray spectra with $\Delta \log \mathcal{Z} > 4.6$ or $\Delta \log \mathcal{Z} < -4.6$ relative to the baseline model, in other words, how many times a model setup is strongly favoured or disfavoured relative to the baseline model.

Table 3.4 shows that the Thomson scattering component is strongly favoured by the data. The total logarithmic evidence of the model setups with the scattering component are larger by typically 100 compared to the same model without the scattering. Moreover,

Table 3.4: Table presenting the evidence comparison between the different model setups relative to our baseline model that includes Thomson scattering and has an inclination angle of i=45°. The second column is the ensemble evidence difference relative to the baseline model. The ensemble evidence of a given model is defined as the sum of the evidences of individual X-ray sources and is listed in brackets. The error bars are estimated by bootstrapping (see text for details). The third column displays the number of individual sources having a higher evidence than the baseline model and in parentheses is the number of sources for which the model is strongly favoured over the baseline model. Similarly, the last column indicates the number of individual sources with lower evidence, and in parentheses, the number of sources for which the model can be ruled out.

Models	Sum difference (Sum total)	$\Delta \log \mathcal{Z} \geq 0$ ($\Delta \log \mathcal{Z} > 4.6$)	$\Delta \log \mathcal{Z} < 0$ ($\Delta \log \mathcal{Z} < -4.6$)
i=18.2° scattering	18.7 ± 12.3 (-1120795.3)	1514 (0)	1451 (0)
i=18.2° no scattering	-153.7±41.7 (-1120965.7)	1426 (0)	1539 (4)
i=45° scattering	0 (-1120814.3)	2965 (0)	0 (0)
i=45° no scattering	-201.5±39.7 (-1121013.0)	1353 (0)	1612 (5)
i=70° scattering	-40.7±11.3 (-1120855.8)	1389 (0)	1576 (0)
i=70° no scattering	-256.3±42.6 (-1121080.5)	1303 (0)	1662 (7)

the 18.2° inclination is slightly favoured with a $\log \mathcal{Z}$ difference of 18.7 ± 12.3, although the uncertainty is large. The 70° inclination is performing worse with a $\log \mathcal{Z}$ difference of -40.7 ± 11.3.

We compare the column density distributions obtained by the different model setups in Figure 3.2. These histograms are constructed using the median of the corresponding $N_{\rm H}$ posterior distribution for each source. The resulting $N_{\rm H}$ distribution is not sensitive to the adopted model setup. Table 3.5 further explores differences in the total number of CTK AGN among the diverse model setups. The number of CTK sources decreases slightly with the increasing inclination angle, but overall, all six models yield similar numbers of CTK sources. Moreover, most of these CTK sources (a total of 222) are common in all six model setups. The fraction of CTK sources also decreases by $\sim 1\%$ when the model does not have a scattering component. One can also look at the posterior distribution instead of the median values to get a more nuanced estimation of the Compton-thickness of the sample. We simply average the fraction of the posterior distribution in the CTK

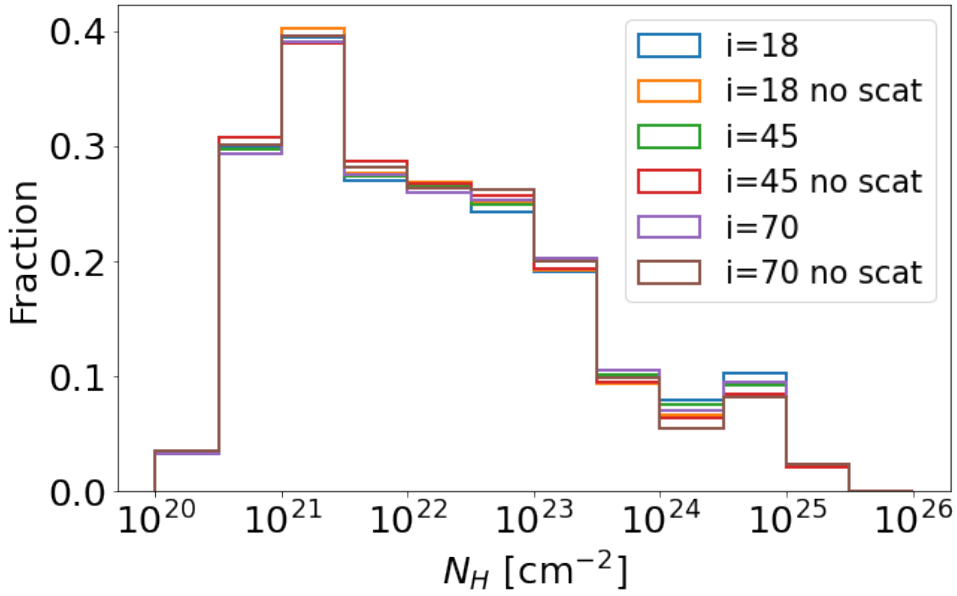

Figure 3.2: $N_{\rm H}$ distribution for different inclination angles and scattering parameters in the UXCLUMPY model. There are no significant differences between the different model setups.

.

regime for each source. We see that the similarities among the different model setups are maintained.

Based on the analysis above, our baseline X-ray spectral model includes a soft-scattering component, which is strongly favoured by the data, and assumes an inclination angle fixed to 45°. Although the evidence analysis shows a weak preference for lower inclinations angles (18.2°; nearly face-on orientation), we opt for the intermediate group of sight-lines in UXCLUMPY (the 30-60° bin) that probe a wider range of column densities between the central engine and the observer. Figure 3.2 nevertheless demonstrates that our results are not sensitive to the inclination angle choice.

3.3.4 Comparison with Previous Studies

This Section compares the physical parameters inferred by our X-ray spectral analysis with those derived in previous studies using the *Chandra* COSMOS-Legacy data. Since one of the main motivations of our work is the characterization of the LOS obscuration of AGN, we limit this comparison to the hydrogen column density. Marchesi et al. (2016b) fit the X-ray spectra of *Chandra* Legacy sources with more than 30 net counts in the

Table 3.5: CTK sources for each X-ray spectral model setup. The first and second column provides a description of the model setup. The third column is the number of sources with median posterior $N_{\rm H} > 10^{24}\,{\rm cm}^{-2}$ and, in parenthesis, the fraction of the total sample it represents. Finally, the last column shows the averaged fraction of the $N_{\rm H}$ posterior distributions above the CTK limit.

inclination	soft scattering	number of CTK sources	fraction of CTK chains (%)
18.2°	yes	302 (10.2%)	10.9
18.2°	no	266 (9.0%)	9.2
45°	yes	280 (9.4%)	10.5
45°	no	251 (8.5%)	8.6
70°	yes	281 (9.5%)	10.5
70°	no	238 (8.0%)	8.2

0.5-7 keV band using a power-law spectral model modified by photoelectric absorption. The adopted model is valid for moderately obscured AGN ($N_{\rm H} \lesssim 10^{23}\,{\rm cm}^{-2}$) but becomes increasingly inaccurate for higher levels of obscuration. This is because of the increasing importance of the Compton scattering for $N_{\rm H} \gtrsim 10^{23}\,{\rm cm}^{-2}$ and degeneracies between the fitted parameters, i.e. power-law photon index and absorbing column density. L18 updates the spectral analysis results of Marchesi et al. (2016b) for sources that show evidence of high levels of LOS obscuration. AGN with an estimated spectral index < 1.4 or a hydrogen column density $N_{\rm H} > 10^{23}{\rm cm}^{-2}$ are selected. This subsample is refitted using the MYTORUS physically-motivated model (Murphy & Yaqoob, 2009) that includes processes such as Compton scattering and fluorescent line emission assuming a toroidal obscurer geometry. L18 presents the physical properties of 1832 sources within the *Chandra* Legacy survey. It includes the original results of Marchesi et al. (2016b) updated with the MYTORUS model fitting results for the obscured candidates. This catalogue is cross-matched with ours within 1.7 arcsec to yield a total of 1805 common sources. A larger radius would not significantly increase the source numbers (1814 sources at 2 arcsec) and would lead to source misidentification with several sources matched to the same source.

Figure 3.3 compares the $N_{\rm H}$ values obtained for our baseline model using BXA with those from L18. At moderate obscuration, there is overall good agreement between the independently estimated $N_{\rm H}$ values. The L18 spectral catalogue also includes a large number of AGN for which the absorbed power-law fits of Marchesi et al. (2016b) yield an upper limit to the column density. The bulk of these sources are associated with unob-

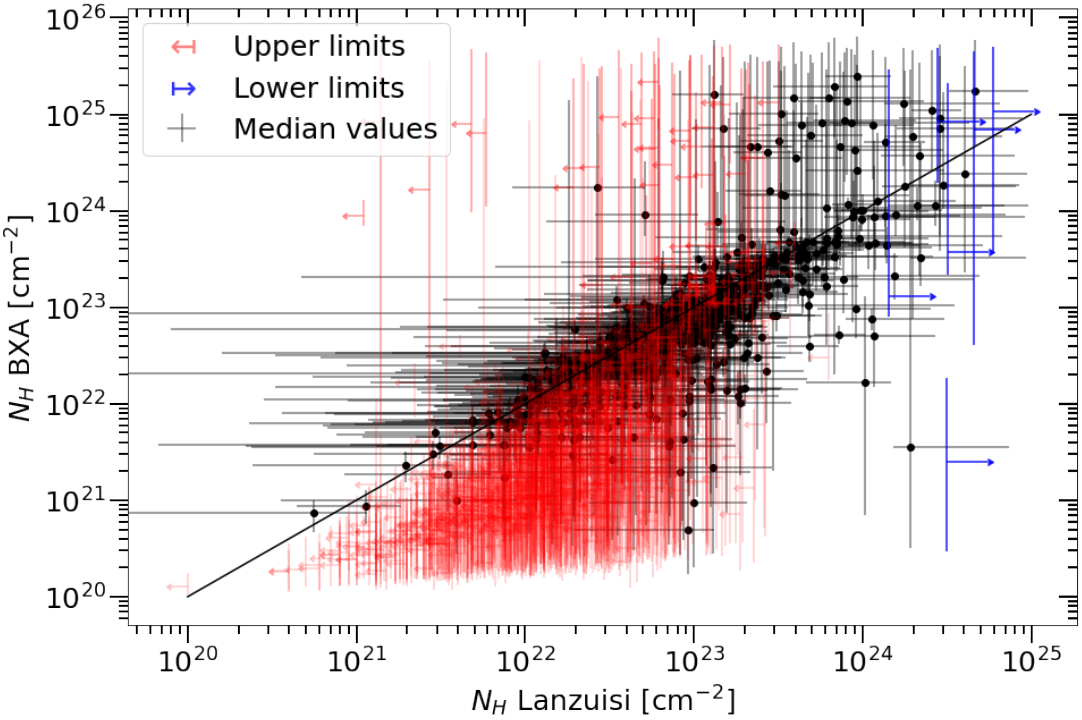

Figure 3.3: $N_{\rm H}$ values from our model compared to the best-fit $N_{\rm H}$ values from L18. The *black dots* represent the median values of our BXA fit estimations and their error bars represent their 1σ uncertainties. The *red* (*blue*) *arrows* are upper (lower) $N_{\rm H}$ estimates in L18.

scured AGN in our spectral analysis, with column densities $N_{\rm H} \lesssim 10^{22}\,{\rm cm}^{-2}$. Figure 3.3 further shows that it is in the CTK regime that the most significant discrepancies between our results and those of L18 appear.

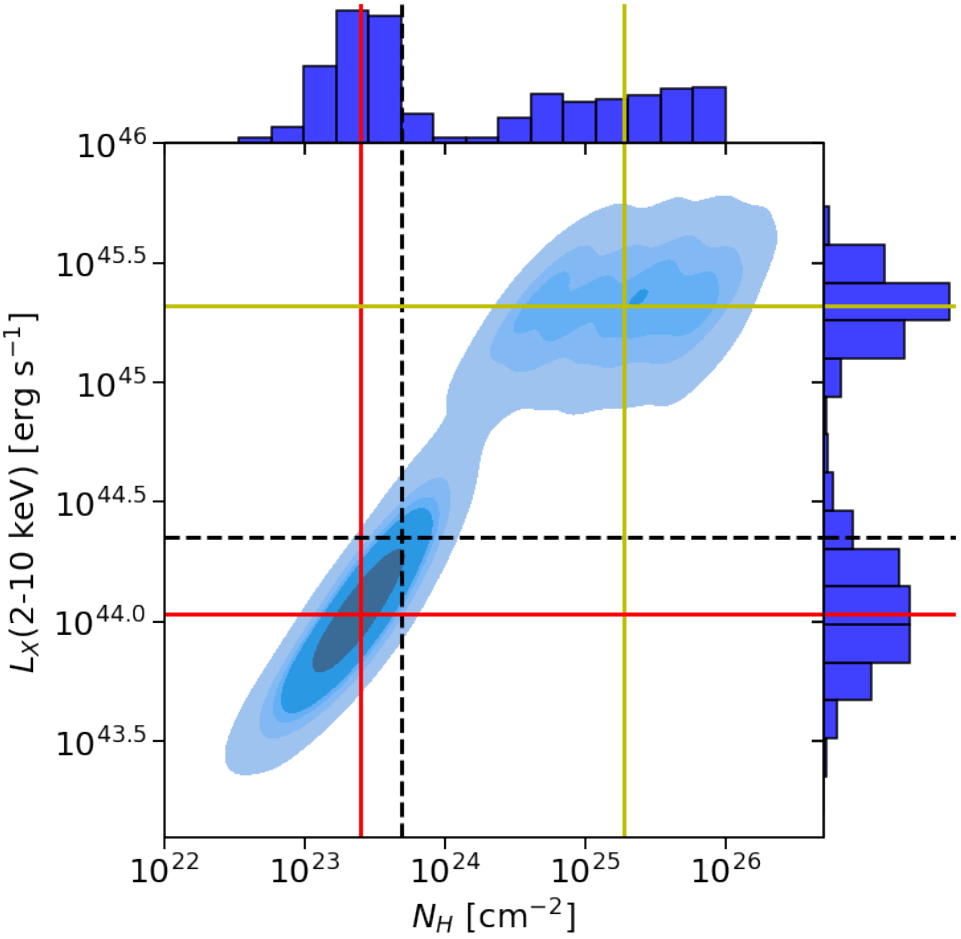

Figure 3.4: Density plot of the posterior probability distribution of the X-ray luminosity $\log L_{\rm X,\,2-10\,keV}$ as a function of the column density $\log N_{\rm H}$ for the source COSMOS_1_420. The 1-dimensional projections of the posterior on the X-ray luminosity and column density axes are shown on the right and top panels, respectively. The median values are plotted in *dashed black lines*, whereas the CTN and CTK median solutions are plotted with the *red* and *yellow solid lines*, respectively.

There are 34 L18 sources with best-fitting $N_{\rm H}$ in the CTK regime compared to 75 AGN in our analysis with median hydrogen column densities distribution $N_{\rm H} > 10^{24}\,{\rm cm}^{-2}$ (19 in common). Many of the 75 sources have broad $N_{\rm H}$ PDFs that extend below $10^{24}{\rm cm}^{-2}$ into the CTN regime but still heavily obscured. As an example, the $N_{\rm H}$ PDF of the source COSMOS_1_420 is represented by the upper histogram in Figure 3.4. It shows two distinct peaks, one below $N_{\rm H} = 10^{24}\,{\rm cm}^{-2}$ and a flatter one above this limit. Multinested-sampling

algorithms like Ultranest used by BXA allow us to explore such posterior distributions efficiently. Standard Markov Chain Monte Carlo algorithms may get stuck in one of the local minima and hence yield unimodal posteriors that do not represent the complexity of the system.

Point parameter estimates, like the median $N_{\rm H}$ value plotted in Figure 3.3 are problematic in the case of a multi-modal PDF (e.g. Figure 3.4). Instead, for this class of sources it is more instructive to show both peaks of the PDF. We first define double-peaked sources as those for which the posterior $N_{\rm H}$ distribution includes at least 25% CTK and CTN solutions. For these sources, both $N_{\rm H}$ peaks (connected with a line) are compared in Figure 3.5 with the best-fit $N_{\rm H}$ inferred by L18. In most cases, the one-to-one relation is bracketed by two peaks of the posterior distribution function. We also notice that for a fraction of the double-peaked sources, the CTK part of the posterior distribution function results from small count statistics as 66% of the double-peaked sources have less than 30 counts in the full band. The bi-modality of the posterior distribution can also be an effect of spectral model degeneracies, like the level of obscuration and the intrinsic X-ray luminosity. One option to break the degeneracies would be to use multi-wavelength information to add parameter priors into the spectral analysis to better constrain the physical properties of the sources. This approach is presented in the next section.

3.4 X-ray Spectral Fitting Improvement with Multi-wavelength Information

In the previous section, several sources were identified with broad or multi-modal column density posterior distributions, resulting from degeneracies between model parameters and small photon statistics. Figure 3.4 plots the posterior distribution in the 2-dimensional space of X-ray luminosity and obscuring hydrogen column density for the double-peaked source COSMOS_1_420. The bi-modality in the column density posterior distribution is also seen in the X-ray luminosity PDF of this source. There is a strong positive correlation between these two parameters in the sense that the inferred $L_{\rm X,\,2-10\,keV}$ increases with increasing column density. Indeed, a higher column density requires a higher intrinsic accretion luminosity to compensate for the stronger photon absorption and reproduce

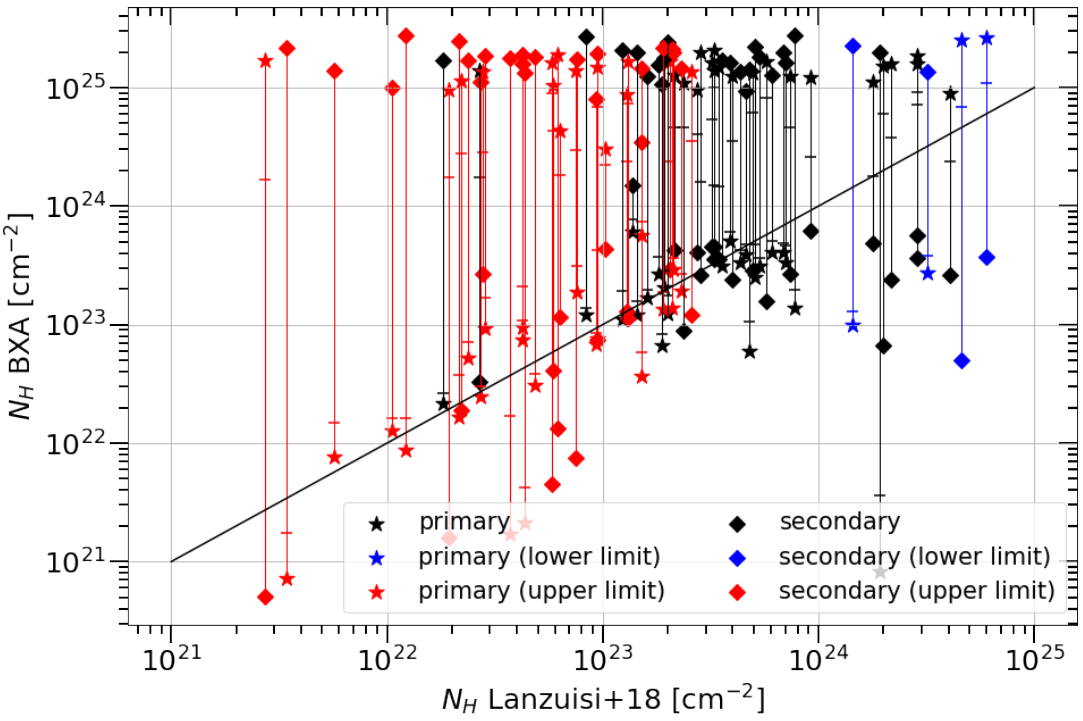

Figure 3.5: Comparison between the best-fit $N_{\rm H}$ determined by L18 and our estimates for AGN with a bi-modal $N_{\rm H}$ posterior PDF in our analysis. For each source, both peaks are plotted and connected with a line. The symbols associated with each peak represent the likelihood of that solution, i.e. the fraction of the posterior associated with the peak in question. *Stars* represent primary peaks (more likely), whereas *diamonds* indicate the secondary (less likely) peaks of the posterior. The *horizontal bars* on the lines connecting two peaks indicate the median from the $N_{\rm H}$ posteriors. The *red* and *blue* colours represent sources that have upper and lower $N_{\rm H}$ limits in L18, respectively. The *black* colours correspond to the best fit $N_{\rm H}$ values in L18.

the observed source flux. An independent estimate of the intrinsic AGN luminosity could therefore provide additional constraints on the X-ray spectral analysis posterior distributions and help break the degeneracies shown in Figure 3.4.

The intuition that X-ray and IR luminosities and LOS obscuration are correlated is not recent, numerous studies in the last 30 years attempted to identify heavily obscured AGN by looking for sources that appear X-ray underluminous for the mid-infrared or optical emission (Risaliti et al., 1999; Alexander et al., 2008; Georgantopoulos et al., 2011). We build upon previous studies but instead of applying strict and arbitrary cuts on the X-ray and IR luminosities ratio to dictate whether a source is CTK or not, we are using the IR luminosity only as a prior in our X-ray spectral analysis. For that purpose, we use the mid-IR νF_ν luminosity at $6\,\mu$m to estimate the intrinsic (unabsorbed) accretion luminosity that is then converted to the intrinsic X-ray luminosity via well-established correlations (e.g. Stern, 2015; Mateos et al., 2015; Chen et al., 2017). The IR-derived X-ray luminosity and uncertainties are then used as a prior to guide the X-ray spectroscopy and improve constraints on the measured obscuration. Our Bayesian approach combines the uncertainties of each measure and proxy relationships in a consistent way throughout our analysis, improving the confidence of our results.

The next Sections describe how templates fits to the observed SEDs of *Chandra* COSMOS-Legacy sources are used to constrain the AGN mid-IR luminosity and how this information feeds back to the X-ray spectral analysis to break parameter degeneracies.

3.4.1 SED Fitting Methodology

SED template fitting is an efficient tool to recover the emission associated with the AGN accretion luminosity, even when the AGN component does not dominate the SED. Observations at mid- and far-IR wavelengths are necessary to separate the AGN emission from the thermal radiation produced by stellar processes. Therefore, we cross-match the positions of the optical counterparts of the *Chandra* COSMOS-Legacy survey X-ray sources with the "super-deblended" far-IR to (sub)millimetre photometric catalogue of (Jin et al., 2018, see Section 3.2). In this exercise, a matching radius of 1.3 arcsec is adopted. For the density of IR sources ($\sim 10^5\,\mathrm{deg}^{-2}$), this search radius corresponds to a spurious fraction of 5.1%. Among the 2965 X-ray sources in our sample, 164 have no counterpart in the Jin

et al. (2018) catalogue. From the remaining 2801 IR associations, 9 sources have redshifts above 4, which is the upper redshift limit of the FortesFit SED fitting algorithm. These sources have not been analysed and are excluded from the sample. This leaves a total of 2792 X-ray sources of *Chandra* COSMOS-Legacy that have been matched with Jin et al. (2018) counterparts and fulfil the redshift criterion for the SED fit.

As explained in the methodology Section 2.4.3, we fit the 2-500 μm SED of these 2792 matched with the Bayesian SED fitting package FortesFit (Rosario, 2019) and using three SED components: the stellar emission (Bruzual & Charlot, 2003), the star formation (Dale et al., 2014) and the AGN model (Mullaney et al., 2011). The setting of the different model parameters are presented in Table 2.7.

3.4.2 Integration of the 6-micron Luminosity Measurements into the X-ray Spectral Analysis

The FortesFit SED code samples the $L_{6\,\mu\mathrm{m}}$ luminosity PDF at the 1st, 16th, 50th, 84th and 99th percentiles. These point estimates are linearly interpolated to reconstruct the $L_{6\,\mu\mathrm{m}}$ luminosity PDFs of the individual AGN of the sample. We caution that the SED fitting approach becomes less efficient in constraining the intrinsic AGN properties if they are weak relative to the stellar emission of the host galaxy. During the SED fit, the AGN $L_{8-1000\mu\mathrm{m}}$ luminosity is a free parameter that has a lower limit of $10^{38}\,\mathrm{erg\,s^{-1}}$. Many X-ray sources have posterior $L_{8-1000\mu\mathrm{m}}$ AGN luminosities that are skewed to this lower boundary. For these sources, the AGN component is essentially not needed to fit the observed SED or, equivalently, the AGN template has a much lower normalisation than the dusty star formation component. In these cases, we use the posterior distribution to determine the 3σ upper limit to the intrinsic AGN luminosity. The empirical criterion adopted to identify such sources is that the 1st percentile of the posterior is lower than $2 \times 10^{38}\,\mathrm{erg\,s^{-1}}$. With this criterion, among the 2792 sources with an SED fit, 1367 are constrained, and 1425 are assigned 3σ upper limits.

Figure 3.6 shows the $L_{\mathrm{X,\,2-10\,keV}}$ as a function of the $L_{6\,\mu\mathrm{m}}$ for the X-ray sources in the *Chandra* COSMOS-Legacy survey. As already demonstrated in previous studies, these two luminosities are well correlated indicating that $L_{6\,\mu\mathrm{m}}$ can be used as a proxy for the intrinsic $L_{\mathrm{X,\,2-10\,keV}}$. Rather than deriving a relation between the X-ray luminosity and the

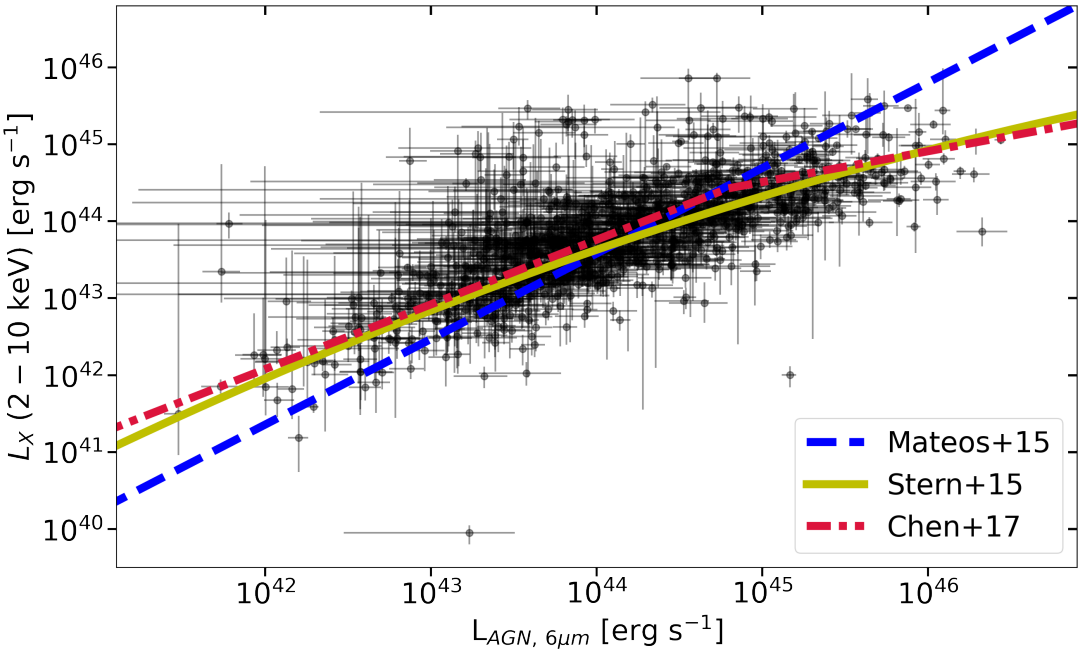

Figure 3.6: AGN X-ray luminosity in the 2–10 keV band (obscuration corrected) vs the AGN νF_ν luminosity at 6 μm. The latter is estimated from the template fits to the observed SED of the X-ray sources in the *Chandra* COSMOS-Legacy field. We choose not to plot the 6 μm luminosity upper limits for the sake of clarity. Sources with multi-modal X-ray luminosity posteriors are also not plotted for the same reason. The *dashed blue*, *solid yellow* and *dash-dotted red lines* correspond respectively to the Mateos et al. (2015), Stern (2015), and Chen et al. (2017) $L_{\mathrm{X,\,2-10\,keV}}$-$L_{6\,\mu\mathrm{m}}$ relationships.

6 μm luminosity from the data plotted in Figure 3.6, we choose to use published relations and test which one describes best our observations. Three recent parametrisations for the $L_{6\,\mu\mathrm{m}}$−$L_{\mathrm{X,\,2-10\,keV}}$ correlation are shown in Figure 3.6. These curves correspond to Equation 3.1 below for the Chen et al. (2017) relation, Equation 3.2 in the case of the Mateos et al. (2015) work and Equation 3.3 for the Stern (2015) sample:

$$l_{\mathrm{X,\,Chen+17}}(l_{6\,\mu\mathrm{m}}) = \begin{cases} 0.84 \cdot (l_{6\,\mu\mathrm{m}} - 45) + 44.6 & \text{if } l_{6\,\mu\mathrm{m}} \leq 44.79 \\ 0.40 \cdot (l_{6\,\mu\mathrm{m}} - 45) + 44.51 & \text{if } l_{6\,\mu\mathrm{m}} > 44.79, \end{cases} \tag{3.1}$$

$$l_{\mathrm{X,\,Mateos+15}}(l_{6\,\mu\mathrm{m}}) = 0.377 + 0.90 \cdot (l_{6\,\mu\mathrm{m}} - 44) + 44\,, \tag{3.2}$$

$$l_{\mathrm{X,\,Stern+15}}(l_{6\,\mu\mathrm{m}}) = 40.981 + 1.024 \cdot (l_{6\,\mu\mathrm{m}} - 41) - 0.047 \cdot (l_{6\,\mu\mathrm{m}} - 41)^2\,, \tag{3.3}$$

with $l_{\mathrm{X}} = \log(\mathrm{L_X\,erg\,s^{-1}})$ and $l_{6\,\mu\mathrm{m}} = \log(\mathrm{L_{6\,\mu m}\,erg\,s^{-1}})$.

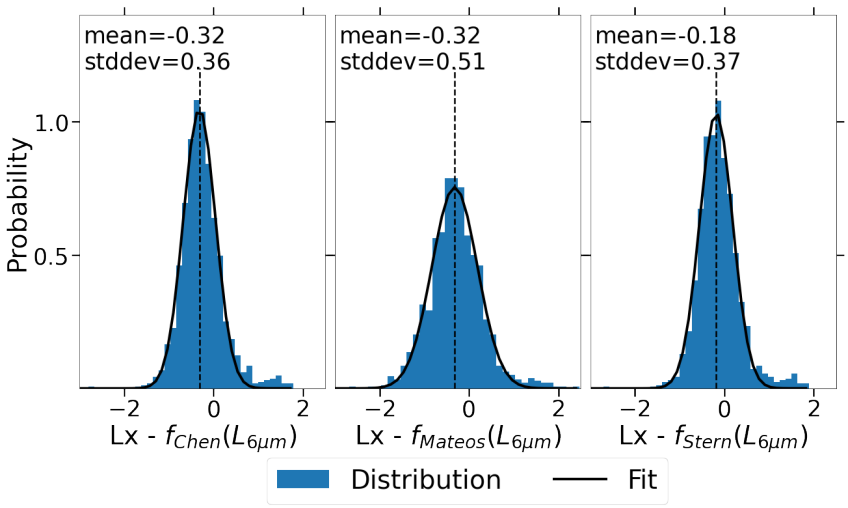

Figure 3.7: Distribution of the difference between the median $\log L_{\mathrm{X,\,2-10\,keV}}$ of the posterior distribution derived by the X-ray spectral analysis and the expected $\log L_{\mathrm{X,\,2-10\,keV}}$ determined from the AGN $L_{6\,\mu\mathrm{m}}$ using the relationships of (Chen et al., 2017, *left panel)*, (Mateos et al., 2015, *middle panel)* and (Stern, 2015, *right panel)*. The best-fit normal distributions are also shown (*black curves*), with their mean represented by a *dashed vertical line*. Their parameters (mean and standard deviation) are also indicated in each panel.

Figure 3.7 shows the offsets distribution between the measured L_{X} and the predicted X-ray luminosity for each of the 3 relations listed above. The offset is the difference between the median of the $\log L_{\mathrm{X,\,2-10\,keV}}$ posterior distribution and the predicted logarithmic luminosity by each relation using the inferred $L_{6\,\mu\mathrm{m}}$ of the sources. The ΔL_{X} distributions are fit with a Gaussian to infer the corresponding mean and scatter. The best-fit parameters are also shown in Figure 3.7. The relations of Chen et al. (2017) and Stern (2015) show a narrower dispersion of the ΔL_{X} distributions than the one by Mateos et al. (2015). Besides, our observations show systematic offsets relative to the Chen et al. (2017) or Mateos et al. (2015) relations. This is smaller in the case of the Stern (2015) relation. We have confirmed that fitting a second-order polynomial to the data points shown in Figure 3.6 yields a $L_{6\,\mu\mathrm{m}}-L_{\mathrm{X,\,2-10\,keV}}$ relation similar to that of Stern (2015). Since the AGN sample used in Stern (2015) is larger than ours, spans a broader luminosity baseline and is independently selected, we choose to use their $L_{6\,\mu\mathrm{m}}-L_{\mathrm{X,\,2-10\,keV}}$ correlation in our analysis. Our final results and conclusions are not sensitive to that choice.

For the SED constrained sources we convert the $L_{6\,\mu\mathrm{m}}$ luminosity PDFs into a $L_{\mathrm{X,\,2-10\,keV}}$

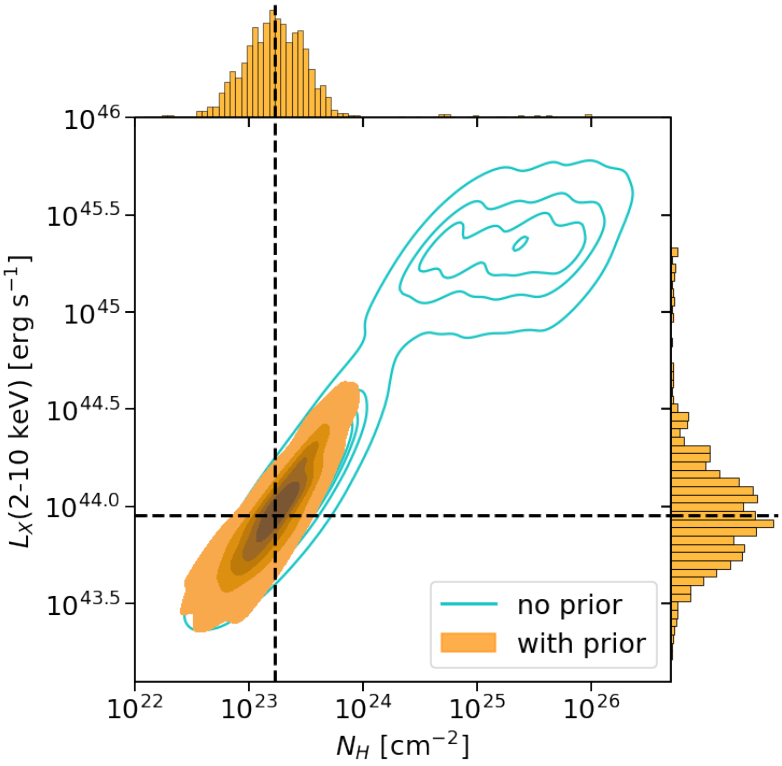

Figure 3.8: Density plot of the posterior distribution of the X-ray luminosity $\log L_{\mathrm{X,\,2-10\,keV}}$ as a function of the column density $\log N_{\mathrm{H}}$ for the source shown in Figures 3.4 and 2.17. The parameter posterior distributions are obtained by X-ray spectral analysis using the $L_{6\,\mu\mathrm{m}}$-based luminosity prior. The 1-dimensional projections of the posterior on the X-ray luminosity and column density axes are shown on the right and top panels, respectively. The median values are plotted in *dashed black lines*. The posterior distribution of the fit without the use of prior is plotted as *cyan contours* in the background.

PDF by using the Stern (2015) relation. We account for the dispersion of this relation by convolving the inferred PDFs with a Gaussian with a 0.4 dex logarithmic standard deviation. The latter value is the dispersion estimated by Stern (2015) and is similar to the standard deviation of our ΔL_{X} distribution in Figure 3.7. In the case of 6 μm AGN luminosity upper limits, we assume that all luminosities below the 3σ upper limits are equiprobable. For this reason, we consider the $L_{6\,\mu\mathrm{m}}$ PDFs to be log-uniform below the upper limits and have a zero-probability for brighter luminosities. We also apply the Stern (2015) relation on it and convolve it with the best fit Gaussian to obtain the L_{X} prior.

The X-ray luminosity is not one of the free parameters of the UXCLUMPY model. Therefore, we translate the X-ray luminosity prior to the UXCLUMPY normalisation parameter prior, which is then applied to the BXA spectral fits. We can then reprocess the X-ray spectra adding the mid-IR information for the selected X-ray AGN. This prior

aims to improve the characterisation of highly obscured AGN and only minimally disrupt the X-ray spectral fits. We, therefore, choose to apply it only to potential CTK sources, defined as those with at least 5% of their posterior $N_{\rm H}$ distribution being above the CTK limit, $10^{24}\,{\rm cm}^{-2}$. This definition is the same as in L18. Changing this cut to 1% or 10% has little impact on the final results. There are 829 CTK candidates among our sources, but 54 of them do not have an IR-counterpart in Jin et al. (2018) catalogue. We then apply our methodology to a sample comprising 775 sources, of which 314 have constrained priors and 461 have upper limits priors.

For the same source shown in Figures 3.4 and 2.17, Figure 3.8 demonstrates how the $\rm L_{6\,\mu m}$-based prior breaks the X-ray spectral modelling degeneracies and improves the column density constraints. Before applying the $L_{6\,\mu\rm m}$-based prior, there is a total of 300 sources with broad or multi-modal X-ray analysis posteriors and IR counterparts. After, only 16 of them remained with multi-modal/broad posteriors. 15 of these sources have less than 35 photons in their X-ray spectra. The lack of certainty in these cases is not surprising, but our methodology nonetheless helps constrain the physical parameters of the bulk of the population.

In Figure 3.9, the $N_{\rm H}$ values obtained from the fit using priors are plotted against the values of L18. The figure is similar to figure 3.3 as we only apply the $L_{6\,\mu\rm m}$-based prior on the potentially CTK sources. There are nonetheless significant differences because our updated spectral fits now yield a smaller number of CTK sources compared to L18. This is because the CTK sources in L18 deviate from the $L_{\rm X} - L_{6\,\mu\rm m}$ correlations (e.g. Stern, 2015) in the sense that they are systematically overluminous at X-rays for their $6\,\mu$m luminosity. This point has been acknowledged by L18, where their CTK sources are systematically offset by more than 1σ from the Stern (2015) relationship (see Figure 4 in L18).

Table 3.6 is an extract of the table summarizing the results of our sample's X-ray spectral analysis after using the $L_{6\,\mu\rm m}$-based prior. The uncertainties of the principal parameters are also indicated. For an overall summary of our sample parameter estimations, Figure 3.10 displays the intrinsic X-ray luminosity (2-10 keV) as a function of the redshift and coloured as a function of the median column density.

Table 3.6: X-ray spectral fitting results. (1) source ID; (2) redshift; (3) redshift type: spectroscopic, photometric or None; (4) X-ray 2-10 keV logarithmic luminosity and its 1-σ uncertainty; (5) logarithmic column density $N_{\rm H}$ and its 1-σ uncertainty; (6) photon index Γ and its 1-σ uncertainty; (7) CTK candidate flag i.e. if the original spectroscopic fit includes more than 5% of its posterior distribution in the CTK regime; (8) double-peaked flag (see definition in Section 3.3.4); (9) source ID_Jin18 in the multi-wavelength catalogue (Jin et al., 2018) if available; (10) logarithmic AGN $L_{6\,\mu\rm m}$ from SED fitting and its 1-σ uncertainty; (11) logarithmic AGN $L_{6\,\mu\rm m}$ upper limit at 99 percentile if the SED fit is unconstrained. Full table electronically available at `https://doi.org/10.5281/zenodo.7014625`.

ID	z	ztype	$\log(L_{\rm X})$ [erg s^{-1}]	$\log(N_{\rm H})$ [cm^{-2}]	Γ	CTK candidate	2-peaked	ID_Jin18	$\log(L_{6\,\mu\rm m})$ [erg s^{-1}]	$L_{6\,\mu\rm m,\,upp.\,lim}$ [erg s^{-1}]
(1)	(2)	(3)	(4)	(5)	(6)	(7)	(8)	(9)	(10)	(11)
COSMOS_0_1	1.342	zphot	$44.25^{+0.08}_{-0.11}$	$21.10^{+0.76}_{-0.76}$	$1.90^{+0.13}_{-0.13}$	False	False	–	–	–
COSMOS_0_10	1.283	zphot	$43.52^{+0.27}_{-0.25}$	$22.38^{+0.36}_{-0.82}$	$1.94^{+0.15}_{-0.14}$	False	False	10043855	–	43.82
COSMOS_0_100	0.582	zphot	$43.01^{+1.18}_{-0.70}$	$22.16^{+0.62}_{-0.31}$	$1.96^{+0.13}_{-0.15}$	False	False	10050161	$42.56^{+0.27}_{-0.19}$	–
COSMOS_0_101	0.619	zphot	$42.98^{+0.12}_{-0.14}$	$22.41^{+0.15}_{-0.19}$	$1.93^{+0.14}_{-0.15}$	False	False	10051883	–	43.14
COSMOS_0_102	0.516	zphot	$42.33^{+0.73}_{-1.17}$	$21.35^{+0.62}_{-0.90}$	$1.93^{+0.14}_{-0.16}$	False	False	–	–	–
⋮	⋮	⋮	⋮	⋮	⋮	⋮	⋮	⋮	⋮	⋮
COSMOS_8_95	2.212	zphot	$44.01^{+0.37}_{-0.93}$	$21.72^{+0.76}_{-1.01}$	$1.87^{+0.14}_{-0.13}$	False	False	10203746	–	44.29
COSMOS_8_96	0.205	zphot	$41.72^{+0.09}_{-0.10}$	$21.37^{+0.35}_{-0.56}$	$1.84^{+0.14}_{-0.13}$	True	True	10203914	$42.34^{+0.10}_{-0.09}$	–
COSMOS_8_97	1.608	zspec	$44.43^{+0.04}_{-0.05}$	$21.57^{+0.42}_{-0.85}$	$1.96^{+0.11}_{-0.11}$	False	False	10204309	$44.63^{+0.18}_{-0.17}$	–
COSMOS_8_98	2.620	zspec	$44.56^{+0.11}_{-0.09}$	$22.00^{+0.67}_{-1.26}$	$1.87^{+0.14}_{-0.14}$	False	False	–	–	–
COSMOS_8_99	0.686	zphot	$42.96^{+0.11}_{-0.15}$	$20.68^{+0.56}_{-0.48}$	$2.05^{+0.13}_{-0.15}$	False	False	20010065	$43.51^{+0.09}_{-0.08}$	–

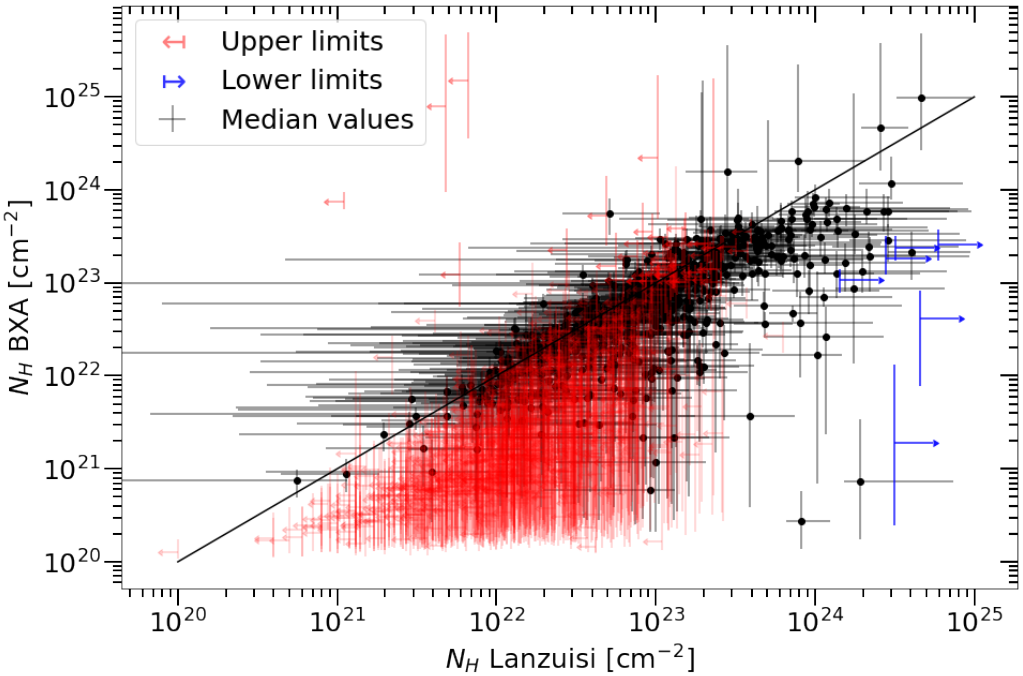

Figure 3.9: Comparison of the $N_{\rm H}$ values derived from our spectral analysis using the $L_{6\,\mu{\rm m}}$ prior (vertical axis) with those derived by L18 (horizontal axis). The *black dots* represent the median values of our spectral fit estimations. The *red* (*blue*) *arrows* are upper (lower) limits in L18.

3.5 Obscured AGN Demographics

3.5.1 Observed Parameter Distribution

One of the motivations of the analysis presented in this Chapter is to place constraints on the demographics of obscured AGN. Therefore, in the next Sections, we focus on the hard-band (2-7 keV) selected sample of the *Chandra* COSMOS-Legacy survey. This is because photons at rest-frame energies $>$ 2 keV can penetrate relatively dense columns of gas clouds, thereby providing a better handle on the obscured AGN population. Figure 3.11 displays the LOS column density $N_{\rm H}$ distribution for all sources selected in the hard X-ray band. The histogram in this figure is constructed from the $N_{\rm H}$ posterior distributions derived by fitting the X-ray spectra of individual COSMOS sources with the baseline X-ray spectral model described in Section 3.3.2 and with the $L_{6\,\mu{\rm m}}$-based prior (i.e. Section 3.4). A bootstrap resampling approach is adopted, whereby the posterior distribution of each X-ray source is resampled with replacement to generate 100 realisations of the population. These are then used to determine, within the different $N_{\rm H}$-bins, the median fraction and

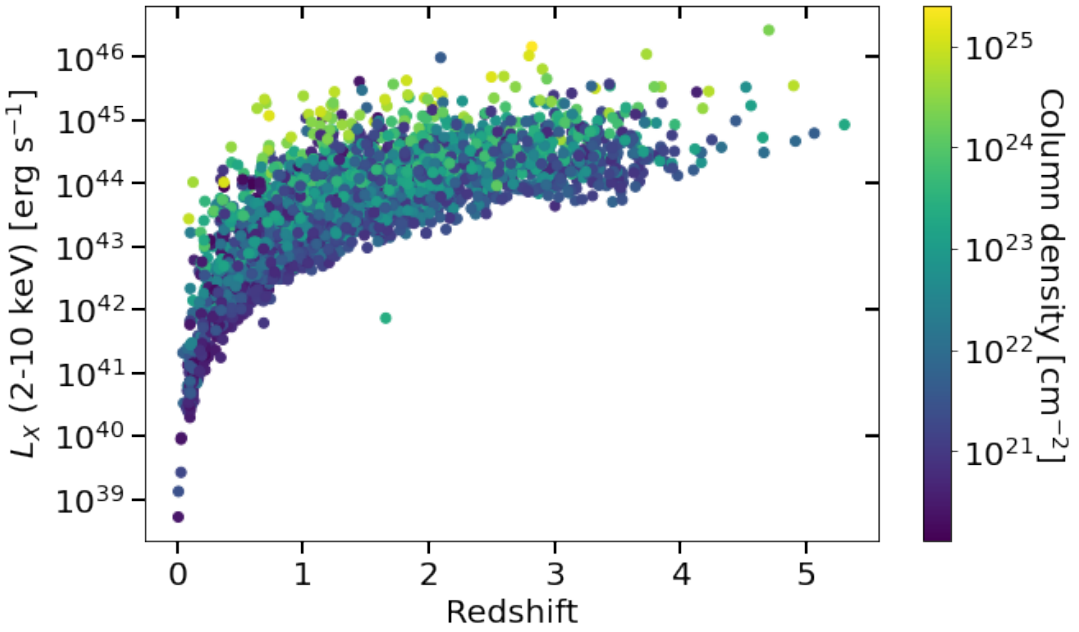

Figure 3.10: Intrinsic X-ray luminosity (2-10 keV) against the redshift for the sources of our sample. The colour indicates the column density of the source in cm^{-2}. The values used in this figure correspond to the median of the posterior distribution of the respective parameters. The points' locations are not very representative in the case of broad distributions, for example, in the case of the outlier source at $z \sim 1.7$ with $L_{\rm X} \sim 10^{42}\,{\rm erg\,s^{-1}}$.

16th and 84th percentiles, corresponding to the 1σ variation lower and upper limits. Figure 3.11 shows that our sample includes a large observed fraction of obscured AGN ($59.7^{+0.2}_{-0.7}\%$) with LOS column densities $\rm N_H > 10^{22}\,cm^{-2}$. However, the sensitivity of this survey drops close to and above the CTK limit. This is evident from the decreasing fraction of AGN in Figure 3.11 toward column densities $\rm N_H \approx 10^{24}\,cm^{-2}$.

We also over-plot in Figure 3.11 the predictions from X-ray Luminosity Function (XLF) models in the literature, Ueda et al. (2014), Aird et al. (2015) and Buchner et al. (2015). The XLFs encapsulate the intrinsic number of sources as a function of their physical properties (obscuration, X-ray luminosity and redshift). To convert these intrinsic source numbers into observed source numbers, we need to convolve them with the *Chandra* sensitivity maps. To calculate the sensitivity maps, we use the UXCLUMPY model to predict the expected *Chandra*/ACIS photon rate for an AGN of a given redshift, 2-10 keV luminosity and absorbing hydrogen column density. For the calculation of photon rates, we assume a Gaussian photon index distribution (mean 1.9, scatter 0.15) for UXCLUMPY

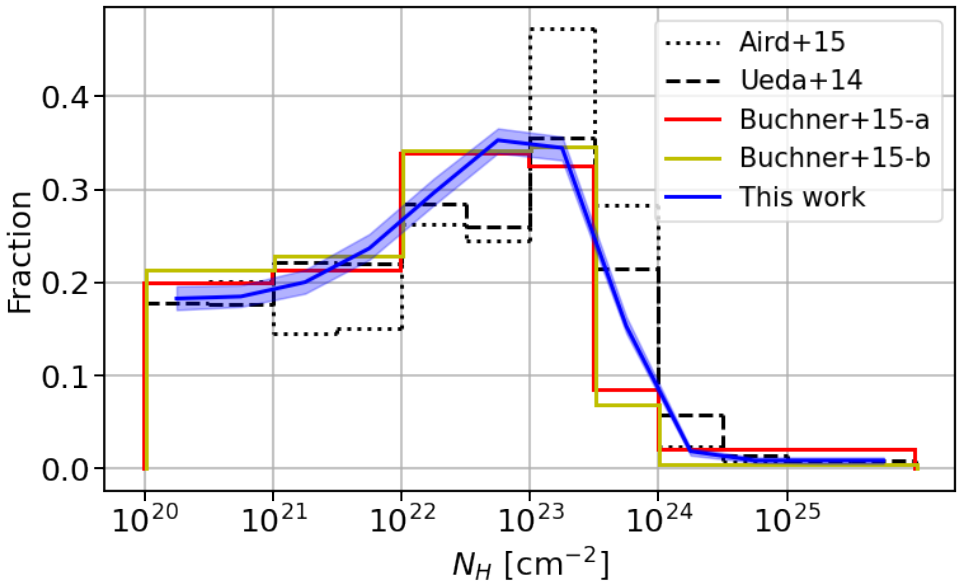

Figure 3.11: $N_{\rm H}$ distribution of the hard band detected sources in the *Chandra* COSMOS-Legacy field. The *thick blue line* corresponds to the constraints from our X-ray spectral analysis. It represents the median of the bootstrap resampling approach described in the text. The *light blue shaded region* corresponds to the 68% confidence interval around the median. The *black dotted* line and the *black dashed histograms* show the predicted $N_{\rm H}$ distributions obtained using the (Aird et al., 2015) and (Ueda et al., 2014) luminosity functions, respectively. The *red* and *yellow lines* represent the redshift distribution estimated in (Buchner et al., 2015) obtained by using a constant-value prior and a constant-slope prior, respectively.

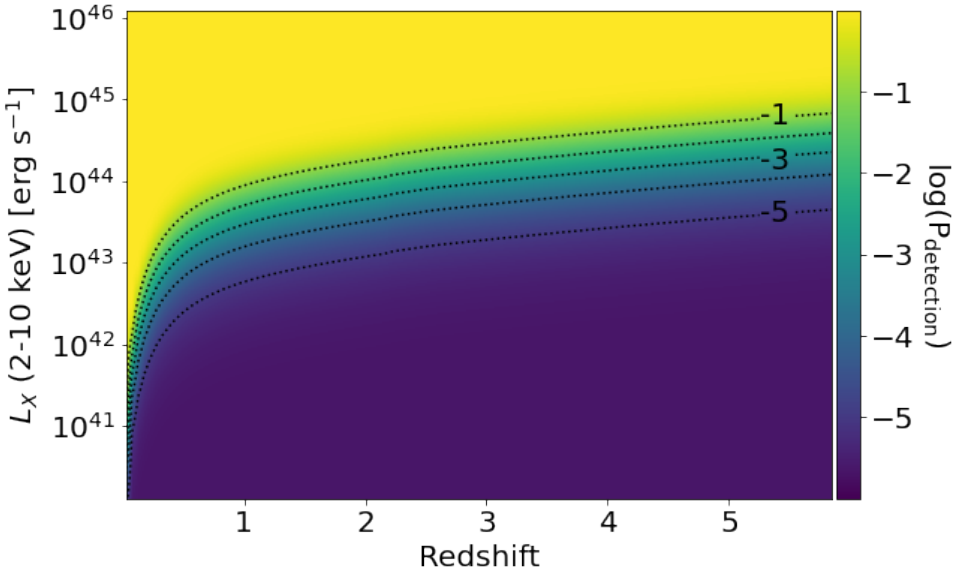

Figure 3.12: Sensitivity map showing the probability of detection of a CTK source with $\log(N_{\rm H}) = 24.1\,{\rm cm}^{-2}$ within *Chandra* COSMOS-Legacy as a function of its intrinsic X-ray luminosity and redshift. The probability is given on a logarithmic scale. The *black dotted lines* indicate detection probabilities from 10^{-1} (top) to 10^{-5} (bottom) in logarithmic steps of 1 dex. As expected, the detection probability rapidly decreases with the increasing redshift and increases with the luminosity.

and a soft-excess component logarithmic normalisation that is uniformly distributed in the range $10^{-7}-10^{-1.5}$. We marginalise over these two parameters to calculate the average photon rate $\nu(z, L_{\rm X}, N_{\rm H})$. This can then be converted into the area over which such a source can be detected by using the COSMOS-Legacy sensitivity curve presented in the methodology Section 2.3.1. The end products of these calculations are cubes describing the survey area available to sources as a function of $L_{\rm X}$, z, $N_{\rm H}$. By normalising them, one obtains the detection probability of a source as a function of its intrinsic characteristics. Figure 3.12 shows the 2-dimensional projection of such a cube on the redshift-luminosity plane for a CTK source with $N_{\rm H} = 1.26\times10^{24}\,{\rm cm}^{-2}$. This figure shows that the probability of detecting such a source decreases toward lower luminosities and higher redshift. The analytic XLFs are convolved with the sensitivity maps and then integrated over luminosity and redshift to yield the predictions on the number of AGN as a function of $N_{\rm H}$ in Figure 3.11.

The comparison with predictions is intended to guide the expected $N_{\rm H}$ distribution of AGN in the COSMOS field based on established knowledge of their demographics. We

caution that comparing these model predictions and the observations should be taken with a grain of salt. This is because the histogram of the posteriors in Figure 3.11 represents the convolution of the intrinsic column density distribution of AGN with the observational uncertainties. Instead, the model XLFs do not include such errors. It is nevertheless interesting that the overall shape of the model/observed column density distributions is similar. There is an increase in the number of sources with increasing column density to $\log N_{\rm H}/{\rm cm}^{-2} \approx 23.5$ followed by a steep decline for higher levels of obscuration.

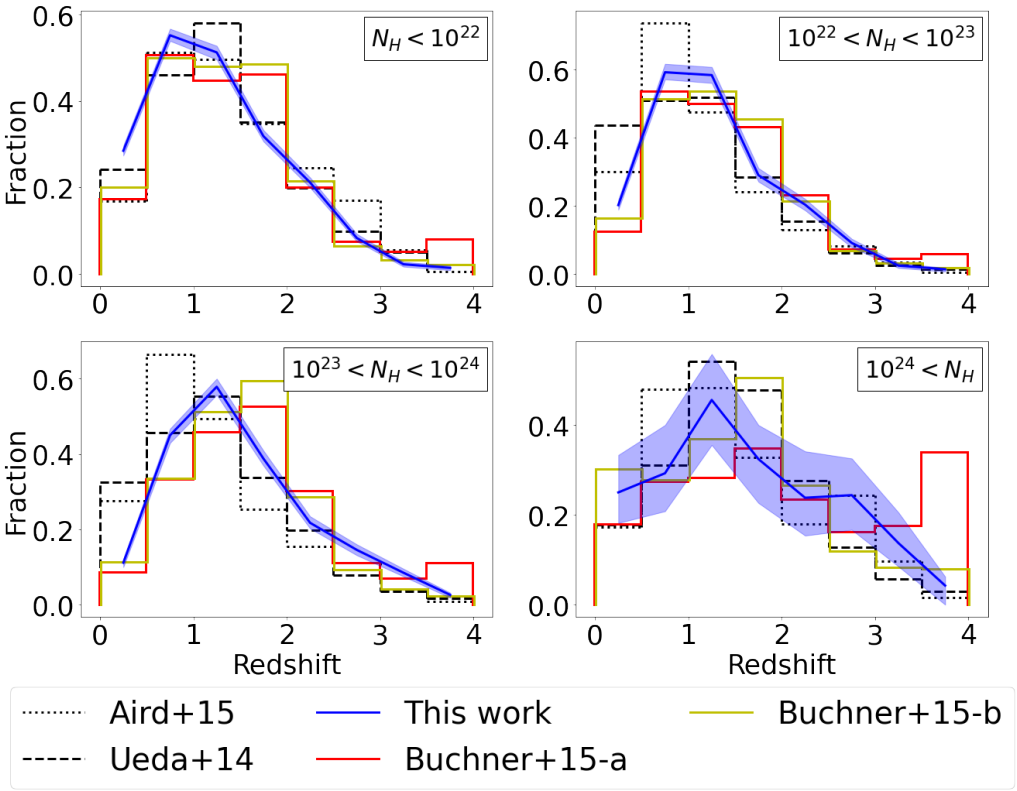

Figure 3.13: Redshift distributions of the hard band detected sources in the *Chandra* COSMOS-Legacy field. Each panel corresponds to a different $N_{\rm H}$ interval. The *thick blue line* is the median of the bootstrap resampling approach described in the text. The *light blue shaded region* corresponds to the 68% confidence interval around the median. When available, the redshift information comes from spectroscopy or otherwise from the redshift posterior distributions generated by the X-ray spectral fitting analysis using the photometric redshift distribution as a prior. The *black dotted line* and the *black dashed histograms* show the predicted $N_{\rm H}$ distributions obtained using the Aird et al. (2015) and Ueda et al. (2014) luminosity functions, respectively. The *red* and *yellow lines* represent the redshift distribution estimated in Buchner et al. (2015) obtained by using a constant-value prior and a constant-slope prior, respectively.

Figure 3.13 further explores the redshift distribution of the AGN for different $N_{\rm H}$ intervals. In this plot, our histograms are constructed using the same bootstrapping method-

ology described above. Both the model and the observed distributions in Figure 3.13 show a broad peak at $z \sim 1$ and a decline to higher redshift. This behaviour can be explained by the overall redshift evolution of the X-ray luminosity function and the flux limit of the COSMOS-Legacy survey, which yields increasingly smaller AGN samples at higher redshift. This trend is broadly reproduced by the XLFs of Ueda et al. (2014), Aird et al. (2015) and Buchner et al. (2015).

3.5.2 Space Density Measurements

This Section describes how the X-ray spectral analysis results are combined with the X-ray selection function of the COSMOS-Legacy survey for the hard band-selected sources, to determine the space density of AGN as a function of the redshift z, X-ray luminosity $L_{\mathrm{X,\,2-10\,keV}}$, and column density N_H.

Given a model of AGN space density, $\phi(L_{\mathrm{X}}, z, N_{\mathrm{H}})$, described by a set of parameters, Ψ, the likelihood of a given a set of observations, D, is described by the product of the Poisson probabilities of individual sources:

$$\mathcal{L}(D|\Psi) = e^{-\lambda} \prod_{i}^{n} \int d\log L_{\mathrm{X}} \int d\log N_{\mathrm{H}} \int \frac{dV}{dz} dz \; p(z, L_{\mathrm{X}}, N_{\mathrm{H}}|D_i)\phi(L_{\mathrm{X}}, z, N_{\mathrm{H}}|\Psi)\,, \quad (3.4)$$

where n is the number of individual sources in the field, i is their index, $\frac{dV}{dz}$ is the differential co-moving volume. Then, $p(z, L_{\mathrm{X}}, N_{\mathrm{H}}|D_i)$ is the probability that a source has a luminosity L_{X}, a redshift z, and column density N_{H}. It encapsulates the uncertainty of deriving these values from the observations, i.e. from X-ray spectral analysis or in the case of photometric redshifts from the multi-waveband SED fits. The quantity λ is the expected number of AGN in the survey as a function of the parameters set and is defined as

$$\lambda = \int d\log L_{\mathrm{X}} \int d\log N_{\mathrm{H}} \int \frac{dV}{dz} dz\, A(z, L_{\mathrm{X}}, N_{\mathrm{H}})\phi(L_{\mathrm{X}}, z, N_{\mathrm{H}}|\Psi)\,, \quad (3.5)$$

where $A(z, L_{\mathrm{X}}, N_{\mathrm{H}})$ is the sensitivity curve representing the area of the survey for which a source with z, L_{X} and N_{H} can be detected and its calculation is described in Section 3.5.1.

We decide to use a non-parametric approach to determine the luminosity function

(following Buchner et al., 2015; Georgakakis et al., 2017c). The z, $L_{\rm X}$, $N_{\rm H}$ parameter space is divided into a 3-dimensional grid, and in each grid cell, the luminosity function is assumed to be constant. Using such a non-parametric approach allows the space density to vary more freely and eventually find large variations of shape across the parameter grid. The edges of the grid pixels in each of the three dimensions are $\log(L_{\rm X}/{\rm erg\,s^{-1}})$ = [40.0, 41.0, 42.0, 42.5, 43.0, 43.5, 44.0, 44.5, 45.0, 46.0, 47.0], z=[0.0, 0.5, 1.0, 1.5, 2.0, 2.5, 3.0, 6.0] and $\log(N_{\rm H}/{\rm cm^{-2}})$ = [20.0, 22.0, 23.0, 24.0, 26.0]. The total number of free parameters is 280. The likelihood (Equation 3.4) is integrated using the principle of the Importance sampling (Press et al., 1992). It is also worth emphasising that in the Bayesian framework of Equation 3.4 the posterior distribution $p(z, L_{\rm X}, N_{\rm H}|D_i)$ of a given source (i.e. contours and shaded regions in Figures 3.4 and 3.8) is weighted by the luminosity function $\phi(L_{\rm X}, z, N_{\rm H})$ when estimating the likelihood. Non-physical posterior solutions, e.g. very high AGN luminosities, can therefore be weighted down a posteriori because they are rare. This is the case of parametric XLF studies that typically assume a double power-law form with a relatively steep bright-end slope. In our non-parametric approach, however, there is no imposed shape, and the AGN space density at each grid point is independently determined. In that respect, our analysis is more sensitive to broad $p(z, L_{\rm X}, N_{\rm H}|D_i)$ posteriors like those shown in Figure 3.4. We nevertheless compensate for that using the multi-wavelength priors described in Section 3.4 to narrow down the X-ray spectral analysis posteriors of the sample sources.

We use STAN, a Hamiltonian Markov chain Monte Carlo code (Carpenter et al., 2017) to sample the likelihood (Equation 3.4) in a Bayesian framework and to obtain the space density posterior distribution for each cell of the 3-dimensional parameter grid. The resulting space density measurements are displayed in Figure 3.14 and compared with different X-ray luminosity functions in the literature. We limit this comparison to $z < 2$, where the COSMOS-Legacy survey provides strong constraints. At higher redshift, the number of X-ray AGN in our sample decreases rapidly, and our space density measurements suffer larger uncertainties.

Our space density measurements have a broad overall agreement with previous studies. In detail, however, there are subtle differences. For example, in the case of unobscured AGN, $N_{\rm H} < 10^{22}\,{\rm cm^{-2}}$, our constraints lie systematically lower than the analytic XLFs

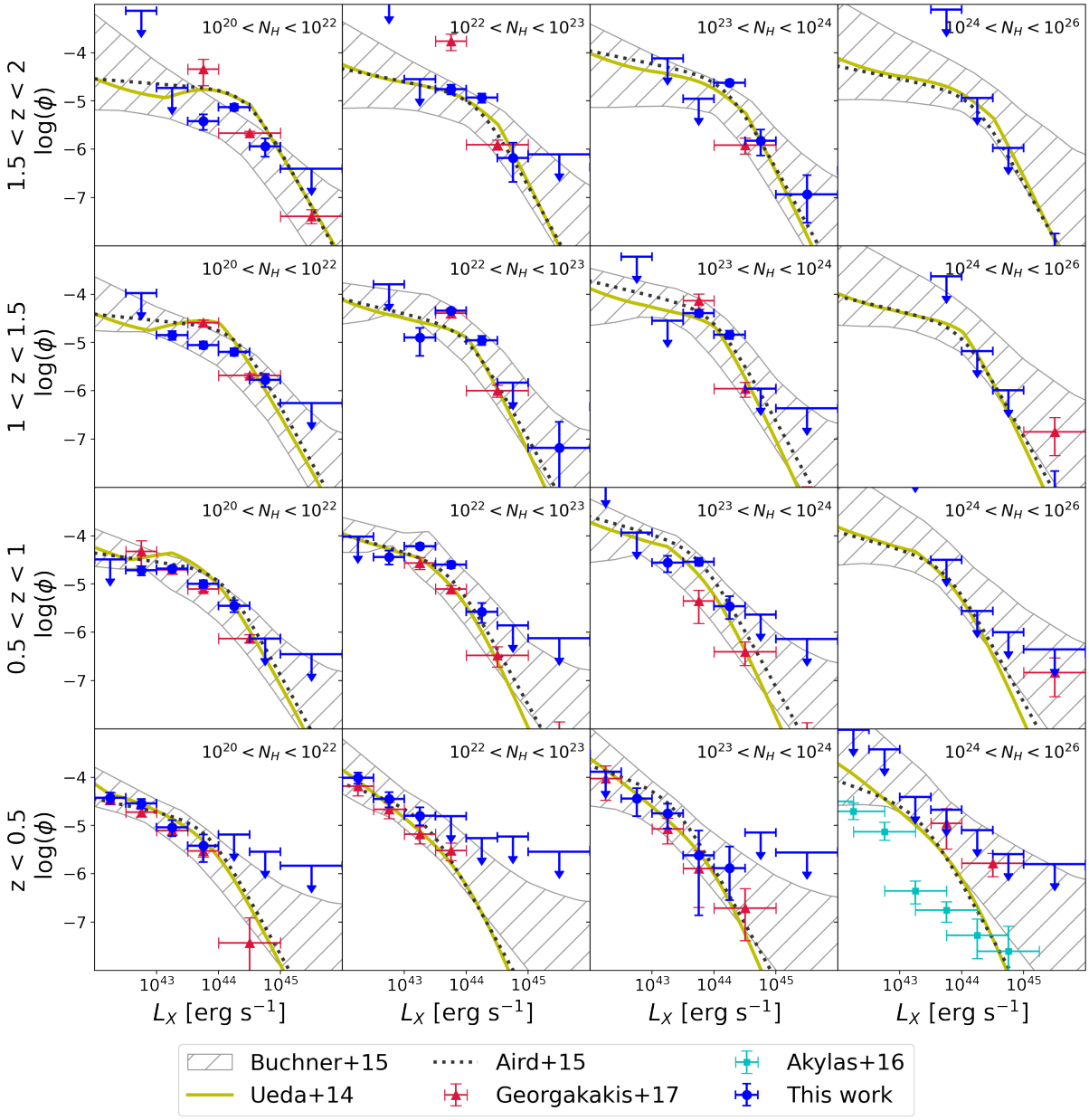

Figure 3.14: Space density curves ($\mathrm{Mpc}^{-3}\,\mathrm{dex}^{-2}$) as a function of the intrinsic X-ray luminosity in the 2-10 keV band for different redshift and column density intervals. The redshift range of each panel row is indicated on its left side. From top to bottom, the rows correspond to $z = 1.5 - 2$, $z = 1 - 1.5$, $z = 0.5 - 1$ and $z = 0 - 0.5$. The column density increases from left to right, as indicated at the bottom of each column. The constraints from our analysis are shown with the *blue dots* and associated with 1σ uncertainties and, in the case of the upper limits, with the *blue arrows* pointing down. A space density is considered an upper limit if its 1σ uncertainty width is larger than 2 dex. These upper limits correspond to the 3σ confidence interval. The *yellow solid line* and the *black dotted line* correspond to Ueda et al. (2014) and Aird et al. (2015) luminosity functions, respectively. The *grey hatched area* represents the non-parametric constraints of Buchner et al. (2015). The *red triangles* are the luminosity function measured by Georgakakis et al. (2017c) in the XMM-XXL field (Pierre et al., 2016). The CTK luminosity function determined by Akylas et al. (2016) in the local Universe is shown with the *cyan squares*.

of Ueda et al. (2014) and Aird et al. (2015), particularly for luminosities $L_{\mathrm{X,\,2-10\,keV}} \approx 10^{43} - 10^{44}\,\mathrm{erg\,s^{-1}}$. This trend is stronger for the redshift intervals $z = 0.5 - 1$ and $1 - 1.5$ but is also evident in other redshift bins. For moderately obscured AGN in the range $N_{\mathrm{H}} = 10^{22} - 10^{23}\,\mathrm{cm^{-2}}$, our measurements are instead systematically higher than those of the analytic XLFs of Ueda et al. (2014) and Aird et al. (2015). These differences are partly related to the fact that the N_{H} constraints in these earlier studies are largely based on hardness ratios, which have limited discriminating power for AGN close to the $10^{22}\,\mathrm{cm^{-2}}$ limit. It is nevertheless reassuring that for the integrated space densities in the interval $N_{\mathrm{H}} = 10^{20} - 10^{23}\,\mathrm{cm^{-2}}$, the agreement between our analysis and the analytic studies above is good. In any case, these differences also highlight the importance of fully non-parametric XLF approaches, like the one presented here, to supplement and guide analytic prescriptions. In the CTK regime, our analysis only yields upper limits in the AGN space density because of the low number of CTK sources in our sample. Nevertheless, the 3σ upper limits, particularly at $z > 0.5$, favour CTK space densities at the low-end of the range covered by the previous observational constraints shown in Figure 3.14.

3.5.3 Compton-Thick Fraction

The intrinsic CTK fraction, f_{CTK}, is an important parameter for characterizing the demographics of heavily obscured AGN. In our analysis, this is defined as the ratio between the number of AGN with column density $N_{\mathrm{H}} = 10^{24} - 10^{26}\,\mathrm{cm^{-2}}$ and those with $N_{\mathrm{H}} = 10^{20} - 10^{26}\,\mathrm{cm^{-2}}$:

$$f_{\mathrm{CTK}} = \frac{N_{24-26}}{N_{20-22} + N_{22-23} + N_{23-24} + N_{24-26}}\,. \tag{3.6}$$

In the equation above, N refers to the intrinsic number of AGN at different logarithmic column density intervals. For the estimation of f_{CTK}, we slightly modify the X-ray luminosity function model used in the Bayesian inference methodology. The space density of CTK AGN at all redshift and luminosity intervals is linked to that of CTN AGN via Equation 3.6 where f_{CTK} is a free parameter of the model. After some algebra, the CTK

space density is estimated as

$$\begin{aligned}\phi(L_{\rm X}, z, \log N_{\rm H} = 24-26) = \frac{f_{\rm CTK}}{2\cdot(1-f_{\rm CTK})}\cdot \\ \Big(2\cdot\phi(L_{\rm X}, z, \log N_{\rm H} = 20-22)+ \\ \phi(L_{\rm X}, z, \log N_{\rm H} = 22-23)+ \\ \phi(L_{\rm X}, z, \log N_{\rm H} = 23-24)\Big).\end{aligned} \tag{3.7}$$

The multiplicative factors of 2 in the above equation account for broader logarithmic column density intervals for CTK ($\log N_{\rm H}/{\rm cm}^{-2} = 24-26$) and unobscured ($\log N_{\rm H}/{\rm cm}^{-2} = 20-22$) AGN. The $f_{\rm CTK}$ is assumed here to depend only on the redshift but not on the luminosity. This is equivalent to assuming that at fixed redshift, the CTK luminosity function is related to the CTN one via a scaling factor (e.g. Aird et al., 2015). The $f_{\rm CTK}$ parameter is therefore independently determined for each of the redshift intervals adopted in Section 3.5.2 with edges $z = [0.0, 0.5, 1.0, 1.5, 2.0, 2.5, 3.0, 6.0]$. The STAN Hamiltonian Markov chain Monte Carlo code then yields a posterior distribution of the $f_{\rm CTK}$ for each of the redshift intervals above.

Figure 3.15 plots the posterior distribution of the $f_{\rm CTK}$ inferred from our analysis as a function of redshift for the hard band selected AGN. This parameter is constrained to be $21.0^{+16.1}_{-9.9}\%$ (1σ) for the lowest redshift interval $z = 0-0.5$. At higher redshifts, only upper limits to $f_{\rm CTK}$ can be securely derived. Also shown in Figure 3.15 are previous results on the CTK fraction that demonstrate the range of values covered by different studies. At $z = 0-0.5$, our analysis favours CTK fractions at the low end of the distribution of $f_{\rm CTK}$ in the literature. At higher redshift, our 3σ upper limits are generous, but at least for $z \lesssim 2$, suggest $f_{\rm CTK} \lesssim 40\%$.

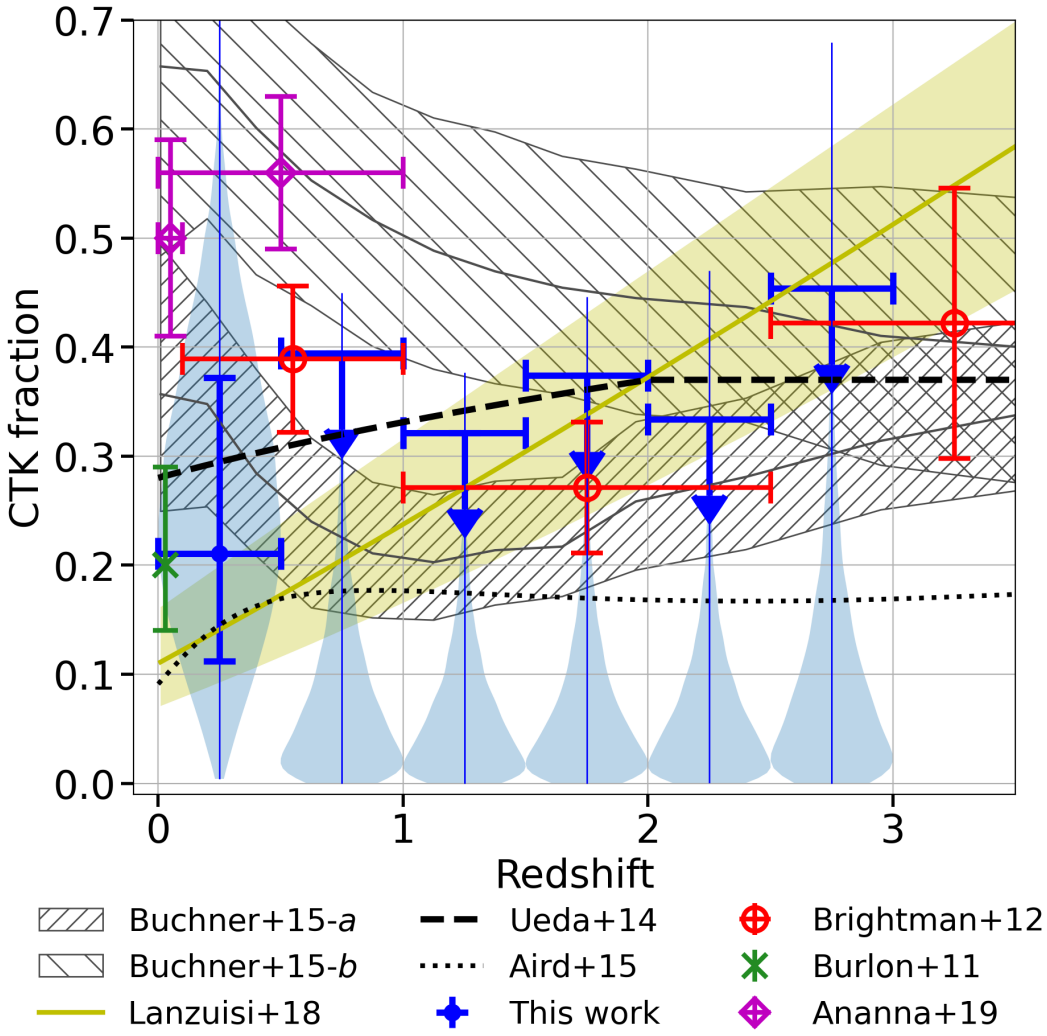

Figure 3.15: Intrinsic CTK fraction as a function of redshift. The *blue violin plots* represent the posterior distribution of our analysis. At $z < 0.5$, the mode of our posterior distribution and the associated 68% confidence interval are indicated by the *blue dot* and its error bars. At higher redshift intervals, the *downward blue arrows* correspond to the 3σ upper limit estimated from the corresponding posterior distributions. The *vertically* (Buchner+15-a) and *horizontally* (Buchner+15-b) *hatched shaded regions* represent the 1σ uncertainty of the CTK fractions presented in Buchner et al. (2015) obtained by using a constant-value prior and a constant-slope prior, respectively. The *solid line* within these regions corresponds to the median. The CTK fraction of the Ueda et al. (2014) and Aird et al. (2015) X-ray luminosity functions are shown with the *black dashed* and the *black dotted lines*, respectively. The *green cross* at $z \sim 0$ is the measured CTK fraction in the local Universe determined by Burlon et al. (2011). The *red circles* are the results of Brightman & Ueda (2012). The *yellow shaded region* is the CTK fraction estimation by L18. The *pink diamonds* correspond to the CTK fraction estimated by Ananna et al. (2019) at redshift $z < 0.1$ and $z < 1.0$.

3.6 Discussion

3.6.1 Obscuration Characterisation

A multi-wavelength Bayesian approach is presented that combines X-ray spectral fits with information from mid-IR wavelengths to constrain the level of LOS obscuration of AGN. This is motivated by the need to resolve degeneracies between two key physical parameters inferred from X-ray spectral analysis, the intrinsic AGN luminosity and the LOS hydrogen column density. These covariances are particularly important for sources with a low number of counts and high levels of obscurations leading to broad or multi-modal posterior distributions. Our methodology addresses this issue by using the mid-IR part of the SED as a prior for the intrinsic AGN luminosity. This is based on the expectation that the short wavelength (X-rays, UV) AGN radiation absorbed by dust and gas clouds emerges as thermal emission in the IR. Support for such an energy balance between different parts of the SED is coming from observed correlations between the intrinsic (i.e. corrected for obscuration) X-ray luminosity and the mid-IR luminosity of AGN (Gandhi et al., 2009; Stern, 2015). These correlations are claimed to apply to AGN over a broad range of LOS obscurations, including CTK sources (Gandhi et al., 2009; Asmus et al., 2015; Annuar et al., 2017). Therefore, our methodology relies on such relations as an independent handle on the intrinsic accretion luminosity, particularly in the case of obscured systems. We caution, however, that in the local Universe, there are (few) examples of heavily obscured (CTK) AGN that appear subdominant in the mid-IR for their intrinsic X-ray luminosity (Krabbe et al., 2001; Gandhi et al., 2015) and, therefore, deviate from the established correlations. For these sources, the mid-IR photons may be absorbed by the obscuring medium. Our methodology is not optimal for this class of AGN.

We apply our approach to X-ray sources in the *Chandra* COSMOS-Legacy survey to constrain in a non-parametric way the space density of AGN in bins of luminosity, redshift and column density. We find small systematic differences between our results and previous parametric estimates of the AGN X-ray luminosity function in the case of unobscured ($N_{\rm H} < 10^{22}\,{\rm cm}^{-2}$) and moderately obscured ($N_{\rm H} = 10^{22} - 10^{23}\,{\rm cm}^{-2}$) systems. This highlights the importance of further work to better constrain the column density

distribution of AGN. Additionally, the *eROSITA* (Predehl et al., 2021) surveys have the potential to address this issue by providing large numbers of moderately obscured AGN out to high redshift and higher $L_{\rm X}$.

At higher but still CTN levels of obscuration ($N_{\rm H} = 10^{23} - 10^{24}\,{\rm cm}^{-2}$), our measurements are in fair agreement with previous analytic XLF determinations within the uncertainties of the individual data points. For CTK column densities, our analysis yields only upper limits to the space density. It is nevertheless interesting that for redshifts $z > 0.5$ and luminosities $L_{\rm X} \approx 10^{44} - 10^{45}\,{\rm erg\,s}^{-1}$, the 3σ upper limits overlap with the Ueda et al. (2014) and Aird et al. (2015) XLFs and therefore provide informative constraints on the space density of AGN with $N_{\rm H} > 10^{24}\,{\rm cm}^{-2}$.

An alternative approach for quantifying the CTK AGN demographics is via their fraction relative to the overall AGN population (see Equation 3.6). Figure 3.15 shows previous estimates of this fraction in comparison with our constraints. At low redshift, $z < 0.5$, our results favour low CTK fractions, although the uncertainties remain large, $f_{\rm CTK} = 21.0^{+16.1}_{-9.9}\%$. Burlon et al. (2011) use the 3-year *Swift*-BAT (Burst Alert Telescope, Barthelmy et al., 2005) serendipitous survey to measure a CTK fraction of about 20% in the local Universe. Their sample is selected at hard energies (14-195 keV) and is, therefore, least biased by obscuration effects. Low CTK fractions in the range $f_{\rm CTK} \approx 10 - 20\%$ are also proposed by Akylas et al. (2016) and Georgantopoulos & Akylas (2019) based on AGN selected from the 70-month *Swift*-BAT survey. These authors also emphasise the importance of the assumptions on the shape of the CTK AGN X-ray spectrum (e.g. the strength of reflection relative to the direct component, high-energy cut-off) for interpreting the high energy spectra of AGN and deriving CTK fractions.

Buchner et al. (2015) analyse the X-ray spectrum of AGN detected in popular extragalactic survey fields. They constrain the AGN space density using a non-parametric approach, similar to that presented here, but also imposing two different continuity priors. They tend to keep either the value or the slope of the XLF constant in areas of the parameter space with little data to provide meaningful constraints. Figure 3.15 shows the CTK fraction of each of these two priors. These are estimated by marginalising the Buchner et al. (2015) posteriors in the luminosity interval $10^{42}-10^{46}{\rm erg\,s}^{-1}$. At low redshift, $z < 0.5$, our results are lower but still marginally consistent with the constant-

value prior estimates of Buchner et al. (2015).

At higher redshift, $z > 0.5$, our 3σ upper limits also favour the constant-value prior estimates of Buchner et al. (2015), at least up to $z \sim 2.5$. These upper limits are also broadly consistent with the constraints presented by Brightman & Ueda (2012) and also track the $f_{\rm CTK}$ redshift evolution inferred by L18. We caution that the latter observational constraint corresponds to a luminosity of $L_{\rm X,\,2-10\,keV} = 10^{45}\,{\rm erg\,s^{-1}}$ at all redshifts. It is also worth noting that the difference between the Ueda et al. (2014) and Aird et al. (2015) curves in Figure 3.15 is because of differences in the space density of CTN AGN ($N_{\rm H} = 10^{22} - 10^{24}\,{\rm cm^{-2}}$). This is also evident by the somewhat higher normalisation of the Aird et al. (2015) XLF relative to that Ueda et al. (2014) in the two middle rows of panels in Figure 3.14.

In Figure 3.15, there is a disagreement between our results and the recent estimates of the CTK fraction of Ananna et al. (2019). They develop an AGN population synthesis model that fits observations of the diffuse X-ray background spectrum using as input the X-ray luminosity function and models for the X-ray spectra of AGN (See Figure 1.18). Their best-fit model predicts CTK AGN fractions of $50 \pm 9\%$ at $z \simeq 0.1$, which is higher than our estimates, but also other studies that use spectral analysis of X-ray selected samples to infer CTK fractions directly (e.g. Ricci et al., 2015). We caution that models of the diffuse X-ray background spectrum suffer strong degeneracies between the adopted shape of the X-ray spectra of AGN (i.e. strength of the reflection component, power-law index) and the assumed CTK fraction (Treister et al., 2009). For example, Akylas et al. (2012) show that low CTK fractions could be compensated by a stronger X-ray reflection component (and vice versa) to yield diffuse X-ray background spectra consistent with observations.

The inferred CTK fractions also have implications on fundamental properties of the accretion flow onto supermassive black holes, such as the radiative efficiency, ϵ. Shankar et al. (2020) develop models that allow the determination of this parameter based on the observed population properties of AGN samples. They argue in particular that observational measurements of the mean X-ray luminosity averaged over galaxy populations as a function of stellar mass (e.g. Yang et al., 2017) provide interesting constraints to ϵ. Their analysis suggests $\epsilon \gtrsim 0.15$ for the black-hole mass vs stellar mass relation of Shankar

et al. (2016), in line with theoretical expectations. A significant source of uncertainty in this analysis is the fraction of heavily obscured and CTK AGN that may be underrepresented in X-ray-selected samples because of their apparent faintness. If there is a large population of such missing sources, then observational measurements of the mean X-ray luminosity as a function of stellar mass are biased, now leading to the underestimation of the AGN radiative efficiency. Our findings for moderate fractions of Compton thick AGN, at least at $z \sim 0.1$, suggest that such an effect is small and hence has a minor effect on the inferred ϵ values.

Additionally, within the context of AGN/galaxy co-evolution scenarios, there are suggestions that heavily obscured AGN represent an important early stage of black-hole growth (e.g. Hopkins et al., 2008). They are systems observed close to the peak of their nuclear (and star formation) activity, at a stage just before the AGN winds blow away the obscuring dust and gas clouds and eventually quench the star formation in the host galaxy. The low fractions of Compton thick AGN estimated in our work have implications for the duty cycle of the obscured phase of the scenario above. Additionally, our proposed methodology can help isolate reliable samples of heavily obscured and CTK AGN to test the co-evolution scenario above by studying the properties of their host galaxies relative to less obscured sources.

3.6.2 Future Missions

One of the core science objectives of the *Athena* X-ray observatory (Nandra et al., 2013) is the characterisation of the demographics of heavily obscured and CTK AGN out to high redshift, $z \sim 4$ (Georgakakis et al., 2013). The means to achieve this goal are multi-tiered surveys with the Wide Field Imager (WFI, Rau et al., 2013) onboard the *Athena* X-ray observatory. The larger collecting area of *Athena* in the energy range 0.5-10 keV (2500 cm^2 at 6 keV) compared to e.g. *Chandra*, 28 cm^2 at 6.5 keV, or *XMM-Newton*, 900 cm^2 at 7 keV, translates into a significant improvement in X-ray spectral quality and ability to identify and characterise the intrinsic properties of heavily obscured and CTK sources.

We demonstrate this capacity using one of the *Chandra* COSMOS-Legacy sources with bi-modal column density posterior distribution that includes both CTK and CTN solution. The source ID is COSMOS_1_420, with a spectroscopic redshift of 1.55. Figure 3.16 shows

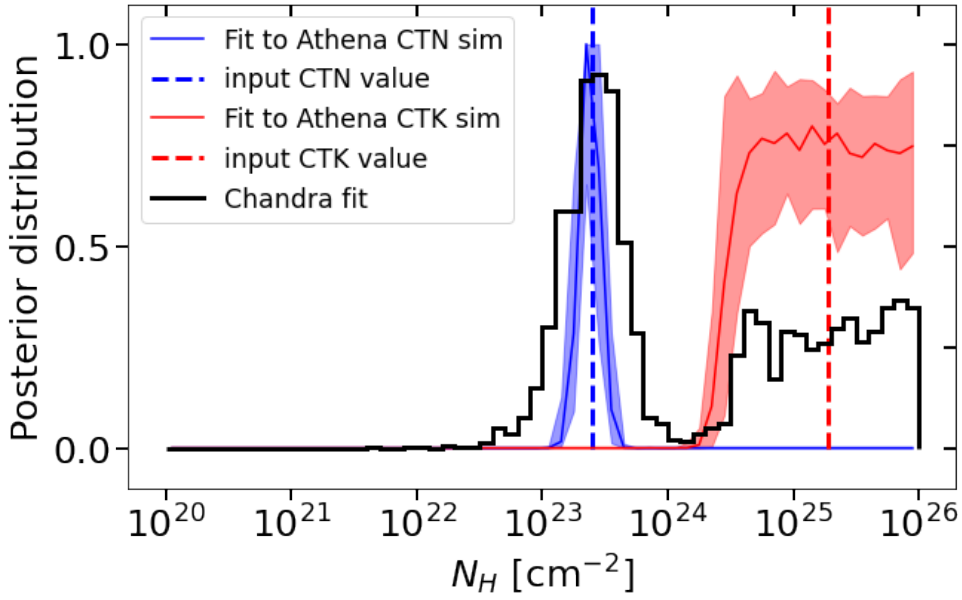

Figure 3.16: The *black histogram* shows the $N_{\rm H}$ posterior distribution of the X-ray spectroscopic fit of *Chandra* COSMOS_1_420 without using prior. From the CTN peak (CTK peak, respectively), we simulate an *Athena*/WFI source at $z = 1.55$ with $N_{\rm H} = 2.51 \times 10^{23}\,{\rm cm}^{-2}$ and $L_{\rm X} = 1.07 \times 10^{44}\,{\rm erg\,s}^{-1}$ ($N_{\rm H} = 1.86 \times 10^{25}\,{\rm cm}^{-2}$, $L_{\rm X} = 2.09 \times 10^{45}\,{\rm erg\,s}^{-1}$, respectively). The spectroscopic $N_{\rm H}$ posterior distribution of these simulations are represented in *blue* (*red*, respectively). The *vertical dashed lines* correspond to the input $N_{\rm H}$ values for the respective simulations.

the posterior distribution of that source using the *Chandra* COSMOS-Legacy observations without applying a $L_{6\,\mu{\rm m}}$ prior. It also displays the most likely CTK and CTN solutions which are ($N_{\rm H} = 1.86 \times 10^{25}\,{\rm cm}^{-2}$, $L_{\rm X} = 2.09 \times 10^{45}\,{\rm erg\ s}^{-1}$) and ($N_{\rm H} = 2.51 \times 10^{23}\,{\rm cm}^{-2}$, $L_{\rm X} = 1.07 \times 10^{44}\,{\rm erg\ s}^{-1}$), respectively. We then use the current *Athena* calibration files[1] to independently simulate the X-ray spectra of both solutions with the UXCLUMPY model.

In this exercise, we adopt an exposure time of 100 ks that approximately corresponds to the wide-area tile of the *Athena*/WFI survey plan. The adopted background model is an updated version of the WFI background file generation model[2]. We assume an extraction aperture of 5 arcsec that corresponds to an EEF of $\sim 69\%$ for the FOV-average *Athena* PSF. The same model is then used with BXA to refit the simulated spectra. The resulting posteriors are also shown in Figure 3.16. It is clear that for luminous X-ray sources like

[1] https://www.mpe.mpg.de/ATHENA-WFI/response_matrices.html
[2] WFI-MPE-ANA-0010_i7.1_Preparation-of-Background-Files.pdf

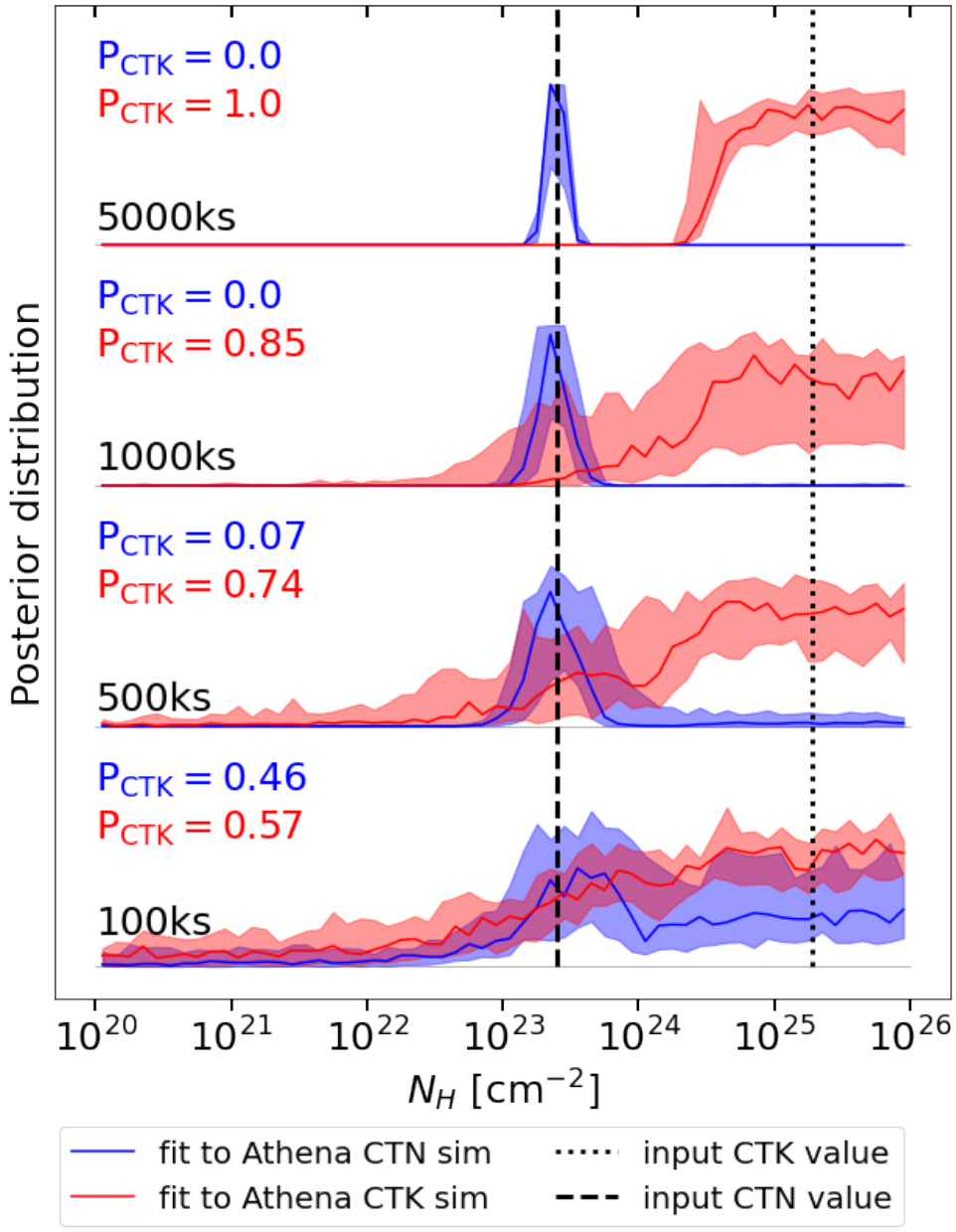

Figure 3.17: Column density posterior distribution of the X-ray spectroscopic fit for the CTN (*blue*) and CTK (*red*) *Athena*/WFI simulations of COSMOS_1_420 at $z = 1.55$. The intrinsic X-ray luminosity are renormalised at $L_{\mathrm{X,2-10\,keV}} = 10^{43}\,erg\,s^{-1}$ and at $L_{\mathrm{X,2-10\,keV}} = 10^{44}\,erg\,s^{-1}$ for the CTN and CTK solutions, respectively. The distributions are shifted as a function of their exposure time for *Athena*/WFI: 100ks, 500ks, 1000ks and 5000ks. The *dashed vertical line* represents the CTN input column density at $N_{\mathrm{H}} = 2.51 \times 10^{23}\mathrm{cm}^{-2}$ and the *dotted vertical line* represents the CTK input column density at $N_{\mathrm{H}} = 1.86 \times 10^{25}\mathrm{cm}^{-2}$. $\mathrm{P_{CTK}}$, the fraction of the posterior distribution in the CTK regime, is indicated for each exposure time and for both the CTN and CTK *Athena* simulation with their respective colour.

the COSMOS_1_420 example, X-ray spectroscopy with the *Athena*/WFI alone is sufficient to yield unimodal posteriors and distinguish between CTK and CTN solutions.

Nevertheless, the Athena/WFI surveys will also be sensitive to heavily obscured AGN of lower luminosity. We, therefore, repeat the analysis by renormalising the 2-10 keV X-ray luminosity of the CTN solution of the source COSMOS_1_420 to $L_{\rm X} = 10^{43}\,{\rm erg\,s^{-1}}$ ($\sim$ 10 times fainter) and the CTK solution to $L_{\rm X} = 10^{44}\,{\rm erg\,s^{-1}}$ ($\sim$ 20 times fainter). The resulting posteriors for different exposure times are shown in Figure 3.17. Short exposure times result in low photon counts leading to broader column density probability distributions that make the determination of the CTK nature of the source uncertain. For instance, with 100 ks exposure time, the fits of the simulation from the CTN and CTK solutions have respectively 46% and 57% of their posterior distribution in the CTK regime. In this example, the obscuration regime of the source is highly uncertain.

The posterior broadening can be compensated by a higher exposure time (e.g. $\gtrsim$ 1000 ks for the CTN source or $\gtrsim$ 5000 ks for the CTK source). It significantly increases the contrast between the posterior distributions from the 2 simulations. However, such large exposure times are unrealistic for large surveys as planned for *Athena*. Alternatively, the methodology based on mid-IR priors proposed in this Chapter could narrow down the posteriors and guarantee the obscuration regime of the source. Doing so would improve the *Athena* constraints on AGN demographics.

In addition to the *Athena* observatory, observations by the James Webb Space Telescope (*JWST*, Gardner et al., 2006) will improve SED constraints and allow a better understanding of the correlation between X-rays and the mid-IR, on which our methodology hinges. The *Euclid* survey (Laureijs et al., 2011) will also provide improved photometric redshifts over large areas of the sky, particularly for the obscured AGN population, for which the optical bands are dominated by the stellar light of the galaxy.

3.7 Summary

To understand the growth of SMBH throughout the Universe, one has to get a complete census of AGN and efficiently constrain their physical parameters. This Chapter proposes a new methodology to extract the properties of X-ray selected AGNs within the *Chandra*

COSMOS-Legacy survey containing 2965 sources (Section 3.2). To our knowledge, this is the first time that these observations have been used to constrain the AGN X-ray luminosity function. The novelty of our analysis is the inclusion of mid-IR priors in the Bayesian-based X-ray spectral analysis (Section 3.4). With SED fitting, we constrain the luminosity of the AGNs at 6 μm that is later used as a proxy for the accretion X-ray luminosity guiding the X-ray spectroscopy. This approach improves the confidence of the constraints on physical parameters by breaking down degeneracies, such as between X-ray luminosity and LOS hydrogen column density. This approach primarily benefits the low photon statistics and the most heavily obscured sources. By carefully considering the X-ray selection function, we measure the AGN space density as a function of the accretion X-ray luminosity, LOS obscuration and redshift. We also estimate the CTK fraction as a function of the redshift (Section 3.5). The main results of our new analysis are:

- Our AGN space density measurements are in broad agreement with previous analytic studies. As we find a small number of CTK AGN (27 sources) in the *Chandra* COSMOS-Legacy field, we can only place upper limits on the space density of this population. (Section 3.5.2)

- Our CTK fraction estimations are at the low-end of the range determined in previous studies. At redshift $z < 0.5$, we find $f_{\rm CTK} = 21.0^{+16.1}_{-9.9}\%$. At $0.5 < z < 2.5$, we determine (3σ) upper limits that suggest a CTK fraction typically lower than 40%, lower than several previous studies. (Section 3.5.3)

- By simulating spectra, we found that future missions like the *Athena* observatory would benefit from this multi-wavelength methodology to better constrain the physical parameters of the faintest and most obscured sources. (Section 3.6.2)

The multi-wavelength-based methodology proposed in this Chapter efficiently increases the confidence of obscuration measurements and AGN demographics. Our results can be used in various fields of SMBH research like their growth, their evolution through time or the AGN co-evolution with the host-galaxy.

CHAPTER 4

Accretion properties of X-ray AGN: Evidence for radiation-regulated obscuration with redshift-dependent host galaxy contribution

Abstract

We adopt a Bayesian X-ray spectral approach to investigate the accretion properties of unobscured ($20 < \log(N_{\rm H}/{\rm cm}^{-2} < 22$) and obscured ($22 < \log(N_{\rm H}/{\rm cm}^{-2} < 24$) active galactic nuclei (AGN) to shed light on the orientation vs evolution scenarios for the origin of the obscuring material. For a sample of 3882 X-ray-selected AGN from the *Chandra* COSMOS-Legacy, AEGIS-XD and CDFS extragalactic surveys, we constrain their stellar masses, $M_\star$, intrinsic X-ray luminosities, $L_{\rm X}$, obscuring column densities, $N_{\rm H}$, and specific accretion rates $\lambda \propto L_{\rm X}/M_\star$. By combining these observables within a Bayesian non-parametric approach, we infer, for the first time, the specific accretion rate distribution (SARD) of obscured and unobscured AGN to $z \sim 3$, i.e. the probability of a galaxy with mass $M_\star$ at redshift z hosting an AGN with column density $N_{\rm H}$ and specific accretion rate λ. Our findings indicate that (1) both obscured and unobscured SARDs share similar shapes, shifting towards higher accretion rates with redshift, (2) unobscured SARDs exhibit a systematic offset towards higher λ compared to obscured SARD for

all redshift intervals, (3) the obscured AGN fraction declines sharply at $\log \lambda_{\rm break} \sim -2$ for $z < 0.5$, but shifts to higher λ values with increasing redshift, (4) the incidence of AGN within the theoretically unstable blow-out region of the $\lambda - N_{\rm H}$ plane increases with redshift. These observations provide compelling evidence for AGN "downsizing" and radiation-regulated nuclear-scale obscuration with an increasing host galaxy contribution towards higher redshifts.

4.1 Introduction

SuperMassive Black Holes (SMBHs), living in the centre of most massive galaxies are growing through the accretion of matter that releases large amounts of radiative energy. Although SMBHs experiencing such accretion events (Active Galactic Nuclei, AGN) are being observed throughout the Universe, the details of the physical conditions that initiate them, as well as the impact of the produced energy on the host galaxy, are still debated.

One approach to address these issues is to study, in a statistical manner, the accretion properties of AGN in relation to the characteristics of their host galaxies. Any underlying trends or covariances that such a methodology may reveal hints about the physical processes governing the feeding and feedback cycle of SMBHs (e.g. Alexander & Hickox, 2012). Of particular importance in this respect is the Eddington ratio, $\lambda_{\rm Edd} = L_{\rm bol}/L_{\rm Edd} \propto L_{\rm bol}/M_{\rm BH}$, of an accreting system. As indicated in Section 1.3.2, this fundamental characteristic of AGN measures how fast or slow a SMBH accretes material relative to its maximum capacity, i.e. the Eddington limit, where radiation pressure becomes dominant and may regulate the flow of matter (e.g. Di Matteo et al., 2005; Fabian, 2012). Therefore, the Eddington ratio contains information on both the efficiency of the accretion process and the potential of the system to launch winds or outflows into the interstellar medium of its host galaxy. In recent years it has become possible to measure Eddington ratios or proxies of that quantity for large samples of AGN both in the local Universe (e.g. Kauffmann & Heckman, 2009; Schawinski et al., 2010; Birchall et al., 2023; Torbaniuk et al., 2024) and at higher redshift (e.g. Bongiorno et al., 2012; Georgakakis et al., 2014; Schulze et al., 2015; Bongiorno et al., 2016; Aird et al., 2018). A broad picture emerging from these studies is a preference for AGN residing in star-forming hosts (Mul-

laney et al., 2015; Scholtz et al., 2018; Ni et al., 2021), possibly indicating the availability of gas reservoirs and a sharp decline in the incidence of active SMBHs close to or above the Eddington limit, suggesting self-regulation.

Another fundamental property of AGN is the level of obscuration along the line of sight to the observer. It is well established that most SMBHs accrete material behind dust and gas clouds (e.g. Ueda et al., 2014; Aird et al., 2015; Hickox & Alexander, 2018; Andonie et al., 2022a) that absorb part of the emitted radiation and block the direct view to the central engine, particularly in the UV/optical part of the electromagnetic spectrum (§1.3.4). The nature and origin of the obscuring material are not yet fully understood (e.g. Netzer, 2015), although it is proposed to be associated with the feeding and feedback cycle of AGN (e.g. Sanders et al., 1988; Wada, 2012, 2015), thereby, provide information on the physics of black hole growth. Interestingly, in this respect, recent studies on the statistical properties of AGN samples find covariances between AGN obscuration and Eddington ratio. For example, Ricci et al. (2017b, R17 hereafter) and Ricci et al. (2022, R22 hereafter), use a hard-X-ray-selected AGN sample ($> 10\,\mathrm{keV}$) at low redshift ($<z> = 0.037$, Koss et al., 2022a) to show that the fraction of obscured AGN drops sharply with increasing Eddington ratio above $\lambda_{\mathrm{break}} \approx 10^{-2}$ as shown in Figure 1.12. This trend is consistent with the expectations of AGN radiation-driven outflows acting on a dusty medium (Fabian et al., 2008, 2009), thereby pushing away the obscuring clouds and perhaps regulating the accretion flow onto the SMBH.

In this Chapter, we expand for the first time the results above to higher redshift to explore if the trends between obscuration and Eddington ratio established in the local Universe persist to earlier cosmic times during the peak of the accretion history of the Universe (redshfits $z \sim 1 - 3$, Ueda et al., 2014; Aird et al., 2015). We adopt the specific accretion rate (SAR, Bongiorno et al., 2012; Aird et al., 2012), i.e. the ratio between AGN X-ray luminosity and stellar mass of the host galaxy, as a proxy of the Eddington ratio. This is because the direct determination of black hole masses (and hence Eddington ratios) for obscured AGN outside the local Universe (e.g. via measurements of the velocity dispersion of the host galaxy bulge), is challenging and expensive in observing resources. Similarly to the work presented in Chapter 3, we use X-ray surveys to define the parent AGN sample used in the analysis. This is because X-ray observations (i) provide a

handle on the line-of-sight obscuration to the active SMBHs (parametrised by the atomic hydrogen column density $N_{\rm H}$) and (ii) have a selection function that can be accurately quantified, thereby allowing inference on the demographics of the underlying population from an observed X-ray AGN sample (Brandt & Alexander, 2015). Our analysis also measures the incidence of AGN in galaxies as a function of obscuration. For this exercise, we infer from the observations the specific accretion rate distribution (SARD) of AGN, which measures the probability of a galaxy hosting an active black hole of a given SAR. This analysis step extends previous works presented in Section 1.4.3 on the overall SARD of the AGN population (Aird et al., 2012; Bongiorno et al., 2012; Georgakakis et al., 2017c; Aird et al., 2018) that do not discriminate between systems with different levels of line-of-sight obscuration. Section 4.2 describes the X-ray surveys and the multi-wavelength data used in this work. Section 4.3 discusses the analyses of the observations to derive line-of-sight obscuration levels and galaxy stellar masses and infer the AGN incidences. We present our results in Section 4.4 and show how the SARD evolves with redshift and obscuration. In Section 4.5, we discuss the implications of our results on the fueling mechanisms of SMBHs and their evolution. Finally, our findings are summarized in Section 4.6. Throughout the Chapter, we adopt the following cosmological parameters: $H_0 = 70\,{\rm km\,s^{-1}\,Mpc^{-1}}$, $\Omega_{\rm M} = 0.3$ and $\Omega_{\Lambda} = 0.7$.

4.2 Data

In this Chapter, we use X-ray selected AGN detected in three extragalactic survey fields observed by the *Chandra* X-ray observatory (Weisskopf et al., 2000, §2.1): the *Chandra* COSMOS-Legacy (Civano et al., 2016, §2.2.1), the All-wavelength Extended Groth Strip X-ray Deep (AEGIS-XD, Nandra et al., 2015, §2.2.2) and the *Chandra* Deep Field South (CDFS, Luo et al., 2017, 2.2.3). Each survey field and its multi-wavelength photometry from X-ray to radio are extensively presented in Section §2.2. In each field, the X-ray sources are detected independently in four energy bands, 0.5-2 keV (soft), 2-7 keV (hard), 4-7 keV (ultra-hard) and 0.5-7 keV (full) following the methodology of Laird et al. (2009) and Nandra et al. (2015), described in Section 2.3.1. Additionally, Table 4.1 reports the total number of sources in each energy band for the three *Chandra* survey fields after

applying a multi-wavelength coverage filter and removing the sources classified as stars. For the purpose of optimising statistics, this study focuses on the energy band with the highest number of sources, i.e. the full band 0.5-7 keV. Our final sample contains 3882 sources, with 2658, 806 and 418 detections within the COSMOS-Legacy, AEGIS-XD and CDFS, respectively.

The identification of optical to mid-infrared (mid-IR) counterparts for the X-ray sources is based on the Likelihood Ratio method (*LR*, Sutherland & Saunders, 1992; Brusa et al., 2007) presented in Section 2.3.2. Moreover, as detailed in Section 2.3.3, the spectroscopic and photometric redshift data used in this work is compiled in Georgakakis et al. (2017c) (COSMOS-Legacy), Nandra et al. (2015) (AEGIS-XD) and Hsu et al. (2014) (CDFS). Table 4.2 summarises the redshift information available for each field. Overall, 2122 sources have a spectroscopic redshift estimation, whereas 1721 sources have a photometric redshift probability distribution function (PDF). The remaining 39 sources do not have any redshift estimation.

Figure 4.1 presents the distribution of the X-ray sources used in this work across the luminosity-redshift plane. The determination of 2-10 keV luminosities is based on the X-ray spectral analysis results described in Section 4.3.1. Figure 4.1 demonstrates that the combination of the three *Chandra* survey fields with different X-ray depths and areas allows us to explore the AGN population over a reasonably broad luminosity and redshift baseline.

The extraction of X-ray spectra for individual X-ray sources in each of the three deep fields follows the methodology of Laloux et al. (2023), described in the methodology Section §2.4.1.

Table 4.1: Number of unique X-ray detections in different energy bands in each of the three *Chandra* X-ray survey fields used in this work.

Survey	Full 0.5-7 keV	Soft 0.5-2 keV	Hard 2-7 keV	Ultra-hard 4-7 keV	Any band
COSMOS	2658	2172	1754	791	2846
AEGIS-XD	806	683	547	287	878
CDFS	418	406	282	183	486
All	3882	3261	2583	1261	4210

Table 4.2: Number of X-ray sources selected in the 0.5-7 keV band with spectroscopic, photometric or no redshift estimation for each of the three *Chandra* X-ray survey fields used in this work.

Redshift type	COSMOS	AEGIS-XD	CDFS	Total
Spectroscopic	1536	319	267	2122
Photometric	1087	487	147	1721
No estimation	35	0	4	39
Total	2658	806	418	3882

4.3 Analysis

This section outlines the methodological steps that lead to the determination of the SARD for obscured and unobscured AGN from the X-ray selected sample of Section 4.2. The Bayesian X-ray spectral fitting, described in Section 4.3.1, yields PDFs for the intrinsic 2-10 keV X-ray luminosity, $L_{\rm X}$, and line-of-sight column density, $N_{\rm H}$, for individual X-ray AGN. The stellar masses, $M_\star$, of the AGN host galaxies are estimated by fitting templates to their broadband spectral energy distribution (SED) as described in Section 4.3.2. The statistical Bayesian inference approach, combining the outcomes of the X-ray spectral analysis and SED fitting process to derive the SARD as a function of the obscuration, is described in Section 4.3.3.

4.3.1 X-ray Spectral Fitting

To fit the X-ray spectra extracted in the three *Chandra* deep fields, we use the Bayesian X-ray Analysis (BXA) package (Buchner et al., 2014) with the UXCLUMPY spectral model (Buchner et al., 2019). An extensive description of the fitting algorithm and spectral model is provided in the methodology Section 2.4.2. Following the discussion of Section 3.3.3, we only consider the baseline model: a 45° inclination angle and the soft-scattering component is included. The only minor difference is that the normalization of the background model is now set to the value estimated by the `automatic_background()` task of BXA re-scaled to the source area. This decision does not impact the final results. The parameter settings are summarised in Table 4.3.

The left panel of Figure 4.2 displays the distribution of intrinsic 2-10 keV X-ray luminosities for both obscured and unobscured AGN. As expected, obscured AGN have a higher median luminosity, by ~ 0.5 dex. This is due to a selection effect, for a given flux

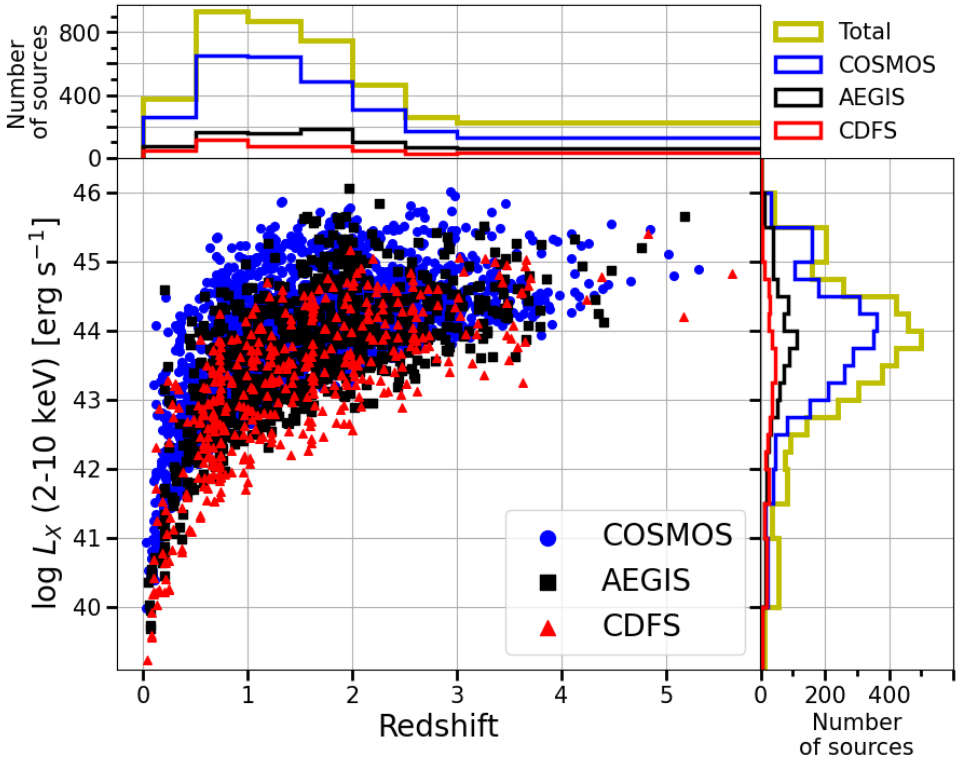

Figure 4.1: *Central panel*: Distribution of the intrinsic 2-10 keV X-ray luminosity (see Section 4.3.1) as a function of redshift. The *blue circles*, *black squares* and *red triangles* correspond to 0.5-7 keV selected X-ray sources in the COSMOS-Legacy, AEGIS-XD and CDFS surveys, respectively. *Top panel*: Redshift distribution of the X-ray sources. The different colours are for COSMOS (*blue*), AEGIS-XD (*black*), CDFS (*red*) and the full sample (*yellow*). *Right panel*: Intrinsic X-ray luminosity distribution of X-ray sources in the different surveys. The colour coding is the same as in the top panel.

limit at the same redshift, an obscured AGN must be brighter than its unobscured counterpart to be detected. The right panel of figure 4.2 shows the 1-σ uncertainty distribution of the X-ray luminosity measurements. One can notice a bump in the obscured distribution, around 1.5. This is due to the double-peaked sources mentioned in Section 3.3.4. For these sources, the $L_{\rm X}$ and $N_{\rm H}$ posterior distributions show two distinct peaks, one in the Compton Thin (CTN, $N_{\rm H} < 10^{24}\,{\rm cm}^{-2}$) obscured regime and one in the Compton Thick (CTK, $N_{\rm H} > 10^{24}\,{\rm cm}^{-2}$) regime, which corresponds, respectively, to the moderate and high luminosity peaks. As a consequence, the 1-σ uncertainty of the luminosity is broad, which explains the $\log \Delta L_{\rm X}$ bump around 1.5 dex.

Table 4.3: Input parameters of the UXCLUMPY model and the adopted fixed value or the prior used in the X-ray spectral analysis.

Parameter	Prior
TORsigma	fixed = 28°
CTKcover	fixed = 0.4
Inclination	fixed = 45°
E_cutoff	fixed = 200 keV
photon index	Gaussian(1.95, 0.15)
$\log(N_{\rm H}/{\rm cm}^{-2})$	uniform(20, 26)
log(norm_torus)	uniform(-8, 3)
log(norm_scattering)	uniform(-7, -1.5)
redshift spectroscopic	fixed at source redshift
redshift photometric	photometric PDF
no redshift estimation	uniform(1, 6)
log(norm_background)	fixed at measured value

4.3.2 Spectral Energy Distribution Fitting

The main objective of the SED fitting process in this Chapter is to constrain the stellar mass of the AGN host galaxy. For that purpose, we employ the SED fitting algorithm CIGALE (Boquien et al., 2019; Yang et al., 2022). The SED fitting models and parameters are detailed in the methodology Section 2.4.3, along with the implementation to account for photometric redshift.

With this approach, we fit the SED of all our sources to measure the stellar mass of their host galaxies. The stellar mass distribution of the three different surveys as a function of the redshift is illustrated in Figure 4.3.

Figure 4.4 displays the distribution of $\log M_\star$ measurements and uncertainties for both AGN populations. The median $\log M_\star$ of obscured AGN is moderately higher than for unobscured AGN by $\sim$ 0.1dex. This could be explained by the fact that more luminous AGN are slightly more massive than their less massive counterparts, and as seen in Figure 4.2, obscured AGN are in average more luminous than unobscured AGN. Nevertheless, the stellar mass uncertainty of both populations is very similar, showing no systematic offset between one or the other population. This result shows that there is no specific bias in terms of host galaxy stellar mass constraints between obscured and unobscured AGN.

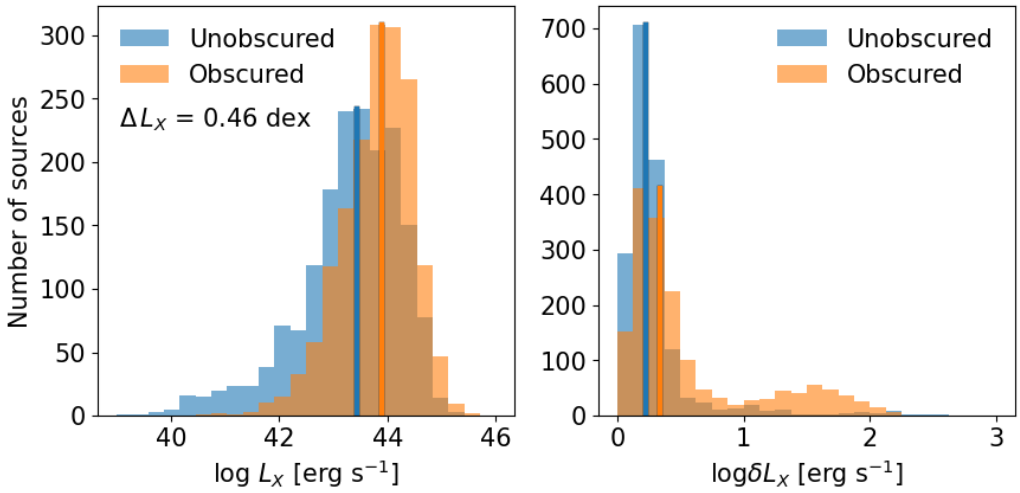

Figure 4.2: *Left panel*: Logarithmic intrinsic 2-10 keV X-ray luminosity distribution for obscured (*orange dashed*) and unobscured (*solid blue*) AGN. The median value for both samples is also indicated by a vertical line of the corresponding colour and style. *Right panel*: Distribution of intrinsic X-ray luminosity uncertainties for unobscured and unobscured AGN. The colour code is identical to the left panel.

4.3.3 Specific Accretion Rate Distribution Calculation

This section describes the algorithm adopted in this work to estimate the SARD of the X-ray selected AGN from Section 4.2 based on their inferred X-ray luminosities (refer to Section 4.3.1) and stellar masses (refer to Section 4.3.2). For each source, the posterior parameter distributions must be merged to obtain the SAR $\lambda_{\rm SAR} = L_{\rm X}/M_{\star}$ posterior distribution. For sources with spectroscopic redshifts, the stellar mass posterior can be straightforwardly merged with the X-ray spectroscopy posteriors, which includes information on obscuration level and intrinsic X-ray luminosity. However, for sources with photometric redshift, the parameter posteriors are matched based on redshift. Once the posteriors are matched, the PDF of the SAR of individual sources can be estimated. Similarly to previous works (Bongiorno et al., 2016; Georgakakis et al., 2017c; Aird et al., 2018), we re-scale the $\lambda_{\rm SAR}$ to Eddington ratio units using the bolometric correction $L_{\rm bol} = 25 \cdot L_{\rm X}(2-10\,{\rm keV})$ (e.g. Elvis et al., 1994) and the scaling relation $M_{\rm BH} = 0.002 M_{\star}$ (Marconi & Hunt, 2003) in the following way:

$$\begin{aligned} \lambda = \frac{L_{\rm bol}}{L_{\rm Edd}} = \frac{L_{\rm bol}}{1.3 \times 10^{38} \cdot M_{\rm BH}} \approx \frac{25 \cdot L_{\rm X}(2-10\,{\rm keV})}{1.3 \times 10^{38} \cdot 0.002 M_{\star}} \\ \sim 10^{-34} \frac{L_{\rm X}}{M_{\star}}, \end{aligned} \tag{4.1}$$

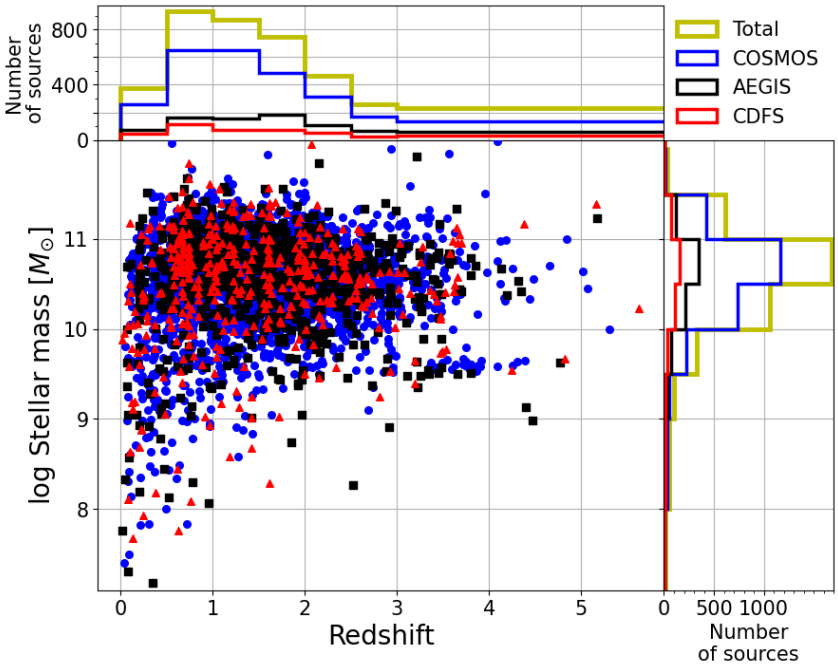

Figure 4.3: *Top panel*: Redshift distribution of the different surveys with COSMOS (*blue*), AEGIS-XD (*black*), CDFS (*red*) and the total sample (*yellow*). *Central panel*: Distribution of our sample stellar mass as a function of the redshift. The *blue circles*, the *black squares* and the *red triangles* correspond to the AGN of the COSMOS-Legacy, AEGIS-XD and CDFS surveys, respectively. *Right panel*: Stellar mass distribution of the different surveys. Same colour code as on the top panel.

with $M_\star$ in solar mass units and X-ray luminosity in erg s^{-1}. We emphasise that these simplistic scaling relations are applied to make the accretion rate $L_{\rm X}/M_\star$ resemble the Eddington ratio. The impact of these assumptions on our results and conclusions is discussed in later sections. Figure 4.5 illustrates the distribution of individual X-ray sources in the COSMOS, AEGIS-XD and CDFS surveys on the $\lambda - z$ parameter space.

The estimation of the SARD relies on the sampling of the Poisson likelihood function originally used to determine the X-ray luminosity function of AGN (XLF, Loredo, 2004; Aird et al., 2010, 2015; Buchner et al., 2015; Georgakakis et al., 2015; Laloux et al., 2023, see Equation 3.4 in Section 3.5.2). We exploit the fact that the AGN XLF can be expressed as the convolution of the Stellar Mass Function (SMF), $\psi(M_\star|z)$, and the SARD, $P(\lambda|z, M_\star)$, which is defined as the probability of a galaxy at redshift z and with stellar mass $M_\star$ hosting an AGN accreting at a specific accretion rate λ (Georgakakis et al., 2017a). We extend this framework to include an additional dependence of the SARD on AGN obscuration, which is parameterised by the line-of-sight hydrogen column

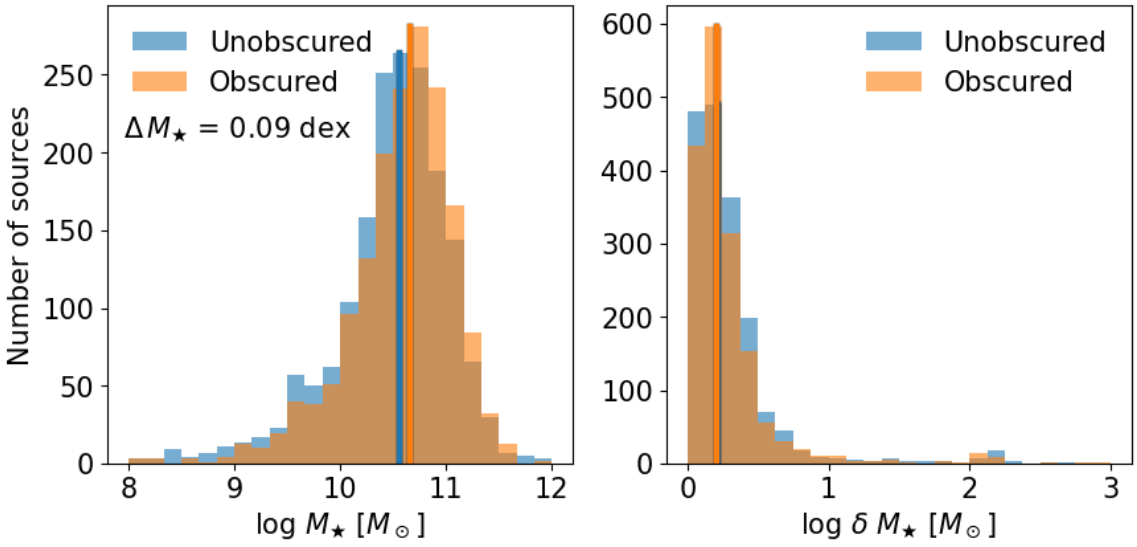

Figure 4.4: *Left panel*: Logarithmic stellar mass histogram for obscured (*orange dashed*) and unobscured (*solid blue*) AGN. The median value for both samples is also indicated by a vertical line of the corresponding colour. The difference between the two medians is $\Delta M_\star = 0.09\,\mathrm{dex}$. *Right panel*: Distribution of stellar mass uncertainties for unobscured and unobscured AGN. The colour code is identical to the left panel.

density N_H. With this extra dimension, the likelihood function can be written as:

$$\mathcal{L}(\mathcal{D}\,|\,\omega) = e^{-\mu(\omega)} \times \prod_{i=1}^{N} \int \frac{dV}{dz} dz\; d\log M_\star\; d\log N_\mathrm{H}\; d\log\lambda \\ p(z, M_\star, N_\mathrm{H}, \lambda\,|\,d_i)\; \psi(M_\star\,|\,z)\; P(\lambda, N_\mathrm{H}, z, M_\star\,|\,\omega), \tag{4.2}$$

where $p(z, M_\star, N_\mathrm{H}, \lambda\,|\,d_i)$ is the probability that a source has a redshift z, a mass $M_\star$, an obscuration N_H and an accretion rate λ given the observational data d_i. $P(\lambda, N_\mathrm{H}, z, M_\star\,|\,\omega)$ is the model of the SARD (at fixed λ, N_H, z, $M_\star$) that is to be constrained by the observations and is described by the set of parameters ω. The SARD is a probability density function and, therefore, at fixed redshift and $M_\star$ interval, it follows the normalisation

$$\int P(\lambda, N_\mathrm{H}, z, M_\star)\, d\log\lambda\, d\log N_\mathrm{H} = 1\,. \tag{4.3}$$

The expected total number of detected AGN in a survey for a particular set of model

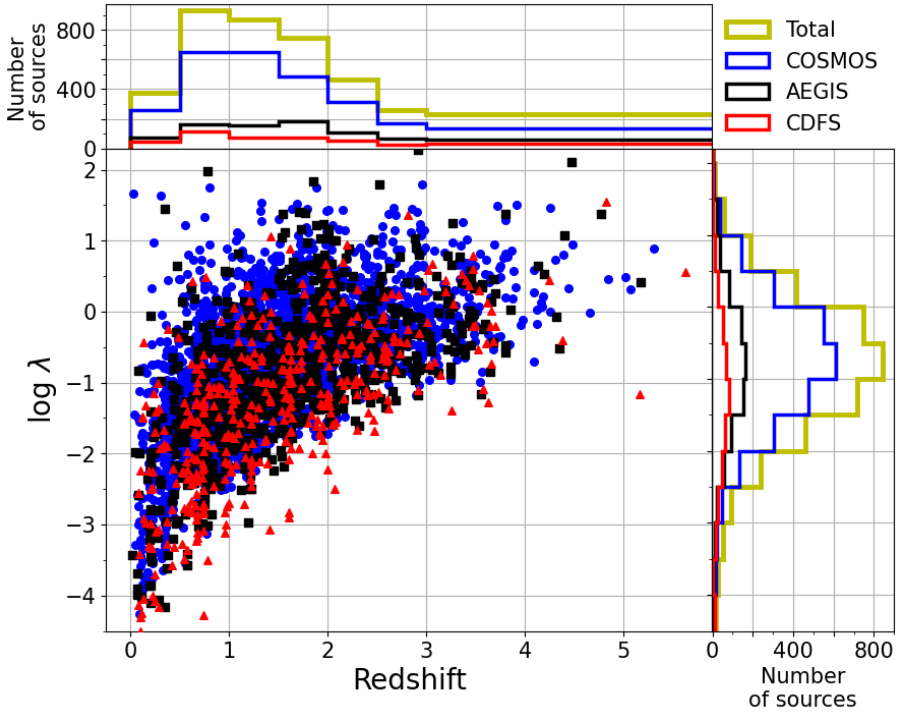

Figure 4.5: *Top panel*: Redshift distribution of the different surveys with COSMOS (*blue*), AEGIS-XD (*black*), CDFS (*red*) and the total sample (*yellow*). *Left panel*: Distribution of our sample specific accretion rate $\lambda \propto L_{\rm X}/M_{\star}$ as a function of the redshift. The *blue circles*, the *black squares* and the *red triangles* correspond to the AGN of the COSMOS-Legacy, AEGIS-XD and CDFS surveys, respectively. *Right panel*: $\log\lambda$ distribution of the different surveys. Same colour code as on the top panel.

parameters ω is

$$\mu(\omega) = \int \frac{dV}{dz} dz \; d\log M_{\star} \; d\log N_{\rm H} \; d\log\lambda \\ A(\lambda, N_{\rm H}, z, M_{\star}) \; \psi(M_{\star} \,|\, z) \; P(\lambda, N_{\rm H}, z, M_{\star} \,|\, \omega), \tag{4.4}$$

where $A(\lambda, N_{\rm H}, z, M_{\star})$ is the sensitivity curve of the X-ray selected sample, quantifying the probability of detection of a source with a given $N_{\rm H}$, λ, z and $M_{\star}$. It is derived from the individual sensitivity maps generated for each survey, following Georgakakis et al. (2008). These maps represent the area sensitive to a source with a given 0.5–7 keV X-ray photon count rate, and their sum gives the total sensitivity map, as displayed in Figure 2.9 in Section 2.3.1. Then, following the method employed in Section 3.5.1, we predict with the UXCLUMPY spectral model the expected count rate for a source for a given parameter set $(\lambda, N_{\rm H}, z, M_{\star})$. Combining the expected count rates with the

total sensitivity map, normalised to the total survey area, yields the sensitivity curve $A(\lambda, N_{\rm H}, z, M_\star)$. In the equations above, we adopt the SMF parametrisation presented by Ilbert et al. (2013), which is consistent with recent observational constraints (e.g. Weaver et al., 2023). Ilbert et al. (2013) use two Schechter functions with parameters evolving with redshift to represent the mass function of galaxies in the redshift interval $z = 0 - 4$.

For computational efficiency, we adopt a non-parametric approach for the determination of $P(\lambda, N_{\rm H}, z, M_\star)$. This involves defining a 4-dimensional grid in SAR, column density, redshift and stellar mass, where the SARD is assumed to be constant within each grid hypercube with dimensions $(\log\lambda \pm \delta\log\lambda,\ N_{\rm H} \pm \delta N_{\rm H},\ z \pm \delta z,\ M_\star \pm \delta M_\star)$. To ensure smoothness, a prior is imposed on the SARD slope along the λ-axis. This prior enforces that the inclination of the slope between two successive grid points is drawn from a Gaussian distribution centred on the slope inclination between the two preceding grid points.

Table 4.4 lists the grid boundaries of the hypercubes that define the non-parametric $P(\lambda, N_{\rm H}, z, M_\star)$ model. Although included for consistency, the highest redshift bin ($3 < z < 6$) is not utilized in our analysis due to its limited number of sources. The logarithmic column density space is split into three bins: unobscured ($20 < \log N_{\rm H}/{\rm cm}^{-2} < 22$), obscured ($22 < \log N_{\rm H}/{\rm cm}^{-2} < 24$) and Compton-thick (CTK, $24 < \log N_{\rm H}/{\rm cm}^{-2} < 26$). However, in this Chapter, we focus solely on Compton Thin AGN (CTN, $\log N_{\rm H}/{\rm cm}^{-2} < 24$) due to challenges in robustly identifying CTK AGN in deep extragalactic survey fields (e.g. Ananna et al., 2019; Laloux et al., 2023). Nonetheless, we include a CTK interval in the analysis to account for the $N_{\rm H}$-PDF of individual sources extending into this regime. Along the λ-axis, the grid is finer for moderate to high accretion rates ($-2 < \log\lambda < 1.5$) to allow more flexibility in this regime where the SARD may vary rapidly. The purpose of the lowest specific accretion rate bin ($-10 < \log\lambda < -5$) is to account for the majority of galaxies that host practically inactive SMBHs at their nuclear regions. We adopt a single logarithmic stellar mass bin in the interval 9.5–11.5. The chosen stellar mass range brackets the majority of our sources, and a finer binning in this axis would result in more noisy SARD constraints.

Normal galaxies with X-ray emission dominated by binaries or hot gas instead of accretion onto SMBHs are present in our sample and are likely to be relevant toward low

Table 4.4: Initial boundaries of the parameter space bins.

Parameter	Bin boundaries
redshift	[0.0, 0.5, 1.0, 1.5, 2.0, 2.5, 3.0, 6.0]
$\log(N_{\rm H}/{\rm cm}^{-2})$	[20, 22, 24, 26]
$\log\lambda$	[-5, -4, -3.5, -3, -2.5, -2, -1.75, - 1.5, -1.25, -1, -0.75,-0.5, -0.25, 0, 0.25, 0.5, 0.75, 1, 1.25, 1.5, 2]
$\log(M_\star/M_\odot)$	[9.5, 11.5]

luminosities ($L_{\rm X} < 10^{42}\,{\rm erg\,s^{-1}}$). We account for this potential source of contamination in a statistical way by adding terms in the likelihood (Equations 4.2, 4.4) that depend on the X-ray luminosity function of normal (i.e. non-AGN) galaxies. The modified likelihood can be written as

$$\begin{aligned}\mathcal{L}(\mathcal{D}\,|\,\omega,\theta_{\rm gal}) =& e^{-\mu(\omega)} \times \prod_{i=1}^{N} \Bigg[\int \frac{dV}{dz} dz\; d\log M_\star\; d\log N_{\rm H}\; d\log\lambda \\ & p(z, M_\star, N_{\rm H}, \lambda\,|\,d_i)\; \psi(M_\star\,|\,z)\; P(\lambda, N_{\rm H}, z, M_\star\,|\,\omega) \\ & + \int d\log L_{\rm X}\; \frac{dV}{dz} dz\; p(L_{\rm X}, z\,|\,d_i)\; \phi_{\rm gal}(L_{\rm X}, z\,|\,\theta_{\rm gal})\Bigg]\,.\end{aligned} \tag{4.5}$$

$$\begin{aligned}\mu(\omega) =& \int \frac{dV}{dz} dz\; d\log M_\star\; d\log N_{\rm H}\; d\log\lambda \\ & A(\lambda, N_{\rm H}, z)\; \psi(M_\star|z)\; P(\lambda, N_{\rm H}, z, M_\star\,|\,\omega) \\ & + \int d\log L_{\rm X}\; \frac{dV}{dz} dz\; A_{\rm gal}(L_{\rm X}, z)\; \phi_{\rm gal}(L_{\rm X}, z\,|\,\theta_{\rm gal}),\end{aligned} \tag{4.6}$$

where $p(L_{\rm X}, z\,|\,d_i)$ is the parameter posterior distribution from X-ray spectroscopy and $\phi_{\rm gal}(L_{\rm X}, z\,|\,\theta_{\rm gal})$ is the normal galaxy XLF, characterised by the set of parameters $\theta_{\rm gal}$. Given that the constraint of this non-AGN galaxy component is outside the scope of this work and well-studied in the past (e.g. Georgantopoulos et al., 2005; Ptak et al., 2007), we decide not to fit this function. We use instead the parametric X-ray luminosity function $\phi_{\rm gal}(L_{\rm X}, z|\theta_{\rm gal})$ of Aird et al. (2015), based on the previous works of Georgakakis et al. (2006, 2007). This function has a Schechter form

$$\phi_{\rm gal}(L_{\rm X}, z) = K \left(\frac{L_{\rm X}}{L^*_{\rm X}}\right)^{-\alpha} e^{-\frac{L_{\rm X}}{L^*_{\rm X}}}, \tag{4.7}$$

Table 4.5: Parameters of the normal galaxy X-ray luminosity function $\phi_{\rm gal}$.

Parameter	$\log K$	$\log L_0$	α	β	z_c
Value	-3.59	41.12	0.81	2.66	0.82

where $L_{\rm X}$ is the 2-10 keV X-ray luminosity and $L^*_{\rm X}$ is defined as

$$\log L^*_{\rm X}(z) = \begin{cases} \log L_0 + \beta \log(1+z) & \text{if } z < z_c \\ \log L_0 + \beta \log(1+z) & \text{if } z \geq z_c \end{cases} \tag{4.8}$$

The different parameters are fixed to the best-fit values presented by Aird et al. (2015) and listed in Table 4.5.

The Hamiltonian Markov Chain Monte Carlo code STAN (Carpenter et al., 2017) is used for Bayesian statistical inference. It is used to sample the likelihood of Equation 4.5 and produce posterior distributions for each of the grid hypercubes that define the non-parametric SARD model, $P(\lambda,\, N_{\rm H}\,,z,\, M_\star \,|\, \omega)$.

4.4 Results

4.4.1 Specific Accretion Rate Distribution

Figure 4.6 shows the SARDs for unobscured ($20 < \log N_{\rm H}/{\rm cm}^{-2} < 22$) and obscured CTN ($22 < \log N_{\rm H}/{\rm cm}^{-2} < 24$) AGN at different redshift intervals. For clarity, we only plot the SARDs out to redshift $z = 2$. The shaded regions in this figure correspond to the 68% confidence interval estimated from the SARD posterior distributions, while the solid lines represent the median value of the posterior at fixed SAR and redshift intervals. The individual SARD curves in Figure,4.6 exhibit a complex shape, broadly characterized by three segments. First, a steep-slope regime emerges at high SAR, indicating a rapid decline in the SARD with increasing λ beyond a turnover point. Second, a plateau where the SARD flattens or mildly drops with increasing λ, extending to SAR of about 1-1.5 dex below the turnover point. Finally, at very low SAR ($\lambda \approx 10^{-3} - 10^{-2}$), the median of the SARD curves decreases with decreasing λ. This low λ regime roughly corresponds to X-ray luminosities $\lesssim 10^{42}\,{\rm erg\,s^{-1}}$ for the typical stellar masses of the X-ray selected sample, $M_\star \approx 10^{10} - 10^{11}\,M_\odot$ (see Figure 4.3). At these X-ray luminosities, the contribution of

normal galaxies to the likelihood in Equation 4.5 becomes significant. Furthermore, in the low λ regime, the uncertainties of the SARD measurements increase because of the limited sensitivity of the X-ray selected sample toward low X-ray luminosities.

A striking feature of Figure 4.6 is the redshift evolution of the SARDs, which appear to shift toward higher SAR with increasing redshift. This trend applies to both obscured and unobscured AGN. Therefore the probability of a galaxy hosting a high SAR event increases with redshift, independent of the level of line-of-sight obscuration to the central engine. Additionally, Figure 4.6 reveals a clear difference in the relative normalisation of the unobscured and obscured SARDs at fixed redshift, with the latter being systematically higher. This offset between the two populations reflects the higher fraction of obscured AGN in the Universe, a proportion known to increase with redshift (e.g. La Franca et al., 2005; Hasinger, 2008; Buchner et al., 2015). Our baseline methodology normalises the SARD via Equation 4.3, preserving differences in the relative fraction of obscured/unobscured AGN in the results.

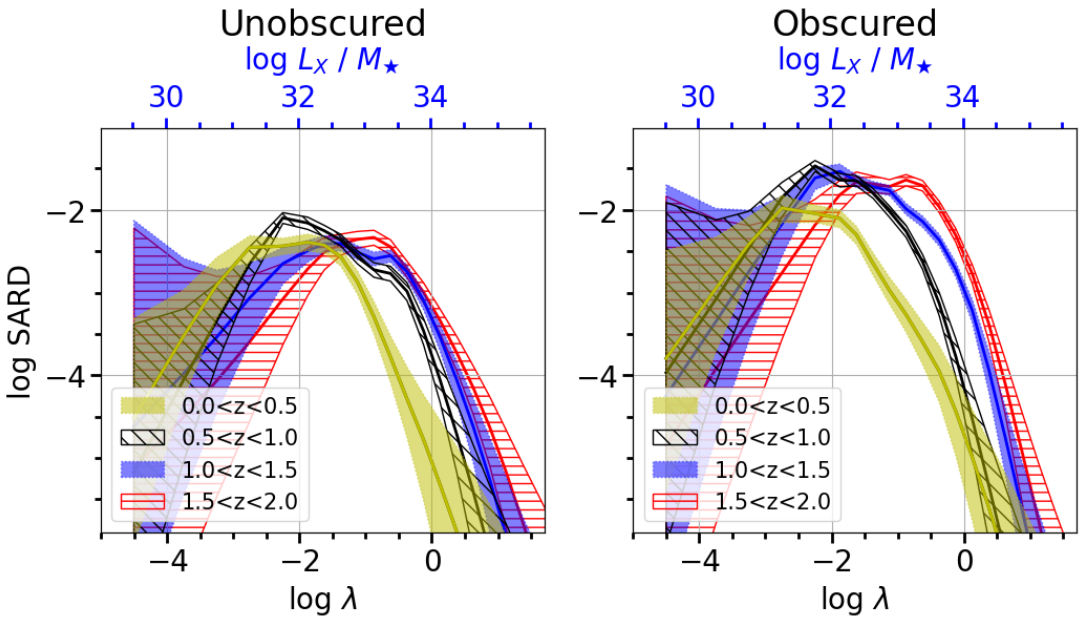

Figure 4.6: Specific accretion rate distribution for the unobscured (*left panel*, $\log N_{\rm H}/{\rm cm}^{-2} < 22$) and obscured CTN (*right panel*, $22 < \log N_{\rm H}/{\rm cm}^{-2} < 24$) populations. The solid lines and corresponding regions represent the median and the 1σ confidence intervals, respectively, for different redshift bins: 0–0.5 (*yellow shaded*), 0.5–1 (*black hatched*), 1–1.5 (*blue shaded*) and 1.5–2 (*horizontal red hatched*). The lower x-axis in each panel is the SAR rescaled to units of Eddington ratio via Equation 4.1. For completeness, we also show the SAR in units of $\rm erg\,s^{-1}\,M_\odot^{-1}$ at the upper x-axis of each panel.

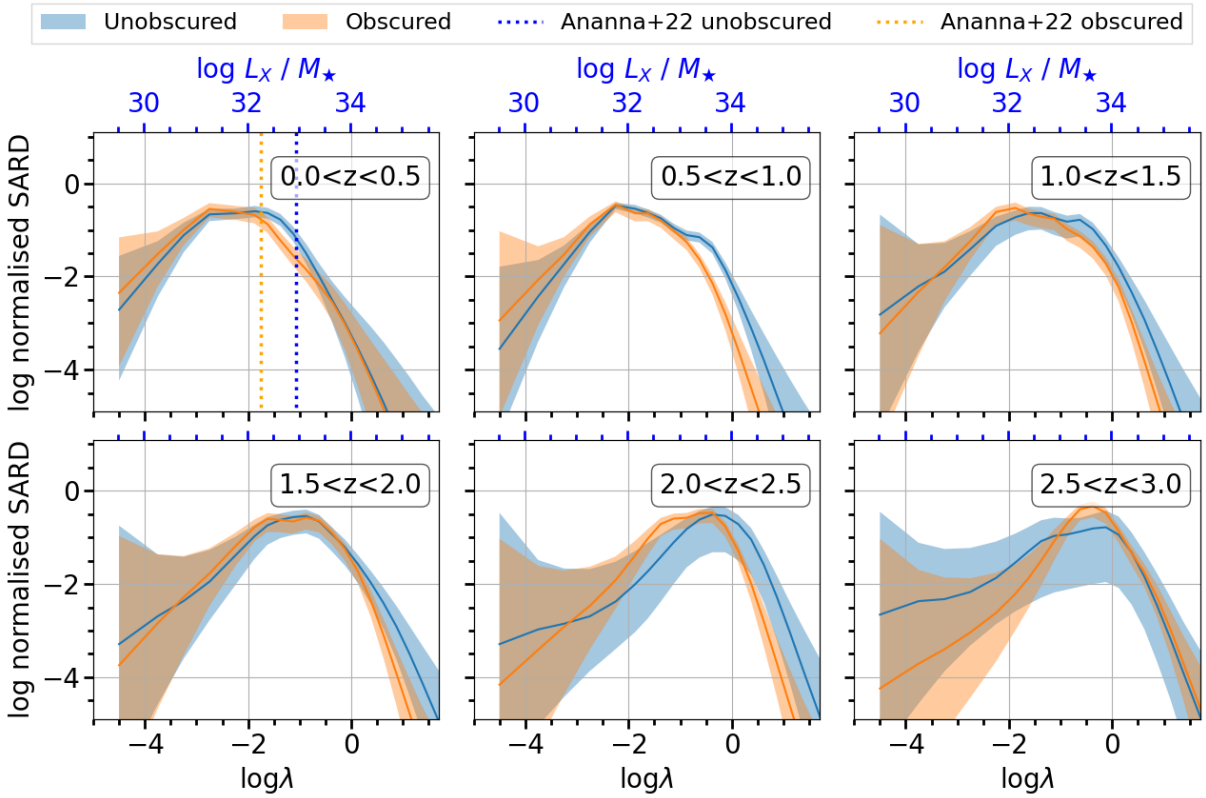

Figure 4.7: Specific accretion rate distributions for the unobscured (*blue*, $\log N_{\rm H}/{\rm cm}^{-2} < 22$) and obscured (*orange*, $22 < \log N_{\rm H}/{\rm cm}^{-2} < 24$) AGN populations. The plotted SARDs are normalised to unity for each obscuration bin following Equation 4.9. The lower x-axis in each panel is the SAR rescaled to units of Eddington ratio via Equation 4.1. For completeness, we also show the specific accretion rate in units of $\mathrm{erg\,s^{-1}\,M_\odot^{-1}}$ on the upper x-axis of each panel. The solid lines and shaded regions represent the median and the 1σ confidence intervals, respectively. Each panel corresponds to a different redshift interval from $z = 0-0.5$ to $z = 2.5-3$. In the $z < 0.5$ redshift interval, the blue and orange dotted vertical lines correspond, respectively, to the break of the Eddington ratio distribution function of unobscured and obscured AGN in A22b.

Despite the normalisation difference, the similarities between the shape of unobscured and obscured SARDs at fixed redshift in Figure 4.6 are striking. This is further demonstrated in Figure 4.7. The SARDs in this figure are independently normalised to unity for each obscuration interval to allow comparison of their shapes. Mathematically, this can be expressed by modifying Equation 4.3 as

$$\int P(\lambda, N_{\rm H}, z, M_\star)\, d\log\lambda = 1\,. \tag{4.9}$$

Therefore, the SARDs of Figure 4.7 represent the probability of an AGN in a given obscuration and redshift interval to accrete at a rate λ. Both unobscured and obscured AGN in Figure 4.7 have SARDs with overall shapes that, to the first order, are quite similar. However, a closer examination suggests a small ($\approx 1\sigma$ significance) but systematic offset between the SARDs of two populations at fixed redshift, with unobscured extending to higher specific accretion rates. Similar claims for such a trend exist in the literature (e.g. Mountrichas et al., 2024). If this effect is true, it can be interpreted as evidence that fast-accreting black holes are more likely to be unobscured. In Section 4.5.2, we discuss further the observed offset and explore systematic uncertainties that could produce it.

Another way to demonstrate this effect is to explore the redshift evolution of the mean SAR, $<\log\lambda>$, of the two AGN sub-populations, as shown in Figure 4.8. The averages are estimated from the SARDs of Figure 4.7 for the interval $-3.5 < \log\lambda < 2$. Unobscured AGN systematically exhibit higher $<\log\lambda>$ with respect to obscured ones, up to $z \sim 2.5$. Additionally, figure 4.8 includes the inferred mean accretion rate evolution of broad line QSOs of Shen & Kelly (2012). These independent estimates for a subpopulation of active SMBHs also show an increasing trend with redshift and are of the same order of magnitude as our results. Also shown in Figure 4.8 are the predictions of the cosmological hydrodynamic simulations presented by Hirschmann et al. (2014) and Habouzit et al. (2019). In these models, the mean accretion rate of SMBHs also increases with redshift as a result of the intensity of the adopted AGN (and star formation) feedback prescriptions that act to remove gas in the nuclear regions of galaxies toward later cosmic epochs. The shallower increasing trend in the case of the Illustris TNG100 simulation (Habouzit et al., 2019) is likely related to the implementation details of the AGN feedback.

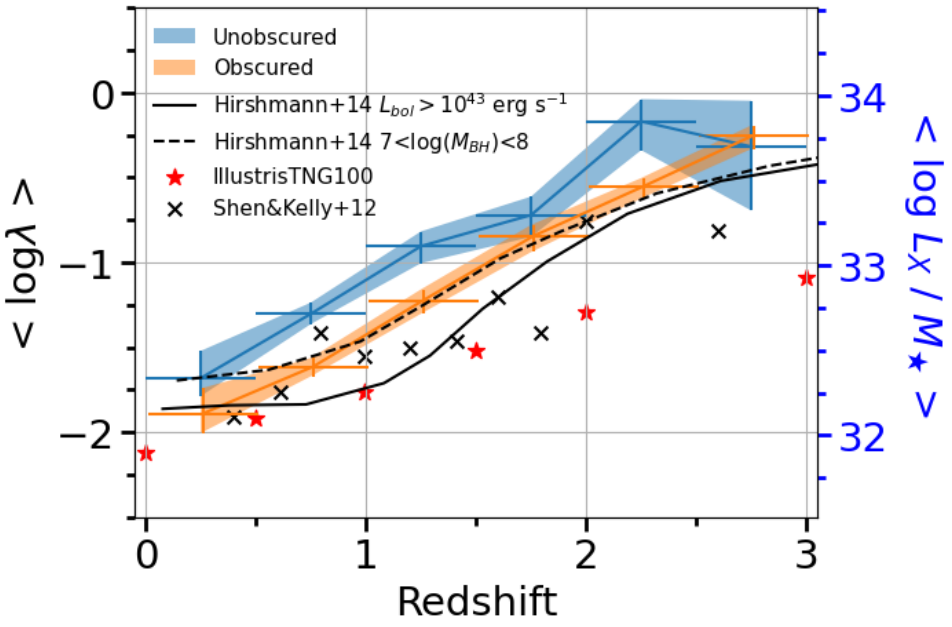

Figure 4.8: Mean SAR as a function of the redshift for the unobscured (*blue*, $\log N_{\rm H}/{\rm cm}^{-2} < 22$) and obscured (*orange*, $22 < \log N_{\rm H}/{\rm cm}^{-2} < 24$) populations based on the normalised SARD (Figure 4.7). The solid lines show the median for each subpopulation while the shaded regions correspond to the 1σ confidence interval. The black solid line is the mean accretion rate from the cosmological hydrodynamic simulations of Hirschmann et al. (2014) for AGN with bolometric luminosity $L_{\rm bol} > 10^{43}\,{\rm erg\,s^{-1}}$. The black dashed line corresponds to the subpopulation with $7 < \log(M_{\rm BH}/M_\odot) < 8$ from the same study. The red stars are the Illustris TNG100 cosmological simulation (Habouzit et al., 2019). The black crosses are the mean Eddington rates of broad line quasars estimated by Shen & Kelly (2012).

Figure 4.9 provides a further comparison of our SARD measurements with the previous estimates of Aird et al. (2012), Bongiorno et al. (2016), Georgakakis et al. (2017c) and Aird et al. (2018). We caution that from the studies above, only Bongiorno et al. (2016) include corrections to account in a statistical manner for the impact of obscuration on the AGN incidence measurements. For this comparison, we add the unobscured and obscured SARDs of Figure 4.6 to obtain the total CTN AGN SARD. While there is broad agreement in both shape and normalisation between the different SARD estimates presented in Figure 4.9, indicating a consistent emerging picture of the incidence of AGN in galaxies, second-order discrepancies are evident and are attributed to differences in methodology. Our non-parametric SARDs have a systematically higher normalisation at intermediate specific accretion rates $-2 \lesssim \log \lambda \lesssim 0$, compared to previous works. This is attributed to the fact that we explicitly estimate obscuration corrections for individual sources and also account for these effects in the X-ray selection function. Also, at low SAR, $\log \lambda \lesssim -2$, our SARD estimates lie below previous estimates. This difference is partly related to the obscuration corrections that act to move obscured AGN to higher intrinsic luminosities and hence, at fixed stellar mass, to higher SAR. Notably, the SARD of Aird et al. (2018) drops slower toward high λ values compared to ours and other estimates in Figure 4.9, reflecting their Bayesian Gamma distribution mixture model methodology.

We also compare our low redshift results with the recent work of Ananna et al. (2022a,b, A22a; A22b hereafter) based on the second data release of the BAT AGN spectroscopic survey (BASS DR2). BASS is a low-redshift ($z < 0.3$) serendipitous hard X-ray (14-195 keV) AGN survey, carried out by the *Swift*-BAT telescope (Gehrels et al., 2004; Barthelmy et al., 2005). This AGN sample is least biased by obscuration because high-energy photons can efficiently penetrate high columns of obscuring material. A22a determine simultaneously the black hole mass function and Eddington-ratio distribution function (ERDF) from the XLF of type I and type II AGN, defined by the presence or absence of broad Balmer emission lines, respectively. A22b further extend this study to X-ray unobscured ($N_{\rm H} < 10^{22}\,{\rm cm}^{-2}$) and obscured ($10^{22} \leq N_{\rm H} < 10^{25}\,{\rm cm}^{-2}$) AGN. It is crucial to note that the ERDF, which represents the space density of AGN in logarithmic Eddington ratio bins, is a distinctly different quantity from the SARD, which expresses the probability of a galaxy hosting an accretion event with a specific accretion rate λ.

Therefore, a direct comparison between the two statistical measures is not straightforward. We, therefore, do not display the results of A22b in Figure 4.9, but provide a qualitative comparison with our findings. In their work, A22b parametrise the ERDF by a broken power-law and infer breaks for unobscured and obscured AGN at Eddington ratios of -1.06 and -1.75, respectively. These break values are over-plotted as vertical lines in the $z < 0.5$ panel of Figure 4.7. Similarly to our results, A22b find that at high-λ unobscured AGN are more likely than their obscured counterparts. Moreover, the ERDF break values above are consistent, at least to the first approximation, with the SAR where the SARDs in Figure 4.7 show a significant change in their slopes. We caution, nevertheless, that the ERDFs of A22b use the Eddington ratio of individual AGN in their sample through direct measurements of their bolometric luminosities and black hole masses (Koss et al., 2022a). Instead, we use stellar masses as a proxy of the Eddington ratio under the assumption of an underlying $M_\star - M_{\rm BH}$ correlation. The impact of these assumptions is further discussed in Section 4.4.2.

4.4.2 Obscured Fraction

Next, we explore the CTN obscured AGN fraction as a function of the SAR. This is motivated by recent findings (R17; R22) suggesting that this parameter space provides a handle on AGN feedback mechanisms (Alonso-Herrero et al., 2021; Venanzi et al., 2020).

Figure 4.10 shows the dependence of the obscured CTN AGN fraction, $f_{\rm obs}$, with specific accretion rate for different redshift intervals up to $z = 2$. We obtain $f_{\rm obs}$ by dividing the obscured AGN SARDs presented in Figure 4.6 by the sum of both unobscured and obscured SARDs within each redshift bin. The general trend is that $f_{\rm obs}$ decreases with increasing SAR and this decline becomes steeper toward high λ values. The turnover point, $\lambda_{\rm break}$, where the slope changes substantially, appears to evolve with redshift, moving progressively to higher SAR.

At low redshift $z < 0.5$, our constraints are in reasonable agreement with the results of R17; R22; A22b up to $\log \lambda \approx -1$. These studies are based on the BASS sample of local AGN (Koss et al., 2017, 2022b). We find evidence for a significant change of slope at $\log \lambda \approx -2$, consistent with the findings of the studies above. However, the uncertainties in our measurements are important at both very low and high λ values due to the limited

volume of our sample at low redshift ($z < 0.5$).

According to R17 and R22, the λ dependence on $f_{\rm obs}$ and, more specifically, the steep decline toward high SAR in Figure 4.10 are suggestive of AGN radiation pressure acting on a dusty medium. While the standard Eddington limit, $\lambda = 1$, is typically calculated for a fully ionised gas, the AGN obscuring material is known to be partially ionised dusty gas with a cross-section larger than the Thomson one. A larger cross-section induces a lower effective Eddington limit dependent on the column density (Fabian et al., 2008, 2009). For a dusty gas at $N_{\rm H} = 10^{22}\,{\rm cm}^{-2}$, i.e. the column density limit adopted in this work to separate unobscured from obscured AGN, the effective Eddington limit is $\log \lambda_{\rm eff} \approx -1.7$ (Fabian et al., 2008). Thus, above this $\lambda_{\rm eff}$ limit, an AGN effectively accretes at super-Eddington rates and the radiation pressure is expected to blow away the surrounding CTN clouds. As a consequence, the covering factor is reduced, impacting the probability that the AGN is observed as obscured, i.e., the obscured fraction (Ramos Almeida & Ricci, 2017b). At $z < 0.5$, the results on the obscured AGN fraction plotted in Figure 4.10, i.e. the sharp decrease of $f_{\rm obs}$ at $\log \lambda_{\rm break} \approx -2$, are broadly consistent with this expectation.

At higher redshifts, the turnover point moves to increasingly higher λ values, deviating from local Universe results. This shift could indicate a change in the $\lambda_{\rm eff}$ limit to drive away the obscuring material. For instance, Fabian et al. (2009) argue that a lower dust grain abundance would increase the low-$N_{\rm H}$ effective Eddington limit. Additionally, the presence of stars in the environment can increase the inward gravitational pull, thereby, shifting the $\lambda_{\rm eff}$ limit towards higher accretion rates. The amplitude of these effects, however, is not expected to be sufficient to explain the shift of the $f_{\rm obs}$ turnover point to high SAR.

The adopted scaling relations to convert the SAR, $L_{\rm X}/M_\star$, to Eddington ratio might also influence the observed trends of the obscured fraction with redshift in Figure 4.10. For example, a systematic shift towards heavier black hole masses at fixed stellar mass at higher redshifts compared to the adopted local $M_\star - M_{\rm BH}$ relation would lead to a shift of our $f_{\rm obs}$ curves in Figure 4.10 toward lower Eddington ratios. However, studies of the $M_\star - M_{\rm BH}$ relation suggest only mild evolution with redshift (Aversa et al., 2015; Suh et al., 2020; López et al., 2023), insufficient to explain the 1–2 dex shift of $\lambda_{\rm break}$ at $z = 2$ in

Figure 4.10. Also, in our analysis, the bolometric correction used to convert the 2-10 keV luminosity to bolometric is fixed to $K_{\rm bol} = 25$. Instead, it is suggested that $K_{\rm bol}$ increases with increasing luminosity (e.g. Marconi & Hunt, 2003; Duras et al., 2020). We assess the impact of a variable bolometric correction factor by repeating our Bayesian inference analysis using the Duras et al. (2020) luminosity-dependent bolometric corrections. We use the new SARD estimates to measure $f_{\rm obs}$ for different redshift intervals, and we find no significant difference with the $f_{\rm obs}$ shapes shown in Figure 4.10. Furthermore, Duras et al. (2020) find no dependence of the X-ray bolometric correction on redshift. We therefore conclude that the scaling relations adopted to convert the SAR we measure directly from the observations to Eddington ratio cannot account for the redshift evolution pattern of the $f_{\rm obs}$ in Figure 4.10.

Studies of the AGN space density evolution and demographics have long claimed that the obscured AGN fraction depends on AGN luminosity in the sense that obscured AGN become scarcer as the central engine becomes brighter (e.g. Lawrence, 1991; La Franca et al., 2005; Hasinger, 2008; Merloni et al., 2014; Ueda et al., 2014; Buchner et al., 2015; Aird et al., 2015; Vijarnwannaluk et al., 2022). This trend can be interpreted in the context of the receding torus model, in which the opening angle (i.e. width) of the torus decreases with increasing luminosity (Lawrence, 1991). It is also broadly consistent with the hydrodynamic simulations of the radiation-driven fountain model (Wada, 2012), in which the radiation of the accretion disk drives the gas flow and generates a torus-like structure. It is interesting to assess the extent to which the luminosity dependent-obscuration is consistent with the observations in Figure 4.10 suggesting that $f_{\rm obs}$ is dependent of λ. For this exercise, we use the empirical model of Georgakakis et al. (2020). They infer the SARD of AGN by assuming that convolving it with the galaxy SMF at a given redshift reproduces the X-ray luminosity function of AGN. Georgakakis et al. (2020) use the Ilbert et al. (2013) SMF and the Aird et al. (2015) X-ray luminosity function (including obscured AGN) to solve the above inverse convolution problem and estimate a parametric model for the SARD of AGN as a function of redshift. This SARD parametrisation is then used to assign specific accretion rates to mock galaxies drawn from the SMF and hence, produce simulated AGN samples. These AGN are further assigned column densities, $N_{\rm H}$, in a probabilistic way based on the obscuration model of Aird et al. (2015). Inherent

in these mock AGN catalogues is the X-ray luminosity-dependent obscuration inferred by Aird et al. (2015). We use the Georgakakis et al. (2020) empirical model to make predictions on how $f_{\rm obs}$ varies as a function of specific accretion rate and to overplot the results in Figure 4.10. This rather simple empirical model performs reasonably well and, to the first approximation, is consistent with the observations in Figure 4.10 especially at $0.5 < z < 1.5$. In detail, however, there are discrepancies suggesting that AGN luminosity may not be the only parameter that affects the covering factor of the obscuring material in AGN.

4.4.3 Evolution of the Blow-out Region

Figure 4.11 provides an alternative visualization of the obscured fraction evolution, depicting the SARD as a function of both $N_{\rm H}$ and λ. The shading of each cell represents the probability density for an AGN of being in that cell at a given redshift and with a stellar mass within $9.5 < \log(M_\star/M_\odot) < 11.5$. It reflects the intrinsic and unbiased distribution of AGN in this plane. The probability values shown in this figure are computed using the same methodology described in Section 4.3.3, except that the boundaries of the $\log(N_{\rm H}/{\rm cm}^{-2})$ grid are now set at [20, 22, 23, 24]. In each panel of Figure 4.11, the *red solid line* corresponds to the effective Eddington limit for a dusty gas as a function of the column density (Fabian et al., 2008). The region located above the obscuration limit $N_{\rm H} > 10^{22}{\rm cm}^{-2}$ and on the right of the effective Eddington limit curve is referred to as the blow-out or *forbidden* region (Venanzi et al., 2020). As mentioned previously, due to the dustiness of the surrounding gas, sources in this region are effectively accreting at super-Eddington rates despite having $\lambda < 1$. The radiation pressure of these AGN can potentially launch winds that clear up the obscuring material in a short time scale relative to the overall AGN phase. Therefore, due to being short-lived and unstable, the fraction of AGN detected in that region is expected to be small hence, its name (Fabian et al., 2009; Ricci et al., 2017b, 2022).

In the $z < 0.5$ panel of Figure 4.11, the blow-out region is sparsely populated, consistent with the predictions of the theoretical picture presented above. However, with increasing redshift, the *forbidden* region appears progressively more populated. The *white dots* in each panel represent the peaks of the AGN probability distribution for each $N_{\rm H}$

interval and they shift towards higher SAR with increasing redshift. This global increase of the accretion activity of AGN with redshift is better visualised by the probability summed over $N_{\rm H}$ displayed with a *dashed line* at the bottom of each panel in Figure 4.11. Conversely, the probability density summed over λ, represented by the *dashed line* on the right side of each panel, shows an increase of obscured AGN with redshift.

From Figure 4.11, it is possible to estimate the fraction of AGN within the blow-out region as

$$f_{\rm blow-out} = \frac{\sum\limits_{(\lambda, N_{\rm H}) \in \mathcal{R}_f} P(\lambda,\, N_{\rm H} \,|\, z)}{\sum\limits_{\log\lambda > -3.5} P(\lambda,\, N_{\rm H} \,|\, z)}, \tag{4.10}$$

where $P(\lambda,\, N_{\rm H} \,|\, z)$ is the probability in the two dimensional space $(\lambda,\, N_{\rm H})$ of Figure 4.11 and $\mathcal{R}_f$ is *forbidden* region of the parameter space. For the summation of the numerator, we attribute to the cells that partially overlap with the blow-out region a weight corresponding to the fraction of their area within that region. The summation of the denominator is over all cells with $\log\lambda > -3.5$ and represents the AGN duty-cycle, i.e. the probability that a galaxy hosts an AGN with SAR higher than the threshold $\log\lambda > -3.5$. Figure 4.12 illustrates the dependence of the duty-cycle on the chosen λ-threshold for different redshift intervals. The choice of the λ-threshold affects the width of the duty cycle uncertainties (*red violin plot* in each panel), and consequently, also the uncertainties of $f_{\rm blow-out}$. Nevertheless, the λ-threshold choice does not impact our results and conclusions.

The evolution of $f_{\rm blow-out}$ with redshift is shown in Figure 4.13 in the form of violins representing the posterior distribution for each redshift interval. The median $f_{\rm blow-out}$ values increase with the increasing redshift with over 10% of the AGN at $z > 1$ being found in the *forbidden* region. This significant evolution of $f_{\rm blow-out}$ is at odds with the very definition of the *forbidden* region. Nevertheless, we caution that the uncertainties of $f_{\rm blow-out}$ also progressively rise with redshift, becoming significant at $z > 1.5$. These large error bars reflect the increasing uncertainty in the determination of the AGN duty cycle, $\sum_{\log\lambda > -3.5} P(\lambda,\, N_{\rm H} \,|\, z)$, i.e. the denominator of Equation 4.10. For instance, within the redshift range $1.5 < z < 2$ (bottom right panel of Figure 4.12), the median duty cycle and 1σ errors are $12^{+4}_{-2}\%$, but the tails of the posterior distribution are pronounced with the $3\,\sigma$ upper confidence limit being 70%. Consequently, the posterior distribution of $f_{\rm blow-out}$

also has an extended posterior tail to lower values.

In Figure 4.13, we also compare our results with the local Universe measurement of R17 based on the BASS sample. They estimate $f_{\rm blow-out} = 1.4\%$ in good agreement with our measurement at $z < 0.5$, $f_{\rm blow-out} = 1.4^{+0.6}_{-0.4}\%$. Additionally, we include the findings of Toba et al. (2022) in this figure, which investigate the multi-wavelength properties of 692 X-ray selected AGN with WISE W4 counterparts detected in the *eROSITA* Final Equatorial-Depth Survey (eFEDS, Brunner et al., 2022). Under the assumption of a constant AGN blow-out fraction in the redshift interval $z = 0 - 3$, they infer $f_{\rm blow-out} = 5 \pm 2.5\%$, illustrated by the red shaded region in Figure 4.13. Our results, however, suggest an increasing trend for $f_{\rm blow-out}$ toward high redshift, contradicting the constant fraction assumption of Toba et al. (2022). Nevertheless, when these authors split their sample into low ($z = 0 - 1$) and high($z = 1 - 3$) redshift bins, they find a mild increase. It is worth underlying that *eROSITA* is a soft X-ray (0.3-2.3 keV) telescope (Liu et al., 2022) and, therefore, biased against obscured systems. Additionally, Figure 4.13 presents the recent results of Vijarnwannaluk et al. (2024) which, by exploiting the HSC-DEEP *XMM*-LSS survey data, find $f_{\rm blow-out} = 0.18 \pm 0.02$ in the redshift interval $0.8 < z < 1.8$. When splitting the redshift interval in half, an $f_{\rm blow-out}$ increasing trend similar to our results is noticeable with $f_{\rm blow-out} = 0.14 \pm 0.03$ at $0.8 < z < 1.3$ and $f_{\rm blow-out} = 0.21 \pm 0.04$ at $1.3 < z < 1.8$.

The adopted scaling relations to convert the specific accretion rate to Eddington ratio (see Equation 4.1) clearly affects the inferred fraction of AGN within the *forbidden* region of Figure 4.11. For example, if the $M_{BH} - M_\star$ relation evolves with redshift in a way that leads to more massive BHs at fixed stellar mass, then the net effect would be an overall shift of the probabilities of individual cells in Figure 4.11 toward lower Eddington ratios. This would reduce the estimated fraction of AGN in the blowout region in Figure 4.13. However, as discussed in Section 4.4.2, studies of the $M_{BH} - M_\star$ relation suggest little evidence for redshift evolution. Introducing scatter in $M_{BH} - M_\star$ relation would tend to blur the estimated probabilities of individual cells in Figure 4.11 by distributing them to nearby λ bins but is not expected to drastically modify the observed trends. The choice of the X-ray bolometric correction also has little impact on the results shown in Figures 4.11 and 4.13. The increase of $f_{\rm blow-out}$ could potentially indicate a decrease in

the efficiency of the dusty radiation pressure mechanism to launch outflows. Varying the dust grain abundance, for instance, reduces the area of the *forbidden* region (Fabian et al., 2009), resulting in lower $f_{\rm blow-out}$ values. However, changing the abundance from 1 to 0.3 or 0.1 does not change the behaviour of the $f_{\rm blow-out}$ posterior distribution that remains increasing with redshift. The only difference is that the median values are slightly lower compared to those plotted in Figure 4.13, with a maximum difference of $\sim 4\%$ at high redshift.

4.5 Discussion

This thesis Chapter presents the first quantitative analysis of how AGN with varying levels of line-of-sight obscuration inhabit galaxies across cosmic time, from the local Universe to high redshifts, $z \sim 3$. We combine three extragalactic X-ray survey fields (COSMOS, AEGIS-XD, CDFS) with distinct X-ray depths and sizes on the sky to compile a sample of 3882 X-ray selected AGN with 2-10 keV luminosities in the range $10^{40} - 10^{46}\,{\rm erg\,s^{-1}}$ and redshifts spanning $z = 0.01 - 5$ (see Figure 4.1). We employ state-of-the-art Bayesian X-ray analysis techniques to constrain the intrinsic 2-10 keV X-ray luminosity, $L_{\rm X}$, and hydrogen line-of-sight column density, $N_{\rm H}$, of individual sources in the sample. In parallel, template fitting of the observed UV-to-mid-IR SEDs yields constraints of the stellar masses $M_\star$ of the X-ray AGN host galaxies. Combining these observables enables us to derive the specific accretion rate $\lambda \propto L_{\rm X}/M_\star$ and its associated uncertainty for each source. We develop a Bayesian framework that accounts for selection effects and observation uncertainties to derive the SARD, i.e. the probability of a galaxy at a given redshift hosting an AGN with a given λ and $N_{\rm H}$. In the following sections, we discuss the redshift evolution of the SARD (Section 4.5.1) and how our findings provide information on the origin of the obscurer (Section 4.5.2 and 4.5.3).

4.5.1 SARD Redshift Evolution: Evidence for Downsizing?

Our analysis shows that the specific accretion rate of both unobscured ($20 < \log(N_{\rm H}/{\rm cm^{-2}}) < 22$) and CTN obscured ($22 < \log(N_{\rm H}/{\rm cm^{-2}}) < 24$) AGN has a complex shape that can be roughly approximated by a power-law, bending to a steeper slope at

high SARs, and showing evidence for a turnover at the low-SAR end (see Figure 4.6). Interestingly, the high SAR bending point, where the slope of the distribution changes significantly, appears to shift to higher specific accretion rates with increasing redshift. This evolution pattern applies to both the obscured and unobscured AGN population and results in an increase of the mean SAR with increasing redshift, e.g. Figure 4.8. Similar results have been reported in previous studies (Shen & Kelly, 2012; Georgakakis et al., 2017c) and align with the predictions of cosmological models on the evolution of galaxies and their supermassive black holes (Sijacki et al., 2015; Weinberger et al., 2018). The physical interpretation of this trend is tied to the impact of AGN feedback on the gas availability in the vicinity of SMBHs (Hirschmann et al., 2014; Habouzit et al., 2019).

Another perspective on the SARD evolution pattern is presented in Figure 4.14, which plots the probability of a galaxy hosting an AGN at fixed SAR as a function of redshift. With increasing SAR (different panels in Figure 4.14), the peak or plateau of the corresponding curves shift to higher redshift, with the trend being more pronounced in the case of obscured AGN. Figure 4.14 is reminiscent of the concept of AGN "downsizing" (Barger et al., 2005; Hasinger et al., 2005; Shankar et al., 2013), originally defined as the fact that the accretion density of low-luminosity systems peaks at lower redshift compared to luminous AGN. Previous studies indeed suggest a connection between AGN downswing and the evolution of the incidence of AGN in galaxies. Georgakakis et al. (2017c) for example, find evidence that at earlier times, the relative probability of high versus low specific accretion rate events among galaxies increases, in qualitative agreement with the trends in Figure 4.14. They argue that this differential redshift evolution of the AGN duty cycle with respect to SAR produces the AGN downsizing trend. Similarly, Bongiorno et al. (2016) argue that the differential redshift evolution of the AGN SARD compared to the weak evolution of the host galaxy SMF are the main factors behind the AGN downswing trend, which is reflected by the evolution of the SARD, i.e. shift to higher SAR with increasing redshift, at fixed $M_\star$ range. Moreover, our analysis adds to the studies above by showing that SARD evolution applies separately to both obscured and unobscured AGN. Therefore, the underlying physical mechanism driving this trend applies nearly uniformly to all AGN, regardless of obscuration level. The well-established increase in the gas content of galaxies to $z \sim 3$ (Santini et al., 2014; Tacconi et al., 2020) likely plays

an important role in establishing the patterns shown in Figures 4.6, 4.8 and 4.14.

4.5.2 Origin of the Obscurer: Support of a Modified Orientation Model

In this subsection, we discuss the results of the comparison of the SARDs of obscured and unobscured AGN, contextualizing them within models explaining the nature of the obscurer. The simplest version of the orientation or unification scenario (Antonucci, 1993; Urry & Padovani, 1995) postulates that all AGN are surrounded by obscuring material with a toroidal shape (Ramos Almeida & Ricci, 2017b; Combes et al., 2019; García-Burillo et al., 2019, 2021; Gámez Rosas et al., 2022) and a universal opening angle. The obscuration properties of individual AGN are determined by geometrical effects, i.e. if the line of sight to the observer intersects the obscurer. In this picture, since obscured and unobscured AGN differ only in their orientation relative to the observer, their SARDs are expected to have similar shapes. Figure 4.6 is consistent with this scenario, showing that, to the first approximation, the SARDs of AGN samples categorized by hydrogen column density $N_{\rm H}$ are similar once differences in their normalisations are factored out.

In detail, however, there is evidence in Figure 4.7 for subtle differences between the SARDs of obscured and unobscured AGN, in the sense that the SARD high-λ turnover point of unobscured systems is located towards higher SAR compared to obscured AGN. As illustrated in Figure 4.10, this offset leads to a fast decline in the obscured AGN fraction, directly related to the opening angle of the dust and gas clouds surrounding the central engine. This finding aligns with studies on the Eddington ratio distribution of type I and type II AGN in the local Universe (R17; R22; A22b). Nevertheless, we caution against potential systematic and random errors that might affect the observed trend, such as biases in determining the stellar mass of galaxies hosting AGN. In particular, for type I AGN, estimating host galaxy properties by fitting templates to the observed SEDs is non-trivial (Vanden Berk et al., 2001; Richards et al., 2006) and requires the decomposition of the stellar emission from the AGN light. For example, an ad-hoc systematic stellar mass bias of +0.3 dex for unobscured AGN suffices to mask any differences between the SARDs of obscured and unobscured AGN in Figure 4.6. However, previous studies either do not find systematic differences in the stellar mass distribution of obscured and unobscured

AGN (Andonie et al., 2022a) or suggest that obscured AGN are actually more massive than unobscured ones (Mountrichas et al., 2021; Mountrichas & Georgantopoulos, 2023). Additionally, the $M_{\rm BH} - M_{\star}$ scaling relation used in our study for converting SAR to Eddington ratio, may impact our results due to its scatter and potential dependence on obscuration (Ricci et al., 2017a). Nevertheless, despite these potential caveats, our results indicate a second-order but significant difference in the accretion properties of unobscured and obscured AGN.

The dependence of the obscured AGN fraction on physical parameters, such as accretion luminosity or Eddington ratio, provides additional information on the origin of the obscuration in AGN. We explore this potential in Figure 4.10, which plots the obscured AGN fraction as a function of λ. The observed trends in this figure broadly align with a modified version of the unification model, suggesting a reduction in the opening angle of the obscurer as luminosities increase (e.g. Lawrence, 1991, see discussion in Section 4.4.2). An alternative scenario for the dependence of the obscured fraction on SAR is the radiation-regulated model (R17; R22) that links AGN obscuration to distinct stages of the growth of black holes. In this picture, AGN feedback acting on dusty gas clouds (Fabian et al., 2008, 2009) regulates the evolution of AGN on the $\lambda - N_{\rm H}$ plane of Figure 4.11. Initially, an accretion event onto an SMBH is triggered by some process (e.g. disk instabilities, galaxy interactions). The quiescent black hole starts off at the far left end of $\lambda - N_{\rm H}$ diagram of Figure 4.11 and moves gradually to higher λ. At the same time, the line-of-sight obscuration of the system increases as a result of the inflowing material of gas and dust clouds. As a result, the AGN moves toward the top left corner of the $\lambda - N_{\rm H}$ plane, where the obscurer has a larger covering factor, e.g. $\sim 85\%$ at $\log\lambda < -2$ in the work of R17. As the Eddington ratio continues to increase, the AGN enters the *forbidden* region of the parameter space, where radiation pressure acting on the dust grains renders the system unstable to outflows (Fabian et al., 2008, 2009) that can act to gradually push away the CTN obscuring material. The final stage of black hole growth consists of a rapidly accreting unobscured AGN with a low covering factor at the bottom right corner of the diagram. Ultimately, as the gas and dust are consumed by the black hole or blown away, the accretion rate gradually decreases, and the system returns to its initial quiescent state.

This modified orientation scenario that includes feedback predicts a decrease in the obscured AGN fraction beyond $\log \lambda_{\rm break} \approx -2$, corresponding to the effective Eddington limit of dust clouds with $N_{\rm H} \approx 10^{22}\,{\rm cm}^{-2}$. As explained in Section 4.4.3, this obscured AGN fraction decline is attributed to the existence of the *forbidden* region (*red-hatched* area in Figure 4.11), in which the incidence of AGN is theoretically very low. Our results in the smallest redshift bin ($z < 0.5$) suggest that $f_{\rm blow-out} \sim 1\%$, in agreement with local Universe studies R17. However, as illustrated in Figure 4.13, the fraction of AGN in this region increases significantly with redshift, exceeding 30% of AGN at $z > 2$, surpassing previous estimations (Toba et al., 2022). Consequently, as depicted in Figure 4.10, $\lambda_{\rm break}$ at which the obscured AGN fraction declines shifts with redshift, from $\log \lambda \sim -2$ to higher SAR, no longer consistent with the radiation-regulated model predictions. The nature of the AGN driving this redshift evolution of the *forbidden* region is key to understand the intrinsic relation between obscuration and accretion.

To start with, it is important to acknowledge that the effective Eddington limit, bordering the blow-out region, is not universal. Its characteristics depend on physical parameters that can differ among various AGN (Arakawa et al., 2022). Fabian et al. (2009) demonstrate that the dust-to-gas ratio can impact the shape of this limit, while the presence of stars can shift the $\lambda_{\rm eff}$ limit to higher accretion rates. Expanding on this, Ishibashi et al. (2018) suggest that radiation trapping makes the high-obscuration end of the $\lambda_{\rm eff}$ limit more vertical, expanding the size of the *forbidden* region. Furthermore, they propose that factors such as the inclination angle of the line-of-sight or external gas pressure due to gas inflow can shift the $\lambda_{\rm eff}$ limit along the λ-axis. Additional assumptions, like the isotropy of the emission, can also impact the effective Eddington limit. While these physical dependencies may contribute to the scatter of AGN in the $\lambda - N_{\rm H}$ plane at low redshifts ($z < 0.5$), they appear too weak to account for the observed redshift evolution.

By definition, AGN in the blow-out region should exhibit outflows that push away the nuclear-scale obscuring material through radiation pressure (Fabian et al., 2008, 2009). For instance, Kakkad et al. (2016) find that 4 out of the 5 AGN selected in the *forbidden* region show clear outflow signatures. Similarly, using the eFEDs catalogue (Brunner et al., 2022), Musiimenta et al. (2023) compare the outflow properties of mid-IR colour-selected AGN (sample A, Brusa et al., 2015; Zakamska et al., 2016; Perrotta et al., 2019) with

AGN selected within the blow-out region (sample B). Remarkably, sample B contains 528 sources ($\sim$ 14% of the parent eFEDS population with black hole mass estimates at $z > 0.5$), reinforcing the idea of a non-empty *forbidden* region. Additionally, both samples A and B exhibit high outflow incidence with respectively 75% and $\sim$ 45%. It is worth mentioning that sample A contains only 4 sources within the redshift of interval and with good enough spectroscopy. However, sample B shows bluer colours than sample A, which could suggest the *forbidden* region is an initial stage of the blowout phase or the presence of inhomogeneous obscuration. These results are supported by the work of Yamada et al. (2021), which suggests that chaotic quasi-spherical inflows in late mergers produce dusty outflows, responsible for the obscuration in the blow-out region. If the expected high incidence of outflows in *forbidden* region AGN is confirmed in larger samples, thereby, the increasing $f_{\mathrm{blow-out}}$ with redshift could indicate an increased incidence of outflows in the overall AGN population with redshift. However, previous studies claim that the fraction of [O III] outflows in AGN does not significantly evolve with redshift (Harrison et al., 2016; Coatman et al., 2019).

4.5.3 Origin of the Obscurer: Evidence for ISM Obscuration

The redshift evolution of f_{obs} and $f_{\mathrm{blow-out}}$ can also be explained by a different origin of the obscuration. According to evolutionary models (e.g. Sanders et al., 1988; Di Matteo et al., 2005; Hopkins et al., 2006; Klindt et al., 2019), obscuration is linked to a specific stage in the life cycle of an AGN. During this stage, infalling gas and dust that fuel the SMBH create a cocoon of obscuring material around it (Lapi et al., 2018; Sicilia et al., 2022). This connection ties AGN growth and feedback activity to host galaxy properties, such as the star formation rate (Lapi et al., 2014). The main distinction from the earlier mentioned radiation-regulated model R17 is that the obscurer is not confined to the nuclear scale. It can also originate from the interaction of the photons with the interstellar medium (ISM) of the host galaxy on larger scales. A direct consequence of this large-scale ISM obscuration is a longer time-scale for the feedback to clear out the ISM obscuring material (e.g. 10^{6-7} yr for distances 10^{2-3} pc from the central engine, King & Pounds, 2015; Jun et al., 2021b) compared to nuclear-scale obscuration (e.g. $\approx 2 \times 10^5$ yr for distances of about 30 pc, Lansbury et al., 2020; Jun et al., 2021b). Therefore, ISM-

obscured AGN can have a higher incidence in the blow-out region compared to torus-obscured AGN. The powerful dust-reddened quasars are believed to be obscured by the ISM (Alexander & Hickox, 2012; Klindt et al., 2019; Andonie et al., 2022a), and represent a younger, transitioning phase than their bluer counterparts (Yi et al., 2022). Interestingly, previous studies found a significant number of such red quasars within the *forbidden* region (Glikman, 2017; Lansbury et al., 2020). Furthermore, in a recent study, Glikman et al. (2024) examine a sample of 10 red quasars from the FIRST-2MASS survey and noticed that all quasars hosted in galaxies exhibiting merging signatures were found within the blow-out region. These findings suggest the importance of the host galaxy evolution on the AGN properties.

However, a limitation of this work is the difficulty of disentangling nuclear-scale and large-scale obscuration from X-ray spectroscopy alone. The ISM contribution to the line-of-sight obscuration $N_{\rm H}$ is considered insignificant at low redshift. Nevertheless, several studies point to an increasing ISM contribution with higher redshifts (Buchner et al., 2017; Gilli et al., 2022; Alonso-Tetilla et al., 2023), which can even dominate in compact starburst galaxies (Andonie et al., 2024). For instance, Buchner et al. (2017) use gamma-ray bursts to probe the host galaxy obscuration and find a $M_\star - N_{\rm H,\,ISM}$ relation suggesting a higher ISM obscuration contribution in the most massive galaxies. Similarly, Buchner & Bauer (2017) observe an ISM obscuration increase with redshift. Moreover, Gilli et al. (2022) estimate that the median ISM surface density evolves with $(1+z)^{4.3}$, suggesting that the ISM obscuration could even exceed the CTK limit at $z \geq 6$. Additionally, the recent work of Andonie et al. (2024) uses a similar methodology as Circosta et al. (2019), independently measuring the size of host galaxies with ALMA observations and the total gas mass in them to constrain ISM obscuration. By doing so, Andonie et al. (2024) find a dependence between obscuration and star formation rate and observationally confirm that ISM obscuration can even be CTK in the most compact starburst galaxies.

The impact of the increasing ISM obscuration with redshift on the *forbidden* region is illustrated in Figure 4.15. In our study, the obscuration lower limit of the blow-out region is fixed to $N_{\rm H} = 10^{22}\,{\rm cm}^{-2}$ (Matt, 2000). Above this threshold, we assume that the obscuration is only attributed to the torus. However, according to the findings of Gilli et al. (2022), the ISM obscuration is increasing with redshift (vertical large *red arrow* in

Figure 4.15) and the median ISM obscuration, $N_{\rm H,\,ISM}$, is larger than the $10^{22}\,{\rm cm}^{-2}$ threshold at $z > 1$. Therefore, at higher redshifts, an AGN in the *forbidden* region would have its nuclear-scale obscurer rapidly blown away as in the local Universe, but, due to longer clearing time scales, the ISM obscurer will maintain the AGN within the blow-out region, increasing the incidence of AGN in that region. One could then consider the definition of a *forbidden* region with a redshift-dependent $N_{\rm H}$-threshold as displayed in Figure 4.15. With increasing redshift, the $N_{\rm H}$-threshold would increase and, subsequently, the intersection with the effective Eddington limit would be shifted towards higher λ (horizontal large *red arrow* in Figure 4.15). This intersection corresponds to the $\lambda_{\rm break}$ at which the obscured AGN fraction strongly decreases. Indeed, only AGN with higher accretion rates $\lambda > \lambda_{\rm break}$ and higher obscuration $N_{\rm H} > N_{\rm H,\,ISM}$ can potentially be impacted by the dusty radiation pressure and have their obscurer rapidly blown away, decreasing the observed obscured AGN fraction. It is important to note, however, that the $\lambda_{\rm break}$ values shown in Figure 4.15 should only be considered illustrative. As mentioned earlier, the effective Eddington limit curve is not universal. Moreover, the $N_{\rm H,\,ISM}$ redshift evolution used here (Gilli et al., 2022) corresponds to the median ISM obscuration, i.e. more heavily ISM-obscured AGN can still occupy the redefined redshift-dependent *forbidden* region. Nevertheless, this scenario explains qualitatively the increasing $f_{\rm blow-out}$ with redshift (Figure 4.13) and the shift of $\lambda_{\rm break}$ toward higher λ with redshift (Figure 4.10).

4.6 Summary and Future Works

In this study, we investigate the incidence of obscuration on the growth of AGN and its evolution up to redshift $z \leq 3$ by combining data from three X-ray field surveys: COSMOS, AEGIS, CDFS (Section 4.2). The X-ray obscuration and intrinsic luminosity are measured by X-ray spectroscopy, while the stellar mass of the host galaxy is estimated through SED fitting (Section 4.3.1 and 4.3.2, respectively). These measurements are combined through a non-parametric Bayesian analysis, with careful propagation of measurement uncertainties throughout the analysis, to constrain the SARD (Section 4.3.3). Pioneer studies (R17; R22; A22b), using hard-X-ray ($> 10\,{\rm keV}$) selected AGN, have investigated the relation between obscuration and accretion rate. However,

our analysis expands this investigation, for the first time, to higher redshift ~ 3 and with a larger AGN sample (~ 4000 sources). Furthermore, an innovative aspect of our study is its non-parametric approach, eliminating dependencies on prior assumptions regarding the shape and evolution of the SARD.

The key results of our research are summarised below:

- Unobscured and obscured SARDs have similar shapes at first approximation, in agreement with the AGN orientation model paradigm (Figure 4.6).

- The SARDs of both unobscured and obscured AGN populations shift toward higher accretion rates with redshift (Figure 4.6) driving a systematic increase in the mean accretion rate (Figure 4.8). These results are consistent with the AGN "downsizing" and suggest that the driver of these increases similarly impacts both AGN populations, possibly due to the increased gas availability in galaxies at higher redshifts (see discussion in Section 4.5.1).

- When normalised over $N_{\rm H}$ (Figure 4.7), the SARD of unobscured AGN show a small systematic offset towards higher accretion rates compared to the obscured population, leading to a ~ 0.5 dex offset in $<\log\lambda>$ (Figure 4.8). These findings argue against the simplest unification model.

- For all redshifts, the obscured AGN fraction is high before declining at a certain $\lambda_{\rm break}$ value. Below $z < 0.5$, our findings behave similarly to the results of R17 up to $\log\lambda < -1$. However, the $\lambda_{\rm break}$ shifts towards higher λ with redshift, leading to an increased obscured AGN fraction at high-λ with redshift.

- In the $\lambda - N_{\rm H}$ plane's *forbidden* region, where radiation pressure is thought to efficiently clear obscuration, a sparse population is expected (R17), as indicated in our observations at $z < 0.5$. However, our results demonstrate a gradual increase in AGN density within this region at higher redshifts (see Figure 4.11 and 4.13).

- The redshift evolution of the obscured AGN fraction and the *forbidden* region AGN fraction may be attributed to either an increased incidence of outflows in AGN (see discussion in Section 4.5.2) or to an increased host-galaxy interstellar medium obscuration with redshift (see discussion in Section 4.5.3 and Figure 4.15).

In conclusion, our novel approach, differentiating between obscured and unobscured AGN populations, provides valuable insights into the relationship between obscuration and SMBH accretion. The similarity of the overall SARD shape and the evolution of the mean accretion rate between obscured and unobscured AGN suggest a shared underlying physical driver, broadly supporting the orientation model. However, at higher accretion rates, a stark divergence emerges, indicating a more complex behaviour. The evolution of this divergence as a function of the redshift can shed light on the growth and outflow mechanisms that drive the AGN life cycle.

Follow-up studies could assess the high outflow incidence expected in *forbidden* region AGN as a function of the redshift to inspect this transitioning stage of AGN. For that purpose, several wavebands can be valuable, for instance, ALMA can also trace molecular outflows. Additionally, optical spectra can inspect the presence of broad absorption lines (BAL, Weymann et al., 1991; Gallagher et al., 2006), characteristic of outflows. An obvious limitation would be the availability of optical spectra, especially since obscuration strongly impacts the emission lines, but future large spectroscopic surveys like MOONRISE (Maiolino et al., 2020), the 4MOST AGN survey (Merloni et al., 2019, Andonie in prep.) or with the MOSAIC instrument on ELT will provide statistically significant spectra samples. Moreover, the recent work of Fawcett et al. (2023) suggests that outflows interacting with the ISM could produce radio-quiet emission, linking radio-detection fraction and obscuration. A follow-up analysis of the radio-detection in the forbidden region is in preparation. Complementary, following the methodology of Circosta et al. (2019); Andonie et al. (2024), ALMA observations of blow-out region AGN could provide constraints on the ISM-obscuration, and doing so, remove ISM-obscured AGN and refine the *forbidden* region selection. Such a rigorous and systematic multi-wavelength analysis of these AGN will provide valuable knowledge on the physics linking obscuration and accretion across cosmic time.

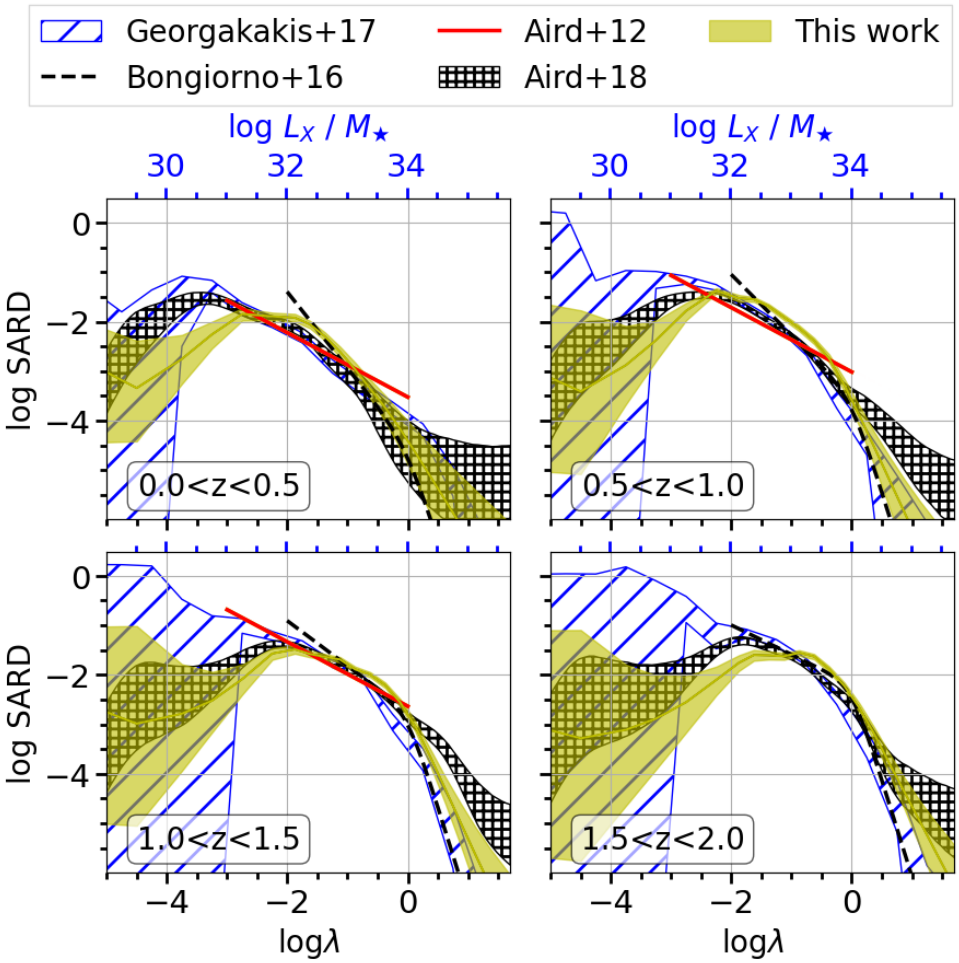

Figure 4.9: The specific accretion rate distribution of CTN AGN ($N_{\rm H} < 10^{24}\,{\rm cm}^{-2}$) compared to previous SARD estimates in the literature. Different panels correspond to different redshift intervals. The *yellow solid lines* represent the median of the SARD posteriors derived in this Chapter, while the *yellow shaded* region marks the extent of the 68% confidence interval around the median. Also overplotted are the results of Aird et al. (2012) (*red solid lines*), Bongiorno et al. (2016) (*black dashed lines*), Georgakakis et al. (2017c) (*blue hatched areas*) and Aird et al. (2018) (*black hatched areas*).

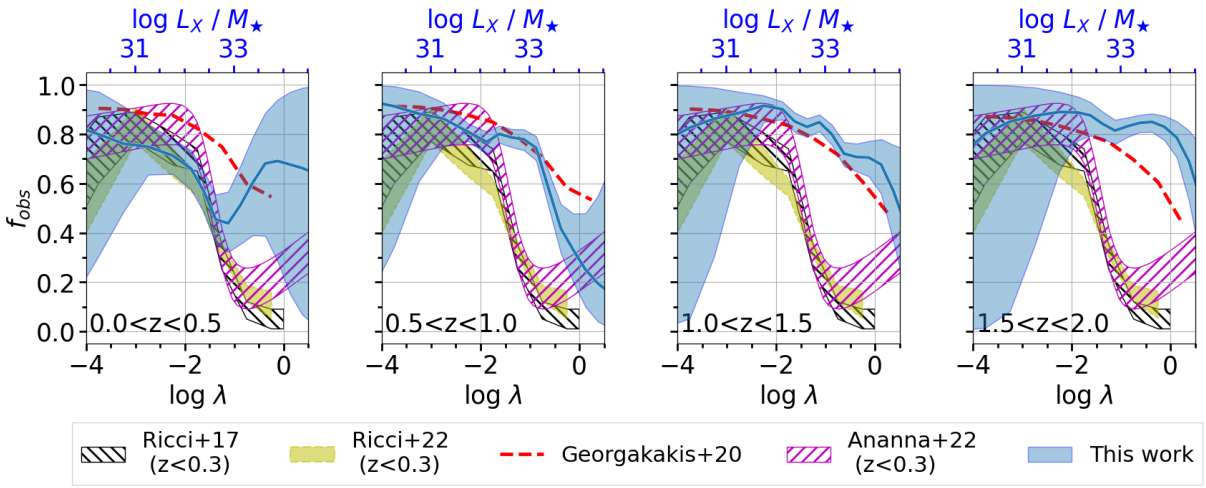

Figure 4.10: The obscured AGN fraction as a function of SAR λ. Each panel corresponds to a different redshift interval. The *blue solid lines* represent the median obscuration fraction, while the *shaded regions* correspond to the 68% confidence interval around the median. The *black-hatched areas* are the results of R17 in the local Universe ($<z>=$ 0.037). The results of R22, based on the BASS DR2 sample, are shown with the *yellow shaded area*. The *purple hatched regions* correspond to the observational constraints of A22b. The *red dashed curves* are the predictions by the forward model with luminosity-dependent obscuration presented in Georgakakis et al. (2020).

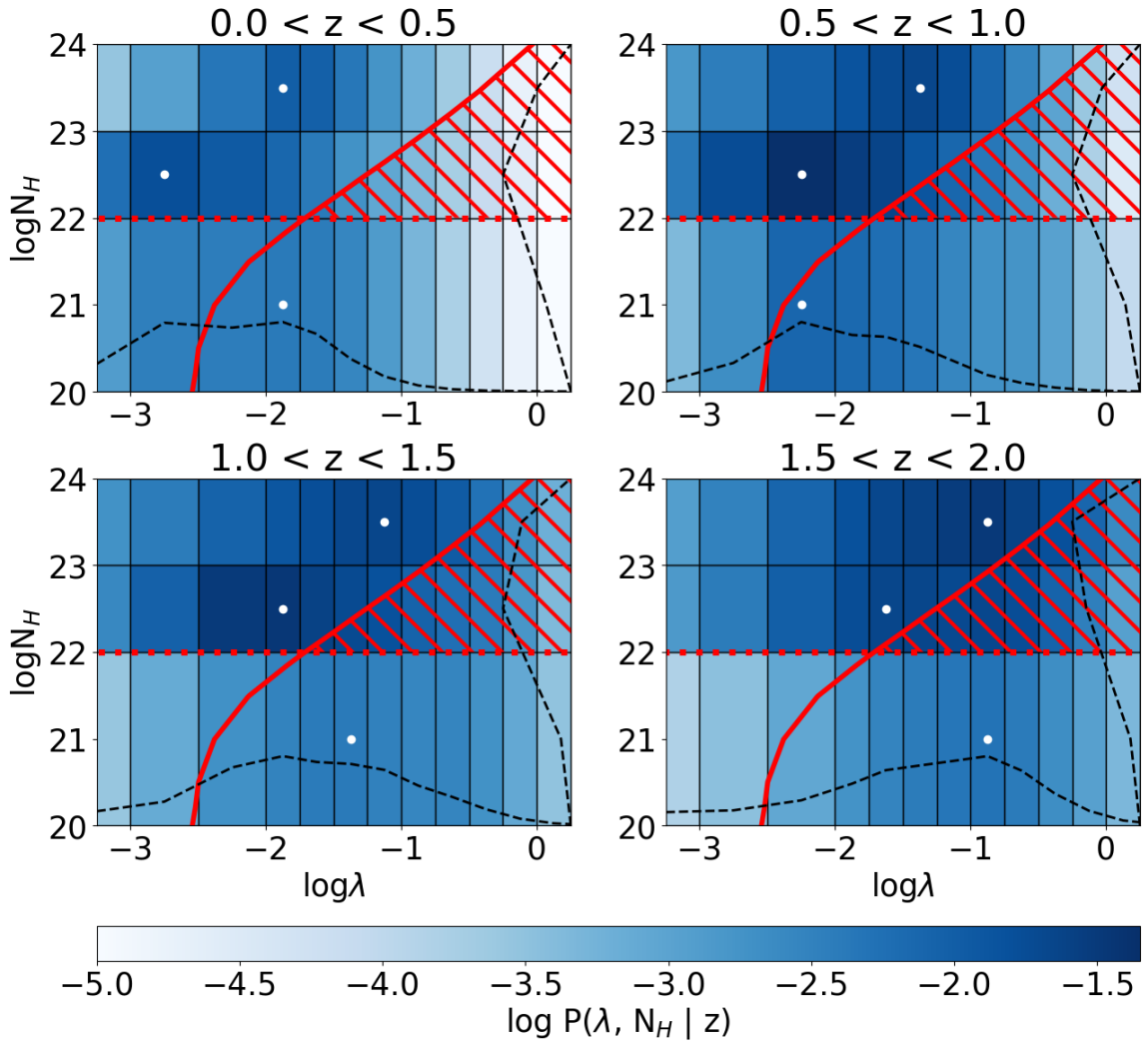

Figure 4.11: Logarithmic probability density $\log P(\lambda, N_{\rm H}|z)$ of a galaxy to host an AGN as a function of SAR ($\log\lambda$) and obscuration ($\log N_{\rm H}$). Each panel represents a different redshift interval from 0 to 2. The *diagonal solid red line* represents the effective Eddington limit as a function of the column density (Fabian et al., 2008) while the *horizontal dashed line* shows the expected contribution of the host galaxy to the obscuration level. The *red-hatched area* in between the two curves is the blowout region, an unstable and short-lived region where the radiation pressure should push away the gas efficiently. The *white dots* indicate, for each redshift and $\log N_{\rm H}$ interval, the λ-bin ($\log\lambda > -3.5$) with the highest probability. At the bottom of each panel, the *horizontal dashed black curve* corresponds to the probability density summed over $\log N_{\rm H}$ as a function of $\log\lambda$. Respectively, the *vertical dashed black curve* is the probability density summed over $\log\lambda$ as a function of $\log N_{\rm H}$.

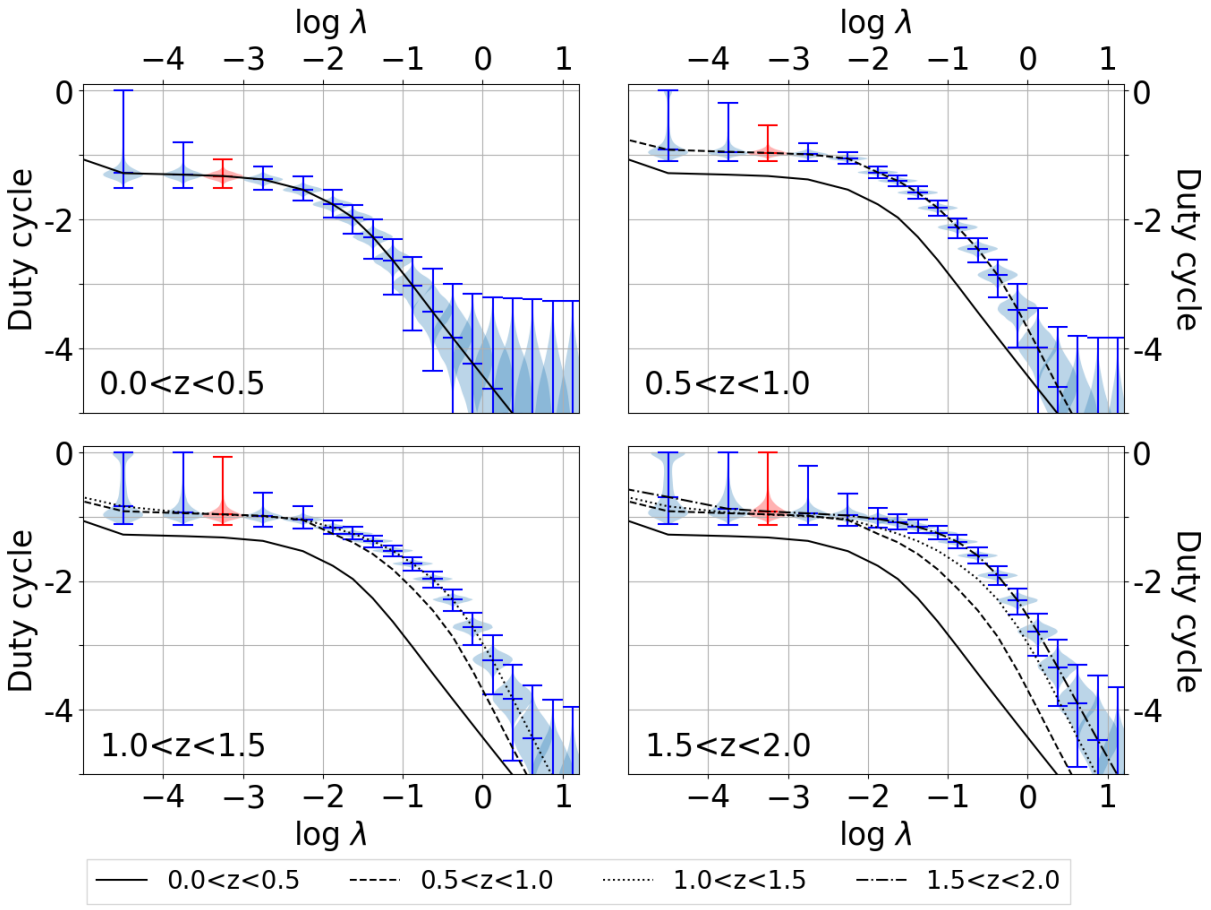

Figure 4.12: Duty cycle for different redshift intervals. It corresponds to the probability that a galaxy hosts an AGN accreting faster than a specific accretion rate. The violin plots represent the duty cycle posterior distribution. The different *black lines* represent the median duty cycle of the corresponding redshift interval. The *red* duty cycle is $P(\log\lambda > -3.5)$ used in Section 4.4.3 to compute $f_{\mathrm{blow-out}}$.

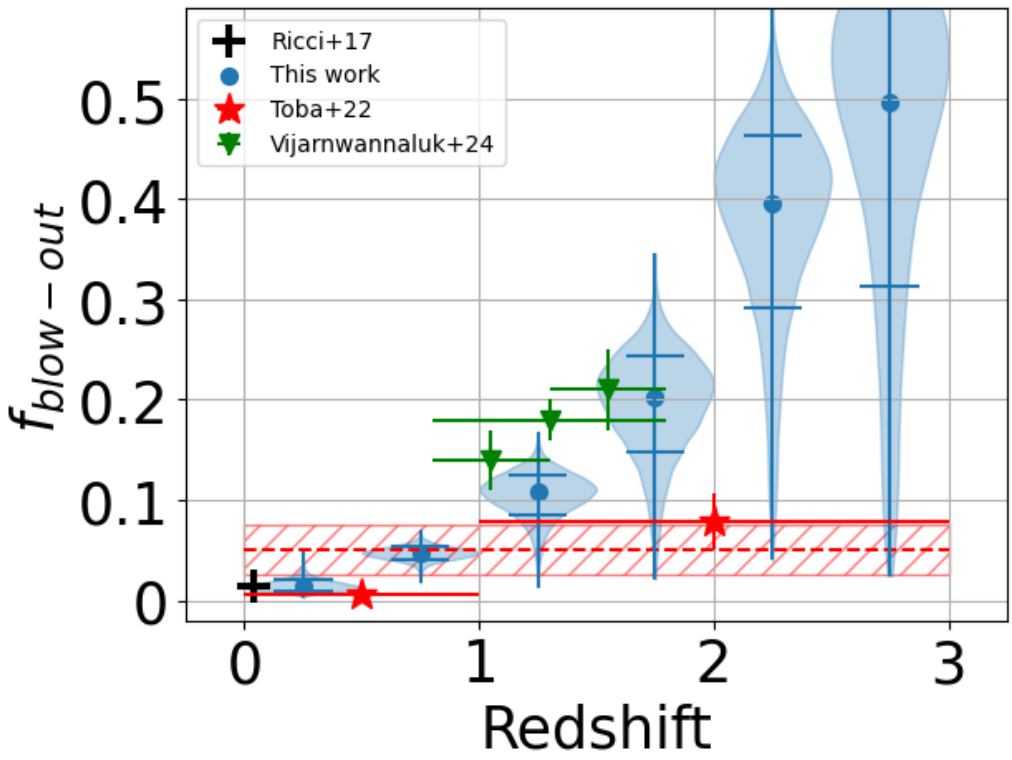

Figure 4.13: Fraction of sources within the *forbidden* region as a function of the redshift. The violin plots represent the posterior distribution of our $f_{\rm blow-out}$ value for each redshift interval, and the blue dots and error bars correspond to the median values and 1σ-uncertainties, respectively. The *black cross* corresponds to the value presented in R17. The *red crosses* are the results of Toba et al. (2022) within the $z = 0 - 1$ and $z = 1 - 3$ redshift intervals, using soft X-ray data from *eROSITA*. Through a Monte Carlo randomization, Toba et al. (2022) find a constant value of $5 \pm 2.5\%$ represented by the *red hatched area*. The green triangles are the $f_{\rm blow-out}$ values from Vijarnwannaluk et al. (2024).

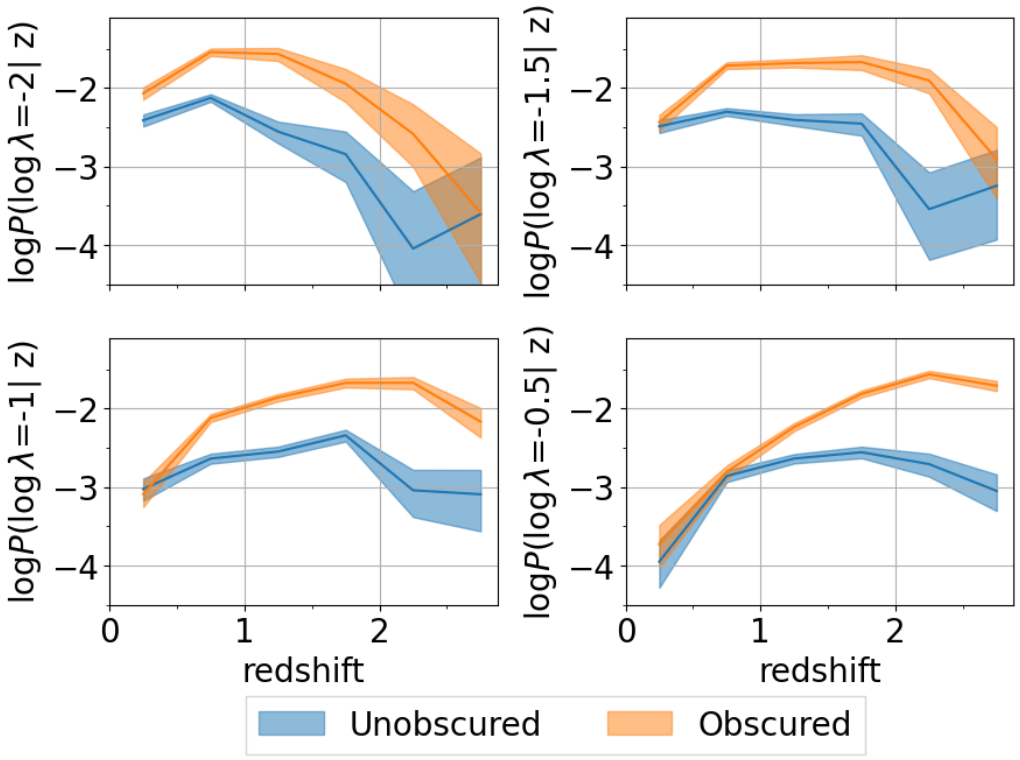

Figure 4.14: Redshift evolution of the probability of an AGN to accrete at a fixed SAR $\log \lambda$ for different λ values. It is a different way to show the redshift evolution of the SARD presented in Figure 4.6. The *blue* and *orange shaded* regions represent the probability when normalised over $N_{\rm H}$ for unobscured ($\log N_{\rm H}/{\rm cm}^{-2} < 22$) and obscured ($22 < \log N_{\rm H}/{\rm cm}^{-2} < 24$) AGN, respectively.

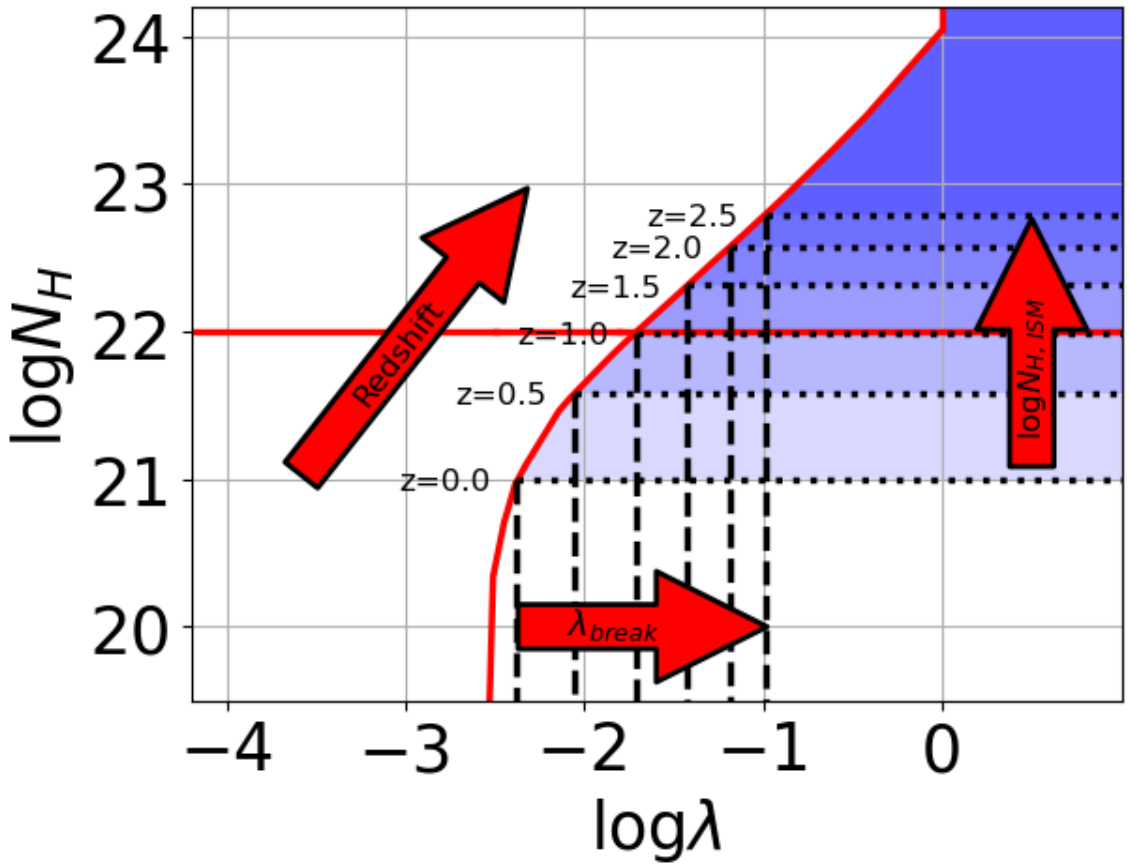

Figure 4.15: Schematic redshift evolution of the impact of the ISM obscuration on the *forbidden* region across the $\lambda - N_{\rm H}$ plane. The diagonal *red solid* line corresponds to the effective Eddington limit (Fabian et al., 2008) while the *horizontal red solid* line corresponds to the $N_{\rm H} = 10^{22}\,{\rm cm}^{-2}$ threshold (Matt, 2000) delimiting the *forbidden* region in this work. With increasing redshift, the median host galaxy ISM obscuration increases following $N_{\rm H,\,ISM} = 10^{21} \times (1+z)^{3.3}\,{\rm cm}^{-2}$ (*horizontal black dotted*, Gilli et al., 2022). As a consequence, $\lambda_{\rm break}$, at which the ISM obscuration and the effective Eddington limit intersect, shifts towards higher SAR (*vertical black dashed* lines). $\lambda_{\rm break}$ corresponds to the SAR at which the obscured AGN fraction drops.

CHAPTER 5

Conclusion & Future Work

In this thesis, I investigated the properties of X-ray AGN with a focus on obscured AGN that are hidden behind clouds of gas and dust. To study these elusive objects (§1.4), I used a multi-wavelength framework exploiting the advantages of the different wavebands. I notably exploited the high-quality data collected by the *Chandra* X-ray space telescope (§2.1) in three deep extragalactic fields: COSMOS-Legacy (§2.2.1), AEGIS-XD (§2.2.2) and CDFS (§2.2.3). In addition to determining the intrinsic X-ray luminosity and line-of-sight hydrogen column density through X-ray spectral analysis (§2.4.2), these X-ray-selected AGN samples provide well-defined selection functions (§2.3.1), allowing the investigation of the intrinsic AGN demographics. Additionally, multi-wavelength SED fitting constrained various physical properties such as the AGN intrinsic accretion luminosity and the stellar mass of the host galaxy (§2.4.3). Throughout this study, I employed a Bayesian framework to account for measurement uncertainties, yielding robust and reliable constraints on AGN demographics.

One of the main results of this AGN demographics study is the increasing obscured AGN fraction with redshift, as illustrated in Figure 5.1. This redshift evolution was previously known (Aird et al., 2010; Buchner et al., 2015; Georgakakis et al., 2015), but the SARD analysis of Chapter 4 provides additional insights into the nature of the obscurer as

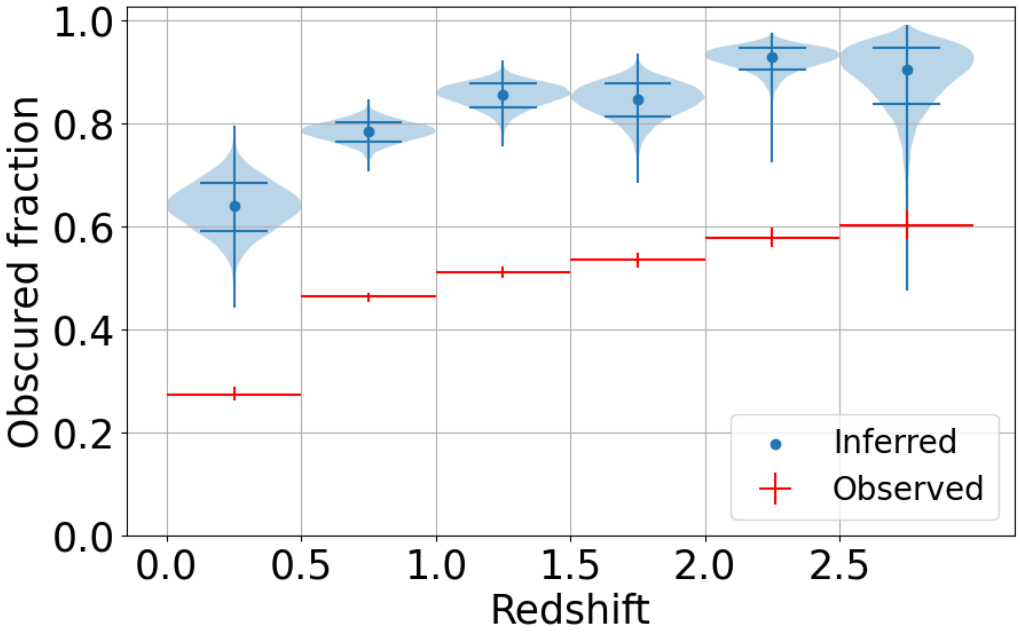

Figure 5.1: Obscured AGN fraction with $\log \lambda >= -3.5$ as a function of the redshift. The *red crosses* indicate the observed obscured AGN fraction with the uncertainties accounted for with a bootstrap approach. The *blue violin plots* represent the posterior distribution of the inferred intrinsic AGN population. The *blue dots* and *horizontal bars* correspond to the median and 1-σ uncertainties of the inferred obscured AGN fraction, respectively.

it the first time the accretion properties of obscured and unobscured AGN are measured and compared up to $z \sim 3$. As discussed in Section 4.5.2, the similar shape of the SARD of obscured and unobscured AGN populations (Figure 4.6) supports the AGN orientation model (§1.2.2) as a first approximation. In detail, a small systematic offset of the unobscured SARD towards higher accretion rates leads to a sharp decrease of the obscured AGN fraction as a function of the SAR (Figure 4.10), supporting the idea of a modified orientation model in which the dusty radiation pressure reduces the torus covering factor (Ricci et al., 2017b; Ananna et al., 2022a). However, the sharp decrease of $f_{\rm obs}$ shifts towards higher accretion rates with increasing redshift, and it is believed to be a consequence of different scales of AGN obscuration, from the nuclear scale (tens of pc) at low redshift to larger scale (hundreds of pc) at higher redshifts.

Nevertheless, the AGN obscuration picture cannot be complete without the investigation of the accretion properties of the CTK AGN population, potentially representing a missing stage in AGN evolutionary models (Hopkins et al., 2008). Our analysis in Chapter 3 Section 3.5.3 finds a CTK fraction of $21.0^{+16.1}_{-9.9}\%$ at $z < 0.5$, and a 3-σ upper limit

$\lesssim 40\%$ at higher redshifts (Figure 3.15). As other works report significantly larger CTK fractions (Ananna et al., 2019; Buchner et al., 2015), the actual demographics of CTK AGN remain largely uncertain. A caveat of our approach is the X-ray-selected sample we used. Indeed, as explained in Section 1.3.4, CTK obscuration absorbs most of the X-ray emission even at high energy ($> 2\,\mathrm{keV}$), leading to a bias against obscured AGN. However, in Chapters 3 and 4, we use the well-defined X-ray selection function, i.e., the survey area sensitive to a given photon count rate, to define the probability of observing an AGN given its physical parameters (see Figure 3.12). Once this A factor is computed in Equation 3.5 and 4.4, the X-ray observational bias due to obscuration is accounted for, revealing the intrinsic population of heavily obscured AGN despite being a minor fraction of the observed total population. It is worth noting that this approach leads to more significant uncertainties in the undersampled population, i.e., the most obscured AGN, and it relies on the accuracy of AGN X-ray spectral modelling, i.e., the expected photon count rates given the physical parameters. Nevertheless, the new multi-wavelength methodology developed in Section 3.4, using the $L_{6\,\mu m}$ luminosity from SED to guide the X-ray spectroscopy, significantly enhances the reliability of the obscuration measurements. Applying this methodology to other X-ray deep fields with sufficient multi-wavelength coverage to robustly estimate $L_{6,\mu m}$, such as CDFS (Luo et al., 2017), AEGIS-XD (Nandra et al., 2015), or Boötes (Masini et al., 2020) observed by *Chandra*, or Stripe-82X (LaMassa et al., 2016), *XMM*-LSS (Chen et al., 2018), or ELAIS-S1 (Ni et al., 2021) observed by *XMM*-Newton, would be crucial for determining for the first time the SARD of the CTK population. As some AGN evolutionary models suggest the heavily obscured and CTK AGN population represents an early stage of their SMBH growth (Kocevski et al., 2015), one may observe differences between the SARD of CTK AGN compared to the SARD of less obscured systems presented in this work (§4.4). Conversely, the orientation unification model does not predict any difference between the SARDs.

However, this new multi-wavelength approach to disentangle the $L_{\mathrm{X}}-N_{\mathrm{H}}$ degeneracy depends on the reliability of the $L_{\mathrm{IR}}-L_{\mathrm{X}}$ relationship used. In this work, I adopted the relation defined by Stern (2015) (§3.4.2). While this relation agrees with other relationships in the literature for moderate luminosity (Asmus et al., 2015; Mateos et al., 2015; Chen et al., 2017, Figure 3.7), it differs at the high-luminosity end, which is crucial for

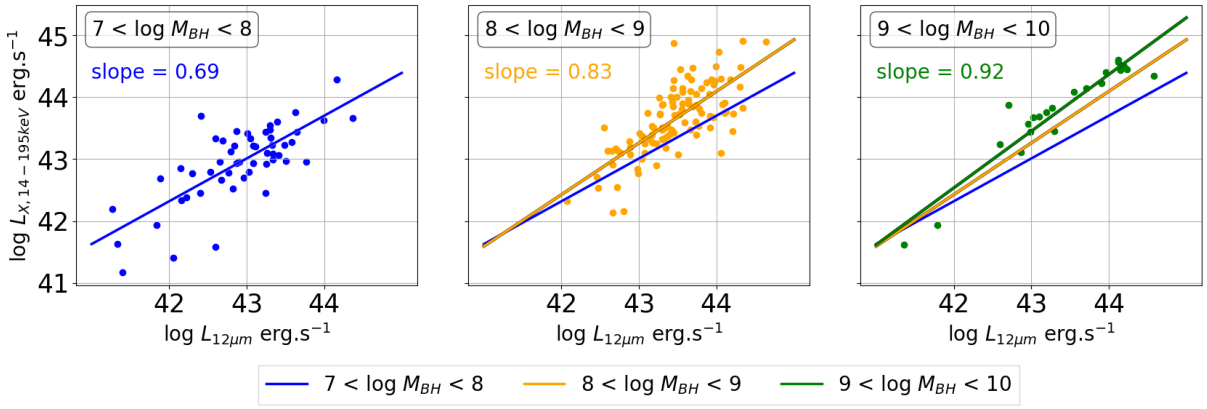

Figure 5.2: X-ray and mid-IR luminosities distribution of the BASS DR1 sample (Koss et al., 2017) for different $M_{\rm BH}$ bins. The *solid lines* indicate the best linear fit for different $M_{\rm BH}$ intervals: $7 < \log\ M_{\rm BH} < 8$ (*blue*), $8 < \log\ M_{\rm BH} < 9$ (*orange*) and $9 < \log\ M_{\rm BH} < 10$ (*green*). The slope of each line is indicated in each panel, showing an increase with $M_{\rm BH}$.

characterising CTK AGN. Furthermore, these relationships were mainly derived from unobscured sources, potentially overlooking any dependence on obscuration. Therefore, a new empirical $L_{\rm IR}-L_{\rm X}$ relationship could be established, notably using the BAT AGN Spectroscopic Survey (BASS) DR2 (Koss et al., 2022a) in the local Universe. This new relationship could also explore dependencies on other physical parameters such as SMBH mass or Eddington rate. Indeed, as shown in Figure 5.2, my preliminary work using the BASS DR1 sample (Koss et al., 2017) shows a slope increase of the $L_{\rm X,\,14-195\,keV}-L_{12\,\mu\rm m}$ relationship with increasing $M_{\rm BH}$. These results could be contextualised with the efficiency and the structure of the AGN accretion disc (Mitchell et al., 2023).

Additionally, this multi-wavelength methodology could be applied to select heavily obscured AGN undetected by *eROSITA* (Merloni et al., 2024). By using mid-IR colour criteria (§1.4.1) in the WISE all-sky survey, a large number of AGN can be selected with relatively high reliability. Therefore, by estimating the AGN $L_{6\,\mu m}$ luminosity, it is possible to constrain the intrinsic $L_{\rm X}$ and the expected X-ray flux to compare with *eROSITA* flux limit, setting lower limits on the AGN column density $N_{\rm H}$. This approach could be an efficient tool for selecting interesting targets, potentially the local Universe counterparts of the *little red dots* (LRDs) observed at high redshift by *JWST*. The presence of broad Hα lines indicates the AGN nature of these LRDs, but as they are mostly undetected in the X-ray, they are believed to be either heavily obscured (Kocevski et al., 2024), intrinsically

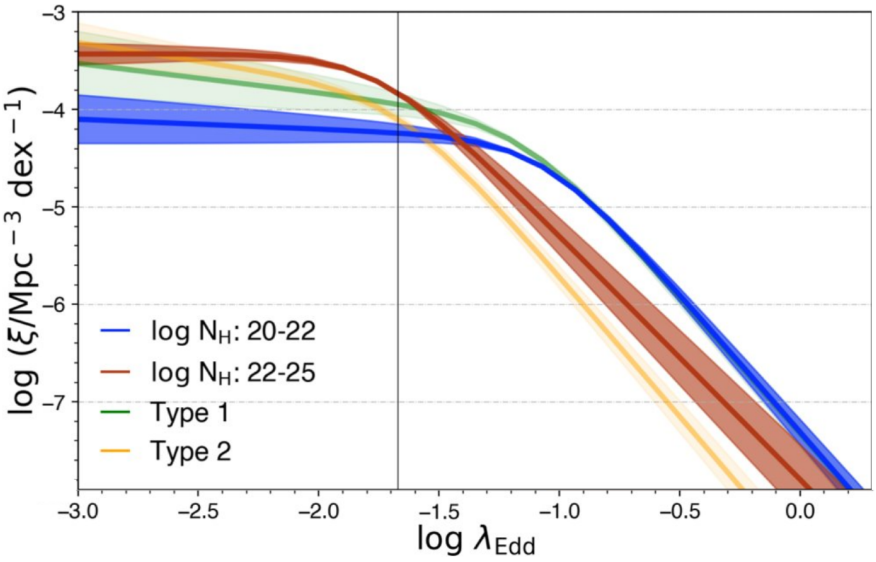

Figure 5.3: Eddington ratio distribution function for X-ray unobscured ($N_{\rm H} < 10^{22}\,{\rm cm}^{-2}$, *blue solid line*) and obscured ($N_{\rm H} > 10^{22}\,{\rm cm}^{-2}$, *red solid line*) AGN and for type I (*green solid line*) and type 2 (*yellow solid line*) AGN. The shaded regions represent the 1-σ uncertainties. Figure adapted from Ananna et al. (2022b).

weak in the X-ray regime (Yue et al., 2024), or host relatively low-mass SMBHs (Ananna et al., 2024). Follow-up surveys of the *eROSITA* missed sources with optical and hard X-ray spectroscopy with, for example, 4MOST (Merloni et al., 2019) and *NuSTAR* (Harrison et al., 2013), respectively, could provide valuable insights into the nature of these weak X-ray AGN.

Furthermore, the AGN demographic study presented in this thesis investigates the AGN feedback mechanisms clearing out the obscuring material. For instance, as discussed in Section 4.4.3, I found that the fraction of AGN within the *forbidden* region increases with redshift (Figure 4.13). In this region of the $\lambda - N_{\rm H}$ plane, the dusty radiation pressure is sufficient to rapidly expel the nuclear scale obscurer, causing the AGN to transition from obscured to unobscured. This increasing density in the *forbidden* region, as schematically illustrated in Figure 4.15, could be a consequence of the increasing ISM obscuration with redshift (Buchner & Bauer, 2017; Gilli et al., 2022). Further multi-wavelength analyses of these sources could be valuable in understanding their physics, for instance, by examining their radio-detection fraction or the presence of outflow signatures in their optical spectra. Moreover, ALMA observations can be used to estimate the ISM obscuration (Andonie et al., 2024) and separate ISM-obscured AGN from nuclear-scale-

obscured AGN in the dusty radiative feedback mode. Studying a sample of broad-line AGN obscured in the X-ray regime could be insightful into the impact of this feedback on the torus obscuration. Indeed, this discrepancy between X-ray and optical obscuration could suggest inhomogeneous obscuration, potentially caused by the AGN feedback. In Figure 5.3 adapted from Ananna et al. (2022b), the difference between the Eddington ratio distribution functions of type I/II and X-ray obscured/unobscured sources suggests that these AGN are located within $-2 < \log \lambda < -1$, close to the effective Eddington limit bordering the *forbidden* region. Additionally, as these sources have broad lines, their black hole masses can be measured to probe the $M_{\rm BH}-M^*$ in the obscured regime and quantify the bias of using the SAR $\frac{L_{\rm X}}{M^*}$ as a proxy of the Eddington ratio. Conversely, the AGN feedback can also have an impact on larger scales, triggering or quenching the star formation in the host galaxy. This motivates a study to measure and compare the SFR inside and outside the *forbidden* region. Fields covered by *Herschel* and compiled in the Herschel Extragalactic Legacy Project (HELP, Shirley et al., 2021) would be ideal for this study, as they provide the necessary far-IR photometry. However, estimating the SFR of galaxies hosting AGN via SED fitting is challenging since luminous AGN can bias the measurements. Fully Bayesian SED fitting algorithms, such as FortesFit or GRAHSP (Genuine Retrieval of the AGN Host Stellar Population, Buchner et al., 2024), offer more flexibility in separating the contributions of the host galaxy and AGN, resulting in less biased results. Additionally, these algorithms can test their accuracy using the new Chimera benchmark (Buchner et al., 2024), a photometric dataset that combines pure AGN SEDs with non-AGN pure galaxies SEDs. As the properties of the pure galaxies are reliably estimated, this benchmark provides hybrid SEDs of AGN-hosting galaxies with known fiducial parameters to assess the performance of SED fitting algorithms. In parallel, as CTK AGN are more often hosted in merging galaxies (Kocevski et al., 2015), a similar morphology analysis could be conducted on AGN in the *forbidden* region using *HST* or *JWST* images. The combination of the results of these different analyses could potentially fit into a refined AGN and host galaxy evolutionary model.

Bibliography

Abbott R., et al., 2023, Physical Review X, 13, 041039 1.3.1

Aihara H., et al., 2019, PASJ, 71, 114 2.2.1

Aird J., et al., 2010, MNRAS, 401, 2531 1.4.2, 4.3.3, 5

Aird J., et al., 2012, ApJ, 746, 90 4.1, 4.4.1, 4.9

Aird J., Coil A. L., Georgakakis A., Nandra K., Barro G., Pérez-González P. G., 2015, MNRAS, 451, 1892 1.18, 1.4.2, 1.20, 1.21, 1.4.3, 2.5, 2.3.3, 3.1, 3.5.1, 3.11, 3.13, 3.5.1, 3.14, 3.5.2, 3.5.3, 3.15, 3.6.1, 4.1, 4.3.3, 4.3.3, 4.3.3, 4.4.2

Aird J., Coil A. L., Georgakakis A., 2017, MNRAS, 465, 3390 1.4.1, 2.3.1, 2.3.2

Aird J., Coil A. L., Georgakakis A., 2018, MNRAS, 474, 1225 1.22, 1.4.3, 4.1, 4.3.3, 4.4.1, 4.9

Ajello M., et al., 2008, ApJ, 673, 96 1.4.2

Akaike H., 1974, IEEE Transactions on Automatic Control, 19, 716 2.4.2

Akylas A., Georgantopoulos I., Georgakakis A., Kitsionas S., Hatziminaoglou E., 2006, A&A, 459, 693 1.3.4

Akylas A., Georgakakis A., Georgantopoulos I., Brightman M., Nandra K., 2012, A&A, 546, A98 1.4.2, 3.1, 3.6.1

Akylas A., Georgantopoulos I., Ranalli P., Gkiokas E., Corral A., Lanzuisi G., 2016, A&A, 594, A73 3.14, 3.6.1

Alam S., et al., 2015, ApJS, 219, 12 2.2.2, 2.3, 2.3.3, 2.4

Alatalo K., et al., 2015, ApJ, 798, 31 1.4.3

Alexander D. M., Hickox R. C., 2012, New A Rev., 56, 93 1.3.1, 1.3.4, 1.3.4, 4.1, 4.5.3

Alexander D. M., Bauer F. E., Chapman S. C., Smail I., Blain A. W., Brandt W. N., Ivison R. J., 2005, ApJ, 632, 736 1.4.1

Alexander D. M., et al., 2008, ApJ, 687, 835 3.4

Alexander D. M., et al., 2013, ApJ, 773, 125 3.1

Allamandola L. J., Tielens A. G. G. M., Barker J. R., 1989, ApJS, 71, 733 1.4.1

Alonso-Herrero A., Quillen A. C., Rieke G. H., Ivanov V. D., Efstathiou A., 2003, AJ, 126, 81 1.3.4

Alonso-Herrero A., et al., 2016, MNRAS, 455, 563 1.3.4

Alonso-Herrero A., et al., 2021, A&A, 652, A99 4.4.2

Alonso-Tetilla A. V., et al., 2023, MNRAS, 4.5.3

Ananna T. T., et al., 2019, ApJ, 871, 240 1.4.2, 1.18, 1.4.2, 3.1, 3.15, 3.6.1, 4.3.3, 5

Ananna T. T., et al., 2022a, ApJS, 261, 9 1.3.4, 1.4.3, 4.4.1, 5

Ananna T. T., et al., 2022b, ApJ, 939, L13 1.4.3, 4.7, 4.4.1, 4.4.2, 4.5.2, 4.6, 4.10, 5.3, 5

Ananna T. T., Bogdán Á., Kovács O. E., Natarajan P., Hickox R. C., 2024, arXiv e-prints, p. arXiv:2404.19010 5

Andika I., 2016, PhD thesis, doi:10.13140/RG.2.2.23303.80809 1.4

Andonie C., et al., 2022a, MNRAS, 517, 2577 1.2.2, 4.1, 4.5.2, 4.5.3

Andonie C., et al., 2022b, A&A, 664, A46 1.3.3, 2.4.3

Andonie C., et al., 2024, MNRAS, 527, L144 4.5.3, 4.6, 5

Annuar A., et al., 2017, ApJ, 836, 165 3.6.1

Antoniadis J., et al., 2023, arXiv e-prints, p. arXiv:2306.16214 1.3.1

Antonucci R. R. J., 1984, ApJ, 278, 499 1.2.2

Antonucci R., 1993, ARA&A, 31, 473 1.2.2, 1.3.4, 3.1, 4.5.2

Antonucci R. R. J., Miller J. S., 1985, ApJ, 297, 621 1.2.2

Appleton P. N., et al., 2004, ApJS, 154, 147 1.4.1

Arakawa N., Fabian A. C., Ferland G. J., Ishibashi W., 2022, MNRAS, 517, 5069 4.5.2

Aretxaga I., et al., 2011, MNRAS, 415, 3831 2.2.1

Arnaud K. A., et al., 1985, MNRAS, 217, 105 1.3.3

Arnouts S., Cristiani S., Moscardini L., Matarrese S., Lucchin F., Fontana A., Giallongo E., 1999, MNRAS, 310, 540 2.3.3

Arnouts S., et al., 2001, A&A, 379, 740 2.2.3

Arun K. G., et al., 2022, Living Reviews in Relativity, 25, 4 1.3.1

Ashby M. L. N., et al., 2013, ApJ, 769, 80 2.2.1, 2.2.2, 2.2.3

Asmus D., Gandhi P., Hönig S. F., Smette A., Duschl W. J., 2015, MNRAS, 454, 766 1.3.4, 3.6.1, 5

Asmus D., Hönig S. F., Gandhi P., 2016, ApJ, 822, 109 1.3.4

Assef R. J., et al., 2013, ApJ, 772, 26 1.4.1, 1.17

Assef R. J., et al., 2015, ApJ, 804, 27 3.1

Aversa R., Lapi A., de Zotti G., Shankar F., Danese L., 2015, ApJ, 810, 74 4.4.2

Avni Y., Bahcall J. N., 1980, ApJ, 235, 694 1.4.2

Awaki H., Koyama K., Inoue H., Halpern J. P., 1991, PASJ, 43, 195 1.4.2

Bañados E., et al., 2016, ApJS, 227, 11 1.3.1

Baade W., Minkowski R., 1954, ApJ, 119, 206 1.1.3, 1.4.1

Balbus S. A., Hawley J. F., 1991, ApJ, 376, 214 1.3.2

Balbus S. A., Hawley J. F., 1998, Reviews of Modern Physics, 70, 1 1.3.2

Baldwin J. A., Phillips M. M., Terlevich R., 1981, PASP, 93, 5 1.4.1, 9

Balestra I., et al., 2010, A&A, 512, A12 2.2.3, 2.3.3

Baloković M., et al., 2018, ApJ, 854, 42 1.3.4

Barger A. J., et al., 2003, AJ, 126, 632 3.1

Barger A. J., Cowie L. L., Mushotzky R. F., Yang Y., Wang W. H., Steffen A. T., Capak P., 2005, AJ, 129, 578 4.5.1

Barmby P., Huang J. S., Ashby M. L. N., Eisenhardt P. R. M., Fazio G. G., Willner S. P., Wright E. L., 2008, ApJS, 177, 431 2.6, 2.2.2

Barro G., et al., 2011, ApJS, 193, 13 2.2.2, 2.3.2

Barthelmy S. D., et al., 2005, Space Sci. Rev., 120, 143 1.4.1, 3.6.1, 4.4.1

Barvainis R., 1987, ApJ, 320, 537 1.3.4

Bautz M. W., et al., 1998, in Hoover R. B., Walker A. B., eds, Society of Photo-Optical Instrumentation Engineers (SPIE) Conference Series Vol. 3444, X-Ray Optics, Instruments, and Missions. pp 210–224, doi:10.1117/12.331238 2.1

Beckmann V., Shrader C. R., 2012, Active Galactic Nuclei 1.5, 1.3.5

Beckwith S. V. W., et al., 2006, AJ, 132, 1729 2.7, 2.2.3

Begelman M. C., Blandford R. D., Rees M. J., 1984, Reviews of Modern Physics, 56, 255 1.2.2

Behar E., Vogel S., Baldi R. D., Smith K. L., Mushotzky R. F., 2018, MNRAS, 478, 399 1.3.6

Behroozi P. S., Wechsler R. H., Conroy C., 2013, ApJ, 770, 57 1.4.3

Bennert N., Falcke H., Schulz H., Wilson A. S., Wills B. J., 2002, ApJ, 574, L105 1.3.5

Bentz M. C., Peterson B. M., Netzer H., Pogge R. W., Vestergaard M., 2009, ApJ, 697, 160 1.3.5

Bentz M. C., et al., 2013, ApJ, 767, 149 1.3.1

Bertoldi F., et al., 2007, ApJS, 172, 132 2.2.1

Bessiere P. S., Ramos Almeida C., 2022, MNRAS, 512, L54 1.4.3

Bianchi S., Guainazzi M., Chiaberge M., 2006, A&A, 448, 499 1.3.3, 2.4.2

Birchall K. L., Watson M. G., Aird J., Starling R. L. C., 2023, Monthly Notices of the Royal Astronomical Society, 523, 4756 4.1

Blandford R. D., 1976, MNRAS, 176, 465 1.3.6

Blandford R. D., McKee C. F., 1982, ApJ, 255, 419 1.3.1, 1.3.2

Blandford R. D., Znajek R. L., 1977, MNRAS, 179, 433 1.3.6

Blandford R., Meier D., Readhead A., 2019, ARA&A, 57, 467 1.2.2, 1.3.6, 1.4.1

Boissay R., Ricci C., Paltani S., 2016, A&A, 588, A70 1.3.3

Boldt E., 1987, Phys. Rep., 146, 215 1.4.2

Boldt E., Leiter D., 1987, ApJ, 322, L1 1.4.2

Boller T., Brandt W. N., Fink H., 1996, A&A, 305, 53 1.3.3

Bolton C. T., 1972, Nature, 235, 271 1.1.1

Bondi H., 1952, MNRAS, 112, 195 1.3.2

Bongiorno A., et al., 2012, MNRAS, 427, 3103 1.4.3, 4.1

Bongiorno A., et al., 2016, A&A, 588, A78 1.4.3, 4.1, 4.3.3, 4.4.1, 4.5.1, 4.9

Boquien M., Burgarella D., Roehlly Y., Buat V., Ciesla L., Corre D., Inoue A. K., Salas H., 2019, A&A, 622, A103 2.4.3, 2.4.3, 4.3.2

Bowyer S., Byram E. T., Chubb T. A., Friedman H., 1965, Science, 147, 394 1.1.1

Bowyer C. S., Lampton M., Mack J., de Mendonca F., 1970, ApJ, 161, L1 1.1.3

Brammer G. B., van Dokkum P. G., Coppi P., 2008, ApJ, 686, 1503 2.3.3

Brandt W. N., Alexander D. M., 2015, A&A Rev., 23, 1 1.3.3, 1.4.1, 4.1

Brandt W. N., Hasinger G., 2005, ARA&A, 43, 827 1.4.2

Brenneman L. W., Reynolds C. S., 2006, ApJ, 652, 1028 1.3.1

Brightman M., Nandra K., 2011, MNRAS, 413, 1206 1.3.4, 2.4.2

Brightman M., Ueda Y., 2012, MNRAS, 423, 702 1.20, 3.15, 3.6.1

Brinkman A. C., et al., 2000, ApJ, 530, L111 2.1

Brocklehurst M., 1971, MNRAS, 153, 471 1.4.1

Brunner H., et al., 2022, A&A, 661, A1 4.4.3, 4.5.2

Brusa M., et al., 2005, A&A, 432, 69 2.3.2

Brusa M., et al., 2007, ApJS, 172, 353 2.3.2, 2.3, 4.2

Brusa M., et al., 2015, MNRAS, 446, 2394 4.5.2

Bruzual G., Charlot S., 2003, MNRAS, 344, 1000 2.4.3, 2.7, 2.4.3, 2.8, 3.4.1

Bruzual A. G., 1983, ApJ, 273, 105 1.4.1

Buchner J., 2014, arXiv e-prints, p. arXiv:1407.5459 2.4.2

Buchner J., 2019, PASP, 131, 108005 2.4.2

Buchner J., 2021, The Journal of Open Source Software, 6, 3001 2.4.2

Buchner J., Bauer F. E., 2017, MNRAS, 465, 4348 1.4.1, 4.5.3, 5

Buchner J., et al., 2014, A&A, 564, A125 2.4.2, 3.3.2, 3.3.3, 4.3.1

Buchner J., et al., 2015, ApJ, 802, 89 1.3.4, 1.3.4, 1.4.1, 1.18, 1.4.2, 1.20, 3.1, 3.5.1, 3.11, 3.13, 3.5.1, 3.5.2, 3.14, 3.15, 3.6.1, 4.3.3, 4.4.1, 4.4.2, 5

Buchner J., Schulze S., Bauer F. E., 2017, MNRAS, 464, 4545 4.5.3

Buchner J., Brightman M., Nandra K., Nikutta R., Bauer F. E., 2019, A&A, 629, A16 1.11, 1.3.4, 2.4.2, 2.4.2, 2.4.2, 3.3.2, 4.3.1

Buchner J., et al., 2024, arXiv e-prints, p. arXiv:2405.19297 5

Bundy K., et al., 2006, ApJ, 651, 120 2.2.2

Burlon D., Ajello M., Greiner J., Comastri A., Merloni A., Gehrels N., 2011, ApJ, 728, 58 1.3.4, 1.4.2, 1.20, 3.1, 3.15, 3.6.1

Burtscher L., et al., 2013, A&A, 558, A149 1.3.4

Caldwell J. A. R., et al., 2008, ApJS, 174, 136 1, 2.10

Calzetti D., Kinney A. L., Storchi-Bergmann T., 1994, ApJ, 429, 582 1.4.1

Calzetti D., Armus L., Bohlin R. C., Kinney A. L., Koornneef J., Storchi-Bergmann T., 2000, ApJ, 533, 682 2.4.3, 2.8

Campbell W. W., Moore J. H., 1916, Lick Observatory Bulletin, 278, 1 1.1.2

Canizares C. R., et al., 2005, PASP, 117, 1144 2.1

Cano-Díaz M., Maiolino R., Marconi A., Netzer H., Shemmer O., Cresci G., 2012, A&A, 537, L8 1.4.3

Capak P., et al., 2007, ApJS, 172, 99 2.3.2

Capellupo D. M., Netzer H., Lira P., Trakhtenbrot B., Mejía-Restrepo J., 2016, MNRAS, 460, 212 1.3.1

Capetti A., Axon D. J., Macchetto F., Sparks W. B., Boksenberg A., 1996, ApJ, 469, 554 1.3.5

Cappelluti N., et al., 2009, A&A, 497, 635 2.2.1

Carpenter B., et al., 2017, Journal of Statistical Software, 76, 1–32 3.5.2, 4.3.3

Casey C. M., Chapman S. C., Smail I., Alaghband-Zadeh S., Bothwell M. S., Swinbank A. M., 2011, MNRAS, 411, 2739 2.2.3

Casey C. M., et al., 2023, ApJ, 954, 31 2.2.1

Cash W., 1979, ApJ, 228, 939 2.4.2

Chabrier G., 2003, PASP, 115, 763 2.4.3, 2.7, 2.4.3, 2.8

Chandrasekhar S., 1931, ApJ, 74, 81 1.1.1

Chen C.-T. J., et al., 2017, ApJ, 837, 145 (document), 3.4, 3.6, 3.4.2, 3.7, 3.4.2, 5

Chen C. T. J., et al., 2018, MNRAS, 478, 2132 5

Chiu H.-Y., 1964, Physics Today, 17, 21 1.1.3

Ciliegi P., Zamorani G., Hasinger G., Lehmann I., Szokoly G., Wilson G., 2003, A&A, 398, 901 2.3.2, 2.3.2

Circosta C., et al., 2019, A&A, 623, A172 4.5.3, 4.6

Civano F., et al., 2012, ApJS, 201, 30 2.3

Civano F., et al., 2015, ApJ, 808, 185 2.2.1

Civano F., et al., 2016, ApJ, 819, 62 2.2.1, 2.3, 2.3.1, 3.2, 4.2

Coatman L., Hewett P. C., Banerji M., Richards G. T., Hennawi J. F., Prochaska J. X., 2019, MNRAS, 486, 5335 4.5.2

Coil A. L., et al., 2004, ApJ, 609, 525 2.2.2

Coil A. L., et al., 2009, ApJ, 701, 1484 2.2.2, 2.3.3, 2.4

Coil A. L., et al., 2011, ApJ, 741, 8 2.3

Comastri A., Setti G., Zamorani G., Hasinger G., 1995, A&A, 296, 1 1.1.3, 1.4.2

Combes F., et al., 2019, A&A, 623, A79 1.3.4, 4.5.2

Condon J. J., Kellermann K. I., Kimball A. E., Ivezić Ž., Perley R. A., 2013, ApJ, 768, 37 1.3.6, 1.4.1

Conroy C., 2013, ARA&A, 51, 393 2.4.3

Cooper M. C., et al., 2011, ApJS, 193, 14 2.2.2, 2.3.3, 2.4

Cooper M. C., et al., 2012, MNRAS, 425, 2116 2.2.3, 2.3.3

Cresci G., et al., 2015, A&A, 582, A63 1.4.3

Crummy J., Fabian A. C., Gallo L., Ross R. R., 2006, MNRAS, 365, 1067 1.3.3

Czerny B., et al., 2015, Advances in Space Research, 55, 1806 1.3.5

Dale D. A., Helou G., Magdis G. E., Armus L., Díaz-Santos T., Shi Y., 2014, ApJ, 784, 83 2.4.3, 2.7, 2.4.3, 2.8, 3.4.1

Davidson K., Netzer H., 1979, Reviews of Modern Physics, 51, 715 1.3.5

Davis S. W., Laor A., 2011, ApJ, 728, 98 1.3.2

Davis S. W., Tchekhovskoy A., 2020, ARA&A, 58, 407 1.3.2

Davis M., et al., 2003, in Guhathakurta P., ed., Society of Photo-Optical Instrumentation Engineers (SPIE) Conference Series Vol. 4834, Discoveries and Research Prospects from 6- to 10-Meter-Class Telescopes II. pp 161–172 (arXiv:astro-ph/0209419), doi:10.1117/12.457897 2.3.3

Davis M., et al., 2007, ApJ, 660, L1 2.2.2

Davis J. E., et al., 2012, in Takahashi T., Murray S. S., den Herder J.-W. A., eds, Society of Photo-Optical Instrumentation Engineers (SPIE) Conference Series Vol. 8443, Space Telescopes and Instrumentation 2012: Ultraviolet to Gamma Ray. p. 84431A, doi:10.1117/12.926937 2.3.1

Del Moro A., et al., 2016, MNRAS, 456, 2105 1.4.2

Delhaize J., et al., 2017, A&A, 602, A4 1.4.1

Della Ceca R., et al., 2008, A&A, 487, 119 3.1

Delvecchio I., et al., 2014, MNRAS, 439, 2736 3.1

Di Matteo T., Springel V., Hernquist L., 2005, Nature, 433, 604 1.2.2, 1.4.3, 4.1, 4.5.3

Dickinson M., FIDEL Team 2007, in American Astronomical Society Meeting Abstracts. p. 52.16 2.2.2

Dietrich M., Mathur S., Grupe D., Komossa S., 2009, ApJ, 696, 1998 1.3.1

Do T., et al., 2019, Science, 365, 664 1.3.1

Doherty M., Bunker A. J., Ellis R. S., McCarthy P. J., 2005, MNRAS, 361, 525 2.2.3

Done C., Davis S. W., Jin C., Blaes O., Ward M., 2012, MNRAS, 420, 1848 1.3.3

Done C., Jin C., Middleton M., Ward M., 2013, MNRAS, 434, 1955 1.3.1

Donley J. L., Rieke G. H., Rigby J. R., Pérez-González P. G., 2005, ApJ, 634, 169 1.4.1

Donley J. L., et al., 2012, ApJ, 748, 142 1.4.1

Draine B. T., 2003, ARA&A, 41, 241 1.4.1

Draine B. T., Lee H. M., 1984, ApJ, 285, 89 1.4.1

Du P., Wang J.-M., 2019, ApJ, 886, 42 1.3.1

Duras F., et al., 2020, A&A, 636, A73 1.4.3, 4.4.2

Dwelly T., Page M. J., 2006, MNRAS, 372, 1755 1.3.4

Dyson F. W., Eddington A. S., Davidson C., 1920, Philosophical Transactions of the Royal Society of London Series A, 220, 291 1.1.1

Eckart A., Genzel R., 1997, MNRAS, 284, 576 1.3.1

Edge D. O., Shakeshaft J. R., McAdam W. B., Baldwin J. E., Archer S., 1959, MmRAS, 68, 37 1.1.3

Ehman J. R., Dixon R. S., Kraus J. D., 1970, AJ, 75, 351 1.1.3

Einstein A., 1915, Sitzungsberichte der Königlich Preussischen Akademie der Wissenschaften, pp 844–847 1.1.1, 1.3.1

Ekers J. A., 1969, Australian Journal of Physics Astrophysical Supplement, 7, 3 1.1.3

Elbaz D., et al., 2011, A&A, 533, A119 2.2.3

Elvis M., Maccacaro T., Wilson A. S., Ward M. J., Penston M. V., Fosbury R. A. E., Perola G. C., 1978, MNRAS, 183, 129 1.1.3, 1.3.3

Elvis M., et al., 1994, ApJS, 95, 1 1.3.4, 4.3.3

Elvis M., Risaliti G., Zamorani G., 2002, ApJ, 565, L75 1.3.2, 1.3.6

Elvis M., et al., 2009, ApJS, 184, 158 2.2.1

Esparza-Arredondo D., Gonzalez-Martín O., Dultzin D., Masegosa J., Ramos-Almeida C., García-Bernete I., Fritz J., Osorio-Clavijo N., 2021, A&A, 651, A91 2.4.2

Euclid Collaboration et al., 2022a, A&A, 658, A126 2.2.1

Euclid Collaboration et al., 2022b, A&A, 662, A112 2.2.1

Event Horizon Telescope Collaboration et al., 2019a, ApJ, 875, L1 1.1.3

Event Horizon Telescope Collaboration et al., 2019b, ApJ, 875, L6 1.1.3

Event Horizon Telescope Collaboration et al., 2022, ApJ, 930, L15 1.1.3, 1.3.1

Ewing A., 1964, Science News Letter, 85, 39 1.1.1

Faber S. M., et al., 2003, in Iye M., Moorwood A. F. M., eds, Society of Photo-Optical Instrumentation Engineers (SPIE) Conference Series Vol. 4841, Instrument Design and Performance for Optical/Infrared Ground-based Telescopes. pp 1657–1669, doi:10.1117/12.460346 2.2.1

Fabian A. C., 2012, ARA&A, 50, 455 1.4.1, 4.1

Fabian A. C., Celotti A., Erlund M. C., 2006, MNRAS, 373, L16 1.3.4

Fabian A. C., Vasudevan R. V., Gandhi P., 2008, MNRAS, 385, L43 1.3.2, 1.12, 1.3.4, 1.13, 1.4.3, 4.1, 4.4.2, 4.4.3, 4.5.2, 4.11, 4.15

Fabian A. C., Vasudevan R. V., Mushotzky R. F., Winter L. M., Reynolds C. S., 2009, MNRAS, 394, L89 1.3.2, 4.1, 4.4.2, 4.4.3, 4.4.3, 4.5.2

Fabian A. C., Lohfink A., Kara E., Parker M. L., Vasudevan R., Reynolds C. S., 2015, MNRAS, 451, 4375 1.3.3

Fabian A. C., Lohfink A., Belmont R., Malzac J., Coppi P., 2017, MNRAS, 467, 2566 1.3.3

Falcke H., Biermann P. L., 1995, A&A, 293, 665 1.3.6

Fanaroff B. L., Riley J. M., 1974, MNRAS, 167, 31P 1.2.1

Fath E. A., 1909, PASP, 21, 138 1.1.2, 1.1.3

Fawcett V. A., et al., 2023, MNRAS, 525, 5575 1.2.2, 4.6

Fernique P., Boch T., Donaldson T., Durand D., O'Mullane W., Reinecke M., Taylor M., 2019, MOC - HEALPix Multi-Order Coverage map Version 1.1, IVOA Recommendation 07 October 2019 3.2

Feroz F., Hobson M. P., Bridges M., 2009, MNRAS, 398, 1601 2.4.3

Ferrarese L., Merritt D., 2000, ApJ, 539, L9 1.4.3

Feuillet L. M., Meléndez M., Kraemer S., Schmitt H. R., Fischer T. C., Reeves J. N., 2024, ApJ, 962, 104 1.4.1

Figer D. F., 2005, Nature, 434, 192 1.3.1

Fitch W. S., Pacholczyk A. G., Weymann R. J., 1967, ApJ, 150, L67 1.1.3

Frank J., King A., Raine D., 1992, Accretion power in astrophysics.. Vol. 21 1.3.2

Friedman H., Byram E. T., 1967, Science, 158, 257 1.1.3

Fruscione A., et al., 2006, in Silva D. R., Doxsey R. E., eds, Society of Photo-Optical Instrumentation Engineers (SPIE) Conference Series Vol. 6270, Society of Photo-Optical Instrumentation Engineers (SPIE) Conference Series. p. 62701V, doi:10.1117/12.671760 2.3.1, 2.4.1

GRAVITY Collaboration et al., 2019, A&A, 625, L10 1.3.1

GRAVITY Collaboration et al., 2020, A&A, 634, A1 1.3.4

Gallagher S. C., Brandt W. N., Chartas G., Priddey R., Garmire G. P., Sambruna R. M., 2006, ApJ, 644, 709 4.6

Gámez Rosas V., et al., 2022, Nature, 602, 403 1.3.4, 4.5.2

Gandhi P., Horst H., Smette A., Hönig S., Comastri A., Gilli R., Vignali C., Duschl W., 2009, A&A, 502, 457 1.3.4, 3.1, 3.6.1

Gandhi P., Yamada S., Ricci C., Asmus D., Mushotzky R. F., Ueda Y., Terashima Y., La Parola V., 2015, MNRAS, 449, 1845 3.6.1

Gandhi P., et al., 2022, Nature Astronomy, 6, 1364 1.3.3

Gao F., et al., 2020, A&A, 637, A94 1.2.2

García-Bernete I., et al., 2019, MNRAS, 486, 4917 1.3.4

García-Burillo S., et al., 2016, ApJ, 823, L12 1.3.4

García-Burillo S., et al., 2019, A&A, 632, A61 4.5.2

García-Burillo S., et al., 2021, A&A, 652, A98 4.5.2

Gardner J. P., et al., 2006, Space Sci. Rev., 123, 485 1.4.1, 3.6.2

Gaskell C. M., 2009, New A Rev., 53, 140 1.3.5

Gaskell C. M., 2017, MNRAS, 467, 226 1.4.1

Gaskell C. M., Ferland G. J., 1984, PASP, 96, 393 1.4.1

Geach J. E., et al., 2017, MNRAS, 465, 1789 2.2.1

Gebhardt K., et al., 2000, ApJ, 539, L13 1.2.2, 1.4.3

Gehrels N., et al., 2004, ApJ, 611, 1005 1.4.1, 4.4.1

Gendreau K. C., et al., 1995, PASJ, 47, L5 1.4.2

Genzel R., Eisenhauer F., Gillessen S., 2010, Reviews of Modern Physics, 82, 3121 1.3.1

Georgakakis A. E., Chavushyan V., Plionis M., Georgantopoulos I., Koulouridis E., Leonidaki I., Mercado A., 2006, MNRAS, 367, 1017 4.3.3

Georgakakis A., Rowan-Robinson M., Babbedge T. S. R., Georgantopoulos I., 2007, MNRAS, 377, 203 4.3.3

Georgakakis A., Nandra K., Laird E. S., Aird J., Trichas M., 2008, MNRAS, 388, 1205 1.4.1, 2.3.1, 4.3.3

Georgakakis A., et al., 2013, arXiv e-prints, p. arXiv:1306.2328 3.6.2

Georgakakis A., et al., 2014, MNRAS, 440, 339 1.4.3, 4.1

Georgakakis A., et al., 2015, MNRAS, 453, 1946 1.4.2, 4.3.3, 5

Georgakakis A., et al., 2017a, MNRAS, 469, 3232 4.3.3

Georgakakis A., Aird J., Schulze A., Dwelly T., Salvato M., Nandra K., Merloni A., Schneider D. P., 2017b, MNRAS, 471, 1976 1.4.1, 2.3.1, 2.3.3

Georgakakis A., Aird J., Schulze A., Dwelly T., Salvato M., Nandra K., Merloni A., Schneider D. P., 2017c, MNRAS, 471, 1976 2.4.2, 3.5.2, 3.14, 4.1, 4.2, 4.3.3, 4.4.1, 4.5.1, 4.5.1, 4.9

Georgakakis A., Ruiz A., LaMassa S. M., 2020, MNRAS, 499, 710 4.4.2, 4.10

Georgantopoulos I., Akylas A., 2019, A&A, 621, A28 3.6.1

Georgantopoulos I., Georgakakis A., Koulouridis E., 2005, MNRAS, 360, 782 4.3.3

Georgantopoulos I., et al., 2011, A&A, 534, A23 3.1, 3.4

George I. M., Fabian A. C., 1991, MNRAS, 249, 352 1.3.3

Ghez A. M., et al., 2008, ApJ, 689, 1044 1.3.1

Ghisellini G., Haardt F., Matt G., 2004, A&A, 413, 535 1.3.3

Giacconi R., Gursky H., Paolini F. R., Rossi B. B., 1962, Phys. Rev. Lett., 9, 439 1.1.3, 1.4.2

Giacconi R., Murray S., Gursky H., Kellogg E., Schreier E., Matilsky T., Koch D., Tananbaum H., 1974, ApJS, 27, 37 1.4.2

Giacconi R., et al., 2002, ApJS, 139, 369 2.2.3

Gianolli V. E., et al., 2023, MNRAS, 523, 4468 1.3.3

Gierliński M., Done C., 2004, MNRAS, 349, L7 1.3.3

Gilli R., Comastri A., Hasinger G., 2007, A&A, 463, 79 1.4.2, 1.19, 3.1

Gilli R., Vignali C., Mignoli M., Iwasawa K., Comastri A., Zamorani G., 2010, A&A, 519, A92 1.4.1

Gilli R., et al., 2022, A&A, 666, A17 1.4.1, 4.5.3, 4.5.3, 4.15, 5

Giommi P., Padovani P., Polenta G., Turriziani S., D'Elia V., Piranomonte S., 2012, MNRAS, 420, 2899 1.2.1

Glikman E., 2017, Research Notes of the American Astronomical Society, 1, 48 4.5.3

Glikman E., LaMassa S., Piconcelli E., Zappacosta L., Lacy M., 2024, arXiv e-prints, p. arXiv:2401.02859 4.5.3

González-Martín O., et al., 2015, A&A, 578, A74 1.3.4

Górski K. M., Hivon E., Banday A. J., Wandelt B. D., Hansen F. K., Reinecke M., Bartelmann M., 2005, ApJ, 622, 759 3.2

Goulding A. D., Alexander D. M., Bauer F. E., Forman W. R., Hickox R. C., Jones C., Mullaney J. R., Trichas M., 2012, ApJ, 755, 5 1.4.1

Goulding A. D., et al., 2023, ApJ, 955, L24 1.1.3, 1.4.1

Grandi P., Malaguti G., Fiocchi M., 2006, ApJ, 642, 113 1.3.6

Greene J. E., Ho L. C., 2005, ApJ, 630, 122 1.3.1

Greene J. E., Zakamska N. L., Ho L. C., Barth A. J., 2011, ApJ, 732, 9 1.3.5

Greenhill L. J., et al., 2003, ApJ, 590, 162 1.3.1

Grogin N. A., et al., 2011, ApJS, 197, 35 2.2.1, 2.6, 2.2.2, 2.7, 2.2.3

Groth E. J., Kristian J. A., Lynds R., O'Neil Earl J. J., Balsano R., Rhodes J., WFPC-1 IDT 1994, in American Astronomical Society Meeting Abstracts. p. 53.09 2.2.2

Guainazzi M., Bianchi S., 2007, MNRAS, 374, 1290 1.3.3

Guedel M., Benz A. O., 1993, ApJ, 405, L63 1.3.6

Guilbert P. W., Rees M. J., 1988, MNRAS, 233, 475 1.3.3

Gültekin K., King A. L., Cackett E. M., Nyland K., Miller J. M., Di Matteo T., Markoff S., Rupen M. P., 2019, ApJ, 871, 80 1.3.1

Guo Y., et al., 2013, ApJS, 207, 24 2.2.3, 2.8, 2.2.3

Gwyn S. D. J., 2012, AJ, 143, 38 2.6, 2.2.2

Haardt F., Maraschi L., 1991, ApJ, 380, L51 1.3.3, 1.3.3

Haardt F., Maraschi L., 1993, ApJ, 413, 507 1.3.3, 1.3.3

Habouzit M., et al., 2019, MNRAS, 484, 4413 4.4.1, 4.8, 4.5.1

Hamilton T. T., Helfand D. J., 1987, ApJ, 318, 93 1.4.2

Hardcastle M. J., Croston J. H., 2020, New A Rev., 88, 101539 1.3.6

Harrison C. M. C., 2014, PhD thesis, Durham University, UK 1.9

Harrison C. M., Ramos Almeida C., 2024, arXiv e-prints, p. arXiv:2404.08050 1.4.3

Harrison F. A., et al., 2013, ApJ, 770, 103 1.4.1, 2.2.1, 5

Harrison C. M., et al., 2016, MNRAS, 456, 1195 4.5.2

Hasinger G., 2008, A&A, 490, 905 1.3.4, 1.19, 1.4.2, 4.4.1, 4.4.2

Hasinger G., Miyaji T., Schmidt M., 2005, A&A, 441, 417 1.4.3, 4.5.1

Hasinger G., et al., 2007, ApJS, 172, 29 2.2.1

Hasinger G., et al., 2018, ApJ, 858, 77 2.2.1

Heckman T. M., 1980, A&A, 87, 152 1.2.1

Heckman T. M., Best P. N., 2014, ARA&A, 52, 589 1.2.1

Helou G., Soifer B. T., Rowan-Robinson M., 1985, ApJ, 298, L7 1.4.1

Herschel W., 1786, Philosophical Transactions of the Royal Society of London Series I, 76, 457 1.1.2

Herschel W., 1789, Philosophical Transactions of the Royal Society of London Series I, 79, 212 1.1.2

Herschel W., 1802, Philosophical Transactions of the Royal Society of London Series I, 92, 477 1.1.2

Hickox R. C., Alexander D. M., 2018, ARA&A, 56, 625 1.6, 1.8, 1.3.4, 1.4, 1.4.1, 4.1

Hirschmann M., Dolag K., Saro A., Bachmann L., Borgani S., Burkert A., 2014, MNRAS, 442, 2304 4.4.1, 4.8, 4.5.1

Ho L. C., Filippenko A. V., Sargent W. L. W., 1993, ApJ, 417, 63 1.2.1

Ho L. C., Filippenko A. V., Sargent W. L. W., 1997, ApJS, 112, 315 1.4.1

Hoaglin D. C., Mosteller F., Tukey J. W., 1983, Understanding robust and exploratory data anlysis 2.3.3

Hönig S. F., 2019, ApJ, 884, 171 1.3.4

Hönig S. F., Kishimoto M., 2010, A&A, 523, A27 1.4.1

Hönig S. F., Kishimoto M., 2017, ApJ, 838, L20 1.3.4

Hönig S. F., Beckert T., Ohnaka K., Weigelt G., 2006, A&A, 452, 459 1.3.4

Hönig S. F., et al., 2013, ApJ, 771, 87 1.3.4

Hopkins P. F., Hernquist L., Cox T. J., Di Matteo T., Robertson B., Springel V., 2006, ApJS, 163, 1 1.2.2, 1.4.3, 4.5.3

Hopkins P. F., Hernquist L., Cox T. J., Kereš D., 2008, ApJS, 175, 356 1.2.2, 1.4.3, 3.6.1, 5

Horst H., Gandhi P., Smette A., Duschl W. J., 2008, A&A, 479, 389 1.3.4

Houck J. R., et al., 2004, ApJS, 154, 18 1.4.1

Hsieh B.-C., Wang W.-H., Hsieh C.-C., Lin L., Yan H., Lim J., Ho P. T. P., 2012, ApJS, 203, 23 2.2.3

Hsu L.-T., et al., 2014, ApJ, 796, 60 2.3.2, 2.3.3, 2.3.3, 2.5, 4.2

Hubble E. P., 1925, Popular Astronomy, 33, 252 1.1.2

Hubble E. P., 1926a, ApJ, 63, 236 1.1.2

Hubble E. P., 1926b, ApJ, 64, 321 1.1.2

Hubble E., 1929, Proceedings of the National Academy of Science, 15, 168 1.1.2, 1.1.3

Ichimaru S., 1977, ApJ, 214, 840 1.3.2

Ilbert O., et al., 2006, A&A, 457, 841 2.3.3

Ilbert O., et al., 2009, ApJ, 690, 1236 2.3.3

Ilbert O., et al., 2013, A&A, 556, A55 4.3.3, 4.4.2

Imanishi M., Nakanishi K., Izumi T., 2016, AJ, 152, 218 1.3.4

Inayoshi K., Haiman Z., 2016, ApJ, 828, 110 1.3.1

Inayoshi K., Haiman Z., Ostriker J. P., 2016, MNRAS, 459, 3738 1.3.2

Inoue A. K., 2011, MNRAS, 415, 2920 2.4.3, 2.8

Ishibashi W., Fabian A. C., Ricci C., Celotti A., 2018, MNRAS, 479, 3335 1.3.2, 1.12, 1.13, 4.5.2

Ivezić Ž., et al., 2002, AJ, 124, 2364 1.2.1

Ivison R. J., et al., 2007, ApJ, 660, L77 2.2.2

Jansen F., et al., 2001, A&A, 365, L1 1.4.1

Jansky K. G., 1933, Popular Astronomy, 41, 548 1.1.3

Jansky D., 1984. 1.1.3

Jeffreys H., 1961, Theory of Probability (3rd Edition). Oxford University Press, New York 3.3.3

Jin S., et al., 2018, ApJ, 864, 56 2.2.1, 2.3.2, 2.4.3, 2.17, 3.2, 3.4.1, 3.4.2, 3.6

Jun H. D., Assef R. J., Carroll C. M., Hickox R. C., Kim Y., Lee J., Ricci C., Stern D., 2021a, ApJ, 906, 21 1.3.4

Jun H. D., Assef R. J., Carroll C. M., Hickox R. C., Kim Y., Lee J., Ricci C., Stern D., 2021b, ApJ, 906, 21 4.5.3

Juneau S., Dickinson M., Alexander D. M., Salim S., 2011, ApJ, 736, 104 1.4.1

Kaiser C. R., Alexander P., 1997, MNRAS, 286, 215 1.3.6

Kakkad D., et al., 2016, A&A, 592, A148 4.5.2

Kalberla P. M. W., Burton W. B., Hartmann D., Arnal E. M., Bajaja E., Morras R., Pöppel W. G. L., 2005, A&A, 440, 775 2.4.2

Kallman T., Mushotzky R., 1985, ApJ, 292, 49 1.3.5

Kant I., 1755, Allgemeine Naturgeschichte und Theorie des Himmels 1.1.2

Kashino D., et al., 2019, ApJS, 241, 10 2.2.1

Kaspi S., Smith P. S., Netzer H., Maoz D., Jannuzi B. T., Giveon U., 2000, ApJ, 533, 631 1.3.5

Katz J. I., 1976, ApJ, 206, 910 1.3.3

Kauffmann G., Heckman T. M., 2009, MNRAS, 397, 135 1.4.3, 4.1

Kauffmann G., et al., 2003, MNRAS, 346, 1055 1.4.1, 1.16

Keeler J. E., 1908, Publications of Lick Observatory, 8, 1 1.1.2

Kellermann K. I., Owen F. N., 1988, in Kellermann K. I., Verschuur G. L., eds, , Galactic and Extragalactic Radio Astronomy. pp 563–602 1.3.6

Kellermann K. I., Sramek R., Schmidt M., Shaffer D. B., Green R., 1989, AJ, 98, 1195 1.2.1

Kellermann K. I., Condon J. J., Kimball A. E., Perley R. A., Ivezić Ž., 2016, ApJ, 831, 168 1.2.1

Kerr R. P., 1963, Phys. Rev. Lett., 11, 237 1.3.1

Kewley L. J., Dopita M. A., Sutherland R. S., Heisler C. A., Trevena J., 2001, ApJ, 556, 121 1.16

Kewley L. J., Groves B., Kauffmann G., Heckman T., 2006, MNRAS, 372, 961 1.4.1, 1.16

Kewley L. J., Dopita M. A., Leitherer C., Davé R., Yuan T., Allen M., Groves B., Sutherland R., 2013, ApJ, 774, 100 1.4.1

King A., 2016, MNRAS, 456, L109 1.3.1

King A., Pounds K., 2015, ARA&A, 53, 115 4.5.3

King A. R., Pringle J. E., Hofmann J. A., 2008, MNRAS, 385, 1621 1.3.1

Kishimoto M., Hönig S. F., Antonucci R., Kotani T., Barvainis R., Tristram K. R. W., Weigelt G., 2009, A&A, 507, L57 1.3.4

Kishimoto M., Hönig S. F., Antonucci R., Barvainis R., Kotani T., Tristram K. R. W., Weigelt G., Levin K., 2011, A&A, 527, A121 1.3.4

Klindt L., 2022, PhD thesis, Durham University, UK 1.7

Klindt L., Alexander D. M., Rosario D. J., Lusso E., Fotopoulou S., 2019, MNRAS, 488, 3109 1.2.2, 4.5.3

Kocevski D. D., et al., 2015, ApJ, 814, 104 5, 5

Kocevski D. D., et al., 2023, ApJ, 954, L4 1.4.1

Kocevski D. D., et al., 2024, arXiv e-prints, p. arXiv:2404.03576 5

Koekemoer A. M., et al., 2011, ApJS, 197, 36 2.2.1, 2.6, 2.2.2, 2.2.3

Kokorev V., et al., 2023, ApJ, 957, L7 1.1.3, 1.4.1

Kormendy J., Ho L. C., 2013, ARA&A, 51, 511 1.1.3, 1.2.2, 1.3.1, 1.4.1, 1.4.3, 3.1

Koss M., Mushotzky R., Veilleux S., Winter L., 2010, ApJ, 716, L125 1.2.2

Koss M., et al., 2017, ApJ, 850, 74 1.3.1, 4.4.2, 5.2, 5

Koss M. J., et al., 2022a, ApJS, 261, 1 4.1, 4.4.1, 5

Koss M. J., et al., 2022b, ApJS, 261, 6 4.4.2

Krabbe A., Böker T., Maiolino R., 2001, ApJ, 557, 626 3.6.1

Kravtsov A. V., Borgani S., 2012, ARA&A, 50, 353 1.4.1

Kriek M., et al., 2008, ApJ, 677, 219 2.2.3

Kriek M., et al., 2015, ApJS, 218, 15 2.3

Krolik J. H., Begelman M. C., 1988, ApJ, 329, 702 1.3.4

Krolik J. H., Kriss G. A., 1995, ApJ, 447, 512 1.3.3

Kubota A., Done C., 2018, MNRAS, 480, 1247 1.3.3

Kukula M. J., Dunlop J. S., Hughes D. H., Rawlings S., 1998, MNRAS, 297, 366 1.3.6

Kurk J., et al., 2013, A&A, 549, A63 2.2.3

La Franca F., et al., 2005, ApJ, 635, 864 1.3.4, 1.4.2, 4.4.1, 4.4.2

LaMassa S. M., et al., 2016, ApJ, 817, 172 5

Lacy M., et al., 2004, ApJS, 154, 166 1.4.1

Lacy M., Petric A. O., Sajina A., Canalizo G., Storrie-Lombardi L. J., Armus L., Fadda D., Marleau F. R., 2007, AJ, 133, 186 1.4.1

Laigle C., et al., 2016, ApJS, 224, 24 2.2.1, 2.3.2

Laird E. S., Nandra K., Hobbs A., Steidel C. C., 2006, MNRAS, 373, 217 2.3.1

Laird E. S., et al., 2009, ApJS, 180, 102 2.2.2, 2.2.2, 2.6, 2.3.1, 4.2

Laloux B., et al., 2023, MNRAS, 518, 2546 1.5, 4.2, 4.3.3, 4.3.3

Laloux B., et al., 2024, arXiv e-prints, p. arXiv:2403.07109 1.5

Lansbury G. B., Banerji M., Fabian A. C., Temple M. J., 2020, MNRAS, 495, 2652 1.13, 4.5.3

Lanzuisi G., et al., 2018, MNRAS, 480, 2578 (document), 3.3.1, 3.1, 3.2, 3.3.4, 3.3.4, 3.3, 3.3.4, 3.5, 3.4.2, 3.9, 3.15, 3.6.1

Laor A., Behar E., 2008, MNRAS, 390, 847 1.3.6

Lapi A., Raimundo S., Aversa R., Cai Z. Y., Negrello M., Celotti A., De Zotti G., Danese L., 2014, ApJ, 782, 69 1.3.2, 4.5.3

Lapi A., et al., 2018, ApJ, 857, 22 4.5.3

Laplace P. S., 1796, Exposition du Système du Monde. Part 11 1.1.1

Laplace P. S., 1799, Allgemeine Geographische Ephemeriden, 4, 1 1.1.1

Latif M. A., Schleicher D. R. G., Schmidt W., Niemeyer J., 2013, MNRAS, 433, 1607 1.3.1

Laureijs R., et al., 2011, arXiv e-prints, p. arXiv:1110.3193 3.6.2

Lawrence A., 1991, MNRAS, 252, 586 1.3.4, 4.4.2, 4.5.2

Le Fèvre O., et al., 2003, in Iye M., Moorwood A. F. M., eds, Society of Photo-Optical Instrumentation Engineers (SPIE) Conference Series Vol. 4841, Instrument Design and Performance for Optical/Infrared Ground-based Telescopes. pp 1670–1681, doi:10.1117/12.460959 2.2.1

Le Fèvre O., et al., 2004, A&A, 428, 1043 2.3.3

Le Fèvre O., et al., 2013, A&A, 559, A14 2.2.3

Le Fèvre O., et al., 2015, A&A, 576, A79 2.2.1, 2.3

Le Floc'h E., et al., 2009, ApJ, 703, 222 2.2.1

Leauthaud A., et al., 2007, ApJS, 172, 219 2.2.1

Leavitt H. S., 1908, Annals of Harvard College Observatory, 60, 87 1.1.2

Levenson N. A., Heckman T. M., Krolik J. H., Weaver K. A., Życki P. T., 2006a, ApJ, 648, 111 1.4.1

Levenson N. A., Heckman T. M., Krolik J. H., Weaver K. A., Życki P. T., 2006b, ApJ, 648, 111 3.1

Liang E. P. T., Price R. H., 1977, ApJ, 218, 247 1.3.3

Lightman A. P., White T. R., 1988, ApJ, 335, 57 1.3.3

Lilly S. J., Tresse L., Hammer F., Crampton D., Le Fevre O., 1995, ApJ, 455, 108 2.2.2

Lilly S. J., et al., 2007, ApJS, 172, 70 2.2.1, 2.3.3, 2.3

Lilly S. J., et al., 2009, ApJS, 184, 218 2.2.1

Liu D., et al., 2018, ApJ, 853, 172 2.2.1

Liu T., et al., 2022, A&A, 661, A5 4.4.3

López-Gonzaga N., Jaffe W., Burtscher L., Tristram K. R. W., Meisenheimer K., 2014, A&A, 565, A71 1.3.4

López I. E., et al., 2023, A&A, 672, A137 2.4.3, 4.4.2

Loredo T. J., 2004, in Fischer R., Preuss R., Toussaint U. V., eds, American Institute of Physics Conference Series Vol. 735, Bayesian Inference and Maximum Entropy Methods in Science and Engineering: 24th International Workshop on Bayesian Inference and Maximum Entropy Methods in Science and Engineering. pp 195–206 (arXiv:astro-ph/0409387), doi:10.1063/1.1835214 4.3.3

Lotz J. M., et al., 2008, ApJ, 672, 177 2.6, 2.2.2

Lovelace R. V. E., 1976, Nature, 262, 649 1.3.6

Lubiński P., et al., 2016, MNRAS, 458, 2454 1.3.3

Luo B., et al., 2008, ApJS, 179, 19 2.2.3

Luo B., et al., 2010, ApJS, 187, 560 2.3.2, 1, 2.10, 2.3.2

Luo B., et al., 2017, ApJS, 228, 2 2.2.3, 2.7, 2.2.3, 4.2, 5

Lusso E., Risaliti G., 2017, Frontiers in Astronomy and Space Sciences, 4, 66 1.3.3

Lutz D., et al., 2011, A&A, 532, A90 2.2.1, 2.2.3

Lynden-Bell D., 1969, Nature, 223, 690 1.1.3

Lynden-Bell D., 1978, Phys. Scr, 17, 185 1.1.3

Lynden-Bell D., Rees M. J., 1971, MNRAS, 152, 461 1.1.3

Lyu J., et al., 2023, arXiv e-prints, p. arXiv:2310.12330 1.4.1

Maccacaro T., della Ceca R., Gioia I. M., Morris S. L., Stocke J. T., Wolter A., 1991, ApJ, 374, 117 1.4.2

Madau P., Dickinson M., 2014, ARA&A, 52, 415 1.21, 1.4.3

Madau P., Meiksin A., Rees M. J., 1997, ApJ, 475, 429 1.4.1

Madau P., Pozzetti L., Dickinson M., 1998, ApJ, 498, 106 1.4.3

Magdziarz P., Blaes O. M., Zdziarski A. A., Johnson W. N., Smith D. A., 1998, MNRAS, 301, 179 1.3.3

Magorrian J., et al., 1998, AJ, 115, 2285 1.4.3

Maiolino R., Salvati M., Bassani L., Dadina M., della Ceca R., Matt G., Risaliti G., Zamorani G., 1998, A&A, 338, 781 3.1

Maiolino R., Marconi A., Oliva E., 2001, A&A, 365, 37 1.3.4

Maiolino R., Shemmer O., Imanishi M., Netzer H., Oliva E., Lutz D., Sturm E., 2007, A&A, 468, 979 1.3.4, 1.19

Maiolino R., et al., 2020, The Messenger, 180, 24 4.6

Maiolino R., et al., 2023, arXiv e-prints, p. arXiv:2305.12492 1.1.3, 1.4.1

Malkan M. A., Gorjian V., Tam R., 1998, ApJS, 117, 25 1.3.5

Mao M. Y., et al., 2012, MNRAS, 426, 3334 2.2.3

Marchesi S., et al., 2016a, ApJ, 817, 34 2.3, 2.3.3, 2.3.3, 2.5, 2.3.3

Marchesi S., et al., 2016b, ApJ, 830, 100 2.4.1, 3.3.1, 3.1, 3.3.4, 3.3.4

Marconi A., Hunt L. K., 2003, ApJ, 589, L21 1.2.2, 1.4.3, 4.3.3, 4.4.2

Marconi A., Risaliti G., Gilli R., Hunt L. K., Maiolino R., Salvati M., 2004, MNRAS, 351, 169 1.3.2, 3.1

Marinucci A., et al., 2022, MNRAS, 516, 5907 1.3.3

Markowitz A. G., Krumpe M., Nikutta R., 2014, MNRAS, 439, 1403 1.3.4, 2.4.2

Marocco J., Hache E., Lamareille F., 2011, A&A, 531, A71 1.4.1

Marshall F. E., Boldt E. A., Holt S. S., Miller R. B., Mushotzky R. F., Rose L. A., Rothschild R. E., Serlemitsos P. J., 1980, ApJ, 235, 4 1.4.2

Martin D. C., et al., 2005, ApJ, 619, L1 2.2.1, 2.2.3

Martocchia A., Matt G., 1996, MNRAS, 282, L53 1.3.3

Masini A., et al., 2020, ApJS, 251, 2 5

Mateos S., et al., 2012, MNRAS, 426, 3271 1.4.1

Mateos S., et al., 2015, MNRAS, 449, 1422 (document), 1.3.4, 3.4, 3.6, 3.4.2, 3.7, 3.4.2, 5

Matt G., 2000, A&A, 355, L31 4.5.3, 4.15

Matt G., Perola G. C., Piro L., 1991, A&A, 247, 25 1.3.3

McCracken H. J., et al., 2012, A&A, 544, A156 2.2.1

Mercedes-Feliz J., et al., 2023, arXiv e-prints, p. arXiv:2310.19863 1.4.3

Merloni A., et al., 2014, MNRAS, 437, 3550 4.4.2

Merloni A., et al., 2019, The Messenger, 175, 42 4.6, 5

Merloni A., et al., 2024, A&A, 682, A34 5

Messier C., 1781, Catalogue des Nébuleuses et des Amas d'Étoiles (Catalog of Nebulae and Star Clusters), Connoissance des Temps ou des Mouvements Célestes, for 1784, p. 227-267 1.1.2

Mezcua M., 2017, International Journal of Modern Physics D, 26, 1730021 1.10, 1.3.1

Michell J., 1784, Philosophical Transactions of the Royal Society of London Series I, 74, 35 1.1.1, 1.1.2

Mignoli M., et al., 2005, A&A, 437, 883 2.2.3, 2.3.3

Miller J. S., Goodrich R. W., Mathews W. G., 1991, ApJ, 378, 47 1.2.2

Miller N. A., et al., 2013, ApJS, 205, 13 2.2.3

Miniutti G., Fabian A. C., 2004, MNRAS, 349, 1435 1.3.3

Mitchell J. A. J., Done C., Ward M. J., Kynoch D., Hagen S., Lusso E., Landt H., 2023, MNRAS, 524, 1796 5

Miyazaki S., et al., 2018, PASJ, 70, S1 2.2.1

Molyneux S. J., Harrison C. M., Jarvis M. E., 2019, A&A, 631, A132 1.3.6

Momcheva I. G., et al., 2016, ApJS, 225, 27 2.3

Montgomery C., Orchiston W., Whittingham I., 2009, Journal of Astronomical History and Heritage, 12, 90 1.1.1

Mor R., Netzer H., Elitzur M., 2009, ApJ, 705, 298 1.3.4

Mordini S., Spinoglio L., Fernández-Ontiveros J. A., 2021, A&A, 653, A36 1.4.1

Morris A. M., et al., 2015, AJ, 149, 178 2.2.3

Mountrichas G., Georgantopoulos I., 2023, arXiv e-prints, p. arXiv:2312.11609 4.5.2

Mountrichas G., Buat V., Georgantopoulos I., Yang G., Masoura V. A., Boquien M., Burgarella D., 2021, A&A, 653, A70 2.4.3, 4.5.2

Mountrichas G., Viitanen A., Carrera F. J., Stiele H., Ruiz A., Georgantopoulos I., Mateos S., Corral A., 2024, arXiv:2401.00045, p. arXiv:2401.00045 4.4.1

Mullaney J. R., Alexander D. M., Goulding A. D., Hickox R. C., 2011, MNRAS, 414, 1082 1.3.4, 2.4.3, 2.7, 3.4.1

Mullaney J. R., et al., 2015, MNRAS, 453, L83 4.1

Murphy K. D., Yaqoob T., 2009, MNRAS, 397, 1549 1.3.4, 2.4.2, 3.3.4

Murray S. S., et al., 1997, in Siegmund O. H., Gummin M. A., eds, Society of Photo-Optical Instrumentation Engineers (SPIE) Conference Series Vol. 3114, EUV, X-Ray, and Gamma-Ray Instrumentation for Astronomy VIII. pp 11–25, doi:10.1117/12.283772 2.1

Murray S. S., et al., 2000, in Flanagan K. A., Siegmund O. H., eds, Society of Photo-Optical Instrumentation Engineers (SPIE) Conference Series Vol. 4140, X-Ray and Gamma-Ray Instrumentation for Astronomy XI. pp 144–154, doi:10.1117/12.409108 2.1

Murray N., Quataert E., Thompson T. A., 2005, ApJ, 618, 569 1.3.2

Mushotzky R. F., 1982, ApJ, 256, 92 1.4.2

Mushotzky R. F., 1984, Advances in Space Research, 3, 157 1.3.3, 1.4.2

Mushotzky R. F., Done C., Pounds K. A., 1993, ARA&A, 31, 717 1.3.3

Musiimenta B., et al., 2023, arXiv e-prints, p. arXiv:2309.16528 4.5.2

Namekata D., Umemura M., 2016, MNRAS, 460, 980 1.3.2

Nandra K., Pounds K. A., Stewart G. C., George I. M., Hayashida K., Makino F., Ohashi T., 1991, MNRAS, 248, 760 1.3.3

Nandra K., George I. M., Mushotzky R. F., Turner T. J., Yaqoob T., 1997, ApJ, 477, 602 2.4.2

Nandra K., et al., 2005, MNRAS, 356, 568 2.2.2, 2.3.1

Nandra K., O'Neill P. M., George I. M., Reeves J. N., 2007, MNRAS, 382, 194 2.3.1, 3.1

Nandra K., et al., 2013, arXiv e-prints, p. arXiv:1306.2307 3.6.2

Nandra K., et al., 2015, ApJS, 220, 10 2.2.2, 2.6, 2.3.1, 2.3.3, 2.3.3, 2.5, 4.2, 4.2, 5

Narayan R., McClintock J. E., 2012, MNRAS, 419, L69 1.2.2

Nardini E., Risaliti G., Salvati M., Sani E., Imanishi M., Marconi A., Maiolino R., 2008, MNRAS, 385, L130 2.4.3

Nardini E., Risaliti G., Salvati M., Sani E., Watabe Y., Marconi A., Maiolino R., 2009, MNRAS, 399, 1373 2.4.3

Nenkova M., Sirocky M. M., Nikutta R., Ivezić Ž., Elitzur M., 2008, ApJ, 685, 160 1.3.4

Netzer H., 1987, MNRAS, 225, 55 1.3.2

Netzer H., 2015, ARA&A, 53, 365 4.1

Newman J. A., et al., 2013, ApJS, 208, 5 2.2.2, 2.3.3, 2.4

Ni Q., et al., 2021, ApJS, 256, 21 4.1, 5

Nims J., Quataert E., Faucher-Giguère C.-A., 2015, MNRAS, 447, 3612 1.3.6

Noll S., Burgarella D., Giovannoli E., Buat V., Marcillac D., Muñoz-Mateos J. C., 2009, A&A, 507, 1793 2.4.3

Novikov I. D., Thorne K. S., 1973, in Black Holes (Les Astres Occlus). pp 343–450 1.3.2, 8

O'Dea C. P., Baum S. A., Stanghellini C., 1991, ApJ, 380, 66 1.3.6

O'Neill S., et al., 2022, ApJ, 926, L35 1.3.1

Oh K., Yi S. K., Schawinski K., Koss M., Trakhtenbrot B., Soto K., 2015, ApJS, 219, 1 1.3.4

Oliver S. J., et al., 2012, MNRAS, 424, 1614 2.2.1, 2.2.3

Opik E., 1922, ApJ, 55, 406 1.1.2

Oppenheimer J. R., Snyder H., 1939, Physical Review, 56, 455 1.1.1, 1.3.1

Oppenheimer J. R., Volkoff G. M., 1939, Physical Review, 55, 374 1.1.1

Osterbrock D. E., 1977, ApJ, 215, 733 1.2.1

Osterbrock D. E., 1981, ApJ, 249, 462 1.2.1

Osterbrock D. E., 1989, Astrophysics of gaseous nebulae and active galactic nuclei 1.3.5

Packham C., Radomski J. T., Roche P. F., Aitken D. K., Perlman E., Alonso-Herrero A., Colina L., Telesco C. M., 2005, ApJ, 618, L17 1.3.4

Pacucci F., Volonteri M., Ferrara A., 2015, MNRAS, 452, 1922 1.3.1

Padovani P., Bonzini M., Kellermann K. I., Miller N., Mainieri V., Tozzi P., 2015, MNRAS, 452, 1263 1.3.6

Padovani P., et al., 2017, A&A Rev., 25, 2 1.1.3, 1.2, 1.2.1, 1.4.1, 1.4.1, 3.1

Panessa F., Baldi R. D., Laor A., Padovani P., Behar E., McHardy I., 2019, Nature Astronomy, 3, 387 1.14, 1.3.6

Patil P., et al., 2020, ApJ, 896, 18 1.3.6

Penna R. F., Narayan R., Sadowski A., 2013, MNRAS, 436, 3741 1.3.6

Pérez-González P. G., et al., 2005, ApJ, 630, 82 2.3.2

Pérez-González P. G., et al., 2008, ApJ, 675, 234 2.3.2

Perrotta S., Hamann F., Zakamska N. L., Alexandroff R. M., Rupke D., Wylezalek D., 2019, MNRAS, 488, 4126 4.5.2

Peterson B. M., 1997, An Introduction to Active Galactic Nuclei 1.3.5

Peterson B. M., et al., 2004, ApJ, 613, 682 1.3.5

Petrucci P. O., et al., 2013, A&A, 549, A73 1.3.3

Petrucci P. O., Ursini F., De Rosa A., Bianchi S., Cappi M., Matt G., Dadina M., Malzac J., 2018, A&A, 611, A59 1.3.3

Pier E. A., Krolik J. H., 1992, ApJ, 401, 99 1.3.4

Pierre M., et al., 2016, A&A, 592, A1 3.14

Piro L., Yamauchi M., Matsuoka M., 1990, ApJ, 360, L35 3.1

Planck Collaboration et al., 2011, A&A, 536, A15 1.3.6

Pope A., et al., 2008, ApJ, 675, 1171 1.4.1

Popesso P., et al., 2009, A&A, 494, 443 2.3.3

Predehl P., et al., 2021, A&A, 647, A1 3.6.1

Press W. H., Teukolsky S. A., Vetterling W. T., Flannery B. P., 1992, Numerical recipes in FORTRAN. The art of scientific computing. Cambridge: University Press, —c1992, 2nd ed. 3.5.2

Ptak A., Mobasher B., Hornschemeier A., Bauer F., Norman C., 2007, ApJ, 667, 826 4.3.3

Pürrer M., Hannam M., Ohme F., 2016, Phys. Rev. D, 93, 084042 1.3.1

Ramos Almeida C., Ricci C., 2017a, Nature Astronomy, 1, 679 1.8, 1.3.4

Ramos Almeida C., Ricci C., 2017b, Nature Astronomy, 1, 679 4.4.2, 4.5.2

Ramos Almeida C., et al., 2009, ApJ, 702, 1127 1.3.4, 2.4.2

Ramos Almeida C., Dicken D., Tadhunter C., Asensio Ramos A., Inskip K. J., Hardcastle M. J., Mingo B., 2011, MNRAS, 413, 2358 2.4.2

Ranalli P., et al., 2013, A&A, 555, A42 2.2.3

Rau A., et al., 2013, arXiv e-prints, p. arXiv:1308.6785 3.6.2

Ravikumar C. D., et al., 2007, A&A, 465, 1099 2.2.3, 2.3.3

Reber G., 1944, ApJ, 100, 279 1.1.3

Rees M. J., 1984, ARA&A, 22, 471 1.1.3

Rees M. J., Silk J. I., Werner M. W., Wickramasinghe N. C., 1969, Nature, 223, 788 1.3.4

Reines A. E., Volonteri M., 2015, ApJ, 813, 82 1.4.3

Reynolds C. S., 2014, Space Sci. Rev., 183, 277 1.3.1, 1.3.6

Reynolds C. S., 2021, ARA&A, 59, 117 1.3.1, 1.3.1

Rhodes J., Refregier A., Groth E. J., 2000, ApJ, 536, 79 2.2.2

Ricci C., Paltani S., 2023, ApJ, 945, 55 1.3.4

Ricci C., Ueda Y., Koss M. J., Trakhtenbrot B., Bauer F. E., Gandhi P., 2015, ApJ, 815, L13 1.3.4, 1.4.2, 3.1, 3.6.1

Ricci F., et al., 2017a, MNRAS, 471, L41 4.5.2

Ricci C., et al., 2017b, Nature, 549, 488 1.3.4, 1.3.4, 1.4.3, 4.1, 4.4.2, 4.4.2, 4.4.3, 4.4.3, 4.5.2, 4.5.3, 4.6, 4.10, 4.13, 5

Ricci C., et al., 2022, ApJ, 938, 67 1.12, 1.3.4, 1.4.3, 4.1, 4.4.2, 4.4.2, 4.4.3, 4.5.2, 4.6, 4.10

Ricci C., et al., 2023, ApJ, 959, 27 1.3.4, 1.3.4, 1.13

Richards G. T., et al., 2002, AJ, 123, 2945 1.4.1, 1.15

Richards G. T., et al., 2006, ApJS, 166, 470 1.3.4, 4.5.2

Risaliti G., Maiolino R., Salvati M., 1999, ApJ, 522, 157 3.1, 3.4

Risaliti G., Elvis M., Nicastro F., 2002, ApJ, 571, 234 1.3.4, 2.4.2

Risaliti G., et al., 2013, Nature, 494, 449 1.3.1

Roche P. F., Packham C., Telesco C. M., Radomski J. T., Alonso-Herrero A., Aitken D. K., Colina L., Perlman E., 2006, MNRAS, 367, 1689 1.3.4

Rosario D. J., 2019, FortesFit: Flexible spectral energy distribution modelling with a Bayesian backbone (ascl:1904.011) 2.4.3, 2.4.3, 3.4.1

Ross R. R., Fabian A. C., 1993, MNRAS, 261, 74 1.3.3, 1.3.3

Rosse T. E. O., 1850, Philosophical Transactions of the Royal Society of London Series I, 140, 499 1.1.2, 1.1

Rowan-Robinson M., 1977, ApJ, 213, 635 1.2.2

Rybicki G. B., Lightman A. P., 1979, Radiative processes in astrophysics 1.3.3, 1.3.3

Ryle M., Smith F. G., Elsmore B., 1950, MNRAS, 110, 508 1.1.3

Ryu T., Tanaka T. L., Perna R., Haiman Z., 2016, MNRAS, 460, 4122 1.3.2

Saha T., Markowitz A. G., Buchner J., 2022, MNRAS, 509, 5485 3.1

Sala L., Valentini M., Biffi V., Dolag K., 2023, arXiv e-prints, p. arXiv:2312.07657 1.3.1

Salpeter E. E., 1964, ApJ, 140, 796 1.1.3

Salvato M., et al., 2009, ApJ, 690, 1250 2.2.1, 2.3.3

Salvato M., et al., 2011, ApJ, 742, 61 (document), 2.3.3, 2.11

Sandage A., 1964, ApJ, 139, 416 1.1.3

Sandage A., 1965, ApJ, 141, 1560 1.1.3

Sanders D. B., Soifer B. T., Elias J. H., Madore B. F., Matthews K., Neugebauer G., Scoville N. Z., 1988, ApJ, 325, 74 1.4.3, 4.1, 4.5.3

Sanders D. B., et al., 2007, ApJS, 172, 86 2.3.2

Santini P., et al., 2014, A&A, 562, A30 4.5.1

Sawicki M., et al., 2019, MNRAS, 489, 5202 2.2.1

Sazonov S., Revnivtsev M., Krivonos R., Churazov E., Sunyaev R., 2007, A&A, 462, 57 1.3.4

Sazonov S., Churazov E., Krivonos R., 2015, MNRAS, 454, 1202 1.3.4

Schartmann M., Meisenheimer K., Camenzind M., Wolf S., Henning T., 2005, A&A, 437, 861 2.8

Schawinski K., et al., 2010, ApJ, 711, 284 1.4.3, 4.1

Schinnerer E., et al., 2010, ApJS, 188, 384 2.2.1

Schmidt M., 1963, Nature, 197, 1040 1.1.3, 1.4.1

Schmidt M., 1965, ApJ, 141, 1295 1.1.3

Schmidt M., 1968, ApJ, 151, 393 1.4.2

Schmitt J. L., 1968, Nature, 218, 663 1.1.3

Scholtz J., et al., 2018, MNRAS, 475, 1288 4.1

Schulze A., et al., 2015, MNRAS, 447, 2085 4.1

Schwarzschild K., 1916, Sitzungsberichte der Königlich Preussischen Akademie der Wissenschaften, pp 189–196 1.1.1, 1.3.1

Scoville N., et al., 2007, ApJS, 172, 1 2.2.1, 3.2

Seth A. C., et al., 2010, ApJ, 714, 713 1.3.1

Setti G., Woltjer L., 1989, A&A, 224, L21 1.4.2

Seyfert C. K., 1943, ApJ, 97, 28 1.1.3, 1.4.1

Shakura N. I., Sunyaev R. A., 1973, A&A, 24, 337 1.3.2, 1.3.2

Shankar F., Weinberg D. H., Miralda-Escudé J., 2009, ApJ, 690, 20 1.3.2

Shankar F., Weinberg D. H., Miralda-Escudé J., 2013, MNRAS, 428, 421 4.5.1

Shankar F., et al., 2016, Monthly Notices of the Royal Astronomical Society, 460, 3119 3.6.1

Shankar F., et al., 2020, MNRAS, 493, 1500 3.6.1

Shapiro S. L., Lightman A. P., Eardley D. M., 1976, ApJ, 204, 187 1.3.2

Shapley H., 1917, PASP, 29, 213 1.1.2

Sharma R. S., et al., 2024, MNRAS, 527, 9461 1.2.2

Shen Y., Kelly B. C., 2012, ApJ, 746, 169 4.4.1, 4.8, 4.5.1

Shirley R., et al., 2021, MNRAS, 507, 129 5

Sicilia A., et al., 2022, ApJ, 934, 66 4.5.3

Sijacki D., Vogelsberger M., Genel S., Springel V., Torrey P., Snyder G. F., Nelson D., Hernquist L., 2015, MNRAS, 452, 575 4.5.1

Silk J., 2013, ApJ, 772, 112 1.4.3

Silverman J. D., et al., 2010, ApJS, 191, 124 2.2.3, 2.3.3

Simmonds C., Buchner J., Salvato M., Hsu L. T., Bauer F. E., 2018, A&A, 618, A66 2.4.2

Simpson C., 2005, MNRAS, 360, 565 1.19

Skelton R. E., et al., 2014, ApJS, 214, 24 2.7, 2.2.3, 2.3

Smith H. J., Hoffleit D., 1963, Nature, 198, 650 1.1.3

Smith J. D. T., et al., 2007, ApJ, 656, 770 1.4.1

Smolčić V., et al., 2017, A&A, 602, A1 2.2.1

Soltan A., 1982, MNRAS, 200, 115 1.3.1, 1.3.6, 1.4, 3.1

Sopp H. M., Alexander P., 1991, MNRAS, 251, 14P 1.3.6

Spinoglio L., Malkan M. A., 1992, ApJ, 399, 504 1.4.1

Stalevski M., Ricci C., Ueda Y., Lira P., Fritz J., Baes M., 2016, MNRAS, 458, 2288 1.3.4, 2.4.3, 2.8

Stalevski M., Asmus D., Tristram K. R. W., 2017, MNRAS, 472, 3854 1.3.4

Stawarz Ł., Ostorero L., Begelman M. C., Moderski R., Kataoka J., Wagner S., 2008, ApJ, 680, 911 1.3.6

Steidel C. C., Adelberger K. L., Shapley A. E., Pettini M., Dickinson M., Giavalisco M., 2003, ApJ, 592, 728 2.2.2, 2.3.3, 2.4

Stern D., 2015, ApJ, 807, 129 (document), 1.3.4, 3.4, 3.6, 3.4.2, 3.7, 3.4.2, 3.4.2, 3.6.1, 5

Stern D., et al., 2005, ApJ, 631, 163 1.4.1

Stern D., et al., 2012, ApJ, 753, 30 1.4.1

Stickel M., Padovani P., Urry C. M., Fried J. W., Kuehr H., 1991, ApJ, 374, 431 1.2.1

Strittmatter P. A., Serkowski K., Carswell R., Stein W. A., Merrill K. M., Burbidge E. M., 1972, ApJ, 175, L7 1.1.3

Suganuma M., et al., 2006, ApJ, 639, 46 1.3.4

Suh H., Civano F., Trakhtenbrot B., Shankar F., Hasinger G., Sanders D. B., Allevato V., 2020, ApJ, 889, 32 4.4.2

Sunyaev R. A., Truemper J., 1979, Nature, 279, 506 1.3.3

Sutherland W., Saunders W., 1992, MNRAS, 259, 413 2.3.2, 4.2

Szokoly G. P., et al., 2004, ApJS, 155, 271 2.2.3, 2.3.3

Tacconi L. J., Genzel R., Sternberg A., 2020, ARA&A, 58, 157 4.5.1

Tananbaum H., et al., 1979, ApJ, 234, L9 1.1.3

Taniguchi Y., et al., 2007, ApJS, 172, 9 2.2.1

Taniguchi Y., et al., 2015, PASJ, 67, 104 2.2.1

Tanimoto A., Ueda Y., Odaka H., Kawaguchi T., Fukazawa Y., Kawamuro T., 2019, ApJ, 877, 95 1.3.4

Tasca L. A. M., et al., 2017, A&A, 600, A110 2.2.3

Thorne K. S., Price R. H., 1975, ApJ, 195, L101 1.3.3

Tielens A. G. G. M., 2008, ARA&A, 46, 289 1.4.1

Toba Y., et al., 2014, ApJ, 788, 45 1.3.4

Toba Y., Ueda Y., Matsuoka K., Shidatsu M., Nagao T., Terashima Y., Wang W.-H., Chang Y.-Y., 2019, MNRAS, 484, 196 1.3.4

Toba Y., et al., 2022, A&A, 661, A15 1.3.4, 4.4.3, 4.5.2, 4.13

Torbaniuk O., Paolillo M., D'Abrusco R., Vignali C., Georgakakis A., Carrera F. J., Civano F., 2024, MNRAS, 527, 12091 4.1

Tozzi P., et al., 2006, A&A, 451, 457 1.3.4

Trakhtenbrot B., Netzer H., 2012, MNRAS, 427, 3081 1.3.1

Treister E., Urry C. M., 2005, ApJ, 630, 115 1.4.2

Treister E., Urry C. M., Virani S., 2009, ApJ, 696, 110 1.4.2, 2.2.3, 2.3.3, 3.6.1

Treister E., Schawinski K., Urry C. M., Simmons B. D., 2012, ApJ, 758, L39 1.2.2

Tristram K. R. W., Burtscher L., Jaffe W., Meisenheimer K., Hönig S. F., Kishimoto M., Schartmann M., Weigelt G., 2014, A&A, 563, A82 1.3.4

Trump J. R., et al., 2007, ApJS, 172, 383 2.2.1

Tucker W., Giacconi R., 1985, The x-ray universe 1.1.3

Tueller J., Mushotzky R. F., Barthelmy S., Cannizzo J. K., Gehrels N., Markwardt C. B., Skinner G. K., Winter L. M., 2008, ApJ, 681, 113 1.4.2

Türler M., et al., 1999, A&AS, 134, 89 1.1.3

Turner T. J., Pounds K. A., 1989, MNRAS, 240, 833 1.3.3, 1.3.4

Ueda Y., Akiyama M., Ohta K., Miyaji T., 2003, ApJ, 598, 886 1.4.3, 3.1

Ueda Y., Akiyama M., Hasinger G., Miyaji T., Watson M. G., 2014, ApJ, 786, 104 1.3.4, 1.4.2, 1.18, 1.4.3, 3.1, 3.5.1, 3.11, 3.13, 3.5.1, 3.14, 3.5.2, 3.15, 3.6.1, 4.1, 4.4.2

Urry C. M., Padovani P., 1995, PASP, 107, 803 1.2.2, 1.3.4, 3.1, 4.5.2

Ursini F., Matt G., Bianchi S., Marinucci A., Dovčiak M., Zhang W., 2022, MNRAS, 510, 3674 1.3.3

Uttley P., Cackett E. M., Fabian A. C., Kara E., Wilkins D. R., 2014, A&A Rev., 22, 72 1.3.1

Vanden Berk D. E., et al., 2001, AJ, 122, 549 4.5.2

Vanzella E., et al., 2008, A&A, 478, 83 2.2.3, 2.3.3

Vazquez B., et al., 2015, ApJ, 801, 127 1.3.4

Veilleux S., Osterbrock D. E., 1987, ApJS, 63, 295 1.4.1

Veilleux S., Kim D. C., Sanders D. B., Mazzarella J. M., Soifer B. T., 1995, ApJS, 98, 171 1.2.1

Venanzi M., Hönig S., Williamson D., 2020, ApJ, 900, 174 1.3.4, 4.4.2, 4.4.3

Vestergaard M., Gültekin K., 2023, arXiv e-prints, p. arXiv:2304.10233 1.3.1

Vijarnwannaluk B., et al., 2022, ApJ, 941, 97 4.4.2

Vijarnwannaluk B., et al., 2024, MNRAS, 529, 3610 4.4.3, 4.13

Villar V., Gallego J., Pérez-González P. G., Pascual S., Noeske K., Koo D. C., Barro G., Zamorano J., 2008, ApJ, 677, 169 2.2.2

Villforth C., et al., 2017, MNRAS, 466, 812 1.2.2

Vitale S., Lynch R., Veitch J., Raymond V., Sturani R., 2014, Phys. Rev. Lett., 112, 251101 1.3.1

Volonteri M., Haardt F., Madau P., 2003, ApJ, 582, 559 1.3.1

Wada K., 2012, ApJ, 758, 66 1.3.4, 1.4.3, 4.1, 4.4.2

Wada K., 2015, ApJ, 812, 82 1.3.4, 4.1

Wang J.-M., et al., 2014, ApJ, 793, 108 1.3.1

Weaver J. R., et al., 2022, ApJS, 258, 11 2.4, 2.2.1, 2.5

Weaver J. R., et al., 2023, A&A, 677, A184 4.3.3

Webster B. L., Murdin P., 1972, Nature, 235, 37 1.1.1

Weedman D. W., 1970, ApJ, 159, 405 1.1.3

Weedman D. W., 1977, ARA&A, 15, 69 1.1.3, 1.2.1, 1.4.1

Weinberger R., et al., 2018, MNRAS, 479, 4056 4.5.1

Weisskopf M. C., Tananbaum H. D., Van Speybroeck L. P., O'Dell S. L., 2000, in Truemper J. E., Aschenbach B., eds, Society of Photo-Optical Instrumentation Engineers (SPIE) Conference Series Vol. 4012, X-Ray Optics, Instruments, and Missions III. pp 2–16 (arXiv:astro-ph/0004127), doi:10.1117/12.391545 1.4.1, 2.2, 2.1, 4.2

Weisskopf M. C., et al., 2022, Journal of Astronomical Telescopes, Instruments, and Systems, 8, 026002 1.3.3

Werner M. W., et al., 2004, ApJS, 154, 1 1.4.1

Weymann R. J., Morris S. L., Foltz C. B., Hewett P. C., 1991, ApJ, 373, 23 4.6

Whitaker K. E., et al., 2011, ApJ, 735, 86 2.2.2

Wilms J., Allen A., McCray R., 2000, ApJ, 542, 914 1.4.1

Winkler C., et al., 2003, A&A, 411, L1 1.4.1

Woltjer L., 1959, ApJ, 130, 38 1.1.3

Wright T., 1750, An original theory or new hypothesis of the universe : founded upon general phaenomena of the visible creation; and particularly the Via the laws of nature, and solving by mathematical principles : the Lactea ...compris'd in nine familiar letters from the author to his friendand : illustrated with upward of thirty graven and mezzotinto plates ..., doi:10.3931/e-rara-28672. 1.1.2

Wu X.-B., et al., 2015, Nature, 518, 512 1.3.1

Wu J., Wu Q., Xue H., Lei W., Lyu B., 2023, ApJ, 950, 106 1.4.1

Wyithe J. S. B., Loeb A., 2003, ApJ, 590, 691 1.3.1

Wylezalek D., Zakamska N. L., 2016, MNRAS, 461, 3724 1.4.3

Xia L., et al., 2011, AJ, 141, 64 2.2.3

Xue Y. Q., et al., 2011, ApJS, 195, 10 2.2.3, 2.3.1

Yamada S., Ueda Y., Tanimoto A., Imanishi M., Toba Y., Ricci C., Privon G. C., 2021, ApJS, 257, 61 4.5.2

Yan R., Blanton M. R., 2012, ApJ, 747, 61 1.2.1

Yan R., et al., 2011, ApJ, 728, 38 1.4.1

Yang G., et al., 2017, Monthly Notices of the Royal Astronomical Society, 475, 1887 3.6.1

Yang J., et al., 2021, ApJ, 923, 262 1.3.1

Yang G., et al., 2022, ApJ, 927, 192 2.4.3, 2.4.3, 4.3.2

Yang G., et al., 2023, ApJ, 950, L5 1.4.1

Yang D.-M., et al., 2024, MNRAS, 1.3.1

Yi W., et al., 2022, ApJ, 930, 5 4.5.3

Yu Q., Tremaine S., 2002, MNRAS, 335, 965 1.3.2, 1.3.6

Yuan F., Narayan R., 2014, ARA&A, 52, 529 1.3.2

Yue M., Eilers A.-C., Ananna T. T., Panagiotou C., Kara E., Miyaji T., 2024, arXiv e-prints, p. arXiv:2404.13290 5

Zakamska N. L., Greene J. E., 2014, MNRAS, 442, 784 1.3.6

Zakamska N. L., et al., 2016, MNRAS, 459, 3144 4.5.2

Zamojski M. A., et al., 2007, ApJS, 172, 468 2.2.1

Zdziarski A. A., Lubiński P., Smith D. A., 1999, MNRAS, 303, L11 1.3.3

Zel'dovich Y. B., Novikov I. D., 1964, Soviet Physics Doklady, 9, 246 1.1.3

Zhang X., Feng Y., Chen H., Yuan Q., 2020, ApJ, 905, 97 1.4.1

Zheng W., et al., 2004, ApJS, 155, 73 2.3.3

Zheng X. Z., et al., 2009, ApJ, 707, 1566 1.4.3

Zubovas K., Bourne M. A., 2017, MNRAS, 468, 4956 1.4.3

Zubovas K., King A., 2013, ApJ, 769, 51 1.3.2

van Allen J. A., Fraser L. W., Floyd J. F. R., 1948, Science, 108, 746 1.1.3

van Speybroeck L. P., 1997, in American Astronomical Society Meeting Abstracts #190. p. 34.03 2.1